THE STRUCTURE AND DYNAMICS OF ALKALI METAL-AMINE SOLUTIONS

University College London

A thesis submitted in accordance with the
requirements of the University of London
for the degree of Doctor of Philosophy

Helen Thompson

November 2003

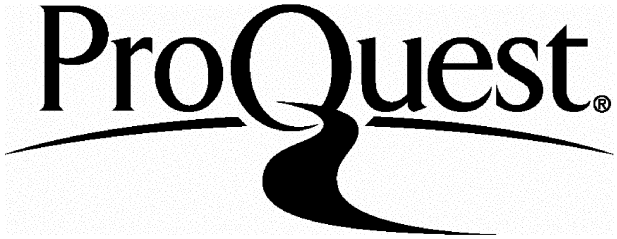

ABSTRACT

The structure of lithium-ammonia and lithium-ammonia-methylamine solutions has been studied using the technique of isotopic substitution in neutron diffraction. In pure ammonia, there is evidence for ~2.1 hydrogen bonds per nitrogen atom, with an average N-H distance of 2.4 Å. In the mixed solvent system, the ammonia molecules and the amine groups on the methylamine molecules are found to be responsible for the hydrogen-bonding present. The hydrogen-bonding is disrupted with increasing metal concentration due to both electron and ion solvation, such that no trace of hydrogen bonding remains at saturation.

Classical simulation techniques have been used to produce three-dimensional molecular configurations which are consistent with the measured data. The resulting models have identified the structure of a second cation solvation shell, in which the nitrogen atoms reside above the faces and edges of the primary shell tetrahedron. The models have also enabled the investigation of orientational correlations between molecules, as well as the propensity and distribution of polaronic electron cavities. At dilute metal concentrations, the electrons are fully solvated by approximately 9 ammonia molecules. As the metal content is increased, the molecules re-orientate such that at saturation, percolation channels are formed between the solvated cation complexes.

The dynamics of ammonia and lithium-ammonia solutions have been measured using the techniques of quasi-elastic neutron scattering and molecular dynamics simulation. The proton diffusion rates of the liquids at 230 K are found to increase with metal concentration to 7.84×10^{-5} $cm^2 s^{-1}$ at 12 MPM and decrease thereafter. The proton diffusion rate of the saturated solution decreases upon a decrease in temperature, and can be modelled as a jump-diffusion process. At temperatures below the liquid-solid phase transition temperature, a localised rotation of the solvent molecules in saturated lithium-ammonia compounds at 75 K and 40 K and ammonia at 150 K is observed.

ACKNOWLEDGEMENTS

I would like to thank my supervisor, Neal Skipper, for his advice, encouragement and support over the course of my PhD. Thanks must also go to Jonathan Wasse, Chris Howard and Tom Weller for their friendship and unstinting help and good humour, especially during the long nights at ISIS!

I would also like to thank the instrument scientists on SANDALS and IRIS: Alan Soper, Daniel Bowron, Piers Buchanan, Spencer Howells and Myles Hamilton, for their assistance with the experimental work and data analysis. Thanks also go to Peter Edwards and Robert McGreevy for their invaluable discussions and advice. I am grateful to the Rutherford Appleton Laboratory for the beam time and financial support, and would like to thank all the sample environment staff at ISIS, particularly John Dreyer, Chris Goodway, Jon Bones and Duncan Francis.

Thanks to everyone at UCL for their friendship and encouragement: Jonathan Allen, Eamonn Beirne, Simon Armitage, Louise Affleck, Hayley Spiers, Daniel Ucko and Gary Martin, as well as those further afield: Katherine Cooper, Jo Wyld, Susan Sturton, Ian Cockburn, Rob Knowles and Jeremy Samuel. I owe particular thanks to Shusaku Hayama for his continual patience and support, and a careful proof-reading of the manuscript. Finally, thankyou to my family for the love and support they have given me throughout my life.

CONTENTS

LIST OF FIGURES

Chapter 1 Introduction

LIST OF TABLES

CHAPTER 1

INTRODUCTION

1.1 Historical Perspectives

Ammonia and amines are hydrogen-bonded solvents with the unique ability to accommodate high concentrations of metastable solvated electronic species, thereby forming a highly expanded metallic state. Such 'metal solutions' offer the opportunity to study many fundamental physical phenomena, including liquid-liquid phase separation, extreme redox reactivity, very low density and viscosity, the metal-nonmetal transition and the concomitant role of hydrogen-bonding.[1-8] Much interest now lies in the structure of these solutions, particularly the nature of the solvent-solvent interactions and the way in which the excess electrons are accommodated.

Sir Humphry Davy was the first to observe the striking metallic appearance of a concentrated solution of potassium in ammonia and the 'fine blue colour' obtained upon its subsequent dilution, during a series of experiments carried out in 1808 to demonstrate that potassium was indeed an element.[2] Since then, other alkali

metals, alkaline earth metals and rare earth metals have also been found to dissolve in anhydrous liquid ammonia, methylamine and a variety of other solvents.[1,2] The resulting metal solutions have been at the centre of much experimental and theoretical research over the last century. In 1946, Ogg proposed the possibility of a Bose-Einstein condensation of trapped electron pairs in quenched metal-ammonia solutions, reporting that the solid solutions became superconducting at 180 – 190 K.[9] A series of conferences focusing on metal-amine solutions and their properties, 'Colloque Weyl', was begun in 1964. Recently, the advent of both classical and ab-initio molecular modelling, together with advances in neutron and X-ray diffraction techniques, has initiated a new wave of interest in these fascinating solutions.

It is only recently that the molecular structure of metal-amine solutions has been extensively investigated, primarily due to the difficulty of achieving a stable sample environment for these highly reactive liquids. A wide range of structural data, obtained via neutron and X-ray diffraction, is now detailed in the literature. This information is crucial if we are to gain further understanding into the processes which give rise to these remarkable macroscopic properties.[10-12]

More recent work has included the intercalation of metal-amine solutions into materials such as graphite and molybdenum disulphide, in order to change the conducting properties of the substrate. High concentrations of C_{60} fullerenes have also been found to dissolve in metal-amine solutions: ammonia is used as a solvent catalyst in the production of many M_3C_{60} superconducting compounds.[13]

1.2 Ammonia and methylamine as solvents

Interest in the microscopic structure of liquid ammonia and methylamine arises mainly from the propensity of the amine groups to form hydrogen bonds,[8,14,15] and their ability to act as a stable solvent for a variety of chemically reactive species. For example, liquid ammonia is used as a catalyst for many common organic reactions.[16] Ammonia and amines are also unique in their ability to dissolve alkali metals, releasing the valence electrons into solution.

Structurally, the ammonia molecule has a trigonal pyramidal arrangement with the three hydrogen atoms at ~1.01 Å from the apex nitrogen atom, the internal H-N-H angles being ~107° (figure 1.1(a)). The structure of a methylamine molecule (figure 1.1(b)) is similar, with one hydrogen atom being replaced by a methyl ($-CH_3$) group at ~1.5 Å from the nitrogen atom. Ammonia and methylamine are similar to water in the respect that they both exhibit a degree of hydrogen bonding.[8,14,15] However, ammonia and methylamine molecules have only one lone pair of electrons available to accept hydrogen bonds, leading to relatively weak association in the liquid state. The internal energy of liquid ammonia is around 21 kJ mol^{-1}, approximately half the value for bulk water, and the hydrogen-bonding occurs at a N-H distance of ~2.4 Å, compared to the hydrogen-bonded O-H distance of ~1.9 Å in water.[17] Previous neutron and X-ray diffraction experiments and computer simulations on ammonia and methylamine have pointed to relatively weak hydrogen-bonding in the liquid phase, giving ~2.0 and ~1.0 hydrogen bonds per nitrogen atom in liquid ammonia and methylamine respectively.[14,15,18-20]

Methylamine has a lower polarisability than ammonia: the dipole moment is only 1.479 Debye as compared to 1.847 Debye in ammonia. The dissolution process of alkali metals in methylamine is also somewhat slower than in ammonia: this is likely to lead to critical differences in the way in which the ions and electrons are solvated.

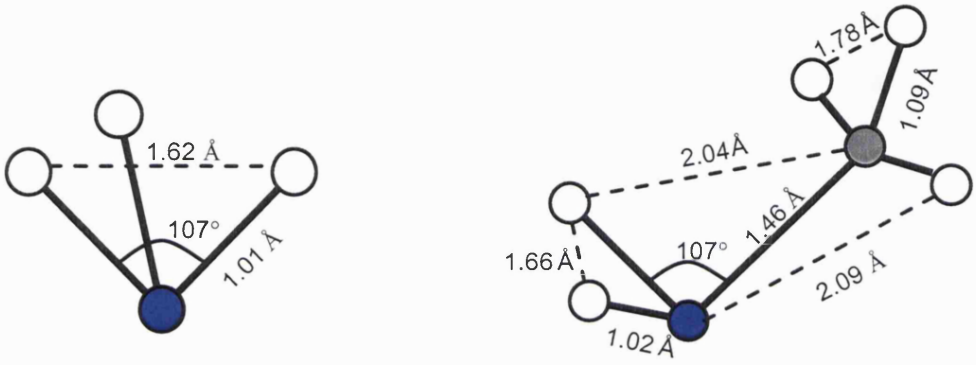

Figure 1.1 The structure of an ammonia and a methylamine molecule.

	Ammonia	Methylamine
Melting point	195.41 K	179.71 K
Boiling point	239.82 K	266.83 K
Density of liquid	0.68 g cm^{-3} at 240 K	0.75 g cm^{-3} at 220 K
Molecular Weight	31.057 g/mol	17.03 g/mol
Vapour pressure	0.608 bar at 230 K 1.52 bar at 248 K	0.404 bar at 248 K
Dielectric constant ε	16.5 at 293 K	9.4 at 293 K
Dipole moment	1.847 Debye	1.479 Debye

Table 1.1 Physical properties of ammonia and methylamine, taken from Ref. [21].

1.3 Properties of alkali metal-amine solutions

The dissolution of an alkali-metal in an amine solvent produces metastable solutions in which the valence electron is released into solution via solvation of the metal cation (eq. 1.1). This process occurs spontaneously without chemical reaction, and is fully reversible: all the solvent can be recovered after the preparation of these solutions.[1-6]

$$M \leftrightarrow M_S^+ + e_S^- \tag{1.1}$$

In the presence of impurities, the metal solutions may decompose to form the metal-amide and hydrogen:

$$M_S^+ + NH_3 \rightarrow M^+(NH_2^-) + \frac{1}{2}H_2(g) \tag{1.2}$$

Concentrated metal-ammonia solutions of 7-20 mole percent metal (MPM) assume a bronze-coloured metallic appearance: here the electrons are genuinely delocalised, and the conductivity reaches 15000 $\Omega^{-1}cm^{-1}$ at saturation.[1-6] Upon dilution to ~4 MPM, the solution undergoes a metal-nonmetal transition. Cooling at this composition leads to a small region of liquid-liquid phase separation. Below this concentration, the conductivity decreases sharply by an order of magnitude (figure 1.2), yielding an insulating solution of an intense blue colour – the signature of solvated electrons. The phase diagram (figure 1.3) shows the onset of the metal-nonmetal transition, in addition to the region of liquid-liquid phase separation associated with the transition. The dissolution of lithium in methylamine produces solutions with similar properties to those of the lithium-ammonia system, in which

solvation of the ions also produces a rich variety of ionic and electronic species. These include isolated polarons, spin-paired bipolarons, solvated metal cations, ion triples and ion-dielectron pairs[2,6] (figure 1.5). In contrast to lithium-ammonia, saturated solutions of lithium in methylamine have a conductivity of only 400 Ω^{-1} cm^{-1}. The solutions are deep-blue in colour throughout the entire concentration range, indicating the presence of solvated electrons.[1] Upon dilution to 12 MPM, the conductivity decreases by two orders of magnitude, with a metal-nonmetal transition occurring at approximately 15 MPM.

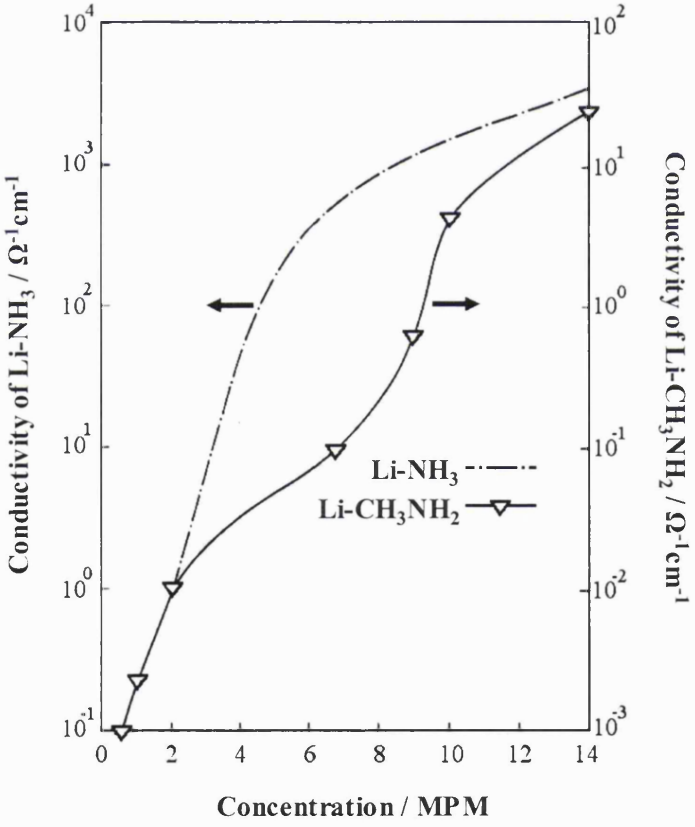

Figure 1.2 Conductivity of lithium-ammonia and lithium-methylamine solutions.[1] Note that the conductivity of lithium-methylamine is lower than that of lithium ammonia, and that the metal-nonmetal transition occurs at ~14 MPM rather than 4 MPM.

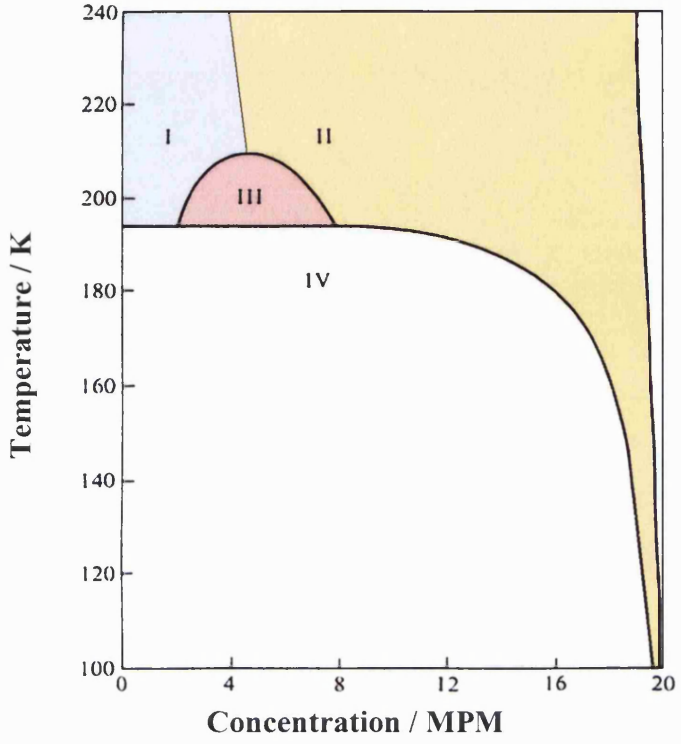

Figure 1.3. Phase diagram of the lithium-ammonia solution.[1] I) Non-metallic dilute phase, II) Metallic concentrated phase, III) Liquid-liquid phase separation, IV) Solid ammonia & expanded metal.

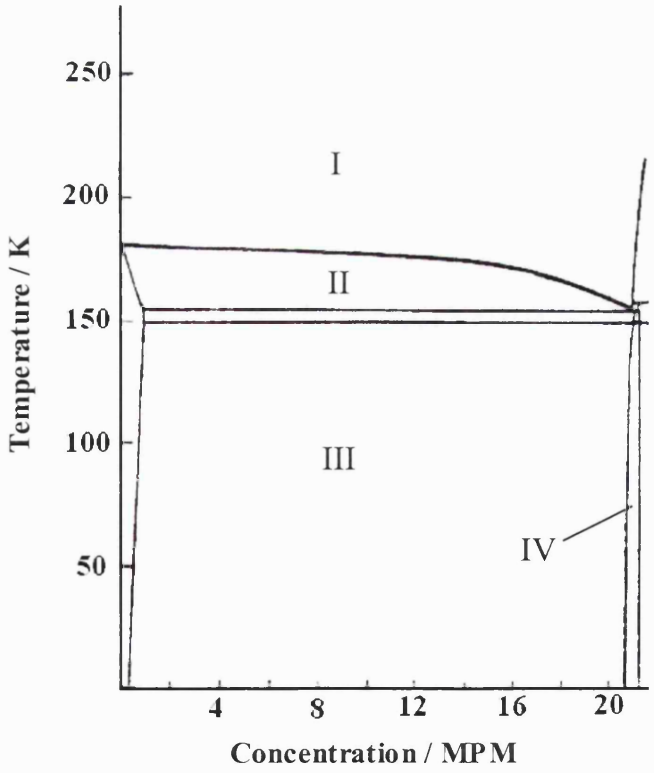

Figure 1.4: Phase diagram of the lithium-methylamine solution.[22] I) Liquid lithium-methylamine, II) Solid methylamine & liquid lithium-methylamine solution, III) Solid methylamine and Li-$(CH_3NH_2)_4$, IV) Solid Li-$(CH_3NH_2)_4$

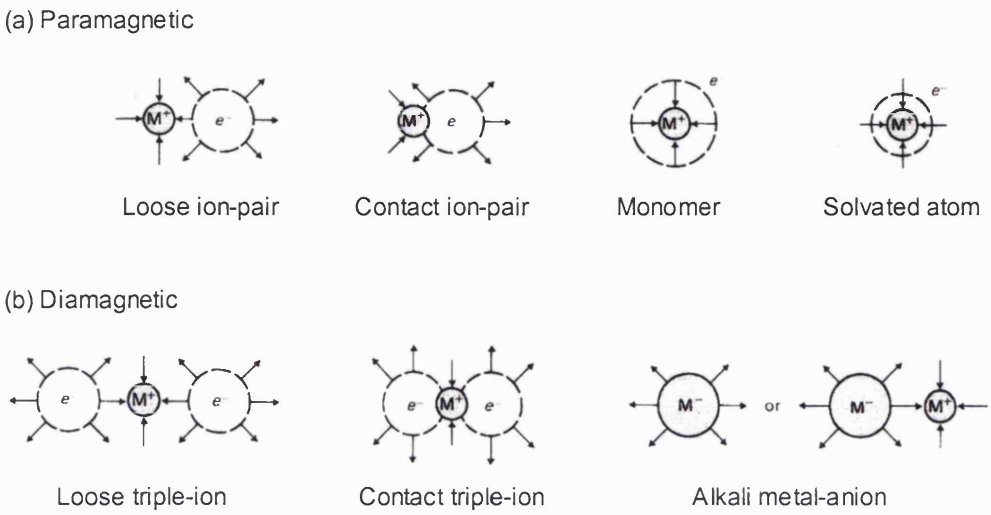

Figure 1.5 Schematic of the proposed paramagnetic and diamagnetic species in the dilute and intermediate concentration range.[2]

1.3.1 Concentrated Solutions

Metallic solutions of alkali-metal ammonia solutions are bronze coloured and the conductivity of a lithium ammonia solution reaches 15000 $\Omega^{-1}cm^{-1}$ at saturation. The dominant species are solvated metal cations, solvent molecules not bound to a cation, and genuinely delocalised electrons[23] (figure 1.7). This is confirmed by self-diffusion measurements,[24,1] which show that the self-diffusion coefficient of the lithium ion in metal-ammonia solutions is smaller than that for a simple lithium atom, indicating that the motion of the ion is impeded in some way. Furthermore, the self-diffusion coefficients of hydrogen and lithium are equal in the saturated solution (20 MPM: one lithium atom to four ammonia molecules), showing that the lithium ions are fully solvated by ammonia molecules.[1]

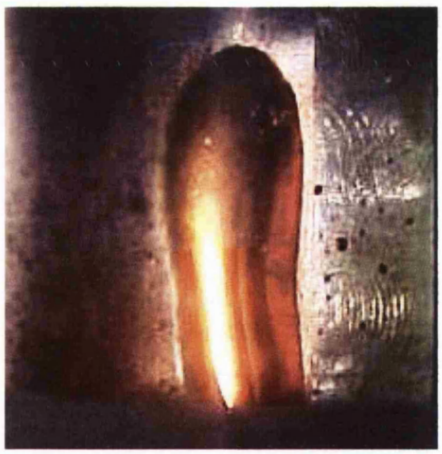

Figure 1.6 Saturated solution of lithium in ammonia.

The resistivity in this region is likely to be due to scattering of itinerant electrons by solvated cations and the dipole moments of ammonia molecules not bound to the cations. The drop in the number of 'unbound' ammonia molecules with

increasing metal concentration then accounts for the rapid increase in conductivity.[25] In this regime the measured Hall coefficient[26-28] is the same as for the free-electron model; the carrier density is equal to the density of metal valence electrons and is temperature-independent, except as the density of the solutions varies with temperature. These observations confirm that these concentrated solutions are indeed liquid metals.[1]

The electrical conductivity of a saturated lithium-methylamine solution is 400 $\Omega^{-1}cm^{-1}$, a value which is an order of magnitude lower than that for saturated lithium-ammonia solutions, and which lies just above Mott's minimum criterion for a metal. These solutions also remain blue in colour even at high metallic concentrations of 16 – 22 MPM. This implies a much stronger localisation of the electrons: it has been suggested that the electrical properties here lie in the strongly scattering regime. The conduction process here is best described by a diffusive, Brownian-like hopping of weakly interacting electrons between cavities about 7Å apart.[29,30]

Perhaps the most-studied property of metal-amine solutions is their large increase in volume with metal concentration,[31-38] illustrated in Figure 1.8. The density of a saturated lithium-ammonia solution is only 0.477 g cm^{-3}, making it one of the lightest liquids known.[1,6] There exist several possible explanations for this volume expansion. One theory supposes that cavities are still formed (as in the dilute solutions), the metallic electrons having large values of their wavefunction, ψ, within the cavities.[39] The density of states would then not be unlike those for an impurity band, and the positive dependence of conductivity upon temperature would be due to a smearing out of the impurity band as the temperature is raised. However, at high

concentrations the mean free path is so large that no tight binding band due to cavities can exist.[7] Another possible explanation is that volume expansion is caused by Bjerrum defects:[40] site defects in crystals such as ice, at which the positive charges in two dipole moments point towards each other.[41] At high metal concentrations the rate of change of polarisation of the ammonia molecules between cations is so great that a Bjerrum-type expansion is highly probable.[40]

Other bulk properties of concentrated metal-amine solutions include a low vapour pressure which tends to zero at high metal concentrations, and low viscosity, which is found to be a decreasing function of both metal concentration and temperature, becoming immeasurably small at saturation.[1]

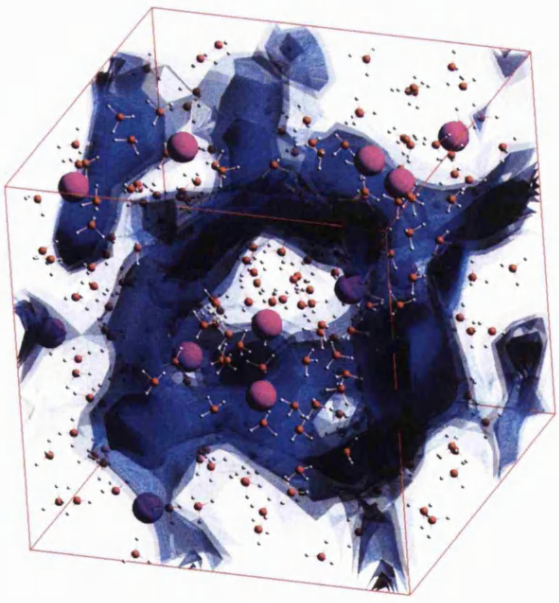

Figure 1.7 Snapshot from a quantum simulation of a saturated caesium-ammonia solution[23] – the blue colour represents regions of high electron density.

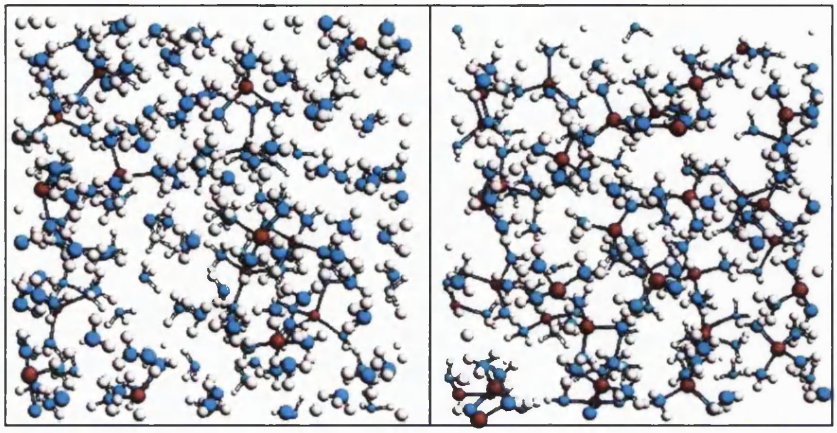

Figure 1.8 Snapshots from molecular dynamics simulations: (a) Li-NH_3 at 8 MPM and (b) Li-NH_3 at 20 MPM, illustrating the volume expansion as the metal concentration is increased.

1.3.2 The metal-nonmetal transition

Upon dilution, the lithium-ammonia solution passes through a metal-nonmetal transition at around 4 MPM. Much interest has centred around the presence of electron spin-pairing and the possibility of bipolaron formation (figure 1.10)[23] at and below the transition region.[6] In 1946, Ogg raised the question of whether high T_c superconductivity and Bose-Einstein condensation is viable in these solutions after quenching in liquid nitrogen, and in fact claimed to have observed persistent electric currents in dilute sodium-ammonia solutions which did not decay with time after the magnetic field was removed.[9] Unfortunately, this observation of superconductivity has not been reproduced since with any degree of consistency. However, since the

time of Ogg, strong evidence for the presence of spin-pairing in metal-amine solutions has come to light,[3-5] which will be discussed in the next section.

Figure 1.9 Lithium-ammonia solution at 3 MPM

In lithium-methylamine solutions, there exists a sharp change in the conductivity between 11 MPM and 7 MPM,[27,42] from 10 $\Omega^{-1}cm^{-1}$ to 0.1 $\Omega^{-1}cm^{-1}$. There is also evidence for a wider range of solvated electronic species to exist within lithium-methylamine solutions, for example: metal anions and contact triple ions.[3-5,29] In metal-ammonia solutions, the localisation of the electron on sites separate from the cation leads to a stronger tendency for the solvated electron wavefunction to have appreciable amplitude outside the cavity.[1] In methylamine, however, the larger size of the solvent molecule together with the tighter binding arising from the presence of the metal cation within a two-electron cavity apparently precludes a truly metallic phase.[1,43,44]

In metal-ammonia solutions between 6 and 3 MPM, the Hall coefficient rises above the free electron value[27] and the conductivity falls to between 10 and 100

$\Omega^{-1}cm^{-1}$. This, and the paramagnetic behaviour, lead to the conclusion that the metal-nonmetal transition is a 'band-crossing' type: two bands are present, one for an extra electron on a molecular dimer (a spin-paired diamagnetic species) and one for a hole on the dimer. The transition occurs when these two bands overlap.[7] Both the transitions across the pseudogap and the singlet-triplet transitions within the spin-paired species will have small oscillator strength, thus a low high-frequency dielectric constant. Mott's condition that a screened Coulomb well contains no bound states (necessary for the onset of metallization), is:

$$n^{\frac{1}{3}} a_H = 0.25, \quad \text{where } a_H = h^2 \varepsilon / m^* e^2 .$$

It is clear then that a small low-frequency dielectric constant leads to a large jump in the number of free carriers, *n*, as the transition occurs. This discontinuity produces a kink in the free energy versus composition curve, and accounts for the region of liquid-liquid phase separation around 4 MPM for temperatures below ~ 200 K.[7] Thus the dominant mechanism for the metal-nonmetal transition appears to be of Mott type rather than Anderson (disorder) type. Indeed, Mott himself suggested that the electrostatic repulsion between ions in concentrated metal ammonia solutions dictates short-range order, and the remaining disorder is not sufficient to get rid of the discontinuity in the free energy versus composition curve.[3]

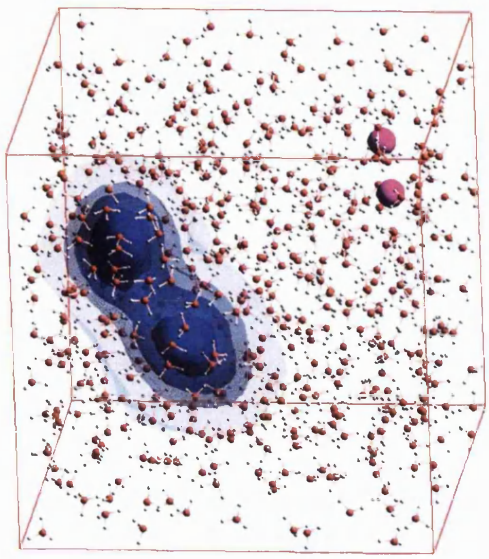

Figure 1.10 Formation of a peanut-shaped bipolaron in a caesium ammonia solution, predicted by quantum simulation.[23]

1.3.3 Dilute Solutions

Below ~3 MPM the alkali metal-ammonia solution is of an intense blue colour and the conductivity is below that required for a metal.[1,7] Between 3 and 0.3 MPM the system may be likened to an intrinsic semiconductor. At ~1 MPM, d (ln σ)/dT has a maximum, and d(ln σ)/dp a minimum. Before dσ/dT rises, the current is carried by electrons at the Fermi energy (overlapping of electron and hole bands on the dimers). When the states become Anderson-localised (i.e: the system's disorder is such that an electron, trapped on a given site, is unable to find another site which is sufficiently close and has a state at the same energy), the current is carried mainly by electrons at the mobility edge - the excitation energy here is low enough. Hopping conduction is not observed, and the change of sign in dS/dT (rate of change of

thermopower with temperature) signifies the change from metallic to semiconducting behaviour.[7] The decrease of conductivity with pressure is thought to be due to contraction of the electronic cavity which consequently produces an increase in the Coulombic repulsion.[7]

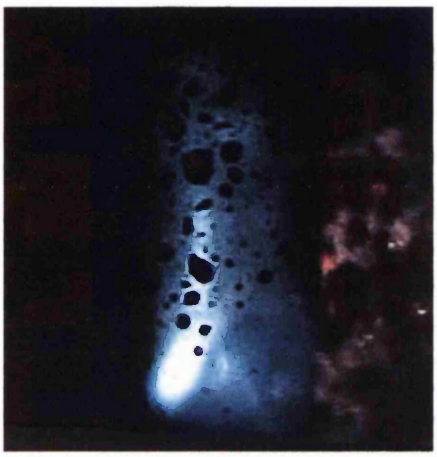

Figure 1.11 Lithium-ammonia solution at 2 MPM.

The current is carried by the mass movement of the solvated electron, the evidence of which lies in the relatively low ratio of the conductances of anion and cation at infinite dilution.[45] This indicates that the electron cannot be free as in the metallic sense. There is also a lack of variation of optical absorption with solute, suggesting that the excess electron is independent of the cation. The large density decrease with respect to the pure solvent implies some kind of cavity formation,[45-46] and the relaxation of the electronic spins by nitrogen interaction and the correlation of hydrogen and nitrogen Knight shifts point to the presence of solvent molecules on the boundary of such a cavity.[1,29] Proposed species in the dilute regime therefore include solvated metal cations, solvated electrons, neutral and charged agglomerates and various polaronic states.[6]

Near the metal-nonmetal transition, compelling evidence for the formation of diamagnetic 'molecular dimers' is the fact that the electronic contribution to the paramagnetism decreases with decreasing concentration.[7] The observed increase of the electronic contribution to the paramagnetism with temperature may well be due to dissociation of these molecular dimers.[7,22] In addition, the molar spin susceptibility of metal-ammonia solutions in the range 10^{-3} to 1 MPM is below that expected for an assembly of non-interacting electrons.[3] This represents direct evidence for the formation of diamagnetic complexes containing an even number of excess electrons, being spin-paired in a singlet (S = 0) ground state. The precise nature of this electron-pair state is still debatable; some possibilities are illustrated in Figure 1.5. However, quantum calculations have demonstrated that a spherical cavity containing two electrons is likely to be stable against separation into two isolated solvated electrons.[47-56]

As the concentration is decreased still further to ~10^{-3} to 10^{-4} MPM, the metal-ammonia solution becomes electrolytic in nature; ion-pairing and species such as the ion-pair $M_s^+e_s^-$ are signalled by the behaviour of both the metal (Knight-shifted) NMR and the equivalent conductance which exhibits a minimum in the conductance vs. concentration curve.[6] The ion-pairing association $M_s^+ + e_s^- \leftrightarrow M_s^+e_s^-$ is best viewed as a short-lived (10^{-12} s) encounter complex in the solution.

The absorption spectrum of dilute solutions was measured by Burow and Lagowski: the high energy tail extends into the visible spectrum, giving rise to the characteristic blue colour of solvated electrons.[57] The broad absorption band in the near infra-red is associated with the 1s $\rightarrow$ 2p transition of the electron within the

potential well, in accordance with the solvated electron model proposed by Jortner.[58-59,39,40] This model envisages the electron moving in a cavity of radius R ≈ 3Å, around which the surrounding liquid is polarized. This produces a constant potential within the cavity which is dependent upon the polarisability of the solvent:

$$V(r) = \frac{-e^2}{R}\left(\frac{1}{\varepsilon_\infty} - \frac{1}{\varepsilon_0}\right), \mathrm{r} < \mathrm{R}. \qquad (1.3)$$

This potential acts back on the electron. Here, ε_∞ and ε_0 are the high and low frequency dielectric constants of the solvent, respectively. Outside the cavity, the electron will experience a different potential:

$$V(r) = \frac{-e^2}{r}\left(\frac{1}{\varepsilon_\infty} - \frac{1}{\varepsilon_0}\right), \mathrm{r} > \mathrm{R}, \qquad (1.4)$$

giving a total potential for the solvated electron as shown in figure 1.12.

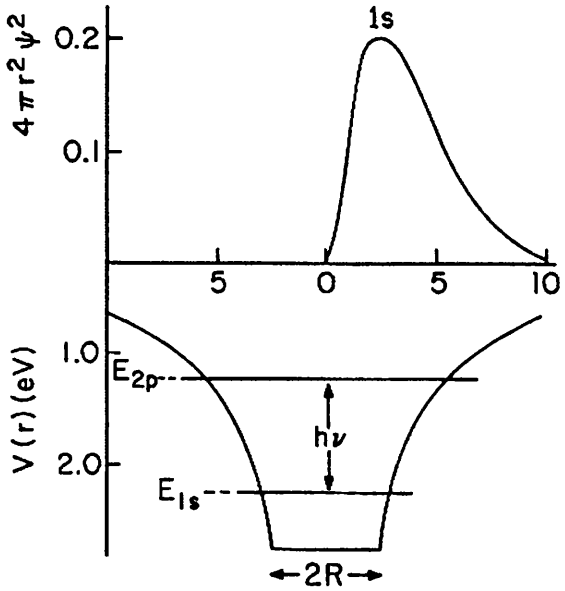

Figure 1.12 Diagram showing the total potential for the electron and the corresponding 1s wavefunction.[39] Jortner's model required $V_0 = 0$ (that of an electron in free space) to obtain agreement with experiment. A cavity of radius ~3 Å leads to a ground state energy of 1.6 eV.

There are several possible explanations for the origin of the cavity; the following are the two most likely theories:

i) The Bjerrum defect:[40] a site in which the positive charges in two dipolar molecules point towards each other.[41] Around a self-trapped electron the direction of polarization must change rapidly, and energy ought to be lowered if a cavity is formed on account of the repulsion between like charges on ammonia molecules. A schematic of the steps involved in the solvation of an electron, leading to overall expansion of the first solvation

shell and rotation of solvent molecules in order to reduce such effects, is shown in figure 1.13.

ii) A region of low density around the electron rather than a cavity.[60-61]

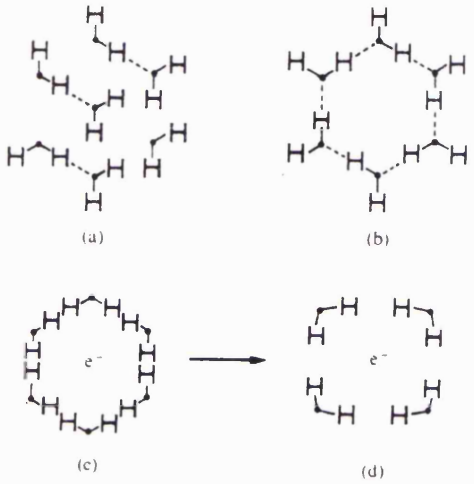

Figure 1.13 Steps in the formation of a Bjerrum-type expansion:[40] (a) Hydrogen-bonded ammonia, (b) Cavity formation in the liquid, of radius ~1.5 Å, the size of a single ammonia molecule, (c) Presence of an electron tends to orient the dipoles in the first shell, (d) Orientation opposition by thermal agitation, dipole-dipole repulsion and H-H repulsion (Bjerrum defect).

The diffusion coefficient and mobility of a solvated electron are much smaller than that of a free electron. However, they are five times larger than those of a solvated cation. Hence there is considerable doubt as to whether the electron diffuses with its solvation shell, or whether conduction occurs via hopping of the electrons from one low density region to another.[7]

The solvated electron species is similar in lithium-ammonia and lithium-methylamine solutions, although details of the solvated electron radius and coordination number vary. In lithium-ammonia solutions, magnetic resonance studies suggest that the excess electrons are solvated by a first shell of 6 solvent molecules and a second shell of 12 molecules, with nitrogen-14 coupling constants of ~12 G and ~3 G for each of the solvent molecules in the first and second shells respectively.[5] In lithium-methylamine solutions, a first shell of ~4 solvent molecules with a nitrogen-14 coupling constant of ~10 G per molecule is consistent with the electron spin resonance data. This indicates a high degree of localization of the electron (spin) wavefunction within the solvent cavity and on the primary solvation shell. In addition, the characteristic residence time for an electron is $2 - 5 \times 10^{-11}$ s in lithium-methylamine solutions, compared to $\sim 5 \times 10^{-13}$ s in dilute lithium-ammonia solutions.[5]

Nevertheless, the basic structure of Jortner's model still holds: the dielectric constant of the solvent medium is the key factor in determining the strength of the solvated electron potential.[1] The lower dielectric constant of methylamine appears to confine the electron's wavefunction within the cavity, thus reducing the overlap interactions which are the origin of both the spin-pairing and metallization processes.[62]

1.4 Structural information on metal-amine solutions

Knowledge of the structure of materials at a molecular level is crucial if we are to gain a full understanding of their physical properties.[10-12] However, it is only recently that it has become possible to perform detailed structural measurements on metal-amine solutions, primarily due to the difficulty in preparing samples which remain stable over the time periods necessary to collect high-resolution diffraction data.

Isotopic substitution in neutron diffraction and wide-angle X-ray diffraction are now standard techniques for investigating the structure of many materials. These have been used to determine the structure of solutions of lithium, sodium and potassium in ammonia at various concentrations. The measured total structure factors from both neutron diffraction and X-ray experiments show a shift inwards of the principal peak with increasing metal concentration, reflecting the decrease in density as the solution expands to accommodate the excess electrons.[63-67]

Several studies have been made into the role of the ion in metal-amine solutions: it has been found that lithium ions are four-fold solvated by ammonia molecules in a tetrahedral arrangement, with a Li-N distance of ~2.05 Å.[63,65] Sodium[64] and potassium[66] ions are found to be solvated by 5 and 6 ammonia molecules respectively, with Na-N and K-N distances of 2.45 and 2.85 Å.

Saturated solutions of lithium and sodium in ammonia give rise to a pre-peak at ~1 $Å^{-1}$ and 0.85 $Å^{-1}$ respectively.[63,64] The pre-peak positions are attributed to contacts between solvated cations, which have a smaller radius in lithium-ammonia solutions than sodium-ammonia solutions. No such pre-peak is observed in

potassium-ammonia solutions[66] or solutions of lithium or sodium in ammonia at lower concentrations.[65]

X-ray diffraction experiments on a saturated lithium-ammonia solution[67] also reveal a strong pre-peak at ~1.05 $Å^{-1}$. Upon decreasing the metal content, the pre-peak is found to shift to higher Q-values of 1.22 $Å^{-1}$ and 1.29 $Å^{-1}$ for concentrations of 8 MPM and 2 MPM respectively.[67] Knapp and Bale also carried out low-angle X-ray diffraction on metal-amine solutions.[68] Their data, which extend to Q_{max} = 1 $Å^{-1}$, showed that the pre-peak moves to lower Q-values with decreasing metal concentration. This leads to the hypothesis that the pre-peak may split into two components. The component that moves to lower Q values with decreasing metal concentration has been attributed to increased separation between solvated cations.[68] The component that moves to higher Q values therefore arises from solvent molecules which are not involved in the primary ionic solvation shell, and is a signature of the formation of polaronic cavities of radius ~2.6 Å. The dominant species in the dilute solutions are then likely to be weakly interacting solvated electrons, possibly in association with a cation.

Hydrogen/deuterium isotopic substitution[15] and first-order lithium-difference experiments[30] have been performed on lithium-methylamine solutions to determine the effect of changing the solvent on the microscopic structure. The experiments provided evidence of one hydrogen bond per nitrogen atom in the pure methylamine liquid.[15] The hydrogen-bonding was found to be disrupted as the concentration of ions and excess electrons was increased, due to competition for the NH_2 groups from the lithium ions. Lithium-centred difference functions at 8 MPM and 22 MPM revealed that the cations are solvated by ~4 solvent molecules.[30] In the saturated

solution, a pre-peak was observed at ~0.88 $Å^{-1}$, which is again consistent with correlations between solvated cations which have a smaller radius in ammonia than in methylamine.[15]

1.5 Classical and quantum simulation of alkali-metal-amine solutions

Several simulations of amine solvents and metal-amine solutions have been performed to investigate the solvent structure, hydrogen-bonding and the behaviour of both ions and electrons in solution. Early simulations on the pure ammonia system via ab-initio molecular orbital calculations[19] predicted a linear hydrogen-bond dimer geometry. Later simulations using Car-Parrinello molecular dynamics methods[69] found the ammonia dimer equilibrium geometry to be strongly non-linear. These results compared well to neutron data,[14] although the intermolecular peak in the N-H radial distribution function corresponding to hydrogen-bonding was less intense than that in the experimental data, giving only ~2 hydrogen bonds per ammonia molecule. Simulations by Jorgensen, using classical force-field parameters developed by fitting to experimental data for the pure liquid and to hydrogen-bond strengths from gas-phase ab-initio calculations, yielded an average number of 2.56 hydrogen bonds in liquid ammonia.[20]

The solvation of ions in amine solvents has also been the subject of much theoretical work, from classical to ab-initio simulation methods. Classical Monte Carlo (MC)[70] and molecular dynamics (MD)[71] simulations which used potentials parametrized in part to ab-initio molecular orbital calculations, give rise to four-fold

solvation of the lithium cation at a Li-N distance of 2.05 Å. The MD results also show evidence for a second solvation shell around the ion, which is hydrogen-bonded to the first shell.[71] The classical MC simulations suggest that the second shell is less strongly bound to the ion, and behaves as a normal fluid.[70]

'Hot-spot' calculations[72] have also been used to determine the co-ordination numbers and positions of the solvation shells for the lithium ion in solution. The 'hot-spot' method uses a quantum-mechanical treatment for the region surrounding the ion, and a classical simulation technique for the remainder of the system. Hot-spot calculations using semi-empirical potentials give a Li-N first shell co-ordination number of 6 solvent molecules at a distance of 2.42 Å. Ab-initio potentials, however, give a co-ordination number of 4 solvent molecules at a lower distance of 2.15 Å.[72]

Further work included the role of electrons in metal-ammonia solutions. Early path-integral Monte Carlo (PIMC) calculations found the solvated lithium atom to be in a dipolar state.[73] Later studies, which used an electron-ammonia potential parametrized to ab-initio quantum calculations, found that the valence electron spontaneously dissociated from the lithium atom.[74]

PIMC was also used to evaluate the free-energy and entropy change associated with electron solvation in liquid ammonia.[75] The entropy change was found to be negative: this was attributed to the fact that the electron induces local ordering of the solvent molecules. Experimentally, however, the entropy change is positive at constant pressure, due to the work done in expanding the fluid in order that the excess electrons can be accommodated.[76,77]

In addition, PIMC has been used to investigate the structure of electrons in solution. The minimum energy state of the electron was found to be highly localized, with a first shell co-ordination number of ~8 solvent molecules.[78] The results were compared to the solvation of a classical Cl^- anion: the solvation shell of the anion was found to comprise ~9 solvent molecules, and the orientation was such that one hydrogen atom on each of the nearest ammonia molecules was pointing directly towards the anion.[78] The electron-centred radial distribution functions were also found to be less structured than those for the classical anion. The lack of a clear second peak in the e^--H radial distribution function was attributed to a significant degree of disorder in the bond orientation of the electronic solvation shell. This less well-defined orientation of solvent molecules around the diffuse electron charge density distribution thus demonstrated the difference between a quantum and a classical solute.[78]

Car-Parrinello simulations have been used to investigate the solvation of electrons at higher concentrations.[23,79,80] In the concentration region of ~1 MPM, experimental evidence exists for the spin-pairing of the electrons in either a singlet or triplet state.[1] The simulations show that in the singlet state, the electrons assume a peanut-shaped distribution, with a peak in the electron density at a separation of ~7 Å.[79] In the triplet state, the electrons form two distinct spherical cavities. Hopping of the electrons from peanut-shaped cavities to spherical cavities, back to peanut-shaped cavities in different regions is observed, leading to diffusion of the bipolaron through the fluid.[79]

At higher electron concentrations, the simulations show that the bipolarons exhibit a tendency to cluster.[80] At still higher concentrations, the electron density becomes delocalised and spans the system, indicating that the system has become metallic.[23,80]

1.6 Scope of thesis

This chapter has summarized much of the theoretical and experimental work performed so far on metal-amine systems. However, several key questions remain. The first of these is the nature of the solvent-solvent interactions, and their involvement in the metal-nonmetal transition. Lithium-ammonia-methylamine is significant in this respect, as the static dielectric constant of the solvent is controllable, and both this and the molecular size have a strong impact on the degree of electron localization.

Much interest lies in the nature of the electronic states in metal-amine solutions, although work in this particular area has been mainly theoretical, as detailed in section 1.5. It is now important to look from an experimental point of view for evidence that the host solvent is able to form cavities, channels or low-density regions through which these electrons might percolate.

The work presented in this thesis uses the method of hydrogen/deuterium isotopic substitution to focus on the solvent structure in lithium-ammonia and lithium-mixed solvent solutions, as well as the pure solvents: ammonia and ammonia:methylamine mixtures at molar ratios of 20:80, 50:50 and 80:20. This work also draws on classical modelling techniques in order to construct three-

dimensional models which are consistent with the measured data. These models can be used to investigate the way in which the cations and excess electrons are accommodated in the solution, as well as orientational correlations between molecules.

The change in structure of the solvent due to accommodation of electronic and ionic species in the solutions is also likely to lead to changes in the dynamics. Quasi-elastic neutron scattering and molecular dynamics simulations have therefore been performed in order to investigate the diffusion processes and rotational modes of the solvent molecules, and are complementary to previous self-diffusion measurements obtained via nuclear magnetic resonance (NMR).[24]

1.7 References

[1] J. C. Thompson, *Electrons in Liquid Ammonia* (Clarendon, Oxford 1976).

[2] D. Holton, P. P. Edwards, Chemistry in Britain, 1007 (1985).

[3] P. P. Edwards, Phys. Chem. Liq. **10**, 189 (1981).

[4] P. P. Edwards, Adv. Inorg. Chem. Radiochem. **25**, 135 (1982).

[5] P. P. Edwards, J. Phys. Chem **88**, 3772 (1984).

[6] P. P. Edwards, Journal of Superconductivity **13**, 933 (2000).

[7] N. F. Mott, *Metal-Insulator Transitions* (Taylor and Francis, London 1990).

[8] H. Thompson, J. C. Wasse, N. T. Skipper, S. Hayama, D. T. Bowron and A. K. Soper, J. Am. Chem. Soc. **125**, 2572 (2003).

[9] R. A. Ogg, Jr., Phys. Rev. **70**, 93 (1946).

[10] I. Howell and G. W. Neilson, J. Phys. Condens. Matter, **8**, 4455 (1996).

[11] A. K. Soper, J. Phys. Condens. Matter, **9**, 2717 (1997).

[12] D. T. Bowron, J. C. Finney and A. K. Soper, J. Phys. Chem. B. **102**, 3551 (1998).

[13] D. R. Buffinger, R. P. Ziebarth, V. A. Stenger, C. Recchia and C. H. Pennington, J. Am. Chem. Soc. **115**, 9267 (1993).

[14] M. A. Ricci, M. Nardone, F. P. Ricci, C. Andreani, A. K. Soper, J. Chem. Phys. **102**, 7650 (1995).

[15] S. Hayama, J. C. Wasse, N. T. Skipper, J. K. Walters, Mol. Phys. **99**, 779 (2001).

[16] D. Nicholls, *Inorganic Chemistry in Liquid Ammonia* (Elsevier, Amsterdam 1979).

[17] A. K. Soper, J. Chem. Phys. **101**, 6888 (1994).

[18] A. H. Narten, J. Chem. Phys, **66**, 3117 (1977).

[19] W. L. Jorgensen, M. Ibrahim, J. Am. Chem. Soc. **102**, 3309 (1980).

[20] R.C. Rizzo, W. L. Jorgensen, J. Am. Chem. Soc. **121**, 4827 (1999).

[21] *CRC Handbook of Chemistry and Physics*, ed. D. R. Lide (CRC Press, Inc. 1994).

[22] C. J. Page, D. C. Johnson, P. P. Edwards and D. M. Holton, Zeitschrift für Physikalische Chemie, **184**, 157 (1994).

[23] Z. Deng, M. L. Klein, G. J. Martyna, J. Chem. Soc. Faraday Trans. **90**, 2009 (1994).

[24] A. N. Garroway, R. M. Cotts, Phys. Rev. A. **7**, 635 (1973).

[25] N. W. Ashcroft, G. Russakoff, Phys. Rev. A. **1**, 39 (1970).

[26] D. S. Kyser, J. C. Thompson, J. Chem. Phys, **42**, 3910 (1965).

[27] R. D. Nasby, J. C. Thompson, J. Chem. Phys, **53**, 109 (1970).

[28] Vanderhoff, J. C. Thompson, J. Chem Phys, **55**, 105 (1971).

[29] P. P. Edwards, J. Chem. Phys. **72**, 3103 (1980).

[30] S. Hayama, J. C. Wasse, N. T. Skipper, J. Phys. Chem. B. **106**, 11 (2002).

[31] R. E. Lo, Z. Anorg. Allg. Chem, **344**, 230 (1966).

[32] C. A. Kraus, E. S. Carney, W. C. Johnson, J. Am. Chem. Soc, **49**, 2206 (1927).

[33] S. Kikuchi, J. Soc. Chem. Ind. Japan, **42**, 15 (1939).

[34] S. Naiditch, O. Paez, J. C. Thompson, J. Chem. Engng. Data, **12**, 164 (1967).

[35] W. C. Johnson, A. W. Meyer, J. Am. Chem. Soc, **54**, 3621 (1932).

[36] A. Demortier, P. Lobry, G. Lepoutre, J. Chim. Phys. **68**, 498 (1971).

[37] J. W. Hodgkins, Can. J. Res. B**27**, 861 (1949).

[38] W. S. Wong, Ph.D. Dissertation, University of California at Berkeley, (1966).

[39] M. H. Cohen, J. C. Thompson, Adv. Phys. **17**, 857 (1968).

[40] R. Catterall, N. F. Mott, Adv. Phys. **18**, 605 (1969).

[41] N. Bjerrum, Kgl. Danske Vidensk Selsk. Mat.-Fys. Medd. **27**, 3, (1951).

[42] Y. Nakamura, M. Yamamoto and M. Shimoji, in *Properties of Liquid Metals*, ed. S. Takeuchi, (Taylor and Francis, London 1973).

[43] S. Golden, C. Guttman and T. R. Tuttle, J. Am. Chem. Soc. **87**, 135 (1965).

[44] S. Golden, C. Guttman and T. R. Tuttle, J. Chem. Phys. **44**, 3791 (1966).

[45] C. A. Kraus, J. Am. Chem. Soc. **30**, 1197 (1914).

[46] R. A. Ogg, Phys. Rev. **69**, 243 (1946).

[47] R. A. Ogg, J. Chem. Phys. **14**, 295 (1946).

[48] T. L. Hill, J. Chem. Phys. **16**, 394 (1948).

[49] R. H. Land, O'Reilly, J. Chem. Phys. **46**, 4496 (1967).

[50] K. Fueki, J. Chem. Phys. **50**, 5381 (1969).

[51] D. L. Dexter, W. B. Fowler, Phys. Rev. **183**, 307 (1969).

[52] K. Fueki, S. Noda, in '*Metal-Ammonia Solutions*', eds. J. J. Lagowski, M. J. Sienko (Butterworths, London 1970).

[53] D. A. Copeland, N. R. Kestner, J. Jortner, J. Chem. Phys. **53**, 1189 (1970).

[54] D. E. O'Reilly, J. Chem. Phys. **55**, 474 (1971).

[55] N. R. Kestner, in 'Electrons in Fluids', eds. J. Jortner, N. R. Kestner, p1, Springer-Verlag, Heidelberg, (1973).

[56] D. F. Feng, K. Fueki, L. Kevan, J. Chem. Phys. **58**, 3281 (1973).

[57] D. F. Burow, J. J. Lagowski, Adv. Chem. Ser. **50**, 125 (1965).

[58] J. Jortner, J. Chem. Phys. **30**, 839 (1959).

[59] N. F. Mott, Adv. Phys. **16**, 49, (1967).

[60] B. J. McAloon, B. C. Webster, Theor. Chim. Acta, **15**, 385 (1969).

[61] B. Howat, B. C. Webster, J. Phys. Chem. **70**, 3714, (1972).

[62] P. P Edwards, J. Phys. Chem. **84**, 1215 (1980).

[63] J. C. Wasse, S. Hayama, N. T. Skipper and H. E. Fischer, Phys. Rev. B. **61**, 11993 (2000).

[64] J. C. Wasse, S. L. Stebbings, S. Masmanidis, S. Hayama and N. T. Skipper, J. Mol. Liq. **96-97**, 341 (2002).

[65] J. C. Wasse, S. Hayama, S. Masmanidis, S. L. Stebbings and N. T. Skipper, J. Chem. Phys. **118,** 7486 (2003).

[66] J. C. Wasse, S. Hayama, N. T. Skipper, C. J. Benmore and A. K. Soper, J. Chem. Phys. **112**, 7147 (2000).

[67] S. Hayama, J. C. Wasse, N. T. Skipper and H. Thompson, J. Chem. Phys. **116**, 2991 (2002).

[68] D. N. Knapp and H. D. Bale, J. Appl. Crystallogr. **11**, 606 (1978).

[69] M. Diraison, G. J. Martyna and M. E. Tuckerman, J. Chem. Phys, **111**, 1096 (1999).

[70] M. Marchi, M. Sprik and M. L. Klein, J. Phys. Condens. Matter **2**, 5833 (1990).

[71] R. W. Impey, M. Sprik and M. L. Klein, J. Am. Chem. Soc. **109**, 5900 (1987).

[72] T. Kerdcharoen, K. R. Liedl and B. M. Rode, Chem. Phys. **211**, 313 (1996).

[73] M. Sprik, R. W. Impey and M. L. Klein. Phys. Rev. Lett. **56**, 2326 (1986).

[74] G. J. Martyna and M. L. Klein, J. Chem. Phys. **96**, 7662 (1992).

[75] M. Marchi, M. Sprik and M. L. Klein, J. Phys. Chem. **92**, 3625 (1988).

[76] P. Krebs, J. Phys. Chem. **88**, 3702 (1984).

[77] L. C. M. De Maeyer, Pure Appl. Chem. **58**, 1105 (1986).

[78] M. Sprik, R. W. Impey and M. L. Klein, J. Chem. Phys. **83**, 5802 (1985).

[79] Z. Deng, G. J. Martyna and M. L. Klein, Phys. Rev. Lett. **68**, 2496 (1992).

[80] Z. Deng, G. J. Martyna and M. L. Klein, Phys. Rev. Lett. **71**, 267 (1993).

CHAPTER 2

THEORY OF NEUTRON SCATTERING

2.1 Introduction

Neutron diffraction is an important experimental technique in the study of many condensed matter systems.[1] There are several properties of the neutron which make it an ideal tool for investigating structural, dynamical and magnetic properties of materials, outlined below.

Neutrons are scattered by the strong nuclear force, and since neutrons are uncharged, they are highly penetrating and yield information on the bulk material rather than the surface layer. For this reason, thermal neutrons are also non-destructive to the material under study. In contrast to X-ray scattering, the nuclear interaction of the neutron with an atom means that the scattering length is not proportional to the atomic number, Z; instead it depends on the particular nucleus and its spin state. Hydrogen, for example, is virtually transparent to X-rays, but results in strong scattering of neutrons. In materials such as water and ammonia-based systems which contain hydrogen in the presence of heavier atoms, it is thus

possible to investigate the structural correlations involving hydrogen (e.g. hydrogen-bonding and its disruption) and proton dynamics (e.g. diffusion, rotation) via neutron scattering. In addition, isotopes may have significantly different scattering lengths, enabling the labelling of a particular atom/ion type within a material composed of more than one atomic species.

The de Broglie wavelength of thermal neutrons is of the order of interatomic distances in solids and liquids, hence interference effects of scattered neutrons give information on the structure of the system under study. The de Broglie wavelength is given by:

$$\lambda = \frac{h}{mv} \tag{2.1}$$

where h is Planck's constant and mv is the neutron's momentum. Furthermore, the energy of thermal neutrons (5 – 100 meV) is of the order of many excitations in condensed matter systems, so when the neutron is inelastically scattered by the creation or annihilation of an excitation, the energy transfer is a large fraction of the neutron's initial energy.

Neutrons also possess a magnetic moment, which means that the neutron is able to interact with unpaired spins in magnetic materials, providing information on the arrangement and density distribution of unpaired electrons, as well as the energies of magnetic excitations. This thesis is concerned with the structure and dynamic properties of non-magnetic systems, so the theory outlined in this chapter will be limited to the non-magnetic case.

2.2 Neutron scattering theory

In a neutron scattering experiment, the key variables are the change in neutron energy and the corresponding change in the scattering vector, $\boldsymbol{Q}$. Conservation of energy and momentum gives:

$$\hbar\omega = E - E' = \frac{\hbar^2}{2m}\left(k^2 - k'^2\right) \tag{2.2}$$

$$\hbar\boldsymbol{Q} = \hbar\boldsymbol{k} - \hbar\boldsymbol{k}' \tag{2.3}$$

where E and E' are the initial and final energies of the neutron respectively, m is the mass of the neutron, $\boldsymbol{k}$ and $\boldsymbol{k}'$ are the incident and final neutron wavevectors and k and k' are the magnitudes of the wavevectors. If the scattering is elastic, i.e. no energy is transferred to the sample, the magnitude of the scattering vector $\boldsymbol{Q}$ is given by:

$$Q = \frac{4\pi \sin\theta}{\lambda} \tag{2.4}$$

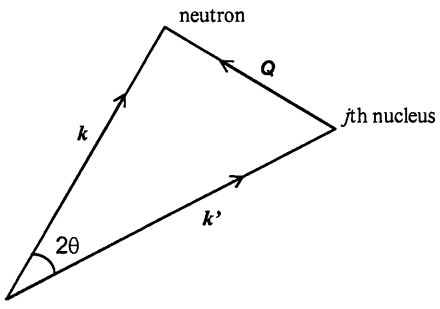

Figure 2.1 Geometry of a scattering event in which a neutron with initial momentum $\hbar\boldsymbol{k}$ and energy E is scattered into a final state with momentum $\hbar\boldsymbol{k}'$ and energy E'.

2.2.1 The differential cross section

The quantity measured in a neutron scattering experiment is the partial differential cross-section. This gives the fraction of neutrons of incident energy E scattered into a solid angle $d\Omega$ in direction θ,ϕ with a final energy between E' and $E' + dE'$. This is denoted by:

$$\frac{d^2\sigma}{d\Omega dE'} = \frac{\begin{array}{c}number\ of\ neutrons\ scattered\ per\ second\ into\ a\ solid\ angle\ d\Omega \\ in\ direction\ \theta,\phi\ with\ a\ final\ energy\ between\ E'\ and\ E'+dE'\end{array}}{\Phi\ d\Omega\ dE'} \tag{2.5}$$

where Φ is the flux of the incident neutrons. The geometry of the scattering event is shown in figure 2.2.

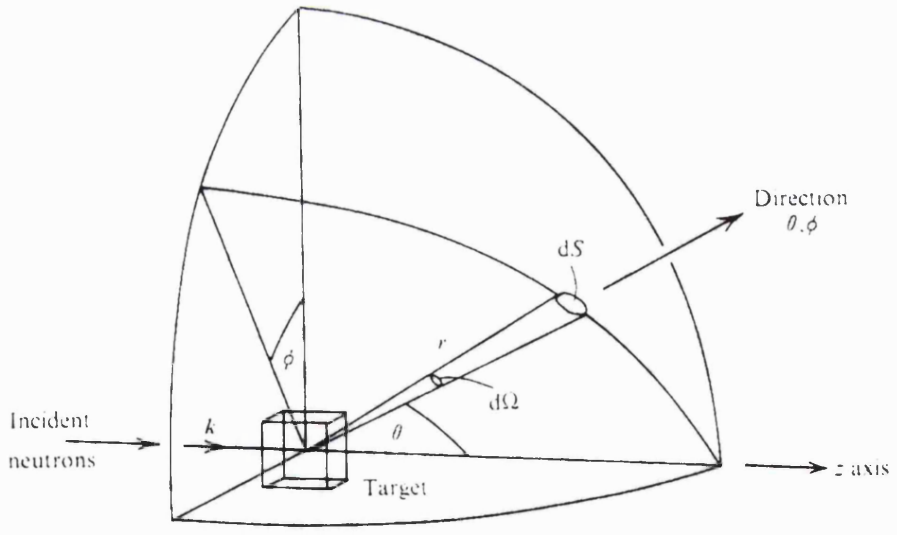

Figure 2.2 The geometry of a typical scattering experiment taken from Ref. [1]: a beam of thermal neutrons are incident on a target and are scattered into a small solid angle dΩ in the direction (θ,ϕ).

In a diffraction experiment, the energy of the scattered neutrons is not analysed. The measured cross-section is known as the differential cross section, and is given by the the integral of eq. 2.5 with respect to energy:

$$\frac{d\sigma}{d\Omega} = \frac{number\ of\ neutrons\ scattered\ per\ second\ into\ d\Omega\ in\ the\ direction\ \theta,\phi}{\Phi\ d\Omega}. \quad (2.6)$$

Finally, the integral of eq. 2.6 over all angles gives the total scattering cross section, which is defined as:

$$\sigma_{tot} = \frac{total\ number\ of\ neutrons\ scattered\ per\ second}{\Phi}. \quad (2.7)$$

This is related to the neutron scattering length by:

$$\sigma_{tot} = 4\pi b^2 \quad (2.8)$$

2.2.2 The single scattering event

If we consider scattering of a thermal neutron from a single fixed nucleus, no kinetic energy can be transferred to the nucleus, and the energy of the neutron is too small to be able to change the internal energy of the nucleus.[1] The scattering is therefore elastic: the energy of the neutron and the magnitude of the initial wavevector, k, is unchanged. If waves of any kind are scattered by a fixed object which is small

compared to the wavelength of the waves, the scattered waves are spherically symmetric. The incident and scattered wavefunctions can then be represented by:

$$\psi_{inc} = \exp(ikz) \tag{2.9}$$

$$\psi_{sc} = -\frac{b}{r}\exp(ikr) \tag{2.10}$$

where k is the magnitude of wavevector $\boldsymbol{k}$, z is the position of the incoming wave on an axis in the direction of $\boldsymbol{k}$, r is the distance of the scattered wave at position $\boldsymbol{r}$ from the fixed nucleus and b is a constant representing the strength of the interaction causing the scattering.

2.2.3 Nuclear scattering by a system of particles

First, an expression for the differential cross-section which is appropriate for elastic scattering (no energy transferred to the sample) will be derived. Let the incident neutron have wavefunction $\psi_{\boldsymbol{k}}$ and the scattered neutron have wavefunction $\psi_{\boldsymbol{k}'}$, and let λ, λ' represent the initial and final state of the scattering system. From the definition of $d\sigma / d\Omega$ given in eq. 2.6 we have:

$$\left(\frac{d\sigma}{d\Omega}\right)_{\lambda\to\lambda'} = \frac{1}{\Phi}\frac{1}{d\Omega}\sum_{\boldsymbol{k}' \text{ in } d\Omega} W_{\boldsymbol{k},\lambda} \to W_{\boldsymbol{k}',\lambda'} \tag{2.11}$$

where $W_{\boldsymbol{k},\lambda} \to W_{\boldsymbol{k}',\lambda'}$ is the number of transitions per second from the state $\boldsymbol{k},\lambda$ to the state $\boldsymbol{k}',\lambda'$, and Φ is the flux of incident neutrons.

The probability of a transition from a plane wave state with wavefunction $\psi_{\boldsymbol{k}}$ to a plane wave state with wavefunction $\psi_{\boldsymbol{k}'}$, both with the same energy $E = \hbar^2 k^2 / 2m$, is given by *Fermi's Golden Rule,* a fundamental result from quantum mechanics:[1]

$$\sum_{\boldsymbol{k}' \text{ in } d\Omega} W_{\boldsymbol{k},\lambda \to \boldsymbol{k}',\lambda'} = \frac{2\pi}{\hbar} \rho_{\boldsymbol{k}'} \left| \langle \boldsymbol{k}' \lambda' | V | \boldsymbol{k} \lambda \rangle \right|^2 \tag{2.12}$$

where $\rho_{\boldsymbol{k}'}$ is the number of momentum states in $d\Omega$ per unit energy range for neutrons in the state $\boldsymbol{k}'$, and V is the potential between the neutron and the scattering system. The sum is taken over all values of $\boldsymbol{k}'$ that lie in the small solid angle dΩ in the direction θ, ϕ, the values of $\boldsymbol{k}$, λ and λ' remaining constant. The matrix element is given explicitly by:

$$\langle \boldsymbol{k}' \lambda' | V | \boldsymbol{k} \lambda \rangle = \int \psi^*_{\boldsymbol{k}'} \chi^*_{\lambda'} V \psi_{\boldsymbol{k}} \chi_{\lambda} d\boldsymbol{R}\, d\boldsymbol{r} \tag{2.13}$$

where $d\boldsymbol{R} = d\boldsymbol{R}_1 d\boldsymbol{R}_2 ... d\boldsymbol{R}_N$, and $d\boldsymbol{R}_j$ is an element of volume for the jth nucleus, $d\boldsymbol{r}$ is an element of volume for the neutron, and $\chi_\lambda, \chi_{\lambda'}$ are the initial and final wavefunctions of the scattering system respectively.

For an array of nuclei, the scattered wavefunction of the neutron will be complicated. However, if the scattering potential is assumed to be much weaker than the energy of the incident neutrons, the scattered wavefunction can be represented by:

$$\psi_{\boldsymbol{k}'} \propto \exp(i\boldsymbol{k}'.\boldsymbol{r}) \tag{2.14}$$

This approximation to the wavefunction is known as the first Born approximation and is based on first order perturbation theory.

To evaluate the density of final scattering states it is necessary to carry out a normalisation of the wavefunctions. For a large box of side L, the initial and final wavefunctions are defined as:

$$\psi_{\boldsymbol{k}} = \frac{1}{L^{3/2}} \exp(i\boldsymbol{k}.\boldsymbol{r}) \tag{2.15}$$

$$\psi_{\boldsymbol{k}'} = \frac{1}{L^{3/2}} \exp(i\boldsymbol{k}'.\boldsymbol{r}) \tag{2.16}$$

By definition $\rho_{\boldsymbol{k}'} dE'$ is the number of states in $d\Omega$ with energy between E' and $E' + dE'$, which is the number of wavevector points in the element of volume $k'^2\, dk'\, d\Omega$. Therefore:

$$\rho_{\boldsymbol{k}'} dE' = \left(\frac{L}{2\pi}\right)^3 k'^2\, dk'\, d\Omega \tag{2.17}$$

The neutron energy is related to its wavevector by:

$$E' = \frac{\hbar^2 k'^2}{2m} \tag{2.18}$$

thus

$$\frac{dE'}{dk'} = \frac{\hbar^2 k'}{m} \tag{2.19}$$

Substituting eq. 2.19 in eq. 2.17 gives

$$\rho_{k'} = \left(\frac{L}{2\pi}\right)^3 \frac{mk'}{\hbar^2} d\Omega \tag{2.20}$$

Finally it remains to determine the incident neutron flux. This is given by the product of their density and velocity:

$$\Phi = \frac{1}{L^3}\frac{\hbar k}{m} \tag{2.21}$$

From equations 2.11, 2.12, 2.20 and 2.21, we have

$$\left(\frac{d\sigma}{d\Omega}\right)_{\lambda\to\lambda'} = \frac{k'}{k}\left(\frac{m}{2\pi\ \hbar^2}\right)^2 \left|\langle \boldsymbol{k}'\lambda'|V|\boldsymbol{k}\lambda\rangle\right|^2 \tag{2.22}$$

Therefore, given eq. 2.3 (conservation of momentum) and the fact that $\chi_\lambda, \chi_{\lambda'}$ are normalised, the expression becomes:

$$\left(\frac{d\sigma}{d\Omega}\right)_{\lambda\to\lambda'} = \frac{k'}{k}\left(\frac{m}{2\pi\ \hbar^2}\right)^2 \left|\int e^{-i\boldsymbol{k}'.\boldsymbol{r}} V e^{i\boldsymbol{k}.\boldsymbol{r}} d\boldsymbol{r}\right|^2 = \frac{k'}{k}\left(\frac{m}{2\pi\ \hbar^2}\right)^2 \left|\int V e^{i\boldsymbol{Q}.\boldsymbol{r}} d\boldsymbol{r}\right|^2 \tag{2.23}$$

It can be seen that all the normalisation factors of L^3 have cancelled out, since the volume of the normalisation box was arbitrary.

Having derived an expression for the differential cross-section, let us turn our attention to the derivation of the partial differential cross section, $d^2\sigma/d\Omega dE'$, which includes the possibility of inelastic scattering events. In this case, the change in neutron energy, $\hbar\omega$, is finite, and is defined such that ω is positive for neutron energy loss and negative for neutron energy gain.

Since $\boldsymbol{k}$, λ and λ' are fixed, the scattered neutrons all have the same energy, determined by conservation of energy (eq. 2.2). Mathematically, the energy distribution of the scattered neutrons is a delta function, given by:

$$\delta(E + E_\lambda - E' - E_{\lambda'}) = \delta(\hbar\omega + E_\lambda - E_{\lambda'}) \tag{2.24}$$

where E and E' are the initial and final energies of the neutron, and E_λ and $E_{\lambda'}$ are the initial and final energies of the scattering system.

Given the result that

$$\int \delta(E + E_\lambda - E' - E_{\lambda'}) dE' = 1 \tag{2.25}$$

the partial differential cross-section becomes:

$$\left(\frac{d^2\sigma}{d\Omega\ dE}\right)_{\lambda\to\lambda'} = \frac{k'}{k}\left(\frac{m}{2\pi\ \hbar^2}\right)^2 \left|\langle \boldsymbol{k}'\lambda'|V|\boldsymbol{k}\lambda\rangle\right|^2 \delta(\hbar\omega + E_\lambda - E_{\lambda'}) \tag{2.26}$$

The partial differential cross-section as defined in eq. 2.26 relates to specific initial and final states, although in general a range of initial states will be accessible, hence the actual quantity measured is the partial differential cross-section defined as:[2]

$$\frac{d^2\sigma}{d\Omega\ dE} = \frac{k'}{k}\left(\frac{m}{2\pi\ \hbar^2}\right)^2 \overline{\sum_{\lambda\lambda'} p_\lambda \left|\langle \boldsymbol{k}'\lambda'|V|\boldsymbol{k}\lambda\rangle\right|^2 \delta(\hbar\omega + E_\lambda - E_{\lambda'})} \tag{2.27}$$

where p_λ is the weighting factor for the state λ, which is in general the product of the thermodynamic factor, $\exp(-E_\lambda / k_B T)$, and the degeneracy factors.

The averaging included in the expression given by eq. 2.27 relates to any relevant distribution not included in the weighting factor p_λ, for example, the distribution of isotopes, the nuclear spin orientations and the precise nuclear positions.

2.2.4 The Fermi pseudopotential

In order to evaluate the integral term in eq. 2.23, it is necessary to insert a specific function for $V(\boldsymbol{r})$. As the range of the scattering potential is small, $V(\boldsymbol{r})$ may be expressed in terms of a sum of Fermi pseudopotentials from individual scattering centres, given by:

$$V(\boldsymbol{r}) = \frac{2\pi\hbar^2}{m}\sum_j^N b_j \delta(\boldsymbol{r} - \boldsymbol{r}_j) \tag{2.28}$$

where $\boldsymbol{r}_j$ is the position of the jth nucleus, and b_j is the scattering length of nucleus j.

Substituting this potential into eq. 2.23 gives:

$$\left(\frac{d\sigma}{d\Omega}\right)_{\lambda\to\lambda'} = \frac{k'}{k}\left(\frac{m}{2\pi\,\hbar^2}\right)^2\left|\int V(\boldsymbol{r})e^{i\boldsymbol{Q}.\boldsymbol{r}}d\boldsymbol{r}\right|^2 = \frac{k'}{k}\left|\int b_j\delta(\boldsymbol{r}-\boldsymbol{r}_j)e^{i\boldsymbol{Q}.\boldsymbol{r}}d\boldsymbol{r}\right|^2 \qquad (2.29)$$

Since $\int F(x)\delta(x-x_j)dx = F(x_j)$, then

$$\left(\frac{d\sigma}{d\Omega}\right)_{\lambda\to\lambda'} = \frac{k'}{k}\left|\int b_j e^{i\boldsymbol{Q}.\boldsymbol{r}_j}d\boldsymbol{r}\right|^2 \qquad (2.30)$$

Similarly, from 2.26,

$$\left(\frac{d^2\sigma}{d\Omega dE}\right)_{\lambda'\to\lambda} = \frac{k'}{k}\left|\sum_j b_j e^{i\boldsymbol{Q}.\boldsymbol{r}_j}\right|^2\delta(\hbar\omega + E_\lambda - E_{\lambda'}) \qquad (2.31)$$

The δ-function for the energy is now expressed as an integral with respect to time:

$$\delta(\hbar\omega + E_\lambda - E_{\lambda'}) = \frac{1}{2\pi\hbar}\int_{-\infty}^{\infty} e^{i(E_{\lambda'}-E_\lambda)t/\hbar}e^{-i\omega t}dt \qquad (2.32)$$

For a scattering system which consists of a single element where the scattering length b varies from one nucleus to another owing to nuclear spin or the presence of isotopes, it has been shown that eq. 2.31 may be written as:[1]

$$\frac{d^2\sigma}{d\Omega dE'} = \frac{k'}{k}\frac{1}{2\pi\hbar}\sum_{jj'} b_j b_{j'}\int_{-\infty}^{\infty}\left\langle e^{-i\boldsymbol{Q}.\boldsymbol{r}_{j'}(0)}e^{i\boldsymbol{Q}.\boldsymbol{r}_j(t)}\right\rangle e^{-i\omega t}dt \qquad (2.33)$$

2.2.5 Coherent and incoherent scattering

The partial differential cross-section in eq. 2.33 may be written as the sum of two contributions:

$$\frac{d^2\sigma}{d\Omega dE'} = \frac{k'}{k}\frac{1}{2\pi\hbar}\left[\bar{b}^2 \sum_{\substack{jj' \\ j'\neq j}} \int \left\langle e^{-i\mathbf{Q}.\mathbf{r}_{j'}(0)} e^{i\mathbf{Q}.\mathbf{r}_j(t)} \right\rangle e^{-i\omega t} dt + \overline{b^2} \sum_j \int \left\langle e^{-i\mathbf{Q}.\mathbf{r}_j(0)} e^{i\mathbf{Q}.\mathbf{r}_j(t)} \right\rangle e^{-i\omega t} dt \right] \tag{2.34}$$

where $$\bar{b} = \sum_j f_j b_j \tag{2.35}$$

and $$\overline{b^2} = \sum_j f_j b_j^2 \tag{2.36}$$

Here, f_j is the relative frequency of the scattering length b_j.

Now let us add the term $\bar{b}^2 \sum_j \int \left\langle e^{-i\mathbf{Q}.\mathbf{r}_j(0)} e^{i\mathbf{Q}.\mathbf{r}_j(t)} \right\rangle e^{-i\omega t} dt$ to the first term in eq. 2.34, and subtract it from the second term in this equation. We then have:

$$\frac{d^2\sigma}{d\Omega dE'} = \frac{k'}{k}\frac{1}{2\pi\hbar}\left[\bar{b}^2 \sum_{jj'} \int \left\langle e^{-i\mathbf{Q}.\mathbf{r}_{j'}(0)} e^{i\mathbf{Q}.\mathbf{r}_j(t)} \right\rangle e^{-i\omega t} dt + (\overline{b^2} - \bar{b}^2) \sum_j \int \left\langle e^{-i\mathbf{Q}.\mathbf{r}_j(0)} e^{i\mathbf{Q}.\mathbf{r}_j(t)} \right\rangle e^{-i\omega t} dt \right] \tag{2.37}$$

The first term in this equation depends on the correlation between the positions of the same nucleus *and* different nuclei at different times, and therefore gives rise to

interference effects. This is known as coherent scattering, and is the term extracted in a diffraction experiment.

The second term in eq. 2.37 is the incoherent scattering which depends only on the correlation between the positions of the *same* nucleus at different times. This does not give rise to interference effects. The scattering length pre-factor, $(\overline{b^2} - \bar{b}^2)$, represents the random fluctuations of the scattering lengths from the average scattering length of the particles.

2.3 Scattering lengths

The average scattering length of a monatomic system of particles depends on their relative isotopic fractions and spin states. If the system were to consist of a single isotope with nuclear spin I, then the spin of the neutron-nucleus system would have the value (I+1/2) or (I-1/2). The scattering lengths for the two spin states are denoted by b^+ and b^- respectively.

The number of states associated with spin (I+1/2) is

$$2(I+1/2)+1 = 2I+2 \tag{2.38}$$

and the number of states associated with spin (I-1/2) is

$$2(I-1/2)+1 = 2I \tag{2.39}$$

If the neutrons are unpolarised and the nuclear spins are randomly oriented, each spin state has the same probability. The scattering length b^+ then occurs with frequency:

$$f^+ = \frac{2I+2}{4I+2} = \frac{I+1}{2I+1} \tag{2.40}$$

and the scattering length b^- occurs with frequency:

$$f^- = \frac{2I}{4I+2} = \frac{I}{2I+1} \tag{2.41}$$

The average scattering length follows from eq. 2.35 and is given by:

$$\bar{b} = \frac{1}{2I+1}[(I+1)b^+ + Ib^-] \tag{2.42}$$

If the scattering system consists of several isotopes, the frequencies f^+ and f^- must be multiplied by the relative abundance of the isotope to obtain the relative frequencies of the scattering lengths. From eqs. 2.35 and 2.36, we have:

$$\bar{b} = \sum_i \frac{c_i}{2I_i+1}[(I_i+1)b_i^+ + I_i b_i^-] \tag{2.43}$$

$$\overline{b^2} = \sum_i \frac{c_i}{2I_i+1}[(I_i+1)(b_i^+)^2 + I_i(b_i^-)^2] \tag{2.44}$$

where c_i is the relative abundance of isotope i, I_i is its nuclear spin and b_i^+ and b_i^- are its two scattering lengths.

The scattering length of a particular isotope may also be complex: in this case b varies rapidly with the energy of the neutron. The scattering from such nuclei is a resonance phenomenon, associated with the formation of a compound nucleus with an energy close to an excited state. The imaginary part of the scattering length corresponds to absorption. The majority of nuclei, however, have a small imaginary component of the scattering length, meaning that the compound nucleus is not formed near an excited state.

2.4 Diffraction measurements

Assuming that there are no corrections to be applied to the data, the partial differential cross-section is equal to the total structure factor, $F(Q,\omega)$, where Q is the magnitude of the momentum transfer vector and $\hbar\omega$ is the energy transferred to the sample. $F(Q,\omega)$ contains both structural and dynamical information about the system under study.

In a diffraction experiment, only structural information is required. The quantity we wish to extract is therefore $F(Q,0)$, i.e. only the elastic scattering from the sample. In practice, however, energy transfer occurs during scattering from a nucleus, due to nuclear recoil. The diffraction data is analysed only as a function of Q, and so the detectors effectively integrate over all energy transfers, obtaining an ensemble averaged 'snap-shot' view of the material at $t = 0$.[3] It is therefore assumed that the measured $F(Q,\omega)$ is equal to $F(Q,0)$. This is known as the static

approximation, and is valid if the energy transferred to the system is small compared to the incident neutron energy.

In the case of liquid samples there is no truly elastic scattering and the static approximation breaks down.[1] Corrections must be made to the static approximation to account for the inelastic scattering events: these are detailed in 'SANDALS data analysis' (section 3.4.2).

The total differential cross-section measured is therefore given by:

$$\frac{d\sigma}{d\Omega} = \int \frac{d^2\sigma}{d\Omega dE'} dE' . \tag{2.45}$$

Then,

$$\left(\frac{d\sigma}{d\Omega}\right) = \frac{1}{N}\sum_{j=j'=1}^{N} \left\langle b_j b_{j'} e^{-i\mathbf{Q}.(\mathbf{r}_j(0)-\mathbf{r}_{j'}(0))} \right\rangle + \frac{1}{N}\sum_{j\neq j'}^{N} \left\langle b_j b_{j'} e^{-i\mathbf{Q}.(\mathbf{r}_j(0)-\mathbf{r}_{j'}(0))} \right\rangle \tag{2.46}$$

$$= \overline{b^2} + \frac{1}{N}\sum_{j\neq j'}^{N} \bar{b}^2 \left\langle e^{i\mathbf{Q}.(\mathbf{r}_j(0)-\mathbf{r}_{j'}(0))} \right\rangle \tag{2.47}$$

$$= (\overline{b^2} - \bar{b}^2) + \bar{b}^2 \frac{1}{N}\sum_{j,j'=1}^{N} \left\langle e^{-i\mathbf{Q}.(\mathbf{r}_j(0)-\mathbf{r}_{j'}(0))} \right\rangle . \tag{2.48}$$

The first term in eq. 2.47 is the *self* or *single atom* scattering. This includes both coherent and incoherent scattering and depends on correlations between the *same* nucleus at different times. The second term is the *interference* or *distinct* scattering, which is dependent on correlations between *different* nuclei at different times, and contains the basic structural information of the sample.

The distinct scattering term in eq. 2.47 can be simplified further if the target system is isotropic. In this case, the distance between the nuclei j and j' is given by:

$$r_{jj'} = \left| \boldsymbol{r}_j - \boldsymbol{r}_{j'} \right| \tag{2.49}$$

and the exponential term can be written as:

$$\left\langle e^{i\boldsymbol{Q}\cdot(\boldsymbol{r}_j(0)-\boldsymbol{r}_{j'}(0))} \right\rangle = \frac{\sin(Qr_{jj'})}{Qr_{jj'}}. \tag{2.50}$$

The density function, $\rho(r)$, is defined as:

$$\rho(r) = \rho_0 g(r) \tag{2.51}$$

where ρ_0 is the atomic number density and $g(r)$ is the pair correlation function, which gives the probability of finding an atom at a distance r from an arbitrary atom.

The measured differential cross-section then becomes:

$$\left(\frac{d\sigma}{d\Omega}\right) = \overline{b^2} + \bar{b}^2 \int 4\pi r^2 \rho_0 [g(r) - 1] \frac{\sin(Qr)}{Qr} dr \tag{2.52}$$

where the forward (zero angle) scattering has been subtracted. The measured diffraction pattern therefore consists of a featureless background on which the coherent scattering is superposed (the self term) plus the structure factor $F(Q)$ (the distinct term) which is a Fourier transform of the pair correlation function, $g(r)$.

2.4.1 Faber-Ziman formalism

For a system consisting of n chemical species, the measured differential cross-section becomes:

$$\frac{d\sigma}{d\Omega} = \sum_{\alpha=1}^{n} c_\alpha \overline{b_\alpha^2} + \sum_{\alpha=1}^{n}\sum_{\beta=1}^{n} c_\alpha c_\beta \bar{b}_\alpha \bar{b}_\beta \left[S_{\alpha\beta}(Q) - 1\right] \tag{2.53}$$

where $S_{\alpha\beta}(Q)$ is the static Faber-Ziman partial structure factor[4] for correlations between atomic species α, β and c_α, c_β are the atomic fractions of chemical species α and β respectively. The partial structure factor, $S_{\alpha\beta}(Q)$, is related to the partial pair correlation function, $g_{\alpha\beta}(r)$, by:

$$S_{\alpha\beta}(Q) - 1 = \frac{4\pi\rho_0}{Q}\int_0^\infty r\left[g_{\alpha\beta}(r) - 1\right]\sin(Qr)dr \tag{2.54}$$

The inverse relationship is given by:

$$g_{\alpha\beta}(r)-1=\frac{1}{2\pi^2\rho_0 r}\int_0^\infty Q[S_{\alpha\beta}(Q)-1]\sin(Qr)dQ \tag{2.55}$$

The average number of atoms of type β surrounding an atom of type α, between radii r_1 and r_2 is calculated from:

$$\bar{n}_\alpha^\beta = 4\pi\rho_0 c_\beta \int_{r_1}^{r_2} r^2 g_{\alpha\beta}(r)dr\,. \tag{2.56}$$

The total Faber-Ziman structure factor, $F(Q)$, and the total pair distribution function, $G(r)$, can now be defined as:[4]

$$F(Q)=\sum_\alpha\sum_\beta c_\alpha c_\beta \bar{b}_\alpha \bar{b}_\beta [S_{ab}(Q)-1] \tag{2.57}$$

$$G(r)=\sum_\alpha\sum_\beta c_\alpha c_\beta \bar{b}_\alpha \bar{b}_\beta [g_{ab}(r)-1]. \tag{2.58}$$

These functions are again related via a Fourier transform pair:

$$F(Q)=\frac{4\pi\rho_0}{Q}\int_0^\infty r\,G(r)\sin(Qr)dr \tag{2.59}$$

$$G(r)=\frac{1}{2\pi^2 r\rho_0}\int_0^\infty Q\,F(Q)\sin(Qr)dQ\,. \tag{2.60}$$

The total Faber-Ziman static structure factor can therefore be extracted from a single diffraction experiment. This quantity is a weighted sum of all the individual partial structure factors, $S_{\alpha\beta}(Q)$: to extract individual or composite partial structure factors, isotopic substitution may be used to label a particular atom type. The method of isotopic substitution, together with the correction procedures which are necessary in order to extract $F(Q)$, are detailed in Chapter 3.

2.5 Quasi-elastic neutron scattering

Quasi-elastic neutron scattering (QENS) is used to probe the dynamics of a system, and is therefore concerned with the correlation between the same nucleus at different times. Let us define $G(\boldsymbol{r},t)$ as the conditional probability density that, given a particle at time $t = 0$ at the origin $\boldsymbol{r} = 0$, any particle is found at time t and at the position $\boldsymbol{r}$, in a volume element $d\boldsymbol{r}$. The correlation function therefore contains a *self* and a *distinct* part:[5]

$$G(\boldsymbol{r},t) = G_S(\boldsymbol{r},t) + G_D(\boldsymbol{r},t)\,. \tag{2.61}$$

The correlation function $G(\boldsymbol{r},t)$ is related to the intermediate scattering function $I(\boldsymbol{Q},t)$ by a Fourier transformation in space. The Fourier transformation of $I(\boldsymbol{Q},t)$ in time then yields the scattering function $S(\boldsymbol{Q},\omega)$.

In QENS experiments, the change in energy of the neutron is analysed, and the quantity measured is thus:

$$\left(\frac{d^2\sigma}{d\Omega dE'}\right)=\left(\frac{d^2\sigma}{d\Omega dE'}\right)_{coh}+\left(\frac{d^2\sigma}{d\Omega dE'}\right)_{incoh} \tag{2.62}$$

The quantity we wish to extract from a QENS experiments is $(d^2\sigma/d\Omega dE')_{incoh}$ which depends only on correlations between the same nucleus at different times. Elements suited to incoherent QENS experiments therefore have a very large incoherent neutron scattering length compared to their coherent scattering length.[5] The incoherent term then dominates in the scattering pattern.

2.5.1 Long range translation diffusion

The form of $G_S(r,t)$ for times which are long compared to the mean time between atomic collisions is governed by the diffusion process. The basic equation for diffusion is known as Fick's Law,[1] given by

$$\frac{\delta}{\delta t}G_S(r,t)=D\,\nabla^2 G_S(r,t) \tag{2.63}$$

where D is the diffusion coefficient. For isotropic diffusion, ∇^2 is given by

$$\nabla^2 = \frac{\delta^2}{\delta r^2} + \frac{2}{r}\frac{\delta}{\delta r}. \tag{2.64}$$

The diffusion process is treated as if all diffusing particles start at time $t = 0$ at the origin. Therefore the initial condition is:

$$G_S(r,t=0) = \delta(r) \tag{2.65}$$

The solution to Fick's Law (eq. 2.63) is given by:[5]

$$G_S(r,t) = \left(4\pi D|t|\right)^{-3/2} e^{(-r^2/4D|t|)} \tag{2.66}$$

A Fourier transformation in space yields the self-part of the intermediate scattering function:

$$\begin{aligned} I_S(Q,t) &= \int_{-\infty}^{\infty} \left(4\pi D|t|\right)^{-3/2} e^{(-r^2/4D|t|)} e^{i\boldsymbol{Q}\cdot\boldsymbol{r}}\, d\boldsymbol{r} \\ &= e^{(-Q^2 D|t|)} \end{aligned} \tag{2.67}$$

Finally, to generate the scattering function, $S_i(Q,\omega)$, a Fourier transformation must be performed with respect to time:

$$S_i(Q,\omega) = \frac{1}{2\pi\hbar}\int_{-\infty}^{\infty} e^{-Q^2D|t|}e^{-i\omega t}dt$$

$$= \frac{1}{2\pi\hbar}\left[\int_{-\infty}^{0} e^{-Q^2D|t|}e^{-i\omega t}dt + \int_{0}^{\infty} e^{-Q^2D|t|}e^{-i\omega t}dt\right]$$

$$= \frac{1}{\pi}\frac{\hbar DQ^2}{(\hbar DQ^2)^2 + (\hbar\omega)^2} \tag{2.68}$$

The incoherent scattering function is therefore a single Lorentzian function with a half width at half maximum given by:

$$\Lambda(Q) = \hbar DQ^2 \tag{2.69}$$

At sufficiently small Q, this relationship is valid irrespective of the details of the diffusion mechanism.

2.5.2 The Chudley-Elliott jump diffusion model

At larger Q values, incoherent quasi-elastic neutron scattering can be used to extract information on the diffusion mechanism. The mechanism can be modelled as a jump diffusion process in both the liquid and solid state. Chudley and Elliott[6] developed a model for such a process, which was originally intended to describe diffusion in liquids and involves the following postulates:[5]

- The sublattice on which the diffusion takes place is a Bravais lattice, i.e. all sites involved are crystallographically equivalent.

- The diffusion process is dynamically independent of other kinds of motion.

- Only jumps to nearest-neighbour sites are allowed, characterised by jump vectors $\boldsymbol{s}_j$, j = 1 to z, where z is the co-ordination number. The jumps therefore all have the same length.

- The particle remains as a site for a mean residence time τ, then instantaneously jumps to a neighbouring site. This means that the jump time is negligibly small compared to the residence time.

- The jump direction is completely random: successive jumps are therefore uncorrelated.

The Chudley-Elliott model is therefore a Markov process, where the outcome of each iteration depends only on the current status. The self-correlation function $G_S(\boldsymbol{r},t)$ thus obeys the master equation, given by:[5]

$$\frac{\delta}{\delta t}P(\boldsymbol{r},t) = -\frac{1}{z\tau}\sum_{j=1}^{z}\left\{P(\boldsymbol{r},t) - P(\boldsymbol{r}+\boldsymbol{s}_j,t)\right\} \tag{2.70}$$

where $\boldsymbol{s}_j$ is the jump vector, z is the co-ordination number of nearest neighbour sites. $P(\boldsymbol{r},t)$ is then replaced with the self-correlation function, $G_S(\boldsymbol{r},t)$.

The initial condition is given by:

$$G_S(\boldsymbol{r},0) = \delta(\boldsymbol{r}) \tag{2.71}$$

as for the simple diffusion model.

If $(\boldsymbol{r} + \boldsymbol{s}_j)$ is replaced with $\boldsymbol{r}'$, Fourier transformations in space yield:[5]

$$\int G_S(\boldsymbol{r},t)\, e^{i\boldsymbol{Q}\cdot\boldsymbol{r}} d^3\boldsymbol{r} = I_S(\boldsymbol{Q},t) \tag{2.72}$$

$$\int G_S(\boldsymbol{r}',t)\, e^{i\boldsymbol{Q}\cdot\boldsymbol{r}'} e^{-i\boldsymbol{Q}\cdot\boldsymbol{s}_j} d^3\boldsymbol{r}' = e^{-i\boldsymbol{Q}\cdot\boldsymbol{s}_j} I_S(\boldsymbol{Q},t) \tag{2.73}$$

The differential equation for $I_S(\boldsymbol{Q},t)$ can now be obtained from eq. 2.70:

$$\frac{\delta}{\delta t} I_S(\boldsymbol{Q},t) = -\frac{1}{z\tau} \sum_{j=1}^{z} \left(1 - e^{-i\boldsymbol{Q}\cdot\boldsymbol{s}_j}\right) I_S(\boldsymbol{Q},t) \tag{2.74}$$

The boundary condition given by eq. 2.71 is also Fourier transformed to give:

$$I_S(\boldsymbol{Q},0) = 1 \tag{2.75}$$

The solution to the differential equation for $I_S(\boldsymbol{Q},t)$ is then:

$$I_S(\boldsymbol{Q},t) = \exp\left\{-\frac{t}{z\tau} \sum_{j=1}^{z} \left(1 - e^{-i\boldsymbol{Q}\cdot\boldsymbol{s}_j}\right)\right\} \tag{2.76}$$

The Fourier transform of $I_S(\boldsymbol{Q},t)$ with respect to time yields:

$$S_i(\boldsymbol{Q},\omega) = \frac{1}{\pi}\frac{\Lambda(\boldsymbol{Q})}{\Lambda^2(\boldsymbol{Q}) + (\hbar\omega)^2} \tag{2.77}$$

where the half width at half maximum, $\Lambda(\boldsymbol{Q})$, is given by:

$$\Lambda(\boldsymbol{Q}) = \frac{\hbar}{z\tau}\sum_{j=1}^{z}\left(1 - e^{-i\boldsymbol{Q}\cdot\boldsymbol{s}_j}\right). \tag{2.78}$$

The Chudley-Elliott model for liquids assumes that an atom or molecule is enclosed in a cage formed from other atoms or molecules, and every so often performs a jump into a neighbouring cage. Again, the assumptions are that the jump length l is identical for all sites, and the jump direction is random. Diffusion in liquids is isotropic, and so eq. 2.78 must be spatially averaged:

$$\begin{aligned}\left\langle\Lambda(\boldsymbol{Q})\right\rangle &= \frac{\hbar}{\tau}\left(1 - \left\langle e^{iQl\cos\theta}\right\rangle\right) \\ &= \frac{\hbar}{\tau}\left(1 - \frac{1}{2}\int_{-1}^{1} e^{iQl\cos\theta}\, d\cos\theta\right) \\ &= \frac{\hbar}{\tau}\left(1 - \frac{\sin(Ql)}{Ql}\right)\end{aligned} \tag{2.79}$$

This is the form of the function fitted to a plot of the half width at half maximum vs. Q in order to extract the mean residence time, τ, and the jump length, l , of a diffusing particle.

The diffusion coefficient is then given by the relation:

$$D = \frac{l^2}{6\tau} \tag{2.80}$$

Measurements of $S_i(Q,\omega)$ over a range of Q values can therefore be used to extract the diffusion rate and details of the diffusion process of an atomic species with a high incoherent scattering cross-section in the system under study. The procedures used in the analysis of measurements of the dynamic structure factor and the Bayesian method used to determine the number of Lorentzian components required to fit the measured data are described in Chapter 3.

2.6 References

[1] G. L. Squires, *Introduction to the Theory of Thermal Neutron Scattering* (Cambridge, New York, Cambridge University Press 1978).

[2] S. W. Lovesey, *Theory of neutron scattering from condensed matter, Volume 1* (Clarendon Press, Oxford, 1984).

[3] A. K. Soper, W. S. Howells, A. C. Hannon, *Atlas-Analysis of Time-of-flight Diffraction data from Liquid and Amorphous Samples* (Rutherford Appleton Laboratory Report RAL-89-046, 1989).

[4] Faber, T. E., and Ziman, J. M., Phil. Mag., **11**, 153 (1965)

[5] R. Hempelmann, *Quasielastic neutron scattering and solid state diffusion* (Clarendon, Oxford, 2000).

[6] C. T. Chudley and R. J. Elliott, Proceedings of the Physical Society (London), **77**, 353 (1961)

CHAPTER 3

EXPERIMENTAL DETAILS AND DATA ANALYSIS

3.1 Sample preparation

Metal-amine solutions are meta-stable: decomposition of the solutions to the metal amide plus hydrogen gas occurs with time, and the presence of impurities, elevated temperatures and catalysts such as aluminium metal surfaces accelerate this process.[1] In addition, great care must be taken when handling the constituents of these solutions. Alkali metals, such as lithium, are flammable and air-sensitive and must be handled under an inert atmosphere, for example, argon or helium. Ammonia and methylamine are highly corrosive, as well as being toxic gases at standard temperature and pressure: high pressure or low temperature is needed to maintain their liquid state. For these reasons, it is technically difficult to prepare metal-amine solutions, especially solutions which are stable over time periods of up to ~48 hours required for neutron scattering studies. In all the experiments, the samples were prepared *in-situ*. This method was found to be highly successful, and is described in detail in this chapter.

3.1.1 Purification of the amine solvents

Prior to the experiments, the gas-handling rig (figure 3.1) was evacuated for at least 24 hours to a pressure of $< 10^{-5}$ millibar. A helium leak-detector was used to ensure that the gas-rig was leak-tight.

The amine solvents; anhydrous NH_3, ND_3, CH_3NH_2, CD_3ND_2, CH_3ND_2, CD_3NH_2 were obtained from Aldrich chemicals or Promochem. In all cases the atomic % atom D was greater than 98%. These were purified to remove any hydrogen, deuterium or nitrogen gas impurities. This was found to be necessary in one of our earlier experiments, when the recovered amine solvent was found to contain a high proportion of volatile gas after only a few hours, despite the fact that no sample decomposition had occurred. Purification was necessary since the presence of hydrogen/deuterium gas would affect the pressure readings, thus giving an inaccurate measure of sample composition. These volatile gases also appeared to hinder the condensation of amine solvent into the sample cell.

Purification was carried out as follows: an amount of solvent gas was decanted from the amine lecture bottle into the empty 300 cc buffer, the lecture bottle was resealed and the pressure of solvent gas in the 300 cc buffer was recorded. A dewar of liquid nitrogen was placed underneath the 150 cc buffer, and the valve was opened in order to cryopump the amine gas into the smaller buffer. This process was repeated until a sufficient amount of ammonia or methylamine required for the experiment was collected in the 150 cc buffer. A final pressure reading which was greater than the base pressure indicated the presence of hydrogen/deuterium gas in the system. The gas-rig was opened to the turbo vacuum pump to remove any such

volatiles, with the dewar of liquid nitrogen remaining underneath the 150 cc buffer to keep the ammonia/methylamine frozen. When the pressure reached $<10^{-5}$ millibar, the valve on the 150 cc buffer was closed and the liquid nitrogen dewar was removed.

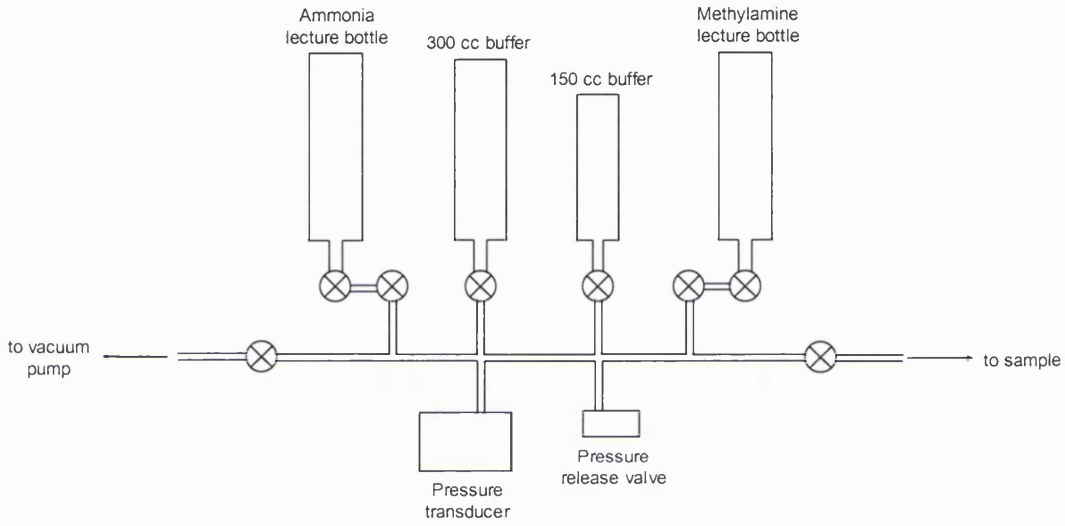

Figure 3.1 Schematic and photograph of the gas-rig set-up.

3.1.2 Alkali metal loading & experimental set-up

The sample cell, the lid with valve attached, the gold seal and cutting utensils were thoroughly cleaned with deionised water and then acetone, to remove any impurities present. These were dried and outgassed in a vacuum drying oven at ~80°C for at least two hours, before placing them in an inert dry argon atmosphere glovebox (O_2 and H_2O less than 10 ppm). A piece of lithium metal was mechanically cleaned, then weighed, and loaded into the sample cell. The cell lid and valve assembly was attached, with a gold o-ring between to ensure the sample container was leak-tight. The cell was then removed from the glove-box and attached to a closed cycle refrigerator (CCR) on the beam-line.

The sample cell was attached to the gas-rig via a 1/8" stainless steel capillary. This was evacuated up to the valve above the sample cell until a pressure of $<10^{-5}$ millibar was achieved. Careful leak checks were again performed, before the valve was opened in order to evacuate the sample cell down to base pressure. Heater wire and a platinum-100 temperature sensor were then wrapped around the capillary below the flange of the CCR, especially near the cold head, to prevent any condensation or freezing of amine solvent in the pipework and around the valve, possibly causing a blockage. The CCR and sample cell were then lowered into position, and the volume around the CCR was evacuated to down to a pressure of $\sim10^{-4}$ millibar, in order to thermally isolate the cell thus keeping the temperature stable, as well as preventing ice deposits forming around the sample container.

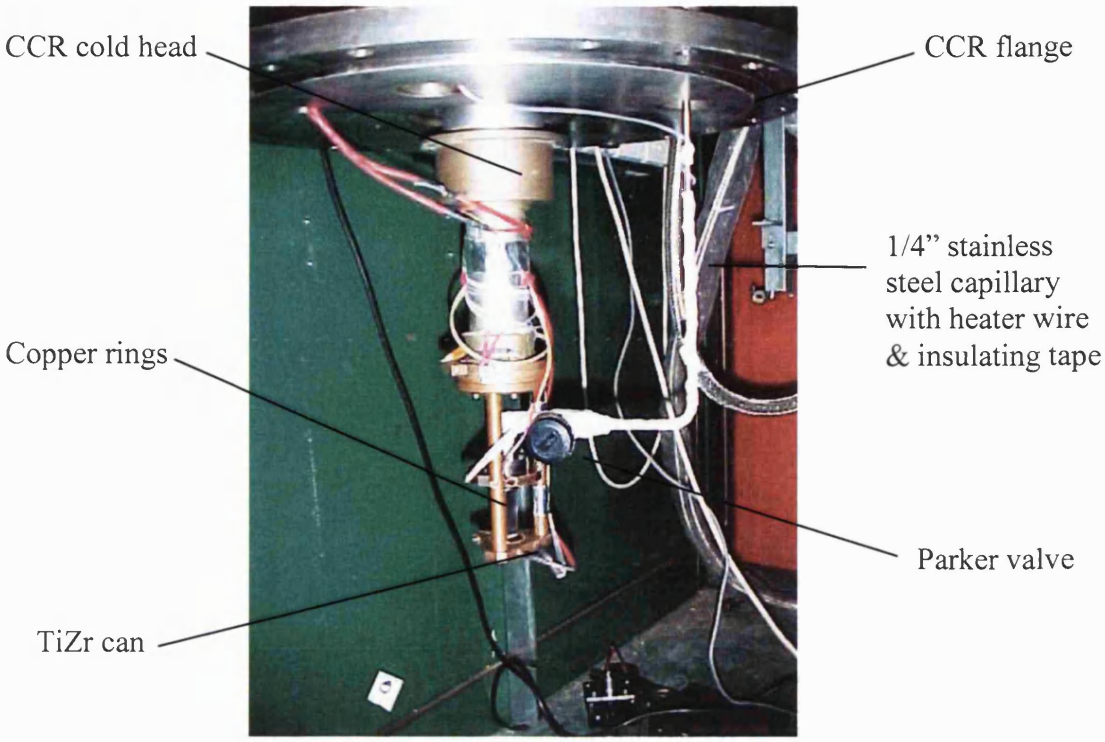

Figure 3.2 The SANDALS experimental set-up, showing the TiZr sample cell attached to the CCR.

3.1.3 Condensation of amine gas

Once a pressure of the order of 10^{-6} millibar was attained, the gas-rig was closed to the turbo vacuum pump. The CCR was switched on, and the sample cell was cooled to 230 K. A voltage of 5-10 volts was applied to the heater wire, so that the temperature of the capillary would be maintained well above 240 K, the boiling point of ammonia.

The number of moles of amine gas required to achieve a particular concentration of metal in solution is calculated via the following equation:

$$Conc.\ in\ MPM = \frac{no.\ of\ moles\ of\ metal}{(no.\ of\ moles\ of\ metal + no.\ of\ moles\ of\ amine\ gas)} \times 100 \qquad (3.1)$$

The total pressure of amine gas required can then be calculated by the ideal gas law:

$$\Delta p \times V = nRT \qquad (3.2)$$

where Δp is the pressure of gas condensed onto the lithium metal, V is the volume of the buffer, n is the number of moles of amine gas, R is the gas constant: 8.314 m^2 kg s^{-2} mol^{-1} K^{-1}, and T is the temperature of the buffer. If the pressure calculated via the ideal gas law for a 300 cm^3 volume of ammonia gas is 2.000 bar, the pressure calculated by the van der Waals equation of state is 1.978 bar. For pressures below ~2 bar, the ideal gas law is therefore a valid approximation.

An amount of purified amine gas was allowed into the 300 cc buffer, and the initial gas pressure, p_i, and the temperature of the buffer, T, were recorded. The maximum pressure of amine gas decanted at any one time was ~2 bars. The valve on the gas panel was then opened to the sample to allow the gas to condense on the alkali metal. Once the pressure reading had settled to the vapour pressure of the solution, or when the requisite pressure, Δp, had been condensed onto the sample, the valve was closed, and the final pressure p_f was recorded. This step was repeated if more solvent was needed to achieve the desired sample composition. The 300 cc buffer was resealed, and the valve to the sample was opened in order to monitor the vapour pressure of the solution. In all the experiments, the pressure remained stable over the timescales of ~48 hours required to perform the neutron scattering experiment, indicating no liberation of hydrogen due to sample decomposition.

3.1.4 Recovery of the amine solvent

After the neutron scattering experiment had been performed, the condensed amine solvent was slowly cryopumped back into the 300 cc buffer. This method of solvent recovery ensured no rapid boiling of the solution, and hence no spitting of alkali metal into the valve and capillary. The sample can containing the metal residue was monitored for radiation, and when safe the cell was opened to air for the metal coating to form the oxide. The can was then dropped into a beaker of isopropanol, and when any rapid effervescence had subsided, deionised water was added to dissolve the metal oxide layer. The can was then rinsed with water, then acetone, in preparation for the next sample.

3.2 Mixed solvent solutions – laboratory preparation

Unlike solutions of alkali metal-ammonia or alkali metal-methylamine, the phase diagram of mixed-solvent solutions is not accurately known. Prior to neutron scattering experiments on such systems, lithium-ammonia-methylamine solutions were made in a silica cell, so that the colour of the solutions and the onset of phase separation could be observed either as the sample was diluted or as the ratio of ammonia to methylamine was varied. The method of loading the lithium-metal and condensation of amine solvent was similar to that performed in the neutron scattering experiments. The temperature of ~230 K was achieved by means of a dry ice/acetone bath. The silica cell containing the lithium metal was lowered into a beaker of antifreeze, housed in the acetone bath. Dry ice was slowly added to the acetone: the boiling of the acetone provided the means by which the bath was cooled to 230 K, while the antifreeze ensured that the temperature remained stable to ±5 K.

Via this method, it was found that a lithium-ammonia-methylamine solution with a methylamine:ammonia molar ratio of 1:1 was homogeneous at concentrations above 19 MPM at 240 K. Below this concentration, a clear phase separation between a metallic bronze coloured solution and a deep blue solution was observed. This phase separation remained down to concentrations as low as 3 MPM. However, a small increase in temperature at this concentration caused the blue and gold phases to mix, and a further dilution to ~2.5 MPM yielded an apparently homogeneous blue solution at 240 K. Similar experiments on a lithium-mixed solvent solution with a methylamine:ammonia ratio of 2:1 was found to be homogeneous at high concentrations. Phase separation was observed upon dilution to 14 MPM.

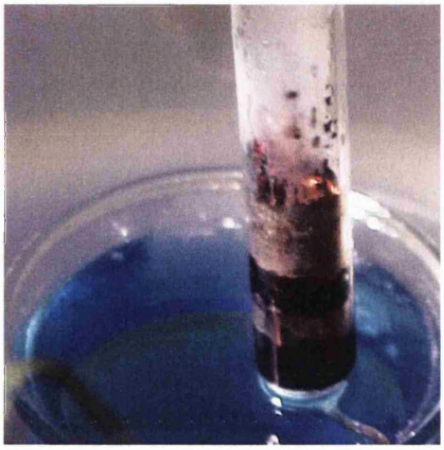

Figure 3.3 Phase separation occurring in a concentrated lithium-ammonia-methylamine solution.

3.3 Neutron production at a spallation source

The neutron experiments presented in this work were performed at ISIS at the Rutherford Appleton Laboratory, currently the most intense pulsed neutron source in the world. The method of neutron production here is via spallation, in which the bombardment of a heavy-metal target with pulsed high-energy protons from an accelerator produces a pulsed neutron beam. The main advantage of this method of neutron production over a nuclear reactor is that it releases much less heat per useful neutron than fission, providing a neutron brightness which far exceeds that of reactor sources. A detailed account of neutron production at a spallation source is given below.[2]

Firstly, an ion-source produces H^- ions for injection into the linac (linear accelerator). Hydrogen gas is fed into the source along with hot caesium vapour such that a discharge plasma is formed, the Cs atoms providing the source of electrons for the H^- ion formation. The ions are extracted and accelerated by a voltage difference between the source and the start of the linac. A beam of charged particles at an energy of 70 MeV is then produced for injection into the ISIS synchrotron. On entry to the synchrotron, the H^- ion beam passes through a 0.3 μm thick aluminium oxide stripping foil which removes the electrons from the H^- ions in the beam, converting the ions to protons. The harmonic RF system then traps the protons into two bunches and accelerates them to 800 MeV. Neutrons are produced by the collision of these synchrotron-accelerated protons with a target nucleus such as uranium, tantalum or tungsten. At ISIS the target consists of several thin tantalum sheets surrounded by flowing cooling water. This collision process produces highly excited nuclear states

in the target, which decay either immediately or following a delay, producing neutrons with a wide range of energies, as well as neutrinos, muons and γ rays. The excited states which decay on impact produce pulses of neutrons which are used for time-of-flight (*tof*) experiments, while the delayed neutrons generate a low-level time-independent background. The neutron pulses are slowed down by moderators, making their wavelengths suitable for neutron scattering experiments. The moderator consists of a hydrogen-containing material, in which multiple scattering of the neutrons from the light atoms leads to a reduction in their energy. The moderator must also be relatively small, in order that the pulsed time structure is not broadened too much. The resulting neutron pulses, which are produced at a rate of 50 Hz, exhibit a range of wavelengths consisting of an epithermal region where the intensity varies as $1/E$, and a Maxwellian region where the neutrons reach a temperature close to that of the moderator.[3] On the assumption of elastic scattering, the neutron wavelengths are related to the time-of-flight (*tof*) by:

$$tof = \frac{L}{v} = \frac{m_n L \lambda}{h} \tag{3.3}$$

where L is the total flight path of the neutron between the moderator and detector, v is the velocity of the neutron and m_n is the neutron mass.

The momentum transfer can then be related to the time-of-flight by:

$$Q = \frac{4\pi \sin\theta}{\lambda} = 4\pi \frac{m_n L}{h \times tof} \sin\theta \tag{3.4}$$

allowing a full scattering profile as a function of Q to be obtained after combining spectra from all the fixed-angle detectors.

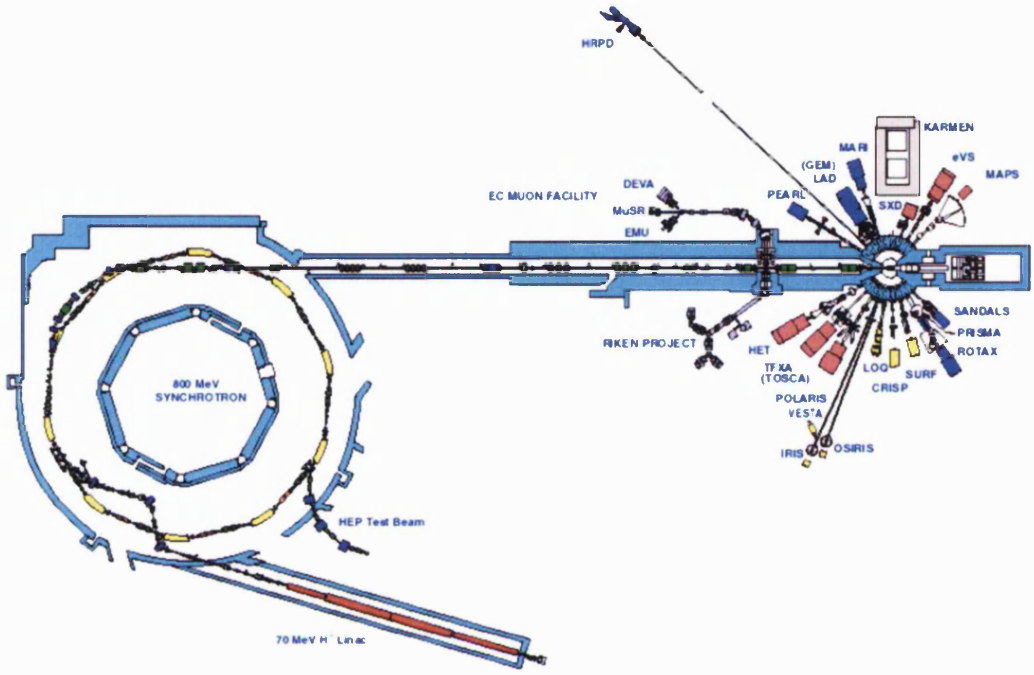

Figure 3.4 Diagram of the ISIS layout.[2] The synchrotron ring has a radius of 26 m, and the distance from the synchrotron to the target is 120 m.

3.4 The SANDALS instrument

The SANDALS instrument at the ISIS facility is a Small Angle Neutron Diffractometer for Amorphous and Liquid Samples, which was built for the study of disordered materials. The large number of detectors at small angles also means that the instrument is especially suited to samples which contain a high fraction of light elements such as hydrogen or deuterium.[4] The intense flux and wide Q-range enables the use of isotopic substitution techniques, particularly second-order hydrogen-deuterium isotopic substitution.

SANDALS uses neutrons with a wavelengths in the range 0.05 to 4.5 Å, which have been slowed down by a liquid methane moderator at 100 K. The full beam size is a circle of diameter 3.2 cm, which can be reduced to any desired rectangular beam aperture using the moveable B_4C (boron carbide) jaws in conjunction with a B_4C beam scraper.[4] For all the experiments performed, the selected beam size was 27 mm high × 17 mm wide. The 18 detector banks comprise a total of 1260 zinc sulphide detectors, shown in figure 3.5, giving full angular coverage from 3.8° to 39°. This arrangement permits continuous Q-range measurements from ~0.1 to 50 $Å^{-1}$.

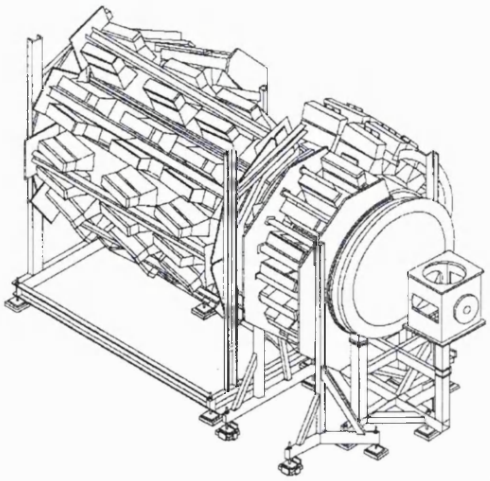

Figure 3.5 Diagram of the SANDALS instrument.[4]

3.4.1 The SANDALS sample container

For all the SANDALS diffraction measurements, specially designed titanium-zirconium containers were used, shown in figures 3.6 and 3.7. The TiZr alloy of 68% Ti and 32 % Zr has null coherent scattering (b_{Ti} = -3.438 fm, b_{Zr} = 7.16 fm), which is important since any Bragg reflections from the container can be difficult to subtract completely.[3] The sample cell has flat-plate geometry, with sample slit and cell walls thicknesses of 1.0 mm, to minimise multiple neutron scattering and absorption. The cell is also equipped with a mixing volume to enable *in-situ* dilution of the metal-amine solution.

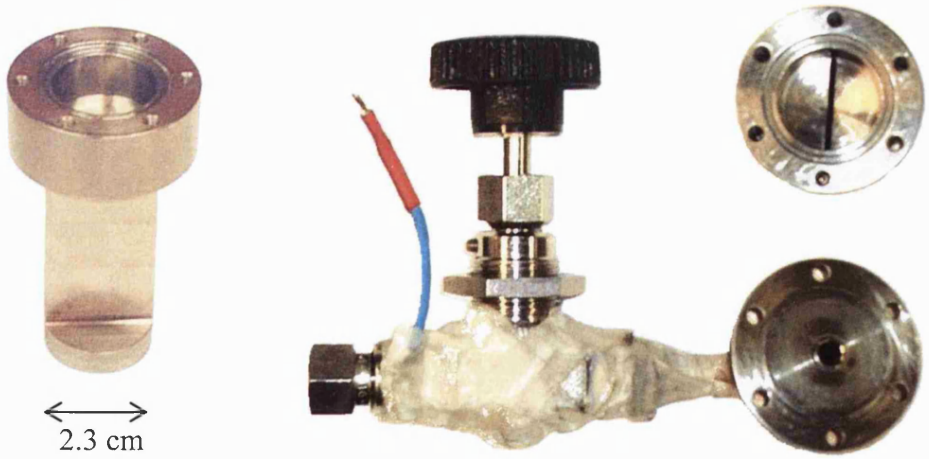

Figure 3.6 Photograph of the TiZr SANDALS sample container with the lid and valve assembly.

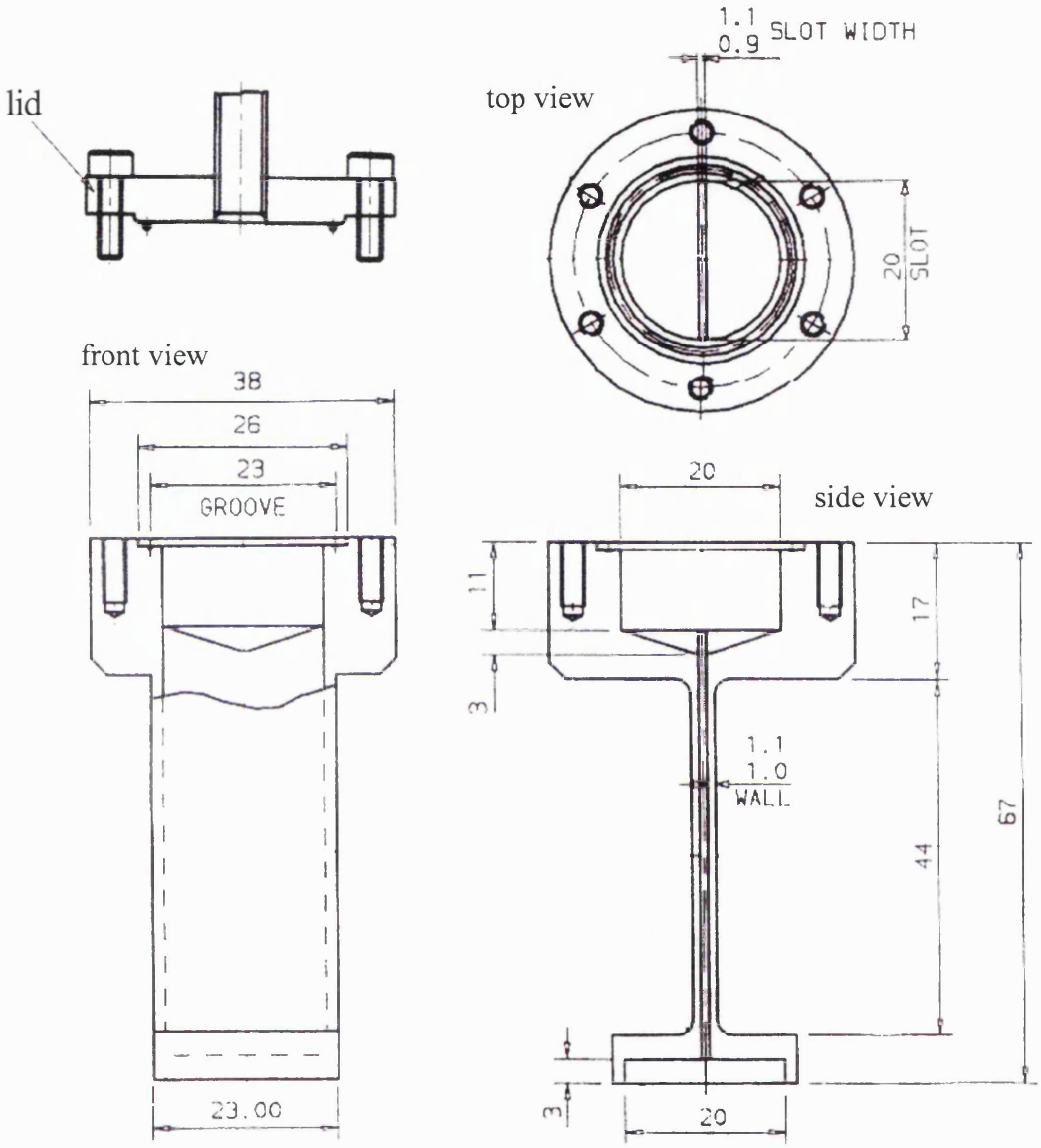

Figure 3.7 Diagram of the flat-plate titanium-zirconium sample cells used on SANDALS.

3.4.2 SANDALS data analysis

The quantity sought in a single diffraction experiment is the structure factor, $S(Q)$, where

$$S(Q) = 1 + \frac{4\pi\rho_0}{Q} \int_0^\infty r\,[g(r) - 1]\,\sin(Qr)\,dr \tag{3.5}$$

For a multicomponent system, the total structure factor $F(Q)$ is the sum of several terms like eq. 3.5 for each pair of atom types, weighted according to the product of their scattering lengths and atomic fractions.[3]

Several measurements need to be made in order to extract $F(Q)$. These are:

1) Vanadium slab (width = 5.0 cm, thickness = 0.348 cm) mounted on the candlestick.
2) Vanadium background (empty candlestick).
3) Empty cell(s) mounted on the CCR.
4) Background (CCR alone).
5) Sample contained in the cell, mounted on the CCR.

The correction procedure for obtaining a normalised total static structure factor is as follows:[3-5]

i) **NORM** – this program corrects the raw detector spectra for deadtime, and converts from time-of-flight to momentum transfer, Q. Two output files are created: the *.SUM file which contains the summed counts as a function of Q for each of the 18 detector groups, and the *.MON file which contains the incident monitor spectrum and transmission monitor spectrum as a function of wavelength.

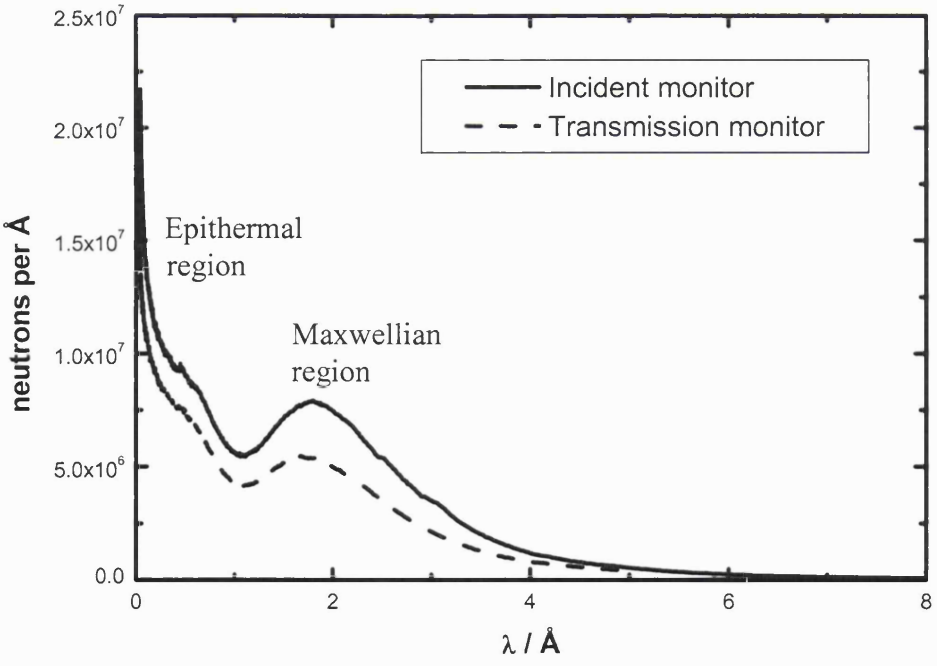

Figure 3.8 The incident and transmission monitor spectra.

ii) **CORAL** – this program allows the calculation of both absorption and multiple scattering for the sample in question. The program should be run for the sample in the cell, the empty cell(s) and the vanadium slab. The input to CORAL requires files with extension .MUT, containing data on the wavelength-dependent total interaction cross-section for the sample, cell and vanadium standard. These can be calculated in one of three ways:

a) using the ratio of the transmission data from sample and background, and fitting a polynomial to the result.

b) calculating the total cross-section from neutron scattering tables (appropriate only for samples containing solely heavier elements, where the ratio of the bound cross-section to the free cross-section is close to unity).

c) using existing total cross-section measurements for the constituent elements (appropriate for lighter samples with wavelength-dependent scattering cross-sections).

In the majority of cases, method (a) was used to calculate the total scattering cross-section. For the experiment on the saturated lithium-ammonia solution, method (c) was used because of problems with the incident monitor. Existing total cross-section files were used for the TiZr cell and vanadium slab.

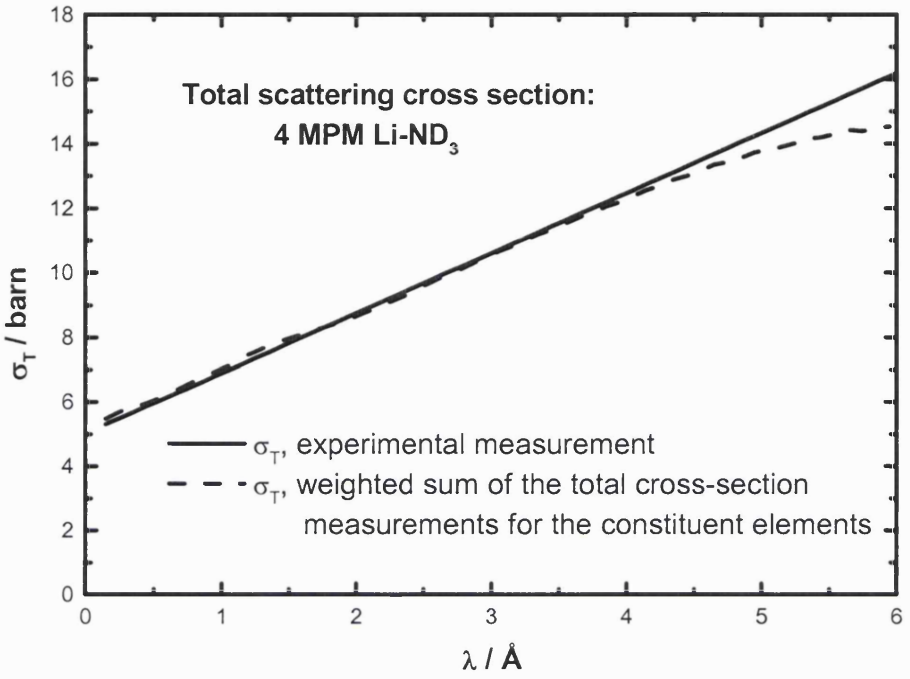

Figure 3.9 The total cross-section for a 4 MPM solution of $Li:ND_3$, calculated (a) from transmission monitor data and (b) using a weighted sum of the total cross-section measurements for the constituent elements.

iii) **VANSLAB** – this routine removes the small Bragg peaks from the vanadium spectrum and smoothes the data using a series of Chebyshev polynomials. The division of the smoothed spectra by the vanadium differential cross section leads to an estimate of the instrument calibration:

$$CAL_V(Q) = \frac{NRM_V(Q)}{N_V \sigma_V^S(Q) A_{V,V} + M_V(Q)} \tag{3.6}$$

where $NRM_V(Q)$ is the normalised vanadium spectrum, N_V is the number of atoms in the sample, σ_V^S is the vanadium scattering cross-section, $A_{V,V}$ is the Paalman and Pings attenuation factor and M_V is the multiple scattering correction. Vanadium is used for the instrument calibration estimation because of its largely incoherent cross-section, allowing the differential cross-section of vanadium to be estimated with a reasonable degree of accuracy.

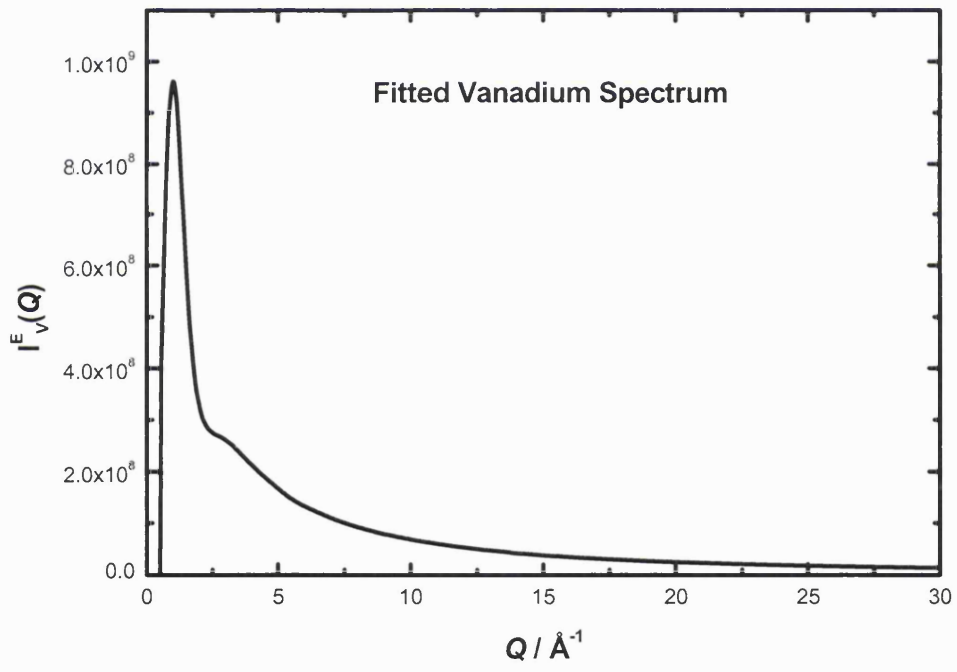

Figure 3.10 Example of a smoothed vanadium spectrum.

iv) **ANALYSE** – this routine normalises the counts from the sample, empty container and background to the incident or transmission monitor spectrum, normalises to the instrument calibration (vanadium spectrum) and applies the background, multiple scattering and absorption corrections to the summed spectra.

The basic algorithm used to perform this procedure is as follows,[3] where *NRM* represents the spectra normalised to the monitor counts, *TOTAL* represents the total scattering, *SINGLE* represents the single scattering and the subscripts *SC*, *C*, *V* and *B* refer to the sample + cell, empty cell, vanadium and background measurements respectively.

a) Subtract background:

$$TOTAL_{SC}(Q) = NRM_{SC}(Q) - NRM_{B}(Q) \tag{3.7}$$

$$TOTAL_{C}(Q) = NRM_{C}(Q) - NRM_{B}(Q) \tag{3.8}$$

b) Normalise to instrument calibration:

$$TOTAL_{SC}(Q) = TOTAL_{SC}(Q) / CAL_{V}(Q) \tag{3.9}$$

$$TOTAL_{C}(Q) = TOTAL_{C}(Q) / CAL_{V}(Q) \tag{3.10}$$

c) Subtract multiple scattering:

$$SINGLE_{SC}(Q) = TOTAL_{SC}(Q) - M_{SC}(Q) \tag{3.11}$$

$$SINGLE_{C}(Q) = TOTAL_{C}(Q) - M_{C}(Q) \tag{3.12}$$

d) Apply absorption corrections:

$$SINGLE_S(Q) = \frac{\left(SINGLE_{SC}(Q) - SINGLE_C(Q) \times \frac{A_{C,SC}}{A_{C,C}} \right)}{A_{S,SC}} \tag{3.13}$$

where $A_{C,SC}$, $A_{C,C}$ and $A_{S,SC}$ are the usual Paalman and Pings attenuation factors, for example: $A_{S,SC}$ is the attenuation factor for scattering in the sample and attenuation in the sample plus can.[6]

e) Divide by number of atoms in sample:

$$DCS(Q) = \frac{SINGLE_S(Q)}{N_S} \tag{3.14}$$

where DCS represents the differential scattering cross-section, and N_S is the number of atoms in the sample.

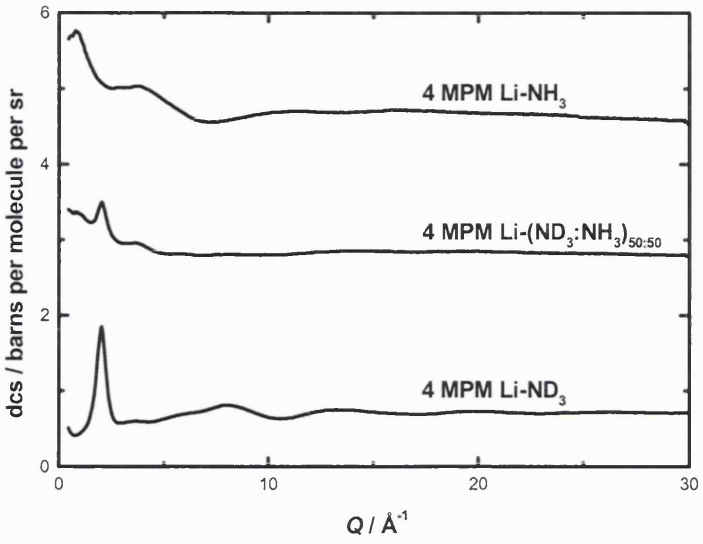

Figure 3.11 The measured differential cross-section for 4 MPM lithium-ammonia solutions of Li-ND_3, Li-NH_3 and Li-$(ND_3{:}NH_3)_{50:50}$. The high-Q scattering levels are determined by the self or single-atom scattering, which is higher for protonated samples due to the large incoherent scattering cross-section for hydrogen. The slope on the data at low Q for the samples which contain a significant fraction of hydrogen atoms is caused by inelastic scattering.

v) Self-scattering corrections

The differential cross-section extracted via ANALYSE is:

$$\left(\frac{d\sigma}{d\Omega}\right)_{eff} = \int_0^{\infty} f(E')\frac{d^2\sigma}{d\Omega dE'}dE' = \frac{\sigma_{coh}}{4\pi}\hbar N \int_{-\infty}^{E/\hbar} f(E')\frac{k'}{k}S(Q,\omega)d\omega \qquad (3.15)$$

where $f(E')$ is the efficiency of the detector for neutrons of energy E'. In the static approximation, $(d\sigma/d\Omega)_{eff}$ is proportional to $S(Q)$, since $S(Q,\omega)$ is effectively a delta function with its peak at $\omega = 0$. A correct calculation of eq. 3.15, however, includes the variation of Q, k' and $f(E')$ with ω. In the case of nuclei much more massive than the neutron, (i.e the mean energy transfer is small compared to the incident neutron energy) Placzek[7] showed that the inelasticity correction is essentially independent of the detailed dynamics, and is related only to the nuclear mass, sample temperature, incident neutron energy and geometry and efficiency of the neutron detection process. An expansion of the integrand in eq. 3.15 gives:

$$\left(\frac{d\sigma}{d\Omega}\right)_{eff} = \frac{\sigma_{coh}}{4\pi} N f_0 \left[S(Q_0) + \frac{m}{M}\left\{\frac{\overline{K}}{3E} - \frac{Q_0^2}{2k^2}\left(1+\frac{\overline{K}}{3E}\right)\right\} + O\left(\frac{m^2}{M^2}\right)\right] \qquad (3.16)$$

where m is the mass of the neutron, M is the mass of a nucleus in the liquid, $\overline{K}$ is the mean kinetic energy of a nucleus and Q_0 is the value of Q for elastic scattering.

In the case of samples containing light atoms such as hydrogen or deuterium, however, the Placzek correction for self-scattering breaks down. Instead, a linear combination of the differential cross-section for the three isotopically distinct samples measured (fully protonated, fully deuterated and a mixture of the two) is used to make an estimate of the average single atom scattering for the system. A low-order polynomial is then chosen to fit the underlying shape of the data, without fitting any of the interference structure.

A suitable fraction of the self-scattering function multiplied by a correction function is then subtracted from the data in each of the detector groups of the DCS file. Finally, all or selected detector groups are merged in order to produce the total static structure factor $F(Q)$.

vi) **Consistency checks**

There are a number of checks which can be performed to test the efficacy of the data correction procedures.[8] These are:

a) Prior to the self-scattering correction, the scattering level of $F(Q)$ at high Q should be around:[4]

$$\text{High-Q scattering level} = \frac{n_0 t_s \sum_i n_i \sigma_i}{4\pi N} \tag{3.17}$$

where n_0 is the atomic number density, t_s is the sample thickness, n_i is the number of atoms of type i in the scattering unit, σ_i is the total scattering cross-section for an atom of type i and N is the total number of atoms in the scattering unit.

b) After self-scattering corrections, $F(Q)$ should oscillate around zero at high Q.

c) $F(Q)$ must satisfy the sum rule, which states that:[9]

$$\int_0^\infty Q^2 F(Q) dQ = -2\pi^2 n_0 \sum_{ij} c_i c_j b_i b_j \tag{3.18}$$

where n_0 is the number density, c_i and c_j are the atomic fractions of atoms of type i,j and b_i and b_j are the neutron scattering lengths of atoms of type i, j.

d) The Fourier transform of $F(Q)$ should oscillate about the low-r limit given by:

$$G_0 = -\sum_{i,j} c_i c_j b_i b_j \tag{3.19}$$

where c_i, c_j and b_i, b_j are again the atomic fractions and neutron scattering lengths respectively, of atoms of type i, j. Thus if the unphysical low-r oscillations in $G(r)$ are set to this G_0 limit, the Fourier back-transform to Q-space should yield a function which closely matches the initial structure factor, $F(Q)$.

vii) **Fourier transformation**

The method of Fourier transform adopted was a 'minimum noise' method.[10,11] This is an iterative technique which attempts to generate a pair correlation function, $G(r)$, which is as smooth as possible, but still consistent with the data. In this way the program produces a radial distribution function containing only real features, thus showing some features in the radial distribution function produced by a simple Fourier transform method to be unphysical, caused by truncation of the structure factor and/or noise within the structural data.

3.4.3 Theory of hydrogen/deuterium isotopic substitution

Hydrogen/deuterium isotopic substitution[12] takes full advantage of the very large difference in neutron scattering lengths between hydrogen ($b_H = -3.74$ fm) and deuterium ($b_D = 6.67$ fm). By performing experiments on three samples, which are identical in every respect apart from the isotopic composition of the hydrogen atoms, it is possible to extract the three partial structure factors: $S_{HH}(Q)$, $S_{XH}(Q)$ and $S_{XX}(Q)$, where the subscript H refers to substituted hydrogen atoms, and X refers to any non-substituted atoms.

After the corrections for background, multiple scattering, absorption and instrument calibration have been applied, the quantity extracted from a single neutron diffraction experiment is the total structure factor, which can be expressed as:

$$F(Q) = \sum_{\alpha\beta} c_\alpha c_\beta b_\alpha b_\beta [S_{\alpha\beta}(Q) - 1] \tag{3.20}$$

where c_α is the atomic fraction of species α, b_α is the neutron scattering length of atom α, $Q = 4\pi \sin\theta / \lambda$ (i.e. the magnitude of the momentum change vector of the scattered neutrons), and $S_{\alpha\beta}(Q)$ is the Faber-Ziman partial structure factor involving atoms α and β only. This total structure factor can be written as a sum of three composite partial structure factors:

$$F(Q) = c_X^2 b_X^2 [S_{XX}(Q) - 1] + 2c_X c_H b_X b_H [S_{XH}(Q) - 1] + c_H^2 b_H^2 [S_{HH}(Q) - 1] \tag{3.21}$$

where the composite coherent scattering length b_X and atomic concentration c_X are defined as:

$$b_X = \sum_{\alpha \neq H} c_\alpha b_\alpha / c_X, \qquad c_X = \sum_{\alpha \neq H} c_\alpha, \qquad c_H = 1 - c_X . \tag{3.33}$$

Specifically, the $S_{HH}(Q)$ partial structure factor is calculated from:

$$S_{HH}(Q) - 1 = \frac{\{xF_H(Q) + (1-x)F_D(Q) - F_{HD}(Q)\}}{\{c_H^2[xb_H^2 + (1-x)b_D^2 - b_{HD}^2]\}} \tag{3.34}$$

where the subscripts H, D and HD refer to the total structure factors for the protonated, deuterated and mixture samples respectively, and x is the fraction of protonated ammonia in the mixture sample. Then

$$b_{HD} = xb_H + (1-x)b_D . \tag{3.35}$$

Similarly, the XH and XX composite partial structure factors are calculated via the following relations:

$$S_{XH}(Q) - 1 = \frac{\{F_H(Q) - F_D(Q) + c_H^2(b_D^2 - b_H^2)[S_{HH}(Q) - 1]\}}{\{2c_H c_X b_X (b_H - b_D)\}} \tag{3.36}$$

$$S_{XX}(Q) - 1 = \frac{\{F_H(Q) - 2c_H c_X b_H b_X [S_{XH}(Q) - 1] - c_H^2 b_H^2 [S_{HH}(Q) - 1]\}}{c_X^2 b_X^2} \tag{3.37}$$

The weighting coefficients of the contributions to the X-H and X-X partial functions are calculated by an expansion of the composite partial structure factors, given by:

$$S_{XH}(Q)-1=\sum_{\alpha\neq H}c_\alpha b_\alpha[S_{\alpha H}(Q)-1]/c_X b_X \tag{3.38}$$

$$S_{XX}(Q)-1=\sum_{\alpha\neq H,\beta\neq H}c_\alpha b_\alpha c_\beta b_\beta[S_{\alpha\beta}(Q)-1]/c_X^2 b_X^2 \tag{3.39}$$

A Fourier transform yields the partial pair correlation function, $g_{\alpha\beta}(r)$, given by:

$$g_{\alpha\beta}(r)-1=\int_0^\infty\{Q[S_{\alpha\beta}(Q)-1]\sin(Qr)dQ\}/(2\pi^2\rho_0 r) \tag{3.40}$$

where Q is the scattering vector, r is position in real-space, and ρ_0 is the atomic number density of the sample.

The average number of atoms of type β surrounding an atom of type α, between radii r_1 and r_2, is then calculated from:

$$\bar{n}_\alpha^\beta=4\pi\rho_0 c_\beta\int_{r_1}^{r_2}r^2 g_{\alpha\beta}(r)dr \tag{3.41}$$

where ρ_0 is again the average atomic number density of the sample.

The above calculations are carried out via the program *PARTIAL*, which yields the three composite partial structure factors, $S_{HH}(Q)$, $S_{XH}(Q)$ and $S_{XX}(Q)$, normalised to unity. Fourier transformation of these data to yield the partial pair correlation functions, as well as the use of classical simulation in conjunction with the data, provides a wealth of information on the solvent structure of metal-amine solutions, described in detail in chapters 5 and 7.

3.5 The IRIS instrument

The IRIS instrument at the ISIS facility is a high-resolution quasi/inelastic neutron scattering (QENS) spectrometer used to measure molecular diffusion and rotational dynamics. In addition the instrument has high-resolution, long wavelength diffraction capabilities. The spectrometer is inverted geometry: neutrons scattered by the sample are energy-analysed by means of Bragg scattering from a large area crystal analyser array.[13,14]

IRIS has access to a large flux of long-wavelength cold neutrons, which have been slowed by a liquid hydrogen moderator at 25 K. A neutron guide, consisting of accurately aligned nickel-plated glass tubes, transports the neutrons to the sample position. A converging nickel-titanium supermirror component serves to focus the beam at the sample position and also increases the flux incident on the sample. Two choppers, located at 6.3 m and 10 m from the moderator respectively, are used to define the range of neutron energies incident on the sample during the course of an experiment.

The secondary spectrometer consists of two crystal analyser arrays (pyrolytic graphite and muscovite mica) and two ZnS scintillator detector banks housed in a vacuum chamber, 2m in diameter. In addition, diffraction spectra may be measured using the detector bank at $2\theta = 170°$, containing ten ^{3}He gas-tubes. Incident and transmission beam monitors are located before and after the sample position. The pyrolytic graphite analyser bank is cooled close to liquid helium temperature, in order to reduce background contributions from thermal diffuse scattering.

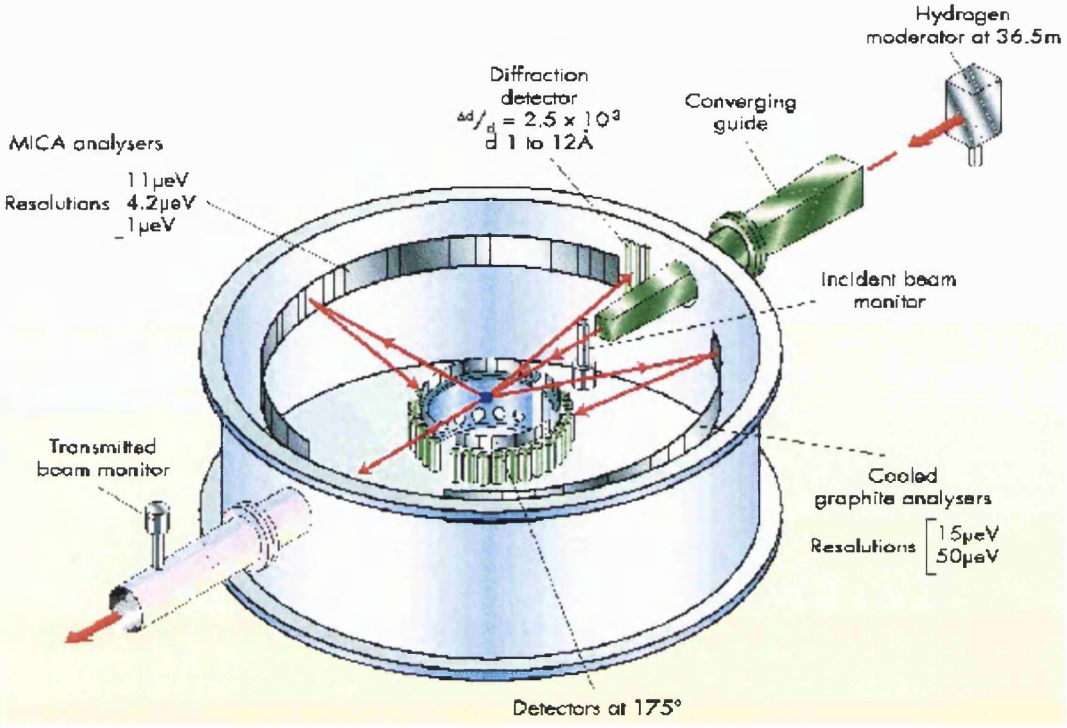

Figure 3.12 Diagram of the IRIS secondary spectrometer.[13] The diameter of the vacuum tank is 2 m and the analyser radius is 0.72 m.

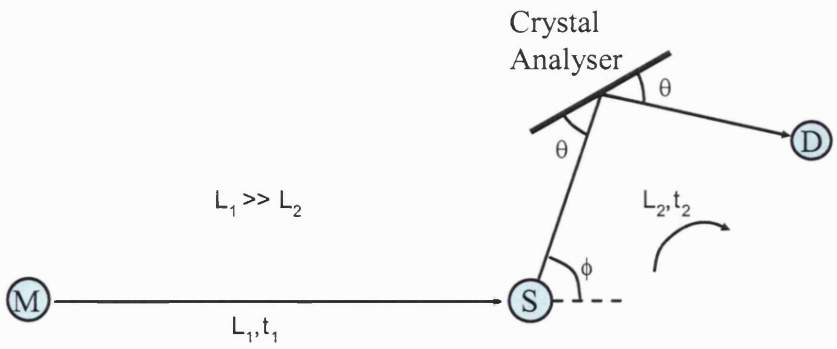

Figure 3.13 Schematic of an indirect geometry inelastic scattering spectrometer.

3.5.1 Quasi-elastic neutron scattering (QENS) – principle of operation

Neutrons scattered by the sample are energy-analysed by means of Bragg-scattering from a large array of single crystals. By recording the total time-of-flight of the neutron from the moderator to the detector, the initial energy of the neutron, hence the energy transferred to the sample, may be calculated.[14]

During an IRIS experiment, the two disc choppers define the range of neutron energies or wavelengths incident on the sample, *S*. However, only those neutrons with a final energy E_2 which satisfies the Bragg condition, $\lambda = 2d\sin\theta$, are scattered towards the detectors. This kinetic energy is defined as:

$$E_2 = \frac{1}{2}m_n v_2^2 = \frac{p^2}{2m_n} \tag{3.42}$$

where m_n is the mass of the neutron.

Via de Broglie's relation: $p = \frac{h}{\lambda}$, and the Bragg condition: $\lambda = 2d\sin\theta$, the final energy E_2 can be rewritten as:

$$E_2 = \frac{h^2}{2m_n\lambda^2} = \frac{1}{2m_n}\left(\frac{h}{2d\sin\theta}\right)^2 \tag{3.43}$$

where d is the d-spacing of the analyser crystal.

The distance from the sample to the detector bank, L_2, is accurately known. The energy equation:

$$E_2 = \frac{1}{2} m_n v_2^2 = \frac{1}{2} m_n \left(\frac{L_2}{t_2} \right)^2 = \frac{1}{2m_n} \left(\frac{h}{2d \sin\theta} \right)^2 \tag{3.44}$$

can be rewritten to give

$$t_2 = \frac{2m_n L_2 d \sin\theta}{h} \tag{3.45}$$

Should interactions within the sample lead to a change in energy of the neutron, a distribution in the total time-of-flight measured will result. By measuring the total time-of-flight, $t = t_1 + t_2$, and having an accurate knowledge of t_2, L_1 and L_2, the energy gain/loss can be determined by:

$$\Delta E = E_1 - E_2 = \frac{1}{2} m_n \left[\left(\frac{L_1}{(t - t_2)} \right)^2 - \left(\frac{L_2}{t_2} \right)^2 \right] \tag{3.46}$$

3.5.2 The IRIS sample container

It was necessary to design a new sample container for use on the IRIS beamline, for which several considerations had to be taken into account. These were:

1) The material had to be suitable for containing the highly-reducing metal-ammonia solutions. Standard IRIS containers are made of aluminium, which is known to increase the rate of decomposition of the sample to the amide plus hydrogen gas.

2) The material was required to be a solely elastic scatterer, with a minimum incoherent scattering cross-section. Stainless steel proved to be the ideal material for the sample container.

3) In order to minimise the need for multiple scattering corrections, it was necessary for the sample to scatter between 10% and 20% of the incident beam. Since hydrogen has a high total scattering cross-section and makes up more than 70 atomic percent of the metal-ammonia samples, it was necessary for the sample thickness to be small: a sample thickness of 1mm was chosen.

4) Cylindrical geometry was preferred over flat-plate geometry, so that all the detector angles could be used. A flat plate cell would have given rise to a 'blind spot' on each of the analyser banks.

5) The width of the container was required to be equal to or greater than the beam width of 2 cm. Given the need for a large diameter, yet small sample thickness, annular geometry was ideal.

6) The container walls needed to be as thin as possible, to minimise absorption and multiple scattering from the can. The limiting factor was the fact that the cell had to withstand pressures twice as large as the working pressure of the ammonia gas. For a sample cell of diameter 2 cm, the minimum allowed wall thickness was 0.2 mm.

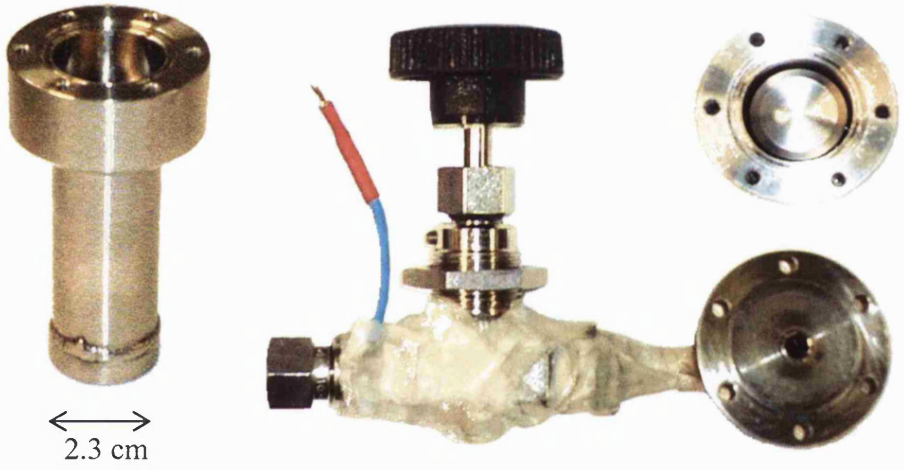

Figure 3.14 Photograph of the IRIS sample container with the lid and valve assembly.

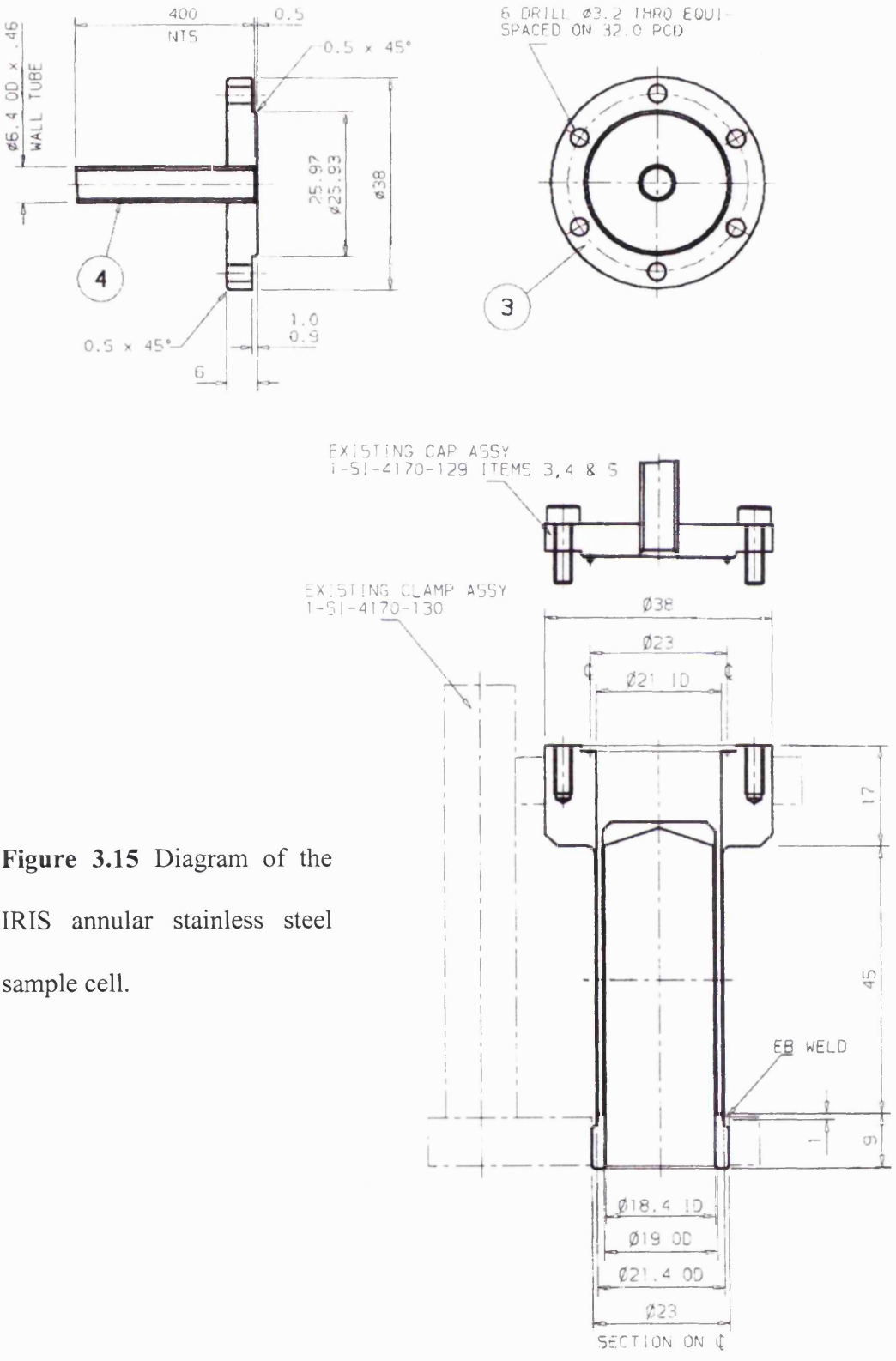

Figure 3.15 Diagram of the IRIS annular stainless steel sample cell.

3.5.3 IRIS data analysis

The QENS experiments produce the dynamic structure factor $S(Q,\omega)$ after corrections for absorption and background and empty can subtraction, implemented using the standard analysis package MODES.[15] This function may be written as a sum of the self and distinct parts:[16]

$$S(Q,\omega) = S_S(Q,\omega) + S_D(Q,\omega) \tag{3.47}$$

where the self-part provides information on the single particle dynamics in the system. The quantity measured in a neutron scattering experiment consists of a weighted sum of the total and self-parts of the dynamic structure factor:[17]

$$\frac{d^2\sigma}{d\Omega d\omega} = \frac{k_f}{k_i} N\left[b_{coh}^2 S(Q,\omega) + b_{incoh}^2 S_S(Q,\omega)\right] \tag{3.48}$$

where k_i and k_f are the incident and final wavevectors of the neutron, N is the number of scattering nuclei, and b_{coh} and b_{incoh} are the coherent and incoherent neutron scattering lengths respectively.

A solution to Fick's law of diffusion can be found for the self-part of the dynamic structure factor, given by:[18]

$$S_S(Q,\omega) = \frac{1}{\pi} \frac{\hbar D Q^2}{(\hbar\omega)^2 + (\hbar D Q^2)^2} \tag{3.49}$$

For constant Q this has the form of a Lorentzian with a full width at half maximum of $2\hbar DQ^2$, where D is the molecular diffusion coefficient.

The dynamic structure factors may be analysed using the Bayesian fitting routine QUASILINES,[19] a method which determines the most likely number of Lorentzian components required to fit the data. The function fitted is:

$$S(Q,\omega) = \left[A_0 \partial(\omega) + \sum_{i=1}^{N} A_i \frac{f(Q)_i}{\pi(\omega^2 + f(Q)_i^2)} \right] \otimes R(\omega) + B(\omega) + \sigma(w) \qquad (3.50)$$

where $R(\omega)$ is the energy resolution of the instrument which is convoluted with a number of Lorentzians, N, and a delta function representing the elastic peak. $B(\omega)$ represents the sloping background and $\sigma(\omega)$ is a term representing statistical noise.

The fitting procedure allows the dependence of the full width at half maximum (FWHM) of the Lorentzian components on Q to be determined. A linear dependence of the FWHM with Q^2 at small Q-values represents a diffusion process, the gradient being equal to twice the diffusion constant. Independence of the FWHM with Q indicates a localized motion.[20]

3.6 References

[1] J. C. Thompson, *Electrons in Liquid Ammonia* (Clarendon, Oxford 1976).

[2] http://www.isis.rl.ac.uk

[3] A. K. Soper, W. S. Howells, A. C. Hannon, *Atlas-Analysis of Time-of-flight Diffraction data from Liquid and Amorphous Samples* (Rutherford Appleton Laboratory Report RAL-89-046, 1989).

[4] C. Benmore and A. K. Soper, The SANDALS Manual, Rutherford Appleton Laboratory Technical Report (RAL-TR-98-006, 1998)

[5] J. Z. Turner, A. K. Soper, W. S. Howells, A. C. Hannon and S. Ansell, *SANDALS Survival Guide*, (ISIS Facility, RAL 1995).

[6] H. H. Paalman and C. J. Pings, J. App. Phys. **33**, 2635 (1962).

[7] G. Placzek, Phys. Rev. **86**, 377 (1952).

[8] P. S. Salmon and C. J. Benmore, *Recent developments in the Physics of Fluids*, ed. W. S Howells and A. K. Soper, (Hilger, Bristol 1992).

[9] J. E. Enderby, D. M. North and P. A. Egelstaff, Phil. Mag. **14**, 961 (1966).

[10] A. K. Soper, in *Neutron Scattering Data Analysis 1990*, pp.57-67, edited by M. W. Johnson (IOP Conference Series Number 107), IOP Publishing, Bristol, (1990).

[11] A.K. Soper, C. Andreani, M. Nardone, Phys. Rev. E. **47**, 2598 (1993).

[12] D. T. Bowron, A. K. Soper, J.L. Finney, J. Chem. Phys. **114**, 6203 (2001).

[13] http://isis.rl.ac.uk/molecularspectroscopy/iris

[14] M. A. Adams, W. S. Howells and M. T. F. Telling, The IRIS User Guide, 2nd edition, Rutherford Appleton Laboratory Technical Report (RAL-TR-2001-002, 2001)

[15] M. T. F. Telling and W. S. Howells, GUIDE – IRIS data analysis, ISIS Facility, RAL 2000. & W. S. Howells, MODES manual (RAL 2003).

[16] J. P. Hansen and I. R. McDonald, *Theory of Simple Liquids* (New York, Academic Press, 1986).

[17] G. L. Squires, *Introduction to the Theory of Thermal Neutron Scattering* (Cambridge, New York, Cambridge University Press 1978).

[18] P. A. Egelstaff, *An Introduction to the Liquid State* (Oxford, Oxford University Press, 1992).

[19] D. S. Sivia, C. J. Carlile, W. S. Howells and S. Konig, Physica B. **182**, 341 (1992).

[20] R. Hempelmann, *Quasielastic neutron scattering and solid state diffusion* (Clarendon, Oxford, 2000).

CHAPTER 4

SIMULATION TECHNIQUES

4.1 Reverse Monte Carlo simulation

Reverse Monte Carlo (RMC) is a method for producing three-dimensional molecular ensembles of disordered materials which are quantitively consistent with the available experimental data.[1] The method uses only known structural and intra-molecular co-ordination number constraints in conjunction with the diffraction data. It has several advantages over simulation methods such as Metropolis Monte Carlo (MMC) and molecular dynamics, which rely on inter-atomic potentials and often demonstrate only qualitative agreement with the measured data. RMC has been used successfully in modelling both glass and liquid structures, such as molten salts,[2] expanded alkali metals[3] and fast-ion conductors.[4]

4.1.1 Principles of RMC

The RMC method as described here details the main stages used in the modelling of liquid ammonia and metallic lithium-ammonia solutions. For a complete guide to running RMC, the reader is referred to the RMC manual.[5]

1) The starting configuration for the RMC simulation is produced as follows: molecular positions are generated at random in the simulation cell, with the required numbers of each molecule type and the molecular number density set to the experimentally determined value. The simulation cell size is chosen according to the minimum Q-value of the data. The minimum Q-value which can be modelled is given by $Q_{\min} = 2\pi / L$, and fitting to smaller Q-values leads to unpredictable effects. If a much smaller $Q_{\min}$ were to be used, density fluctuations of period $2\pi / L$ would appear in the configuration.

2) The random configuration is made consistent with the closest approach distances of individual atom pairs. This is achieved by moving the atoms apart in small steps, until no atoms are closer than the specified minimum distance.

3) If the simulated system includes molecules of more than one atom, additional atoms may be added relative to a particular atom type at a specified distance and direction.

4) The RMC simulation is run with the closest approach distances and known co-ordination number constraints taken into account, until the co-ordination number criteria are fulfilled by more than ~95% of the atoms in question. The lower/higher co-ordination numbers of the remaining atoms have been found to make very little difference to the average structural properties of the system.

5) The RMC simulation proceeds along a Monte Carlo algorithm such that the three-dimensional molecular configuration is driven towards the experimental data. The quantity minimised is χ^2, initially given by:

$$\chi_0{}^2 = \sum_{i=1}^{m} [A_0^C(Q_i) - A^E(Q_i)^2] / \sigma(Q_i)^2 \qquad (4.1)$$

where $A_0^C(Q_i)$ is the structure factor determined from the RMC simulation, $A^E(Q_i)$ is the measured structure factor, $\sigma(Q_i)$ is the experimental error and the sum is over all the experimental data points. If the diffraction data consist of multiple independent data sets obtained by isotopic substitution techniques, they can be modelled simultaneously by adding the respective χ^2 values.

For a multi-component system where the fit is to several total structure factors which are not independent (i.e. the same partial correlation function is contained within more than one of the datasets), χ^2 is given by:

$$\chi_0^2 = \sum_k \chi_k^2 = \sum_k \sum_{i=1}^{m} [A_0^C(Q_i) - A^E(Q_i)]^2 / \sigma(Q_i)^2 \qquad (4.2)$$

where the sum is over the k datasets.

For the RMC simulations of ammonia and metallic lithium-ammonia solutions, the total structure factors from the fully deuterated, fully protonated and mixture samples were used to generate the three-dimensional configuration. The partial structure factors and partial radial distribution functions can then be extracted from the final RMC configuration and compared to the experimental partial functions.

6) One atom is moved at random, and a new radial distribution function and structure factor, $A_n^C(Q_i)$, is calculated. The new χ_n^2 is given by:

$$\chi_n^2 = \sum_{i=1}^{m} [A_n^C(Q_i) - A^E(Q_i)^2]/\sigma(Q_i)^2 \qquad (4.3)$$

If $\chi_n^2 < \chi_0^2$, the move is accepted. If $\chi_n^2 > \chi_0^2$, the move is accepted with probability $\exp[-(\chi_n^2 - \chi_0^2)/2]$. This is the Markov chain sampling method which is used in standard MMC simulations.[6] With repeated iterations of this step, χ^2 will decrease until it reaches an equilibrium value about which it will fluctuate. The resulting configuration will be a three-dimensional structure which is consistent with the available diffraction data, and within

the experimental error. A number of statistically independent configurations may then be collected.

4.1.2 Advantages and disadvantages of RMC simulation

Advantages:

- The resulting RMC model agrees quantitively with the available measured diffraction data. In other simulation techniques such as Monte Carlo and molecular dynamics, the agreement is only qualitative and is based on only a few features of the data, such as peak positions and co-ordination numbers.[5]

- For simulations involving interatomic potentials, it is often not obvious how the potential should be altered to improve the level of agreement with the experimental measurements. Iterative procedures which attempt to modify the potential functions can be computationally expensive.[5]

- RMC uses total or partial structure factors rather than radial distribution functions. This avoids the possibility of the RMC simulation attempting to model any unphysical features in the radial distribution functions which may arise from a Fourier transformation from *k*-space to *r*-space.

- Data from various different sources, such as neutron and X-ray diffraction and EXAFS experiments can be combined and modelled simultaneously.[7]

Disadvantages:

- The RMC simulation is not constrained by the atom-atom correlations which have a very weak weighting in the structural data, for example, Li-N and Li-H correlations in lithium-ammonia solutions. In these cases, the co-ordination number n_α^β of atom type β around atom type α within a certain range must be specified. This leads to partial radial distribution functions which are less robust than those obtained via simulations which make use of inter-atomic potentials.

- The three-dimensional structure produced by the RMC simulation is not unique: it is simply one possible configuration which is consistent with the diffraction data and the constraints imposed. A possible disadvantage is that RMC tends to produce the *most* disordered structure which is still consistent with the data, i.e. the entropy of the system is maximised.[5] However, it is possible to impose additional constraints, such that a range of possible configurations can be investigated and those which are inconsistent with the experimental data may be discounted.

4.2 Empirical Potential Structure Refinement

Empirical Potential Structure Refinement (EPSR)[8-10] is again a method which attempts to generate a three-dimensional configuration which is fully consistent with the available diffraction data. The main difference between EPSR and RMC is that EPSR utilises inter-atomic pair potentials in addition to diffraction data: essentially EPSR is a Monte Carlo simulation of the system under study. There are four types of atom move within EPSR: whole molecule translations, whole molecule rotations, rotation of molecular headgroups and intramolecular atomic moves.

The acceptance of a move is based on the usual Metropolis condition:[6] if the change in potential energy of the system as a result of the move, ΔU, is negative, the move is accepted. If ΔU is positive, the move is accepted with probability $\exp[-\Delta U / kT]$, the Boltzmann factor. Thus the simulation proceeds along a Markov chain, and is able to access a large volume of the available phase space over a period of time.

4.2.1 Principles of EPSR

The EPSR procedure as outlined below is intended as a guide to the way in which the simulations detailed in Chapters 5 and 7 were performed. For a full explanation of the EPSR routines, the reader is referred to the EPSR manual.[11]

1) The initial configuration of the system under study is set up at its correct composition, density and temperature, and the molecules' positions and orientations are randomized, prior to equilibration.

2) Harmonic potentials are set up for the internal structure of the molecules in the system. These are defined by an average atom-atom distance, $d_{\alpha\beta}$, and a width, $w_{\alpha\beta}$. The total intra-molecular energy is then represented by:[10]

$$U_{intra} = C\sum_{i}\sum_{\alpha,\beta\neq\alpha}\frac{(r_{\alpha_i\beta_i} - d_{\alpha\beta})^2}{2w_{\alpha\beta}^2} \tag{4.4}$$

where $r_{\alpha_i\beta_i}$ is the actual separation of the atoms α, β in molecule i, and $w_{\alpha\beta}^2 = d_{\alpha\beta}/\sqrt{\mu_{\alpha\beta}}$, with $\mu_{\alpha\beta} = M_\alpha M_\beta/(M_\alpha + M_\beta)$, the reduced mass of the atom pair $\alpha\beta$ in atomic mass units. C is a constant determined by comparing the simulated and measured structure factors at high Q.

3) Interatomic reference potentials of Lennard-Jones type plus effective Coulomb charges are set up for each atom pair. The potentials are taken from the literature, and are given by:

$$U_{\alpha\beta}(r_{ij}) = 4\varepsilon_{\alpha\beta}\left[\left(\frac{\sigma_{\alpha\beta}}{r_{ij}}\right)^{12} - \left(\frac{\sigma_{\alpha\beta}}{r_{ij}}\right)^{6}\right] + \frac{q_\alpha q_\beta}{4\pi\varepsilon_0 r_{ij}} \tag{4.5}$$

where α,β represent the types of atoms i,j respectively. If the atoms are of different types, the well depth parameter, $\varepsilon_{\alpha\beta}$, and the range parameter, $\sigma_{\alpha\beta}$, are given by the Lorentz-Berthelot mixing rules:[12]

$$\varepsilon_{\alpha\beta} = (\varepsilon_\alpha \varepsilon_\beta)^{1/2} \quad \text{and} \quad \sigma_{\alpha\beta} = \frac{\sigma_\alpha + \sigma_\beta}{2}. \tag{4.6}$$

In addition to the reference potential, the closest approach distance of each atom pair can be specified.

4) Having randomised the cluster of molecules, an initial configuration of non-overlapping molecules must be generated. Only whole molecule translations, whole molecule rotations, and possibly internal head group rotations are necessary to achieve this. The energy of the system will initially decrease rapidly, until after a number of iterations, the intermolecular energy is close to zero or negative.

5) The system is then allowed to equilibrate: EPSR is run as a standard MMC simulation,[6] with the potential refinement switched off. The MMC simulation is continued until the intermolecular energy fluctuates normally about an average value, and any known co-ordination number constraints, such as the ion solvation number, are satisfied.

6) Data sets comprising one or more measured partial or total structure factors, against which the reference site-site potentials are to be refined, are set up. Files containing the weighting coefficients of the individual atom pair

contributions are formed for each of the datasets used. For the total structure factors which have not been normalised, the weighting coefficient is given by:

$$w_{\alpha\beta} = c_\beta^2 b_\beta^2 \quad \text{or} \quad w_{\alpha\beta} = 2c_\alpha c_\beta b_\alpha b_\beta \tag{4.7}$$

for atom pairs of the same or different types, respectively, where c_α,c_β are the atomic fractions of atom type α,β and b_α,b_β are the scattering lengths of atom type α,β respectively.

For a first order isotopic substitution dataset which has not been normalised in any way, the weighting coefficients are defined as:

$$2c_\alpha c_\beta b_\alpha ({}^*b_\beta - b_\beta) \quad \text{or} \quad c_\beta{}^2({}^*b_\beta{}^2 - b_\beta{}^2) \tag{4.8}$$

for correlations between atoms of different types and correlations between pairs of isotopically substituted atoms, respectively. Here, ${}^*b_\beta$ and b_β are the neutron scattering lengths of the two isotopes of atom type β.

Finally, for second order hydrogen/deuterium isotopic substitution data, the weighting coefficients are calculated via eqs. 3.38 and 3.39. Note that for substituted hydrogen atoms which do not undergo in-solution isotopic exchange, the intra-molecular H-H peak is present in the X-H and X-X composite partial pair correlation functions rather than in the H-H pair correlation function.

7) The potential refinement is now switched on, and the EPSR simulation proceeds as follows:[8]

i) EPSR is run using the initial reference potential, $U^0_{\alpha\beta}(r)$, and is used to generate a partial pair correlation function, $g^{sim}_{\alpha\beta}(r)$.

ii) The potential of mean force: $\psi_{\alpha\beta}(r) = -kT \ln g_{\alpha\beta}(r)$, is used to generate a perturbation to the initial potential which is determined by the difference between the simulated and measured composite pair correlation functions. The new potential energy function is given by:

$$U^N_{\alpha\beta}(r) = U^0_{\alpha\beta}(r) + [\psi^D_{\alpha\beta}(r) - \psi^{sim}_{\alpha\beta}(r)]$$

$$= U^0_{\alpha\beta}(r) + kT \ln\left(\frac{g^{sim}_{\alpha\beta}(r)}{g^D_{\alpha\beta}(r)}\right) \qquad (4.9)$$

where the superscript D refers to functions derived from measured data, and *sim* refers to functions derived from the current EPSR iteration.

iii) This new potential, $U^N_{\alpha\beta}(r)$, is used in the EPSR simulation to obtain a new $g^{sim}_{\alpha\beta}(r)$, which will be in closer agreement with the measured data than the previous simulated partial pair correlation function.

iv) The site-site inter-atomic potential is again refined using:

$$U^{N+1}_{\alpha\beta}(r) = U^N_{\alpha\beta}(r) + [\psi^D_{\alpha\beta}(r) - \psi^{sim}_{\alpha\beta}(r)] \qquad (4.10)$$

This potential is again used in the EPSR simulation in order to produce a new simulated partial pair correlation function which is in still closer agreement with the experimental data.

v) This iterative refinement procedure continues until the quantity $[\psi^{D}_{\alpha\beta}(r) - \psi^{sim}_{\alpha\beta}(r)]$ tends to zero. The final pair potential generated in this way is therefore one which is consistent with the measured diffraction data provided.

Although the potential of mean force relates the potential energy function to the pair correlation function, in actual fact the EPSR refinement utilises directly measured partial/total static structure factors, so as to avoid any of the truncation errors associated with transformation from Q-space to r-space. Furthermore, the empirical potential must represent only true differences between the measured data and the simulation: it should not contain any artefacts arising from statistical noise or systematic errors in the data.[11]

The form of the empirical potential used is in the form of a series of power exponential functions:

$$U_{EP}(r) = kT \sum_{i} C_i p_{n_i}(r, \sigma_r) \tag{4.11}$$

where $$p_n(r, \sigma_r) = \frac{1}{4\pi\rho\sigma_r^3 (n+2)!}\left(\frac{r}{\sigma_r}\right)^n \exp\left(\frac{-r}{\sigma_r}\right). \tag{4.12}$$

The C_i are real constants which may be positive or negative, σ_r is a width function which can be specified in the simulation and ρ is the atomic number density of the simulated system.

The function $p_n(r,\sigma_r)$ has an exact three-dimensional Fourier transform to Q-space:

$$P_n(Q,\sigma) = 4\pi\rho \int p_n(r)\exp(i\mathbf{Q}\cdot\mathbf{r})d\mathbf{r}. \tag{4.13}$$

Therefore, the coefficients C_i are estimated directly from the diffraction data in Q-space by fitting a series of the form

$$U_{EP}(Q) = kT \sum_i C_i p_{n_i}(Q,\sigma_Q) \tag{4.14}$$

to the difference between the simulated and measured structure factors. The coefficients generated are then used in eq. 4.11 to produce the required empirical potential.

8) After the EPSR refinement has converged, various auxiliary routines which calculate all individual partial pair correlation functions, bond angle distributions, co-ordination numbers, cluster size distributions, and spatial density and orientational correlation functions[11] may then be run in conjunction with the EPSR simulation, and a number of configurations can be collected.

4.2.2 The spatial density function and orientational correlation function

Within the EPSR potential refinement procedure it is possible to calculate the spherical harmonic expansion[13] for the molecular pair correlation functions in order to show the many-body correlations between molecules. This approach has proved pivotal in studies of other hydrogen-bonded liquids, such as water and alcohols.[10,14]

Firstly, a 'spatial density plot' can be obtained by holding molecule 1 fixed at the origin in a pre-defined orientation, and averaging over all possible positions and orientations of the second molecule within a minimum and maximum distance from the first molecule, i.e. allowing θ_L and ϕ_L to vary. Secondly, it is possible to probe the most probable dipole orientations of the second molecule relative to the first, for each of the lobes appearing in the spatial density plot. In this case, the z-axis of the second molecule must lie parallel to its dipole moment axis. Again molecule 1 is fixed at the origin in its pre-defined orientation, but this time the direction of the centre of molecule 2 from the centre of molecule 1 must also be fixed by setting θ_L, ϕ_L at the angle of interest. Any dependence of the result on θ_m, χ_m is removed, and the most likely orientation of the z' axis of the second molecule relative to the central reference molecule may be investigated. Figure 4.1 shows how the axes are defined for the central and neighbouring ammonia molecules.

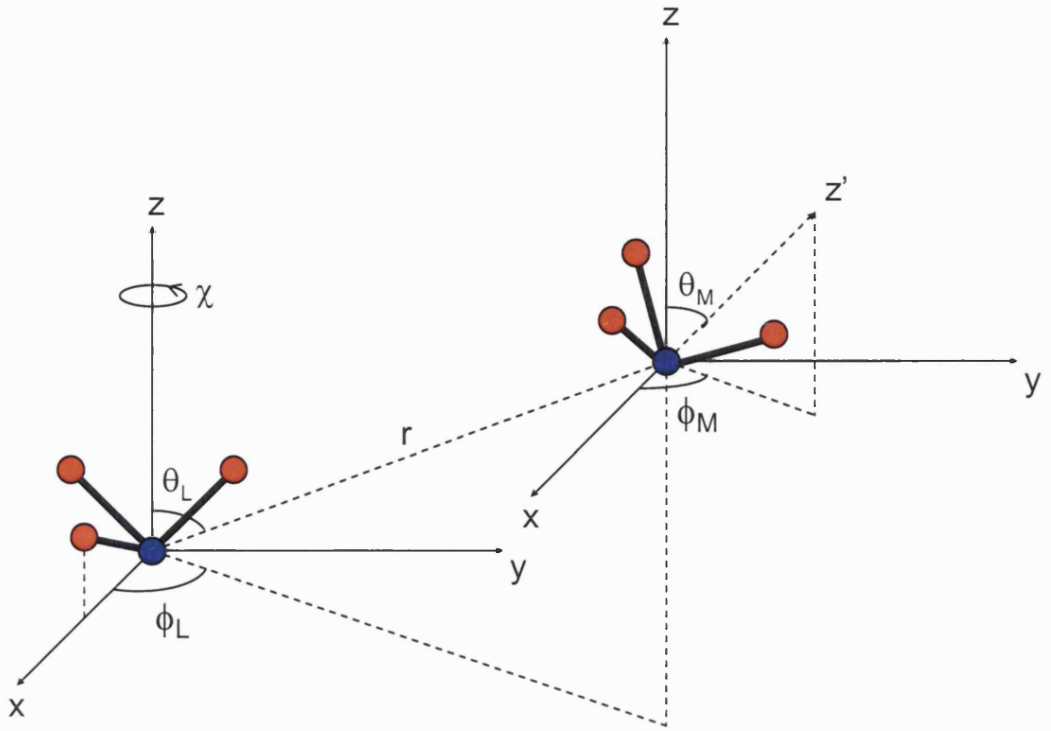

Figure 4.1 The co-ordinate system for the central reference ammonia molecule and a neighbouring ammonia molecule. The spatial density function is achieved by removing any dependence of the result on the orientation of molecule 2, and maps out the distribution of the centre of mass of the second molecule relative to the first. The orientational correlation function shows how the orientation of the second molecule is distributed as a function of r at a given (θ_L, ϕ_L, χ_L).

4.2.3 Advantages and disadvantages of EPSR

Advantages:

- EPSR is able to model accurately the atom pair correlations which have a very weak weighting in the experimentally determined structure factors, since the simulation uses well-characterised pair potentials which are taken from the literature.

- As with RMC, the resulting EPSR model agrees quantitively with the experimental data, unlike MMC and MD simulations where the agreement may be only qualitative.

- EPSR uses total or partial structure factors, so as to avoid any of the truncation errors arising from Fourier transformation from reciprocal space to real space.

- The empirical potential is cumulative: with each iteration of the simulation, a new perturbation to the potential is calculated and added to the existing perturbation. Thus, unlike RMC where the object is to minimize χ^2, the empirical potential develops amplitude and structure as the simulation proceeds, providing some memory of the shape of the empirical potential required to fit the data.

Disadvantages:

- In EPSR there is currently no correction for long-range effects in the potential energy. One reason for this is that the empirical potential cannot be calculated beyond half the simulation cell size, otherwise the effect of the longer range periodicity will come into play. Another reason is that making the necessary long-range corrections would be computationally expensive, and would not significantly alter the local arrangement of the atoms. It is therefore unlikely that EPSR would be able to reproduce the correct thermodynamics of the system under study.

4.3 Molecular Dynamics simulation

In a molecular dynamics (MD) simulation, the particles in the system interact via specified potentials, and their trajectories are predicted by solving Newton's laws of motion. Time is explicitly included in the simulation, and unlike Monte Carlo molecular modelling techniques, the dynamical properties of systems such as diffusion or time-dependent reactions can be studied. The MD code used in this work is MOLDY, an MD algorithm developed by Keith Refson (1988).[15]

4.3.1 The initial configuration – setting up the simulation

The initial configuration for an MD simulation is taken from an equilibrated Monte Carlo simulation. This ensures that the molecules are sufficiently far apart, hence the intermolecular forces are not unphysically large. If the configuration were initially far from equilibrium, the integration algorithm would break down, producing a system still further from equilibrium.

The equilibrated configuration comprises the molecules' quaternions and positions within the simulation cell. The quaternions allow molecular symmetry operations and combinations of rotations to be expressed in terms of simple quaternion algebra, rather than computationally unstable trigonometric functions.[16] They may be expressed in terms of the Euler angles as:

$$q_0 = \cos\frac{\phi+\mu}{2}\cos\frac{\theta}{2}$$

$$q_1 = \sin\frac{\phi-\mu}{2}\sin\frac{\theta}{2}$$

$$q_2 = \cos\frac{\phi-\mu}{2}\sin\frac{\theta}{2}$$

$$q_3 = \sin\frac{\phi+\mu}{2}\cos\frac{\theta}{2} \qquad (4.15)$$

where the first rotation is by an angle ϕ about the z-axis, the second is by an angle μ about the x-axis, and the third is a further rotation about the z-axis by an angle θ.

The initial centre-of-mass velocities are chosen from the Maxwell-Boltzmann distribution at the temperature specified for the simulation, i.e. they are picked from a set of random numbers with a Gaussian distribution which is normalized so that the probability density $p(v)$ of the x,y,z component of the velocity v_{ik} of molecule k is:

$$p(v_{ik}) = \left(\frac{m_k}{2\pi k_B T}\right)^{\frac{1}{2}} \exp\left(-\frac{m_k v_{ik}^2}{2k_B T}\right). \tag{4.16}$$

Finally, periodic boundary conditions are applied to the simulation cell. The size of a simulation cell practical for computer modelling is typically 20 – 30 Å, and edge effects would have a significant effect on the system's behaviour. In order to reduce these effects and reveal the system's bulk behaviour, periodic boundary conditions are applied. The basic computational cell is periodically replicated in the *xy*, *xz* and *yz* planes, so that the whole of space is filled with images of the basic unit.[17] Each replica of the basic simulation cell contains the same number of particles which all behave identically during the course of a simulation. If a particle leaves the simulation cell at one side, one of its periodic images enters the cell from the opposite side. In this way, the total number of particles is held fixed. The configurations of an 'infinite' system can therefore be generated by considering a limited number of particles and their periodic images, such that any boundary effects are suppressed.[17]

4.3.2 Equations of motion and the Verlet algorithm

The MD method simulates the dynamics of the system as described by the classical equations of motion. If the force exerted on atom α of molecule i by atom β of molecule j is denoted by $\boldsymbol{f}_{i\alpha j\beta}$, the total force acting on molecule i is then:

$$\boldsymbol{F}_i = \sum_j \sum_\beta \sum_\alpha \boldsymbol{f}_{i\alpha j\beta} \tag{4.17}$$

and the torque is given by

$$\boldsymbol{N}_i = \sum_\alpha (\boldsymbol{r}_{i\alpha} - \boldsymbol{R}_i) \times \boldsymbol{f}_{i\alpha} \tag{4.18}$$

where $\boldsymbol{f}_{i\alpha}$ is the force exerted on atom α of molecule i, summed over all atoms β and molecules j, and $\boldsymbol{R}_i$ is the centre of mass of molecule i, given by

$$\boldsymbol{R}_i = \frac{1}{M_i} \sum_\alpha (m_{i\alpha} \boldsymbol{r}_{i\alpha}). \tag{4.19}$$

The motion of the molecules is governed by the Newton-Euler equations:

$$M_i \ddot{\boldsymbol{R}}_i = \boldsymbol{F}_i \tag{4.20}$$

$$\boldsymbol{I}_i \cdot \dot{\boldsymbol{\omega}}_i - \boldsymbol{\omega}_i \times \boldsymbol{I}_i \cdot \boldsymbol{\omega}_i = \boldsymbol{N}_i \tag{4.21}$$

where $\ddot{\boldsymbol{R}}_i$ is the acceleration of the centre of mass of molecule i, M_i is the molecular mass, $\boldsymbol{\omega}_i$ is the angular velocity of molecule i and $\boldsymbol{I}_i$ is the inertia tensor, given by

$$\boldsymbol{I}_i = \sum_{\alpha} m_{i\alpha} \boldsymbol{p}_{i\alpha}^2 (1 - \boldsymbol{p}_{i\alpha} \boldsymbol{p}_{i\alpha}) . \tag{4.22}$$

Here, $\boldsymbol{p}_{i\alpha}$ is the atomic site co-ordinate relative to the centre of mass of the molecule:

$$\boldsymbol{p}_{i\alpha} = (\boldsymbol{r}_{i\alpha} - \boldsymbol{R}_i) . \tag{4.23}$$

The Verlet algorithm[18] provides a direct solution to the second order equation (eq. 4.20). It is based on the positions $\boldsymbol{r}(t)$, velocities $\boldsymbol{v}(t)$, accelerations $\boldsymbol{a}(t)$ and positions $\boldsymbol{r}(t\text{-}\delta t)$ from the previous timestep.

Taylor expansions around $\boldsymbol{r}(t)$ give:

$$\begin{aligned} \boldsymbol{r}(t+\delta t) &= \boldsymbol{r}(t) + \delta t \boldsymbol{v}(t) + \frac{\delta t^2 \boldsymbol{a}(t)}{2} + \left\{ \frac{\delta t^3}{6} \frac{d^3 r}{dt^3} + \frac{\delta t^4}{24} \frac{d^4 r}{dt^4} + ... \right\} \\ \boldsymbol{r}(t-\delta t) &= \boldsymbol{r}(t) - \delta t \boldsymbol{v}(t) + \frac{\delta t^2 \boldsymbol{a}(t)}{2} - \left\{ \frac{\delta t^3}{6} \frac{d^3 r}{dt^3} - \frac{\delta t^4}{24} \frac{d^4 r}{dt^4} + ... \right\} \end{aligned} \tag{4.24}$$

where the terms within the brackets are usually neglected.

Adding the two Taylor expansions gives:

$$\boldsymbol{r}(t+\delta t) + \boldsymbol{r}(t-\delta t) = 2\boldsymbol{r}(t) + \delta t^2 \boldsymbol{a}(t) + \left\{ \frac{\delta t^4}{12} \frac{d^4 r}{dt^4} + ... \right\} \tag{4.25}$$

hence

$$\boldsymbol{r}(t+\delta t) = 2\boldsymbol{r}(t) - \boldsymbol{r}(t-\delta t) + \delta t^2 \boldsymbol{a}(t) + \frac{\delta t^4}{12}\frac{d^4 r}{dt^4} \tag{4.26}$$

and the new position is calculated correct to the order of δt^4.

The velocities may be calculated via:

$$\boldsymbol{v}(t) = \frac{\boldsymbol{r}(t+\delta t) - \boldsymbol{r}(t-\delta t)}{2\delta t} \tag{4.27}$$

and are used to calculate quantities such as the kinetic energy and pressure of the system. However, this definition of the velocity is only accurate to the order of δt. The Beeman algorithm[19] is instead implemented in the MOLDY code, which gives velocities which are accurate to the order of δt^3.

The accuracy of numerical integration methods such as the Verlet and Beeman algorithms is critically dependent on the 'finite difference', δt. The timestep δt must therefore be chosen such that the particle trajectories remain on the appropriate constant energy surface in phase space, ensuring that the correct ensemble averages will be generated.[17] A timestep which is too long results in non-conservation of energy, and one which is too short results in an inefficient simulation.

4.3.3 Short-range potentials

The forces between the molecules are derived from the potential function, $\phi_{i\alpha j\beta}(r_{i\alpha j\beta})$. The subscripts i,j represent the molecules in the simulation, and α,β

represent the sites on each molecule. The total potential energy of the system is given by:

$$U = \sum_{i} \sum_{j>i} \sum_{\alpha} \sum_{\beta} \phi_{i\alpha j\beta}(\boldsymbol{r}_{i\alpha j\beta}) \tag{4.28}$$

The force acting on site β of molecule j from site α of molecule i is then:

$$\boldsymbol{f}_{i\alpha j\beta} = -\nabla \phi_{i\alpha j\beta}(\boldsymbol{r}_{i\alpha j\beta}) \tag{4.29}$$

The potential function ϕ, representing the van der Waals inter-molecular forces, can take on a variety of forms such as Lennard-Jones or Buckingham, which include a number of inverse power terms and an exponential repulsion. The potential used in the simulations of lithium-ammonia solutions was of Lennard-Jones type:

$$\phi(r_{ij}) = \varepsilon_{\alpha\beta}\left[\left(\frac{\sigma_{\alpha\beta}}{r_{ij}}\right)^{12} - \left(\frac{\sigma_{\alpha\beta}}{r_{ij}}\right)^{6}\right]. \tag{4.30}$$

Note that within the MOLDY code, the usual well-depth parameter of 4ε is replaced by ε.[15]

The forces $\boldsymbol{f}_{i\alpha j\beta}$ and $\boldsymbol{F}_{ij}$ derived from these potentials are short-ranged, decaying faster than r^{-3}. Therefore interactions between sites whose separation is greater than a specified cut-off radius, r_c, are assumed to be isotropic. The cut-off radius used in the simulations of liquid ammonia and lithium-ammonia solutions was approximately 10 Å. The simulation process is made more efficient if a list of the neighbouring

molecules which fall within the cut-off radius of a particular molecule is maintained.[12,17] In this way, the program need only check through the molecules appearing on the neighbour list, rather than all the molecules in the simulation. The lists must be updated at regular intervals.

In the MOLDY code, the simulation cell is partitioned into a number of smaller cells, known as subcells.[12,20] The neighbour list then contains the positions of all the particles contained in each subcell, and the interactions between all pairs of particles within the cut-off distance is computed by looping over all pairs of subcells within the cut-off and all particles within the subcells. This significantly reduces the computational time required to maintain the neighbour lists, and allows interactions between several periodic images of a site to be computed. The MOLDY code therefore does not follow the minimum image convention used in many MD codes. Since the list of neighbouring cells instead includes *all* periodic images of a particle which are within the cut-off radius, it is possible to use a cut-off of more than half the simulation cell size in any direction.[15]

The truncation of the potential at the cut-off radius, however, causes a finite discontinuity at $r_{ij} = r_c$. Whenever the separation between a pair of molecules crosses this boundary, the discontinuity will result in non-conservation of energy.[17] Therefore the short-range energy calculation must be modified in the following way:

$$U^{sr}(r_{ij}) = U(r_{ij}) - U_C - \left.\frac{dU(r_{ij})}{dr_{ij}}\right|_{r_{ij}=r_c} \times (r_{ij} - r_c) \qquad \text{for } r_{ij} \le r_c$$

$$U^{sr}(r_{ij}) = 0 \qquad \text{for } r_{ij} > r_c. \qquad (4.31)$$

The constant term U_C ensures that the potential remains continuous across the boundary, and cannot affect the forces between the molecule pair or the equations of motion of the system, since these are formed from the derivative of the potential energy. Its contribution to the total energy must be included in calculations which monitor energy conservation, as this will vary with the number of molecule pairs having a separation below r_c.

The linear term ensures that the force between two particles remains continuous across the boundary. This term is essential, since any discontinuity may cause an instability in the numerical solution of the differential equations (eq. 4.24). The thermodynamic properties of a system of particles interacting via the unshifted potential must then be recovered from the results of the simulation of particles interacting via the shifted potential.

4.3.4 Long-range potentials and the Ewald sum

In addition to the van der Waals short-range forces, effective Coulomb charges may be specified for each atomic or ionic site. These are longer-ranged interactions which exceed half the simulation cell size, and so the forces from the periodic images of these particles must also be considered. The computational time involved in calculating the force and potential energy from all the images of the simulation cell is vastly reduced by the imposed periodicity. This periodicity can be exploited to perform the force/energy calculations over an infinite number of images using a mathematical summation technique.

The Ewald sum is one such method, which is designed to ensure the rapid convergence of the long-range potential.[17] The technique uses the force at a point formulation and must consider the sum of the interactions between charges in the central box and all the images of all particles for an infinite number of such boxes. In the limit of a very large number of boxes, the simulation cell array is assumed to be spherical in shape: the potential is then given by:

$$V = \frac{1}{2}\sum_{\boldsymbol{n}}\sum_{i=1}^{N}\sum_{j=1}^{N}\frac{q_i q_j}{4\pi\varepsilon_0 \,|\, r_{ij} + \boldsymbol{n}|} \tag{4.32}$$

where N is the number of particles in the simulation cell and $\boldsymbol{n}$ is a cubic lattice point given by:

$$\boldsymbol{n} = n_x L_x + n_y L_y + n_z L_z \tag{4.33}$$

where n_x, n_y and n_z are integers, and L_x, L_y and L_z are the lengths of the simulation cell in the x, y and z directions respectively.

The Ewald sum technique converts the slowly converging sum in eq. 4.32 into two series, each of which converges far more rapidly.[17] The method is as follows:

i) Each point charge in the simulation cell is surrounded by a Gaussian charge distribution of equal magnitude and opposite sign, which is centred at the point charge.[16] This serves to screen the interactions between neighbouring charges, such that the forces between the point charges are now short-range and can be summed effectively in real space. The Gaussian function is chosen to have a width of $\sqrt{2/\alpha}$, and is given by:[16]

$$\rho_{Gauss}(r) = -q_i(\alpha/\pi)^{3/2}\exp(-\alpha r^2)\,. \tag{4.34}$$

The value of α is chosen by considerations of computational efficiency, depending on the computational time τ_R required to evaluate the real part of the potential between a pair of particles, and the computational time τ_F needed to evaluate the Fourier part of the potential per particle and per k vector. The value of α is given by:[16]

$$\alpha = \left(\frac{\tau_R \pi^3 N}{\tau_F L^6}\right)^{\frac{1}{6}} \tag{4.35}$$

where N is the total number of particles in the simulation cell and L is the simulation cell size.

ii) A charge distribution of the same sign as that of the original point charge, but with the same shape as the screening charge is then added. This is necessary in order to reduce the overall potential to that due to the original set of charges. The cancelling distribution is a smoothly varying function which is also periodic. This function can be represented by a rapidly converging Fourier series, which is then summed in reciprocal space.[16]

iii) In addition, the spurious contribution to the potential energy arising from the interaction between the continuous Gaussian charge cloud of charge q_i and the point charge q_i located at the centre of the Gaussian must be subtracted from the sum of the real-space and reciprocal-space contributions to the Coulomb energy.[16]

4.3.5 Temperature initialization and rescaling

The initial kinetic energy of an MD simulation is set by sampling the particles' velocities from the Maxwell-Boltzmann distribution at the required temperature. The effective temperature of the system is then calculated from the ensemble average of its kinetic energy. However, the initial configuration is usually far from equilibrium and has a high potential energy. As the simulation proceeds, much of the potential energy is converted to kinetic energy, thus raising the temperature of the system.

It is therefore necessary to scale the kinetic energy of the particles during the equilibration period. This is typically achieved by multiplying the linear and angular velocities at periodic intervals by a factor of:

$$s = \sqrt{\frac{gk_BT}{2\mathcal{K}}} \tag{4.36}$$

where g is the number of degrees of freedom, T is the required temperature and $\mathcal{K}$ is the instantaneous value of the kinetic energy. By repeatedly setting the 'instantaneous' temperature to the correct value, the kinetic energy is made to approach its required value.[15]

An MD simulation with scaling does not generate equilibrium particle trajectories, so the scaling must be switched off before any calculations of thermodynamic averages are performed. The simulation can then proceed along the N,V,E ensemble, where the total number of particles, the simulation cell volume and the total energy is held constant, or along an N,V,T ensemble where the temperature, rather than the total energy, is fixed. The latter is achieved by thermostat methods:

the Nosé-Hoover method[21,22] which couples the system to a heat bath, and the Gaussian thermostat[12] which replaces the Newton-Euler equations by variants in which the kinetic energy is conserved. The *N,V,E* ensemble was used in the simulations of liquid ammonia and lithium-ammonia solutions, which are presented in Chapter 6.

4.3.6 Structural and dynamical properties from MD simulations

The MOLDY code enables configurations of the system to be saved at periodic intervals. Particular information such as particle positions and molecule quaternions may then be extracted from these binary dump files, in order that time-averaged radial distribution functions and the mean square displacements of different particle types may be calculated.

4.3.6.1 Radial distribution functions

The radial distribution function (RDF) is one of the most important structural quantities which characterize a liquid system. In the case of a molecular system, the partial RDF for atoms α and β is defined as:[23]

$$g_{\alpha\beta}(r) = \frac{1}{\rho^2 V}\left\langle N(N-1)\delta(\boldsymbol{r} + \boldsymbol{r}_{i\alpha} - \boldsymbol{r}_{j\beta})\right\rangle \tag{4.37}$$

where ρ is the molecular number density, V is the volume of the simulation cell, N is the total number of particles, $\boldsymbol{r}$ is the vector between the centre of mass of molecules i and j, and $\boldsymbol{r}_{i\alpha},\boldsymbol{r}_{j\beta}$ are the vectors from the centres of mass of molecules i,j to the atomic sites α,β respectively. The angled brackets denote a spherical average in addition to the usual configurational average.

In the simulation, the RDF is evaluated by:[12,15]

$$g_{\alpha\beta}(r+\delta r/2)=\frac{3Nn_{his}(b)}{4\pi\rho\ N_{\alpha}N_{\beta}\tau[(r+\delta r)^3-r^3]} \tag{4.38}$$

where $n_{his}(b)$ is the accumulated number of atom pairs per bin, b is the number of the histogram bin, δr is the bin width (hence $r = b\delta r$) and τ is the number of timesteps over which the atom pair distances have been counted.

4.3.6.2 Mean square displacements and diffusion coefficients

The mean square displacement vs. time of a particular species can be calculated from the particle positions extracted from the binary dump files. For a species of N particles, the mean square displacement is calculated via:

$$\langle|r(t)-r(0)|^2\rangle=\frac{1}{N\ N_t}\sum_{n=1}^{N}\sum_{t_0}^{N_t}|r_n(t+t_0)-r_n(t_0)|^2 \tag{4.39}$$

where $r_n(t)$ is the position of particle n at time t, and N_t is the total number of timesteps over which the sum is performed for a particular t. The diffusion coefficient of that species can then be calculated from the gradient of a plot of the mean square displacement against time, using the Einstein relation:[12]

$$\langle | r(t) - r(0) |^2 \rangle = 6Dt \tag{4.40}$$

The radial distribution functions and diffusion coefficients extracted from the MD simulations serve as a basis for comparison with experimental data, as detailed in Chapter 6. The experimental data can also be used as a stringent test for the potential functions used in the MD simulations.

4.4 References

[1] R. L. McGreevy and L. Pusztai, Mol. Sim. **1**, 359 (1988).

[2] L. Pusztai and R. L. McGreevy, J. Phys. Cond. Matter **10**, 525 (1998).

[3] V. M. Nield, M. A. Howe, R. L. McGreevy, J. Phys. Cond. Matter **3**, 7519 (1991).

[4] J. Swenson, R. L. McGreevy, L. Borjesson and J. D. Wicks, Solid State Ionics **105**, 55 (1998).

[5] R. L. McGreevy, *RMC Manual.*

[6] N. Metropolis, A. W. Rosenbluth, M. N. Rosenbluth, A. H. Teller and E. Teller, J. Phys. Chem. **21**, 1087 (1953).

[7] J. D. Wicks and R. L. McGreevy, J. Non-Cryst. Solids **193**, 23 (1995).

[8] A. K. Soper, Chem. Phys. **202**, 295 (1996).

[9] A. K. Soper, Chem. Phys. **258**, 121 (2000).

[10] A. K. Soper, Mol. Phys. **99**, 1503 (2001).

[11] A. K. Soper and D. T. Bowron, *EPSR – A User's Guide* (2000).

[12] M. D. Allen and D. J. Tildesley, *Computer Simulation of Liquids*, OUP, Oxford, (1987).

[13] C. G. Gray and K. E. Gubbins, *Theory of Molecular Fluids – Volume 1: Fundamentals*, Clarendon Press, Oxford, (1984).

[14] D. T. Bowron, A. K. Soper and J. L. Finney, J. Chem. Phys. **114**, 6203 (2001).

[15] K. Refson, *Moldy User's Manual, Revision 2.25.2.6 for release 2.16*, (2001).

[16] D. Frenkel and B. Smit, *Understanding Molecular Simulation – from Algorithms to Applications*, Academic Press (2002).

[17] A. R. Leach, *Molecular Modelling: Principles and Applications*, Prentice Hall, Harlow, (2001).

[18] L. Verlet, Phys. Rev. **165**, 201 (1967).

[19] D. Beeman, J. Comp. Phys. **20**, 130 (1976).

[20] B. Quentrec and C. Brot, J. Comp. Phys. **13**, 430 (1975).

[21] W. G. Hoover, Phys. Rev. A. **31**, 1695 (1985).

[22] S. Nosé, Mol. Phys. **52**, 255 (1984).

[23] J. P. Hansen and I. R. McDonald, *Theory of Simple Liquids*, 2nd ed., Academic Press, London (1986).

CHAPTER 5

RESULTS I:
STRUCTURE OF LITHIUM-AMMONIA SOLUTIONS

5.1 Introduction

The technique of hydrogen/deuterium isotopic substitution in neutron diffraction has been used to extract detailed information concerning the solvent structure in pure ammonia and lithium-ammonia solutions across the metal-nonmetal transition. In pure ammonia there is evidence for approximately 2.1 hydrogen bonds around each nitrogen atom, with an average N-H distance of 2.4 Å. Upon addition of alkali metal, significant disruption of this hydrogen-bonding is directly observed. At 8 MPM there remain only around 0.7 hydrogen bonds per nitrogen atom. No trace of hydrogen-bonding remains in the saturated solution of 21 MPM, as all the ammonia molecules have become incorporated into the primary tetrahedral solvation spheres of the lithium cations. In conjunction with classical three-dimensional computer modelling techniques, it is possible to identify a well-defined second cationic solvation shell. In this secondary shell, the nitrogen atoms tend to reside above the faces and edges of

the primary tetrahedral shell. Furthermore, the models reveal that voids of approximate radius 2.5 to 3.0Å are formed between the solvent molecules upon addition of alkali metal. The data therefore provide new insight into the structure of the polaronic cavities and tunnels which have been predicted for lithium-ammonia solutions.[1-3]

5.2 Experimental and simulation details

The technique of hydrogen/deuterium isotopic substitution[4] has been used to investigate the structure of pure ammonia and lithium-ammonia solutions at concentrations of 2, 3, 4, 8 and 21 MPM. For all concentrations of the lithium-ammonia solutions, three isotopically distinct samples were measured: Li-ND_3, Li-NH_3 and a 50:50 mixture of Li-ND_3 and Li-NH_3 (50:50 being chosen here to maximize the scattering differences between the samples). For pure ammonia, the samples comprised ND_3, NH_3 and a 33:67 mixture of ND_3 and NH_3 (a so-called 'null scattering' mixture).

Background, multiple scattering, absorption and normalization analysis procedures were implemented using the ATLAS suite of programs[5,6] (detailed in Chapter 3). The three target composite partial structure factors, X-X, X-H and H-H, were formed using eqs. 3.34 - 3.37. At this stage it was necessary to perform a further semi-empirical inelastic scattering correction to the low-Q region of these partial structure factors, because of the large number of hydrogen atoms present in the samples.[4] The efficacy of these procedures was verified by checking the self-

consistency of the composite partial structure factors and their Fourier back-transforms. The Fourier transformation of the data to real space was carried out via a minimum noise method,[6,7] described in section 3.4.2. In this way it was possible to focus on real features, and not, for example, those that might be caused by truncation of the structure factor and/or noise within the data.

5.2.1 Reverse Monte Carlo simulation

Reverse Monte Carlo (RMC)[8] is a classical simulation technique which generates a three-dimensional representation of an ensemble of molecules, and therefore provides a great deal more information than the experimentally measured structure factors and partial pair correlation functions alone.

This molecular modelling technique has been applied to liquid ammonia and the 8 MPM and 21 MPM metallic lithium-ammonia systems in order to generate 3-dimensional ensembles which are both consistent with experimental data as well as known structural constraints such as intra-molecular atom-atom distances, the geometry of the ammonia molecule and the tetrahedral solvation of lithium ions.[9-11] The datasets used for the RMC modelling comprised the total static structure factors for the fully deuterated, fully protonated and the mixed samples. In each simulation, the minimum number of atoms used was 3000. The atomic density was set to the experimental value, and a cubic box-side of approximately 35 Å calculated accordingly. This method allowed the angular orientations of the solvent molecules, relative to each other and the lithium cation (the latter using a pre-defined axis for

the Li-$(NH_3)_4^+$ tetrahedron) to be investigated. In addition, the final model was used to find the propensity for the solutions to form cavities or channels in which the excess electrons may be accommodated.

5.2.2 Empirical Potential Structure Refinement

Empirical Potential Structure Refinement (EPSR)[12-14] is a method which involves iterative refinement of an initial interatomic potential energy function, such that the resulting potential is able to produce the closest possible agreement between the simulated and measured site-site composite partial structure factors.

EPSR simulations were carried out on liquid ammonia and lithium-ammonia solutions spanning the metal-nonmetal transition at 2 MPM, 8 MPM and 21 MPM. The datasets used in the refinement procedure comprised the composite partial structure factors $S_{HH}(Q)$, $S_{XH}(Q)$ and $S_{XX}(Q)$ for all the systems,[15] and also included first-order lithium difference data for the metallic lithium-ammonia solutions at 8 and 21 MPM.[9-11] The EPSR procedure uses a Monte Carlo simulation of molecules in a cubic box of side ~30 Å, the number of atoms being approximately 2000 for each system under study. The ammonia molecule used was the 4-site OPLS model,[16,17] initially with Lennard-Jones pair potentials for all atom-atom correlations and effective Coulomb charges, given in table 5.1. In the metallic solutions of 8 MPM and 21 MPM, the electrons were not explicitly included, although the density used reflected the volume expansion due to the accommodation of excess electrons in the solution. For the dilute solution of 2 MPM, the electrons were included and

given a soft Lennard-Jones potential, to model their localisation in space via solvation by ammonia molecules.

Atom type	σ / Å	ε / kcal mol^{-1}	q / e
Li^+	1.26	6.25	1.0
N	3.42	0.17	-1.02
H	0.0	0.0	0.34

Table 5.1 Lennard-Jones pair potentials, of the form $U(r) = 4\varepsilon\left[\left(\frac{\sigma}{r}\right)^{12} - \left(\frac{\sigma}{r}\right)^{6}\right]$.

The EPSR analysis technique provides a complete set of atom-atom partial pair correlation functions, which are consistent with the measured data. In addition, the EPSR procedure allows the implementation of a spherical harmonic expansion of the intermolecular structure in terms of polar coordinates r, θ and ϕ. The angles θ and ϕ are defined relative to the z-axis (dipole moment) of the ammonia molecule and the x-z plane (in which the first intra-molecular N-H bond lies) respectively. Such an analysis yields the orientational molecular distributions of ammonia molecules and lithium ions relative to a central ammonia molecule or lithium ion, and the dipolar molecule-molecule orientations. This allows the directionality of the hydrogen bonding and the distribution and orientation of the ionic solvation shells to be investigated.

In addition, the resulting 3-D configurations have been searched for electron cavities within the solvent, and the angular distribution of the ammonia molecules that solvate these cavities has then been measured.

5.3 Results and Discussion – H/D isotopic substitution and RMC modelling

The measured total structure factors together with the minimum noise fits for the 0, 2, 3, 4, 8 and 21 MPM deuterated lithium-ammonia solutions are presented in figure 5.1(a). The minimum noise fits show excellent agreement with the measured data, and therefore give confidence in the data analysis techniques used.[4] Upon addition of lithium metal to ammonia, a decrease in the position of the principal peak in $F(Q)$ is observed, from 2.08(2) $Å^{-1}$ in liquid ammonia, to 2.07(2) $Å^{-1}$ in the dilute solutions (2, 3 and 4 MPM), and down to 2.01(2) $Å^{-1}$ and 1.85(2) $Å^{-1}$ in the 8 MPM and 21 MPM solutions respectively.[9,18,19] This shift is consistent with the reduction in solution density with metal concentration, as the solvent expands in order to accommodate the excess electrons as they are dissociated from the lithium atoms.[20] For the saturated (21 MPM) solution, the presence of a pre-peak at ~1 $Å^{-1}$ indicates intermediate-range ordering in the solution. This feature is associated with correlations between solvated cation complexes,[9] and is discussed in detail in section 5.3.2.

The corresponding total pair correlation functions are shown in figure 5.1(b). It is clear that these functions are dominated by intra-molecular correlations, thus demonstrating the need for a full hydrogen/deuterium isotopic substitution

experiment to be performed on these solutions to determine the inter-molecular structure within the host solvent.

Figures 5.2 to 5.4 show the composite partial structure factors, $S_{HH}(Q)$, $S_{XH}(Q)$ and $S_{XX}(Q)$, together with the corresponding composite partial pair correlation functions. From these functions it can be seen that all intra-molecular distances within the ammonia molecules are unaffected by the presence of the lithium cations and excess electrons. Furthermore, the principal peak position in all three of the partial structure factors decreases with metal content, in accordance with the total structure factors. This effect reflects the overall reduction in solution density, and leads to corresponding peak shifts in the high-r region of the partial pair correlation functions.

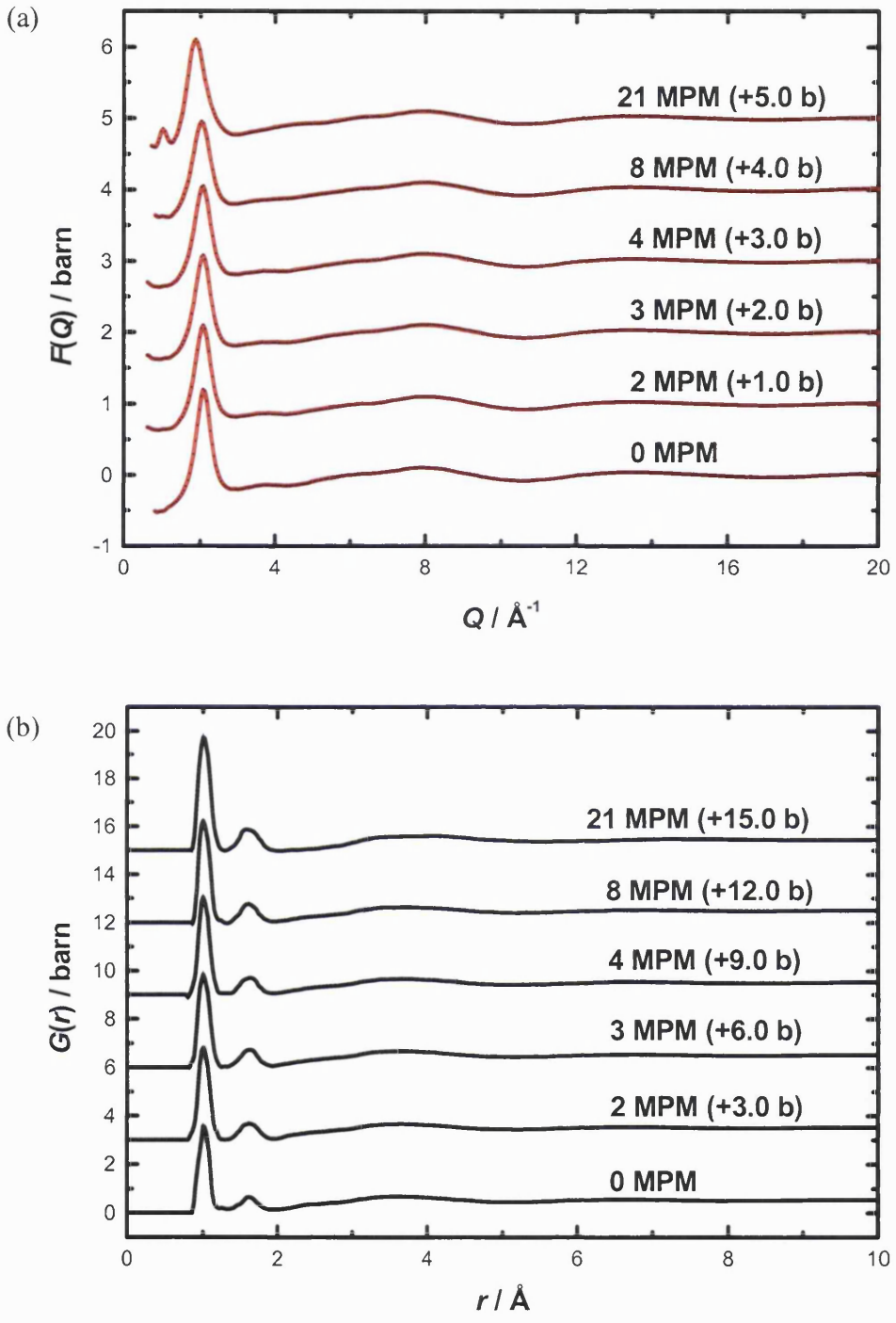

Figure 5.1 (a) Total structure factors (error bars) and minimum noise fit (solid line) and (b) total pair correlation functions for the deuterated samples. Note the shift inwards of the principal peak in $F(Q)$ with increasing metal concentration, and the appearance of the pre-peak at saturation.

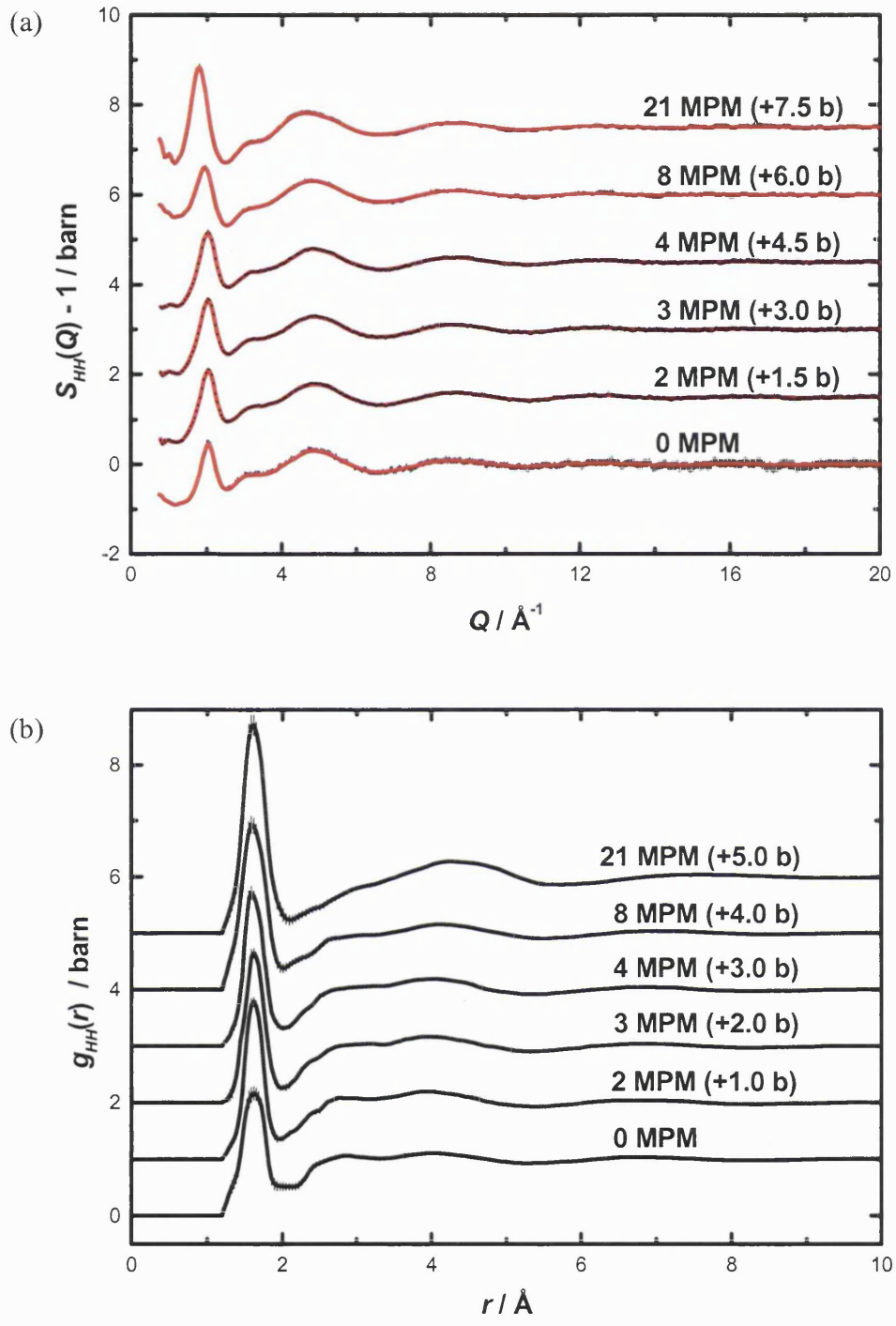

Figure 5.2 (a) H-H partial structure factors (error bars) and minimum noise fit (solid line) and (b) H-H partial pair correlation functions. The peak at ~2.9 Å in $g_{HH}(r)$ represents correlations between hydrogen atoms on adjacent hydrogen-bonded ammonia molecules, and is seen to decrease in size with increasing metal content.

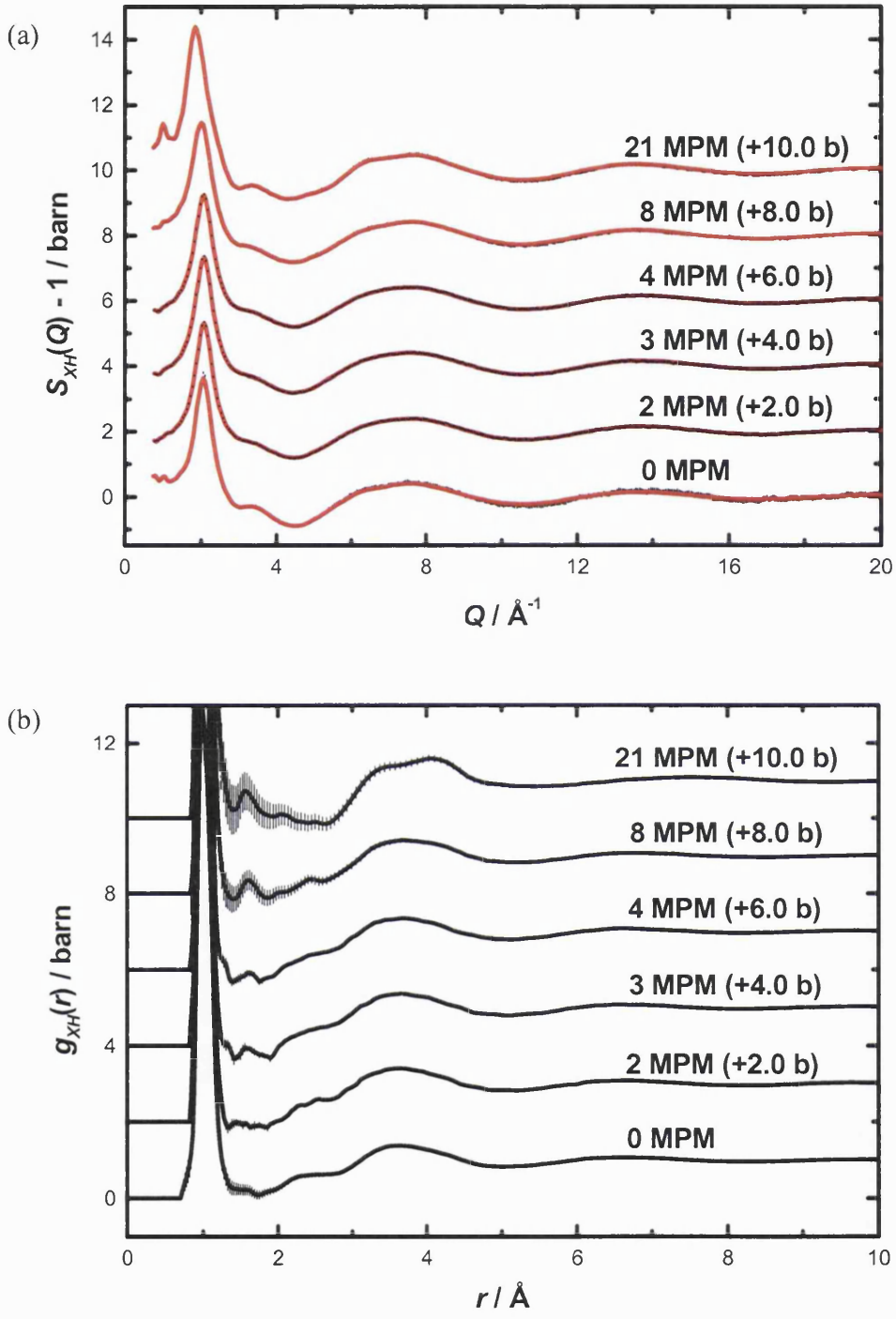

Figure 5.3 (a) X-H partial structure factors (error bars) and minimum noise fit (solid line) and (b) X-H partial pair correlation functions. The shoulder at ~2.4 Å is assigned to N-H hydrogen-bonding which is disrupted as the metal concentration is increased.

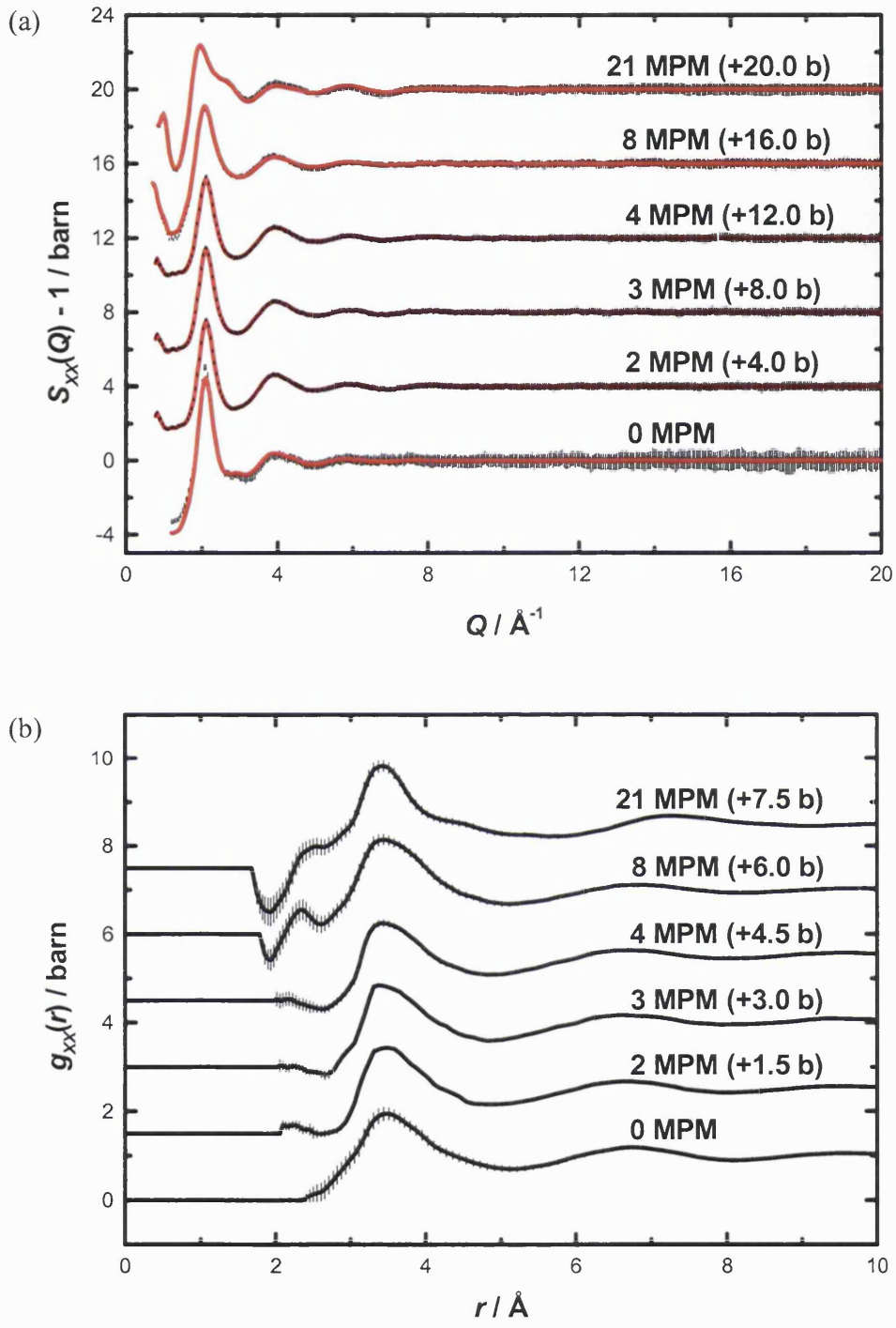

Figure 5.4 (a) X-X partial structure factors (error bars) and minimum noise fit (solid line) and (b) X-X partial pair correlation functions. Note that the first N-N peak position shifts inwards with increasing metal concentration; a trend which is contrary to the density decrease as excess electrons are accommodated in the solution.

In order to determine the nearest-neighbour distances and co-ordination numbers, each of the partial pair correlation functions has been plotted as $r^2g(r)$, and a Gaussian curve fitting procedure has been applied, as shown in figures 5.7 – 5.9 and tables 5.3 – 5.8. This method allows us to separate the quite broad features typical in liquid structures, and therefore provides the basis for quantitative discussion of the local structure in the solutions. The coordination numbers were calculated via eq. 3.41, and have been weighted by the coefficients given in table 5.2.

	0 MPM	2 MPM	3 MPM	4 MPM	8 MPM	21 MPM
H-H Partial:						
H-H	1.000	1.000	1.000	1.000	1.000	1.000
X-H Partial:						
N-H	1.000	1.004	1.006	1.009	1.018	1.057
Li-H	-	-0.004	-0.006	-0.009	-0.018	-0.057
X-X Partial:						
N-N	1.000	1.008	1.013	1.017	1.036	1.117
N-Li	-	-0.008	-0.013	-0.017	-0.036	-0.121
Li-Li	-	1.73E-05	3.99E-05	7.28E-05	0.0003	0.0033

Table 5.2 Weighting coefficients for the individual contributions to the X-X, X-H and H-H functions for the lithium-ammonia solutions.

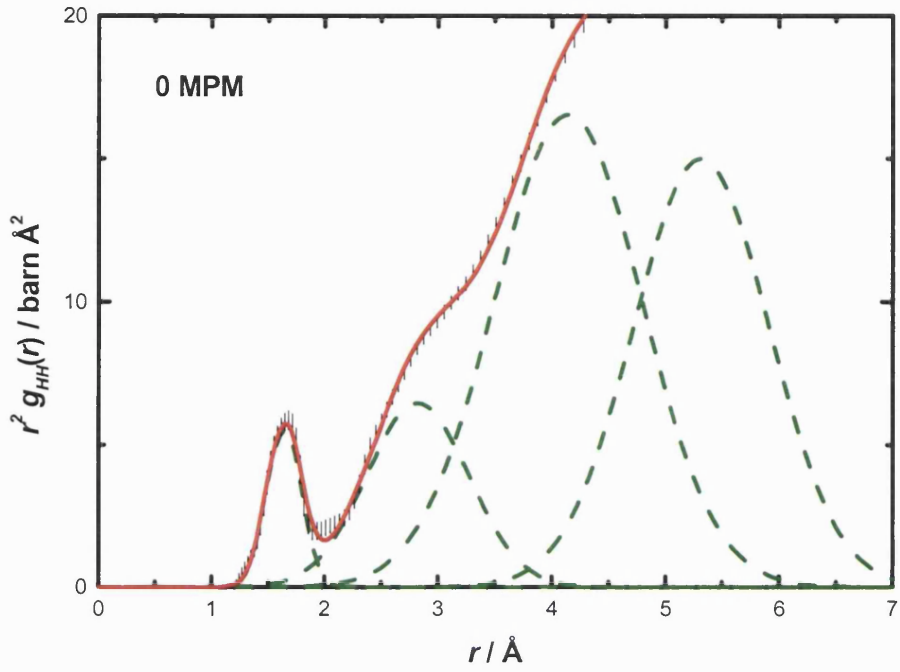
0 MPM
20
10
0
0
1
2
3
4
5
6
7
$r^2 g_{HH}(r)$ / barn Å^2
r / Å

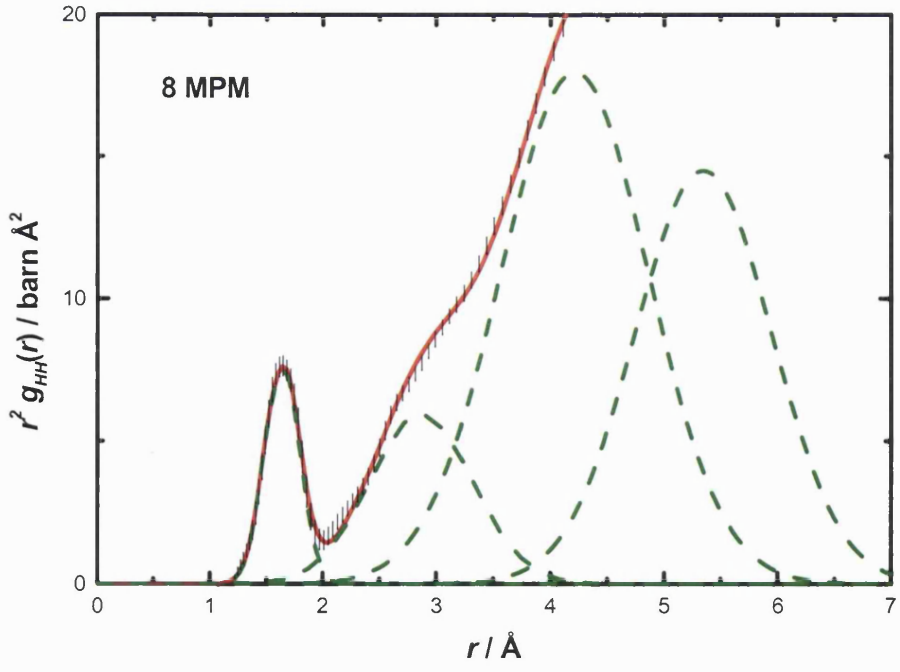
8 MPM
20
10
0
0
1
2
3
4
5
6
7
$r^2 g_{HH}(r)$ / barn Å^2
r / Å

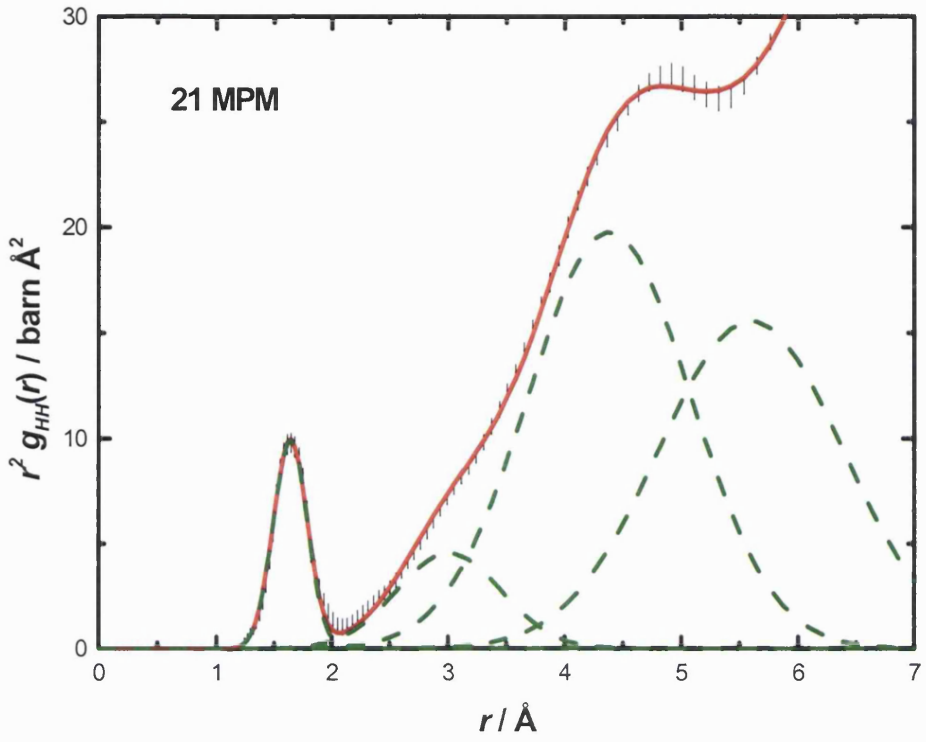

Figure 5.5 Examples of Gaussian fitting to $r^2 g_{HH}(r)$. The error bars show the measured data, the solid lines the total Gaussian fit and the dashed lines the individual Gaussian peaks.

H-H	0 MPM		2 MPM		3 MPM	
Assignment	r / Å	Area/atoms	r / Å	Area/atoms	r / Å	Area/atoms
i) Intra H-H	1.64 ± 0.02	2.2 ± 0.2	1.63 ± 0.02	1.9 ± 0.2	1.64 ± 0.02	1.9 ± 0.2
ii) Inter H-H	2.82 ± 0.05	7.5 ± 1.0	2.79 ± 0.06	5.5 ± 1.0	2.82 ± 0.05	5.3 ± 1.0
iii) Inter H-H	4.14 ± 0.29	28 ± 2	4.04 ± 0.31	23 ± 2	4.03 ± 0.30	21 ± 2
iv) Inter H-H	5.31 ± 0.20	23 ± 2	5.12 ± 0.21	19 ± 2	5.10 ± 0.21	19 ± 2

H-H	4 MPM		8 MPM		21 MPM	
Assignment	r / Å	Area/atoms	r / Å	Area/atoms	r / Å	Area/atoms
i) Intra H-H	1.63 ± 0.02	1.9 ± 0.2	1.64 ± 0.02	2.2 ± 0.2	1.64 ± 0.02	2.2 ± 0.2
ii) Inter H-H	2.82 ± 0.05	5.3 ± 1.0	2.87 ± 0.06	5.0 ± 1.0	3.00 ± 0.07	3.0 ± 1.0
iii) Inter H-H	4.12 ± 0.29	24 ± 2	4.21 ± 0.35	22 ± 2	4.38 ± 0.36	21 ± 2
iv) Inter H-H	5.20 ± 0.23	16 ± 2	5.34 ± 0.23	16 ± 2	5.60 ± 0.25	18 ± 2

Table 5.3 Peak assignments and co-ordination numbers: H-H correlations in ammonia and lithium-ammonia solutions.

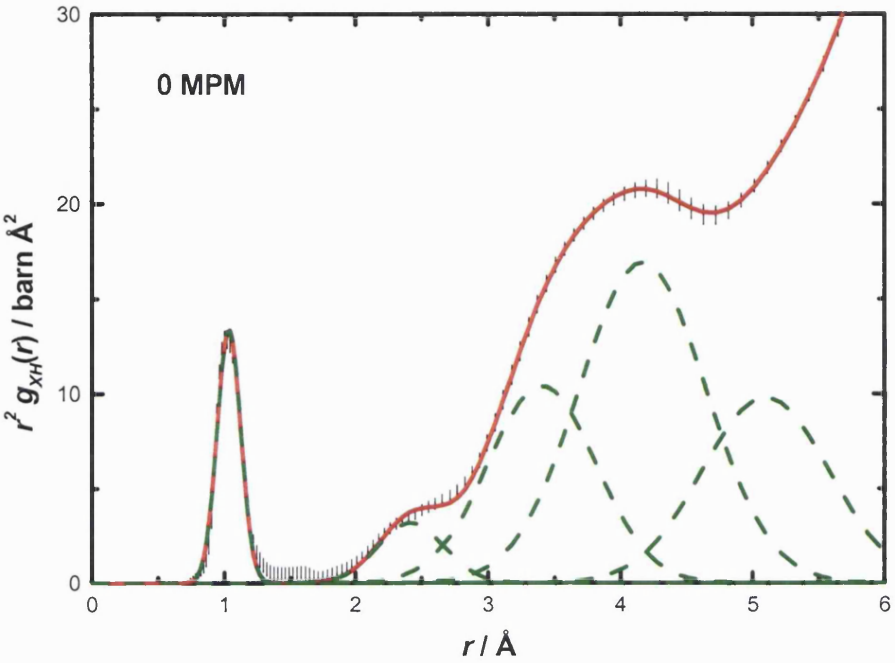
0 MPM
$r^2 g_{XH}(r)$ / barn Å^2
r / Å
0
10
20
30
0
1
2
3
4
5
6

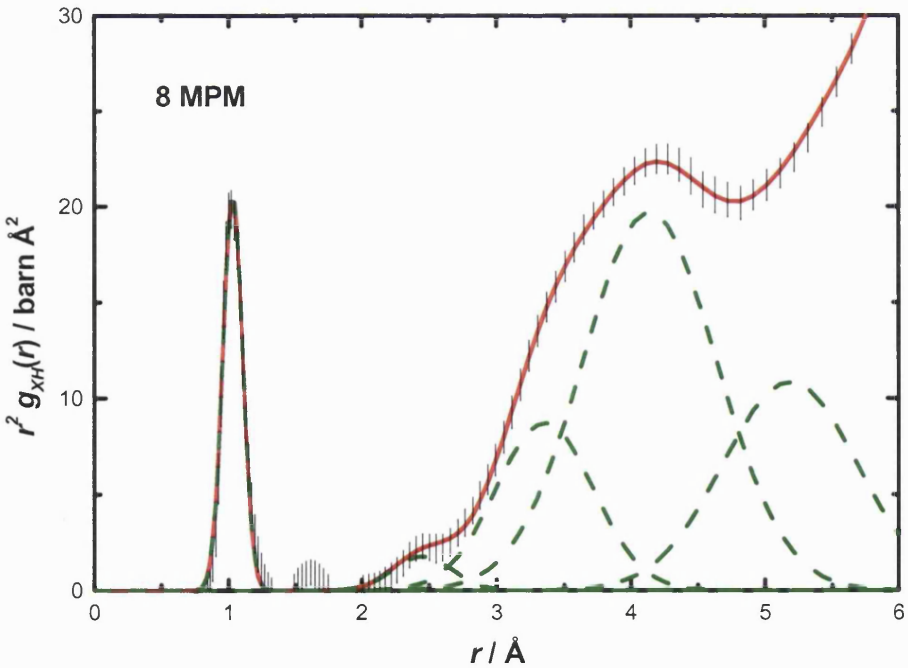
8 MPM
$r^2 g_{XH}(r)$ / barn Å^2
r / Å
0
10
20
30
0
1
2
3
4
5
6

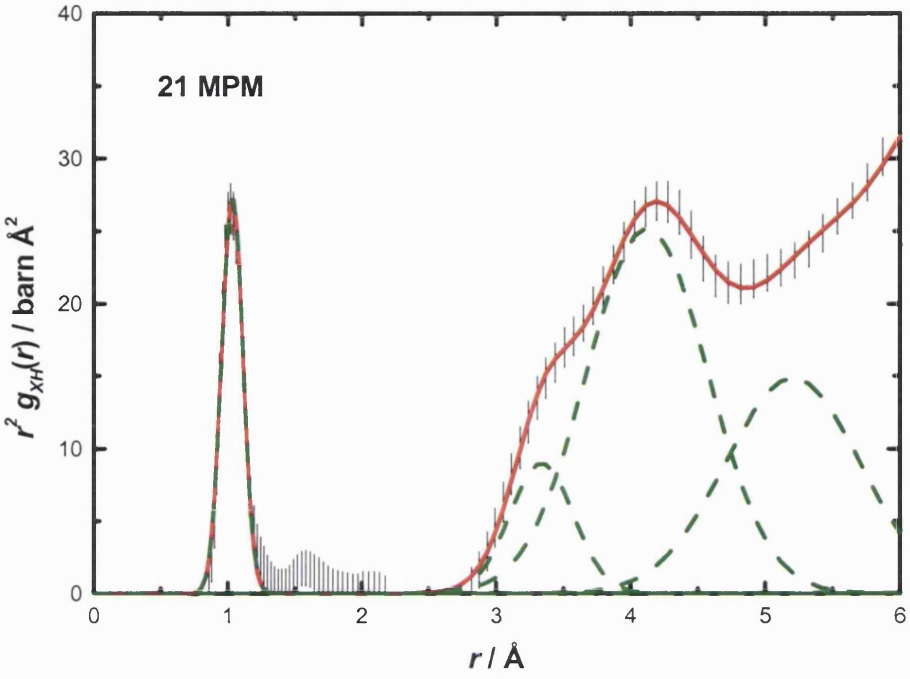

Figure 5.6 Examples of Gaussian fitting to $r^2 g_{XH}(r)$. The error bars show the measured data, the solid lines the total Gaussian fit and the dashed lines the individual Gaussian peaks.

X-H	0 MPM		2 MPM		3 MPM	
Assignment	r / Å	Area/atoms	r / Å	Area/atoms	r / Å	Area/atoms
i) Intra N-H	1.03 ± 0.01	3.1 ± 0.2	1.03 ± 0.01	2.7 ± 0.3	1.03 ± 0.01	2.7 ± 0.3
ii) Inter N-H (H-bonded)	2.42 ± 0.02	2.1 ± 0.3	2.49 ± 0.05	1.3 ± 0.3	2.55 ± 0.05	1.2 ± 0.3
iii) Inter N-H	3.40 ± 0.08	11 ± 1	3.29 ± 0.10	7 ± 1	3.29 ± 0.10	6 ± 1
iv) Inter N-H	4.17 ± 0.08	21 ± 2	4.07 ± 0.10	20 ± 2	4.03 ± 0.10	17 ± 2
v) Inter N-H	5.10 ± 0.15	12 ± 2	5.01 ± 0.15	11 ± 2	5.00 ± 0.12	13 ± 2

X-H	4 MPM		8 MPM		21 MPM	
Assignment	r / Å	Area/atoms	r / Å	Area/atoms	r / Å	Area/atoms
i) Intra N-H	1.03 ± 0.01	2.7 ± 0.3	1.03 ± 0.01	2.8 ± 0.2	1.03 ± 0.01	3.0 ± 0.2
ii) Inter N-H (H-bonded)	2.57 ± 0.05	1.1 ± 0.3	2.45 ± 0.05	0.7 ± 0.2	-	0.0
iii) Inter N-H	3.32 ± 0.10	6 ± 1	3.36 ± 0.10	6 ± 1	3.34 ± 0.10	3.0 ± 0.5
iv) Inter N-H	4.07 ± 0.10	18 ± 2	4.14 ± 0.09	18 ± 1	4.12 ± 0.10	16 ± 2
v) Inter N-H	5.04 ± 0.15	11 ± 2	5.19 ± 0.12	10 ± 2	5.20 ± 0.15	10 ± 2

Table 5.4 Peak assignments and co-ordination numbers: X-H correlations in ammonia and lithium-ammonia solutions.

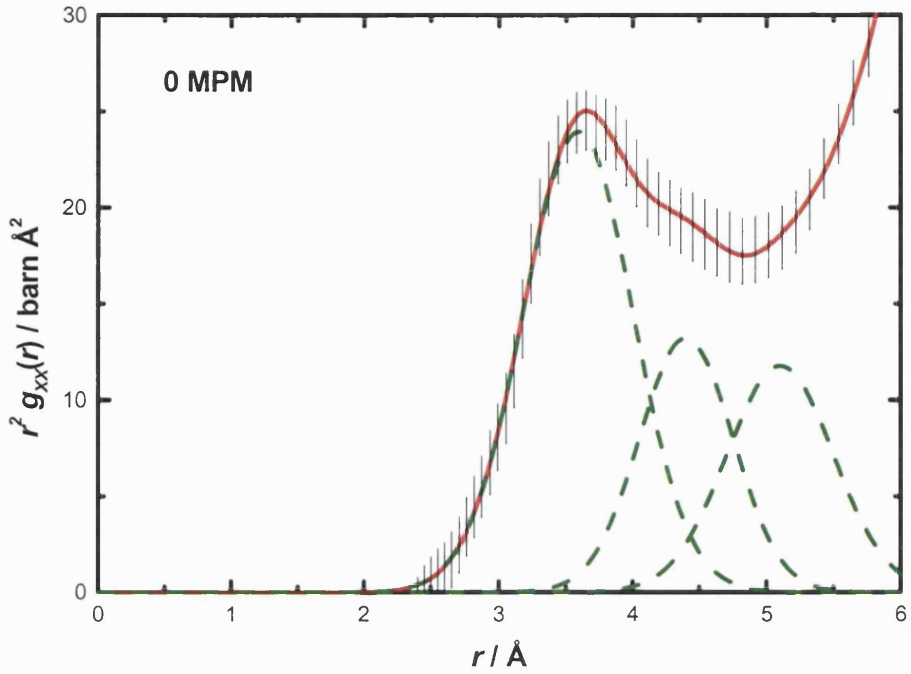
0 MPM
$r^2 g_{xx}(r)$ / barn Å^2
r / Å
0
10
20
30
0
1
2
3
4
5
6

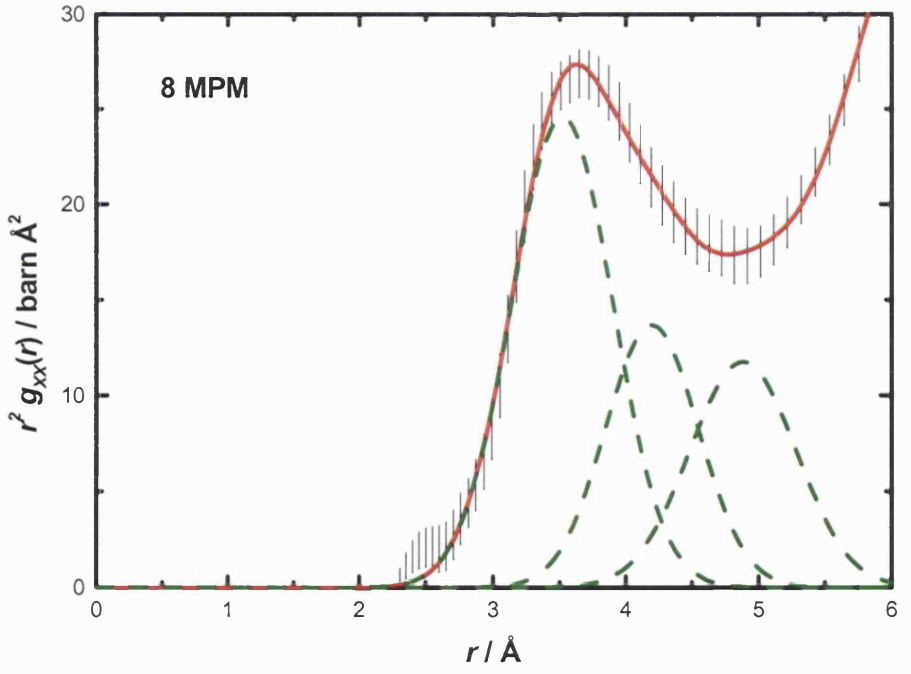
8 MPM
$r^2 g_{xx}(r)$ / barn Å^2
r / Å
0
10
20
30
0
1
2
3
4
5
6

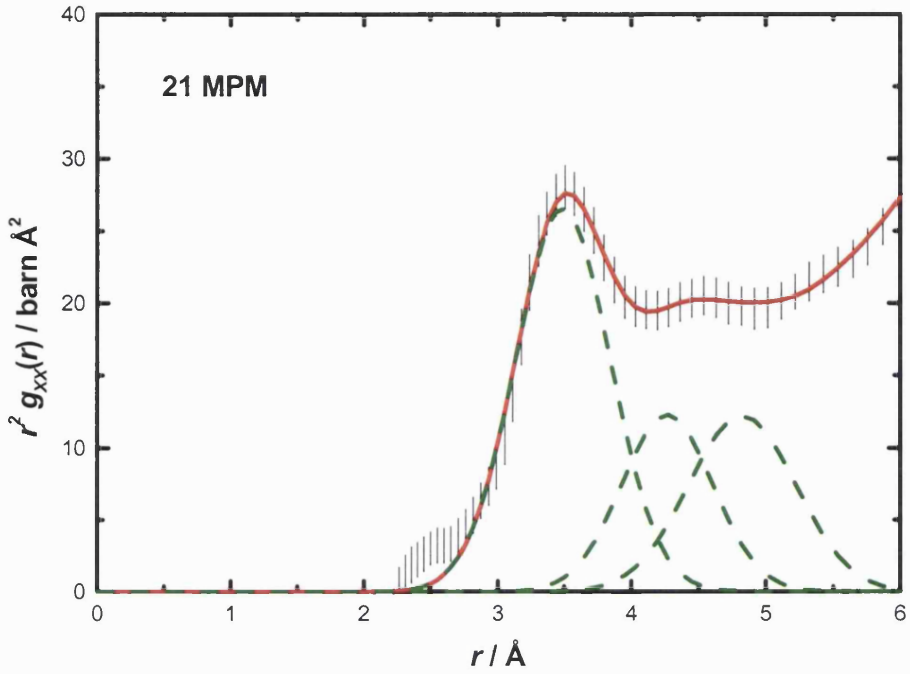

Figure 5.7 Examples of Gaussian fitting to $r^2 g_{XX}(r)$. The error bars show the measured data, the solid lines the total Gaussian fit and the dashed lines the individual Gaussian peaks.

X-X	0 MPM		2 MPM		3 MPM	
Assignment	r / Å	Area/atoms	r / Å	Area/atoms	r / Å	Area/atoms
i) Inter N-N	3.59 ± 0.05	8.5 ± 0.5	3.51 ± 0.05	4.9 ± 0.5	3.51 ± 0.05	4.4 ± 0.5
ii) Inter N-N	4.40 ± 0.12	4.0 ± 0.6	4.16 ± 0.15	3.7 ± 0.5	4.18 ± 0.15	3.6 ± 0.5
iii) Inter N-N	5.10 ± 0.12	4.0 ± 1.0	4.85 ± 0.15	2.1 ± 0.5	4.90 ± 0.15	1.9 ± 0.5

X-X	4 MPM		8 MPM		21 MPM	
Assignment	r / Å	Area/atoms	r / Å	Area/atoms	r / Å	Area/atoms
i) Inter N-N	3.51 ± 0.05	3.9 ± 0.5	3.52 ± 0.07	5.6 ± 0.5	3.49 ± 0.05	4.1 ± 0.5
ii) Inter N-N	4.16 ± 0.15	3.4 ± 0.5	4.20 ± 0.10	2.9 ± 0.5	4.27 ± 0.6	1.8 ± 0.4
iii) Inter N-N	4.91 ± 0.15	2.0 ± 0.5	4.88 ± 0.14	2.8 ± 0.5	4.82 ± 0.11	2.1 ± 0.4

Table 5.5 Peak assignments and co-ordination numbers: X-X correlations in ammonia and lithium-ammonia solutions.

5.3.1 Hydrogen bonding and solvent structure

In the context of hydrogen bonding, the key functions are the X-H partial structure factors and radial distributions (eqs. 3.36 and 3.38). These functions are shown in figures 5.3 and 5.6, and contain direct information about the inter-molecular N-H correlations. It is immediately clear that the size of the shoulder at ~2.4 Å due to N-H hydrogen bonding decreases with metal concentration. This shoulder merges into a broad peak at around 3.6 Å, which is assigned to non hydrogen bonded (van der Waals) contacts. Gaussian fitting to $r^2 g(r)$ in this region (table 5.4) shows that in the pure solvent the number of hydrogen bonds per nitrogen atom is 2.1 ± 0.5, a value which is in good agreement with previous neutron diffraction and computer simulation studies.[16-18] Note that in solid ammonia, there are 3.0 hydrogen bonds per nitrogen atom, as shown by previous X-ray and neutron diffraction experiments. [21-23]

Addition of lithium metal causes a large decrease in the number of hydrogen bonds per nitrogen atom, to 1.3, 1.2 and 1.1 bonds per nitrogen atom in the 2, 3, and 4 MPM solutions respectively, and only 0.7 bonds per nitrogen atom in the 8 MPM solution. This disruption to the hydrogen bonding is greater than that expected if ionic solvation alone were taken into account, suggesting that the solvation of excess electrons does indeed have a role to play in determining the structure of the solutions. This will be explored in detail in section 5.4.2. For the 21 MPM saturated solution, the hydrogen-bonded N-H shoulder disappears altogether as all the remaining ammonia molecules become involved in the solvation shell of the lithium cation. The observed disruption to the hydrogen-bonded network coincides with the formation of the extended polaronic electron cavities which leads to the metallic

state, and the uncommonly low density at saturation. These issues are discussed in subsection 5.3.3.

The H-H partial pair correlation function shown in figure 5.2(b) further confirms these conclusions on the disruption of hydrogen bonding. At 0 MPM (pure ammonia), a large feature is evident at ~2.9 Å. This is equivalent to the distance between two hydrogen atoms on two adjacent hydrogen bonded molecules[18] (taking the hydrogen bonding angle to be 107 degrees). Again the $r^2 g_{HH}(r)$ function has been fitted with Gaussian functions (figure 5.5), and, as may be expected, the estimated co-ordination number of nearest neighbour H-H correlations decreases rapidly, from ~7.5 atoms in pure ammonia, through 5.5, 5.3, 5.3, 5.0 atoms in the 2 MPM, 3 MPM, 4 MPM and 8 MPM solutions respectively, down to only 3 atoms for the saturated solution.

Turning now to the X-X correlations, it is clear that they are dominated by N-N interactions (see table 5.2). It can be seen that the first N-N peak position shifts *inwards* in real-space, from 3.48(2) Å in pure ammonia and the 2 MPM solution, to 3.44(2) Å in the 4 MPM and 8 MPM metallic solutions and 3.42(2) in the 21 MPM saturated solution. This trend has been observed previously via X-ray diffraction[24] and has been attributed to a 'tighter binding' between the ammonia molecules involved in the cationic solvation spheres than that existing between the ammonia molecules in the pure solvent. The concomitant narrowing of the nearest neighbour N-N peak width is consistent with this interpretation. The observed density *decrease* with metal concentration therefore suggests that the electrons are accommodated in low density regions between the solvated cation species.

The first peak in the X-X partial pair correlation function in pure ammonia, relating to first shell N-N correlations, is asymmetric on the high-r side.[18,25] The general shape of the N-N peak presented here, although not split, is consistent with Narten's measured N-N distances of 3.73 Å and 3.40 Å,[25] which show some of the 12 neighbouring ammonia molecules to be in van der Waals contact and some to be hydrogen-bonded at a distance of ~3.4 Å. However at 21 MPM, when no trace of hydrogen-bonding remains, the first shell N-N peak narrows and becomes more symmetric: the asymmetry of the N-N correlation is therefore likely to be a signature of hydrogen-bonding.

Integration of peaks 1 and 2 of the Gaussian fit to $r^2g_{XX}(r)$ (figure 5.7) yields first shell co-ordination numbers of the order of ~12, ~9, ~8, ~7, ~8 and ~6 molecules around a central nitrogen for 0, 2, 3, 4, 8 and 21 MPM solutions respectively. The equivalent integration in r-space of peaks 2 – 4 of the Gaussian fit to $r^2g_{XH}(r)$ (figure 5.6) gives the corresponding number of second shell hydrogen atoms surrounding a central nitrogen atom as 34, 28, 24, 25, 25 and 19, corresponding to ~11, ~9, ~8, ~8, ~8 and ~6 molecules around the nitrogen atom for 0, 8 and 21 MPM solutions. However, the co-ordination numbers of the X-X and X-H peaks in the 21 MPM solution, obtained by integrating to ~4.0 and 4.8 Å respectively, are greater than those expected for an isolated tetrahedron of ammonia molecules around a cation. This suggests the presence of a second shell of solvent molecules surrounding the lithium ion.

5.3.2 Cation solvation and cation-cation structure

Previous studies have shown that lithium is strongly tetrahedrally solvated by ammonia, with an average first shell Li-N distance of ~2 Å.[9-11,24] Via reverse Monte Carlo (RMC) modelling[8] of the 21 MPM and 8 MPM metallic solutions it is now possible to produce a detailed picture of the second solvation shell of ammonia molecules around the lithium cation. This picture takes account of the angular dependence of the molecules relative to the primary tetrahedral solvation shell, as well as their distance from the cation. Figure 5.8 shows the RMC fit to the three total structure factors, while a comparison between the RMC and measured partial pair correlation functions is given in figure 5.9.

Analysis of the relative orientation of the molecules was carried out as follows: for each Li-$(NH_3)_4^+$ in the RMC model, a *z'*-axis was chosen to lie along one Li-N direction. A translation vector was used to map the central lithium ion to the origin, while rotation matrices around the *z*-axis and then the *x*-axis were used to map *z'* to the *z*-axis. A further rotation around the *z*-axis was used to move the remaining three nitrogen atoms into their corresponding positions in the first solvation shell. By applying the same set of translation and rotation matrices to the next nearest nitrogen atoms, it is possible to build up a picture of the second shell's orientation relative to the first shell.

This method reveals a preference for the solvent molecules to lie above the faces and edges of the primary shell tetrahedron. Simple geometric considerations then give a first to second shell N-N distance of 3.6 Å. This arrangement is consistent with the second shell inferred from previous lithium-centred neutron

experiments,[9] which predicted a second shell $r_{Li\text{-}N} \sim 4$ Å. Indeed, the first peak in the current X-X pair correlation function, assigned to N-N correlations, extends further than this distance. The total co-ordination number for this feature is ~6 atoms, which is greater than the 3 atoms which may be expected for an isolated single shell tetrahedron. This is clear evidence of a second solvation shell, in which the N-N peak comprises the three surrounding nitrogen atoms in the primary tetrahedral shell, plus nitrogen atoms above the three nearest faces or edges of the first shell.

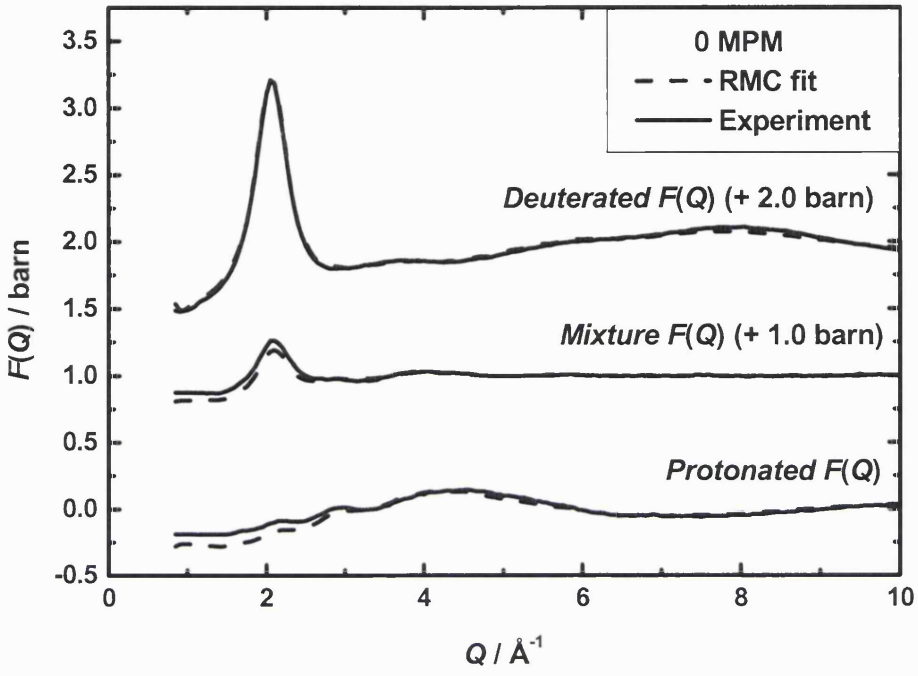
0 MPM
RMC fit
Experiment
Deuterated F(Q) (+ 2.0 barn)
Mixture F(Q) (+ 1.0 barn)
Protonated F(Q)
F(Q) / barn
Q / Å-1
3.5
3.0
2.5
2.0
1.5
1.0
0.5
0.0
-0.5
0
2
4
6
8
10

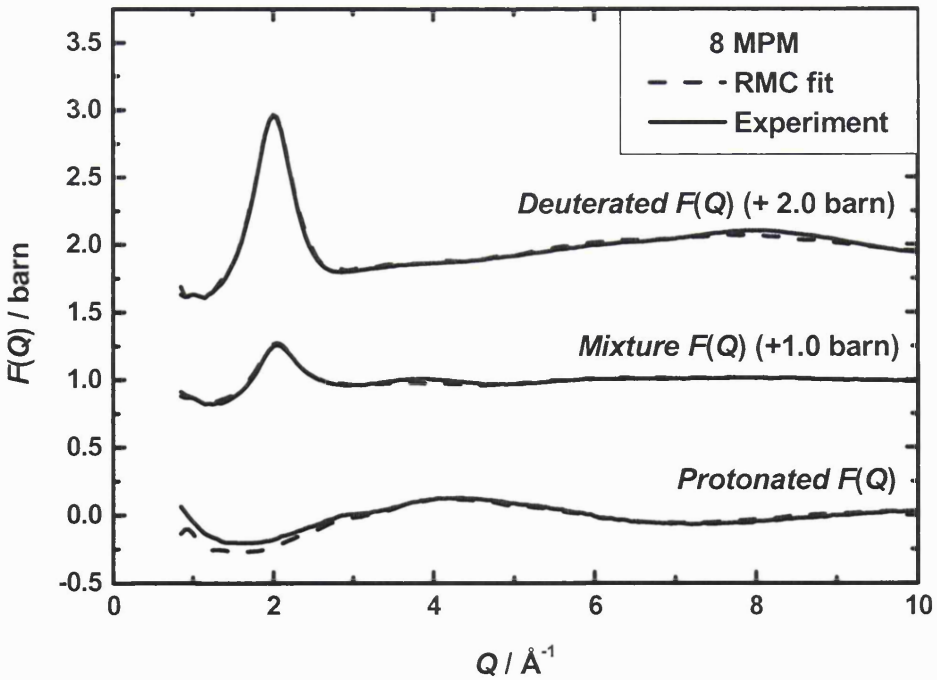
8 MPM
RMC fit
Experiment
Deuterated F(Q) (+ 2.0 barn)
Mixture F(Q) (+1.0 barn)
Protonated F(Q)
F(Q) / barn
Q / Å-1
3.5
3.0
2.5
2.0
1.5
1.0
0.5
0.0
-0.5
0
2
4
6
8
10

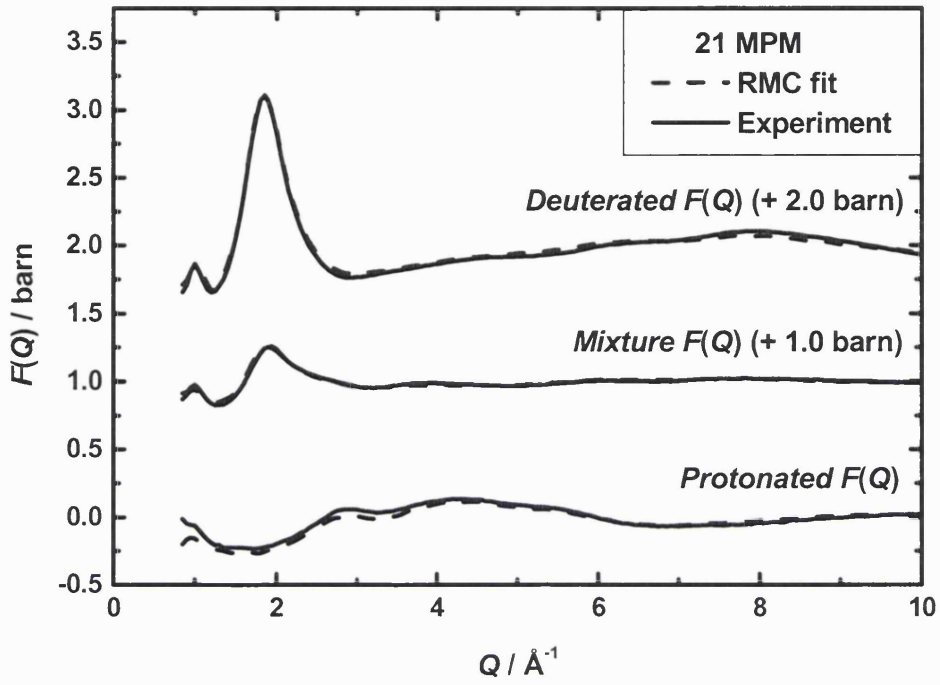

Figure 5.8 Reverse Monte Carlo fit to the measured total structure factors. Top curve: deuterated sample, middle curve: mixture sample, bottom curve: protonated sample.

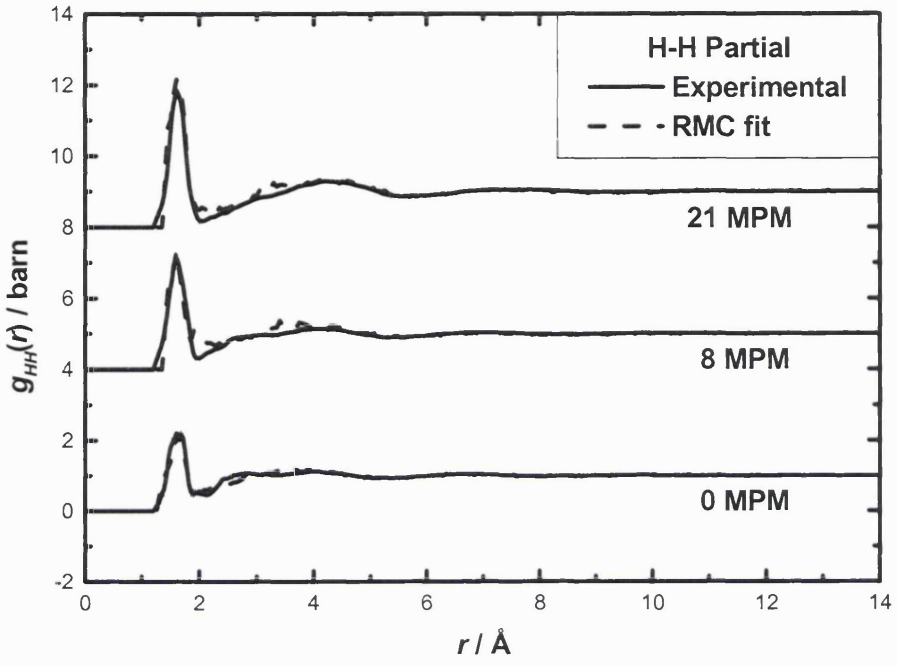
H-H Partial
Experimental
RMC fit
21 MPM
8 MPM
0 MPM
$g_{HH}(r)$ / barn
r / Å

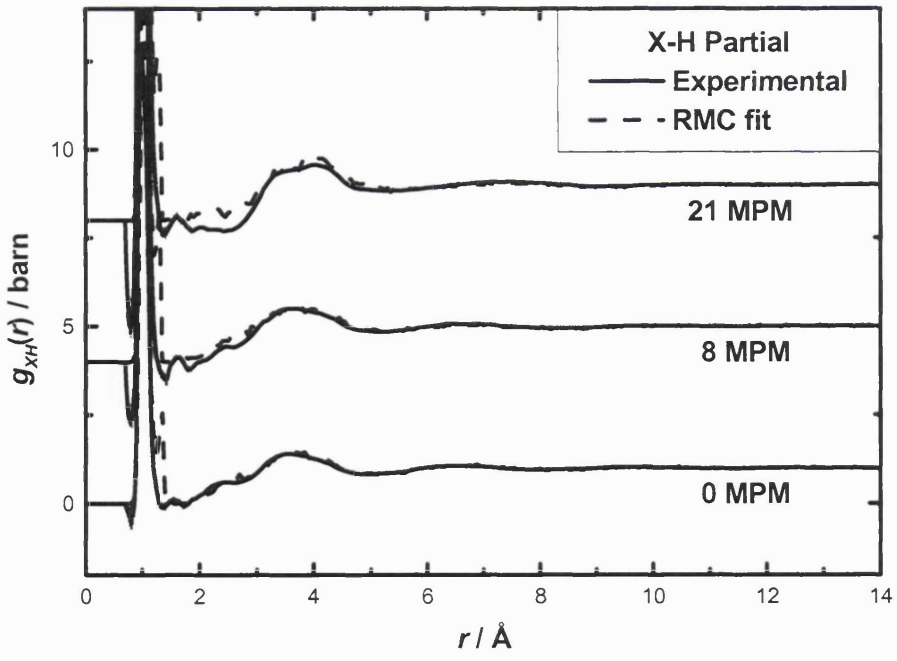
X-H Partial
Experimental
RMC fit
21 MPM
8 MPM
0 MPM
$g_{XH}(r)$ / barn
r / Å

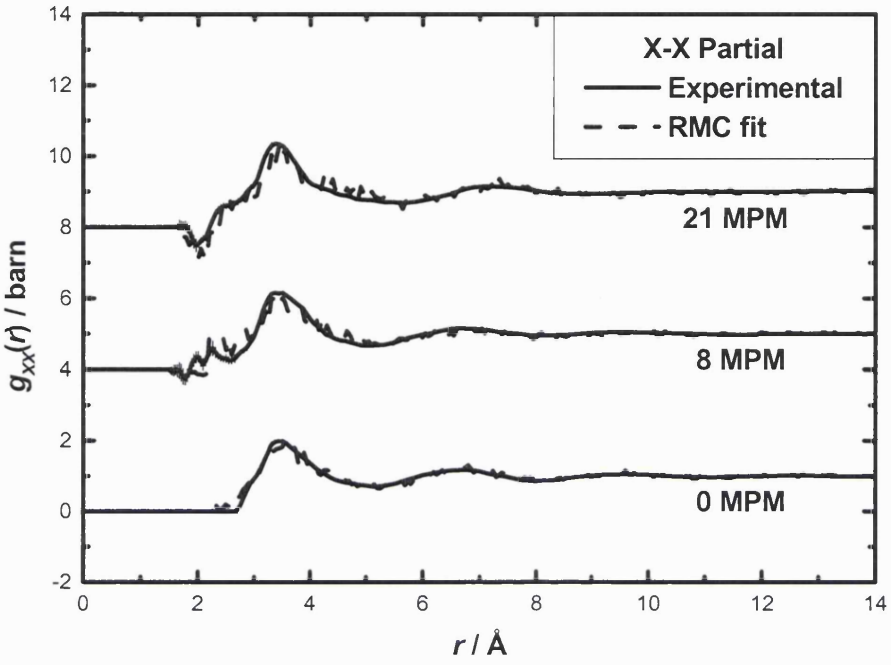

Figure 5.9 Comparison between the RMC model and the measured partial pair correlation functions. Solid line: experiment, dashed line: RMC model.

Further evidence of this arrangement of the Li-$(NH_3)_4^+$ species is present in the X-H pair correlation function (figures 5.3 and 5.6). At saturation, the total number of hydrogen atoms around a nitrogen atom (inter-molecular) is ~19 ± 1 (up to a distance of ~5 Å), as may be expected given the likelihood of three nitrogen atoms around any nitrogen atom in the first shell, and a further three in the second shell. As the metal content is increased to saturation, the emergence of a second peak at ~ 4.1 Å (figure 5.3) is largely due to the fact that at saturation, there will be few, if any, solvent molecules that are not bound to a cation. Any second shell must therefore be formed by ammonia molecules shared between two cations.[9] The solvent molecules' orientations are governed by the nearest cation at ~2 Å distance, so the hydrogen atoms, rather than the nitrogen atoms, on the second shell solvent molecules must point towards their next nearest lithium ion.

In the 8 MPM solution, a number of unbound ammonia molecules remain. The second shell is then likely to consist of some unbound and some cation-bound ammonia molecules. The co-ordination numbers for N-N and N-H inter-molecular correlations are also higher, showing that a greater degree of packing is possible, despite the fact that the nearest neighbour X-H distances show no decrease as the metal content is decreased.

Given this picture of the cation solvation, it is important to consider the origin of the intermediate-range order that is observed in these solutions. At saturation, the first sharp diffraction peak in the total structure factor occurs at 1.00(2) $Å^{-1}$. This feature survives in all three of the composite partial structure factors. This leads to the conclusion that this signature of intermediate-range order must be caused by correlations between the host ammonia molecules at a distance

of $\sim 2\pi / k = 6.3$ Å and with a coherence length extending to $2\pi / \Delta k \approx 25$ Å. This distance is consistent with the previous interpretation that the pre-peak is due to contacts between solvated cations.[26,27] Indeed, in lithium-methylamine solutions it has been found that the corresponding pre-peak shifts to a lower k-value of 0.88(2) $Å^{-1}$, due to the increased solvated cation radius.[26]

5.3.3 Cavity formation

One of the outstanding challenges of metal-ammonia solutions is to understand their fascinating electronic properties in terms of their microscopic structure.[2,3] In this context, a great deal of relevant information has already been collected, particularly from magnetic resonance measurements, X-ray diffraction and *ab initio* simulations,[2,3,20,24,28-32] outlined in Chapter 1. For example, it has been postulated that an isolated excess electron occupies a solvent cavity of approximate radius 3 Å. Very little is known about the snapshot structure of such polaronic voids, channels or low-density regions through which the solvated electrons might percolate. The ideal would be to generate an excess electron centred view of the solutions, much like that for H, N and Li. However, the electrons themselves do not give rise to scattering of neutrons. Therefore, a 3-dimensional RMC model which is constrained by the data has been generated, and the resulting molecular configuration has been analysed for potential solvent cavities.

Analysis of the propensity and relative positioning of cavities within the RMC model was carried out in the following way: points were chosen approximately every 0.2 Å in the x, y and z directions, and a sphere of radius 2.0 Å or 2.5 Å defined around that point. A minimum image convention was applied to the cubic box and the number of atom/ion centres (lithium, nitrogen or hydrogen) lying within each sphere was recorded. One might argue that this definition of a cavity (that is: no atomic *centres* lying within the sphere) leads to an overestimation of the cavity radius, since the atomic sizes have not been taken into account. However, by calculating the co-ordination numbers from the nitrogen-cavity, hydrogen-cavity and lithium-cavity pair-correlation functions, shown in figure 5.10, it is possible to estimate the number of atoms, hence an 'atomic volume' that encroaches on the spherical void. Upon integrating the radial distribution functions to a distance equal to the sum of the cavity radius and the atomic radius, a very low co-ordination number of ~4.8 and ~5.6 atoms in total for 21 MPM and 8 MPM solutions respectively is found. The maximum 'atomic volume' as defined above is less than three percent of the spherical cavity volume, for both the 8 MPM and 21 MPM solutions, so the method of cavity analysis used here is valid.

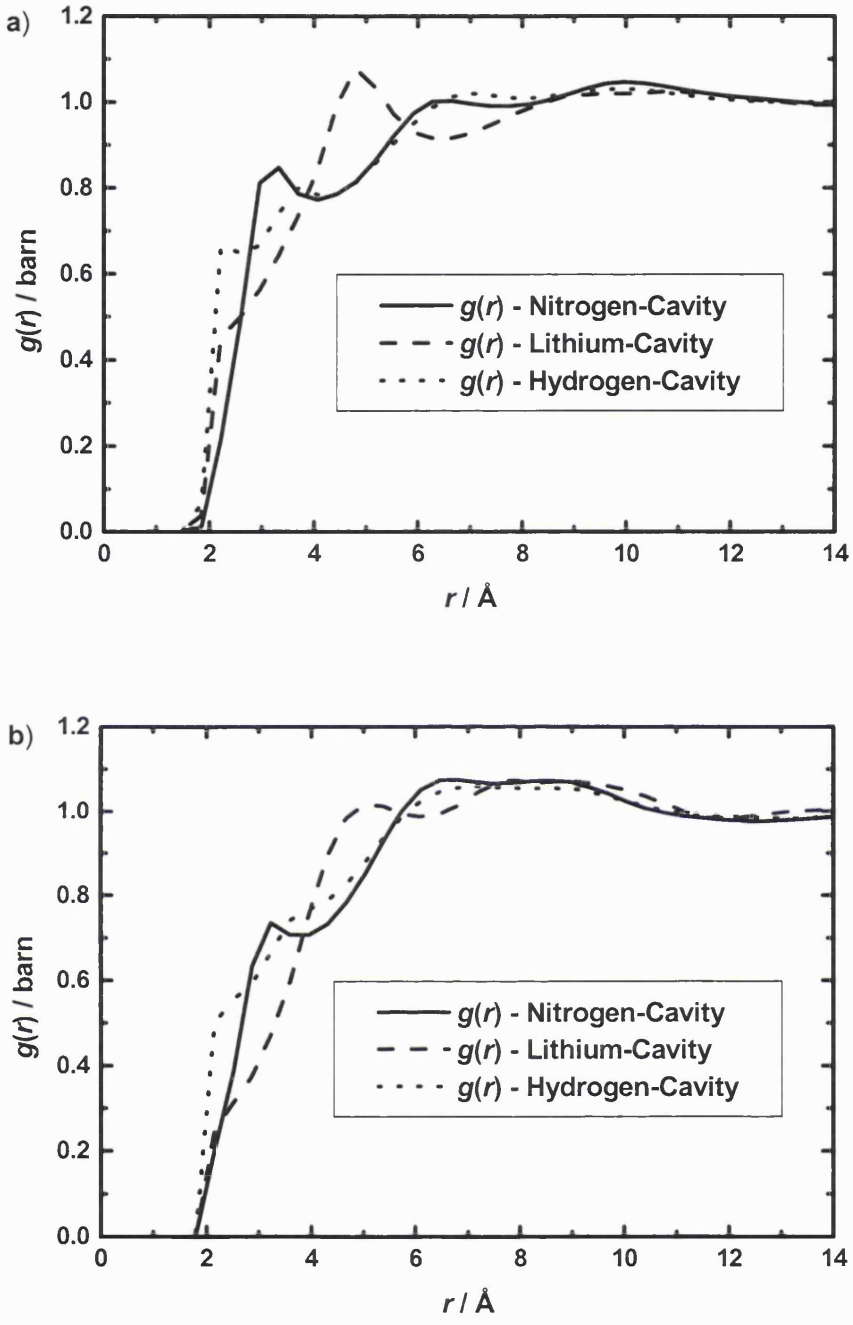

Figure 5.10 Nitrogen-cavity, lithium-cavity and hydrogen-cavity pair correlation functions in (a) the 21 MPM solution, and (b) the 8 MPM solution. The sharp cut-off for the hydrogen-cavity function arises because the cavity is strictly defined as a sphere containing zero atomic centres, and the hydrogen atoms reside closest to these spherical voids.

The graphs in figure 5.11 show the results of the analysis, and give credence to the initial hypothesis. In pure ammonia, there are very few regions of low solvent density; the most likely number of atoms per sphere of radius 2.5 Å is 7, and the distribution is symmetrical about its centre. However, for 8 and 21 MPM the probability distribution shows the presence of a significant number of spheres containing zero or one atoms, demonstrating the existence of regions of lower atomic density throughout the solutions. Figure 5.12 shows the cavity distribution and their tendency to form channels in the 8 and 21 MPM solutions.

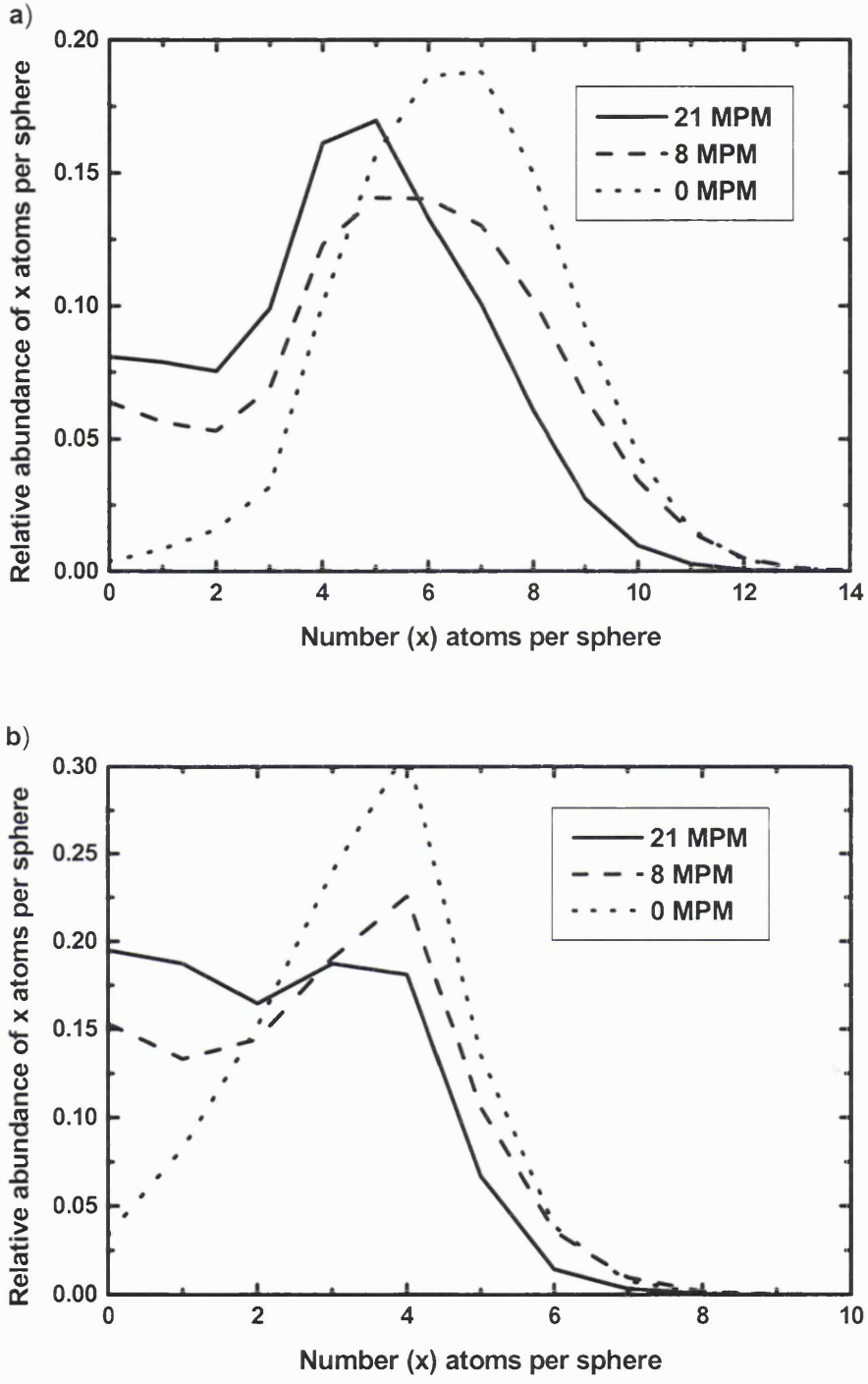

Figure 5.11 The probability of a sphere of (a) radius 2.5 Å and (b) radius 2.0 Å containing x number of atoms: comparison between 0, 8 and 21 MPM solutions: note the significant difference in the probability of finding a sphere of 0 or 1 atoms in the metallic 8 and 21 MPM solutions as compared to the pure ammonia solvent.

(a) (b)

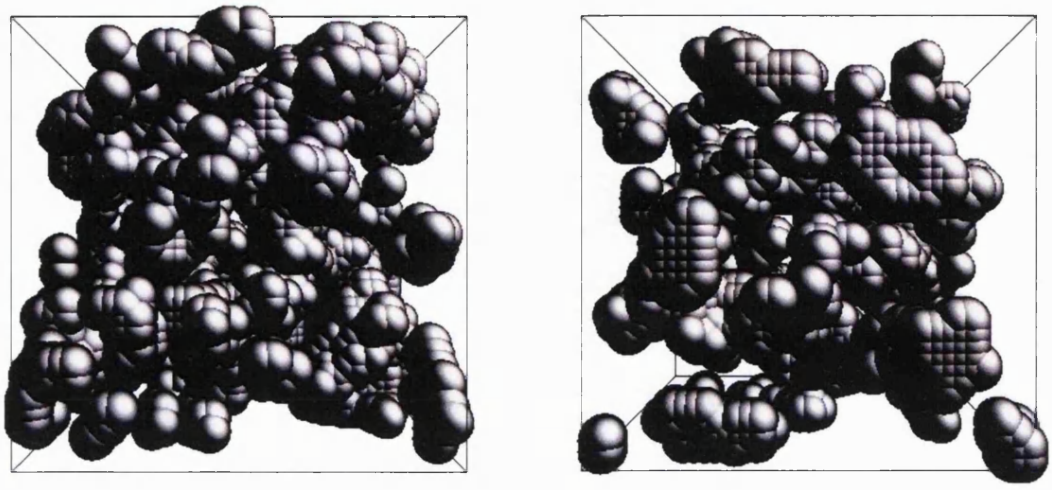

Figure 5.12 Distribution of cavities throughout (a) 21 MPM and (b) 8 MPM metallic solutions of lithium in ammonia: the shaded areas represent spheres containing zero nitrogen, hydrogen or lithium atoms/ions.

5.4 Results and discussion – EPSR analysis

The simulated partial structure factors arising from the final EPSR configurations are presented in figure 5.13, together with the experimental data. Representative interatomic pair correlation functions for the non-metallic 2 MPM lithium-ammonia solutions are shown in figure 5.14. The Li-N and Li-H correlations confirm that lithium is strongly solvated, with Li-$(NH_3)_4^+$ forming the dominant cationic structural motif.[9-11] Orientationally averaged information on the hydrogen bonding is contained within the N-H and H-H pair correlation functions. Integration of the arrowed shoulder at around 2.4 Å in the N-H partial pair correlation function reveals ~1.4 hydrogen bonds per nitrogen atom in the 2 MPM solution. The equivalent integration of the N-H partial pair correlation function for the 0, 8 and 21 MPM lithium-ammonia solutions yields 2.0, 0.7 and 0.0 hydrogen bonds per nitrogen atom. These numbers are consistent with those obtained experimentally,[15] and demonstrate the accuracy of the EPSR simulated ensembles.

5.4.1 Hydrogen bonding: directionality

The resulting 3-D molecular configuration which is consistent with the measured data can then be used to probe for the first time the subtle spatial arrangements and molecular orientations that accompany this breakdown in hydrogen bonding, as the solutions expand and become metallic. The three-dimensional spatial distribution of nitrogen atoms in the first N-N shell is presented as a function of electron concentration in figure 5.15. The orientation of the central reference molecule is

fixed, as shown, and the shaded regions represent the most likely angular distribution of the top 20% and 50% of nitrogen atoms, shown in columns 1 and 2 respectively.

In pure ammonia, the directions in which hydrogen bonding occurs can clearly be seen, with three acceptor lobes positioned above the hydrogen atoms on the central molecule, and a trefoil-shaped donor lobe below. In total, six approach directions are observed, reminiscent of the six hydrogen bonds that are formed in solid ammonia.[21-23] The dipole orientations of the neighbouring ammonia molecules are presented in figure 5.16, showing the tendency for the molecules in the acceptor lobes to direct their dipole moment away from the central reference molecule, and the dipole moments of the molecules in the donor lobe to be towards the central ammonia molecule in the toroidal shape shown.

In the 21 MPM lithium-ammonia solution, no acceptor lobes at (θ,ϕ) = (60,120) are visible, even when the fractional isosurface is increased to 50%. At this threshold, the density surface is inverted from that in pure ammonia, as the molecules approach face to face via Li-$(NH_3)_4^+$ complexes. Furthermore, the dipole moments of the band below the central ammonia (figure 5.16) are directed away from the molecule, and the dipole moments of the ammonia molecules at (θ,ϕ) = (60,120) are now directed *towards* the central reference molecule. This confirms the lack of hydrogen-bonding in a saturated solution which is comprised solely of solvated ions and delocalised excess electrons.

For the 2 MPM and 8 MPM lithium-ammonia solutions, it is apparent that some degree of hydrogen bonding is still present. The dipole moments of the lobes

at (θ,ϕ) = (60,0), (60,120) and (60,240), shown in figure 5.16, are seen to direct themselves away from the hydrogen atoms on the central molecule, as in pure ammonia. The dipole moments of the lobe at (θ,ϕ) = (180,0) below the central molecule, however, consist of some moments directed upwards towards the nitrogen atom of the central molecule, in the toroidal shape characteristic of hydrogen-bonding as in pure ammonia, and some moments pointing directly away from the central ammonia molecule, as in the saturated solution. The sequence of nearest neighbour N-N distributions and dipole orientations from 0 MPM, through 2 MPM and 8 MPM to 21 MPM thus enable us to differentiate between two populations of ammonia molecules, those that are hydrogen-bonded and those responsible for ion solvation. It is primarily the balance between hydrogen-bonding in the solvent and ionic solvation which governs the structure of the lithium-ammonia solution across the metal-nonmetal transition.

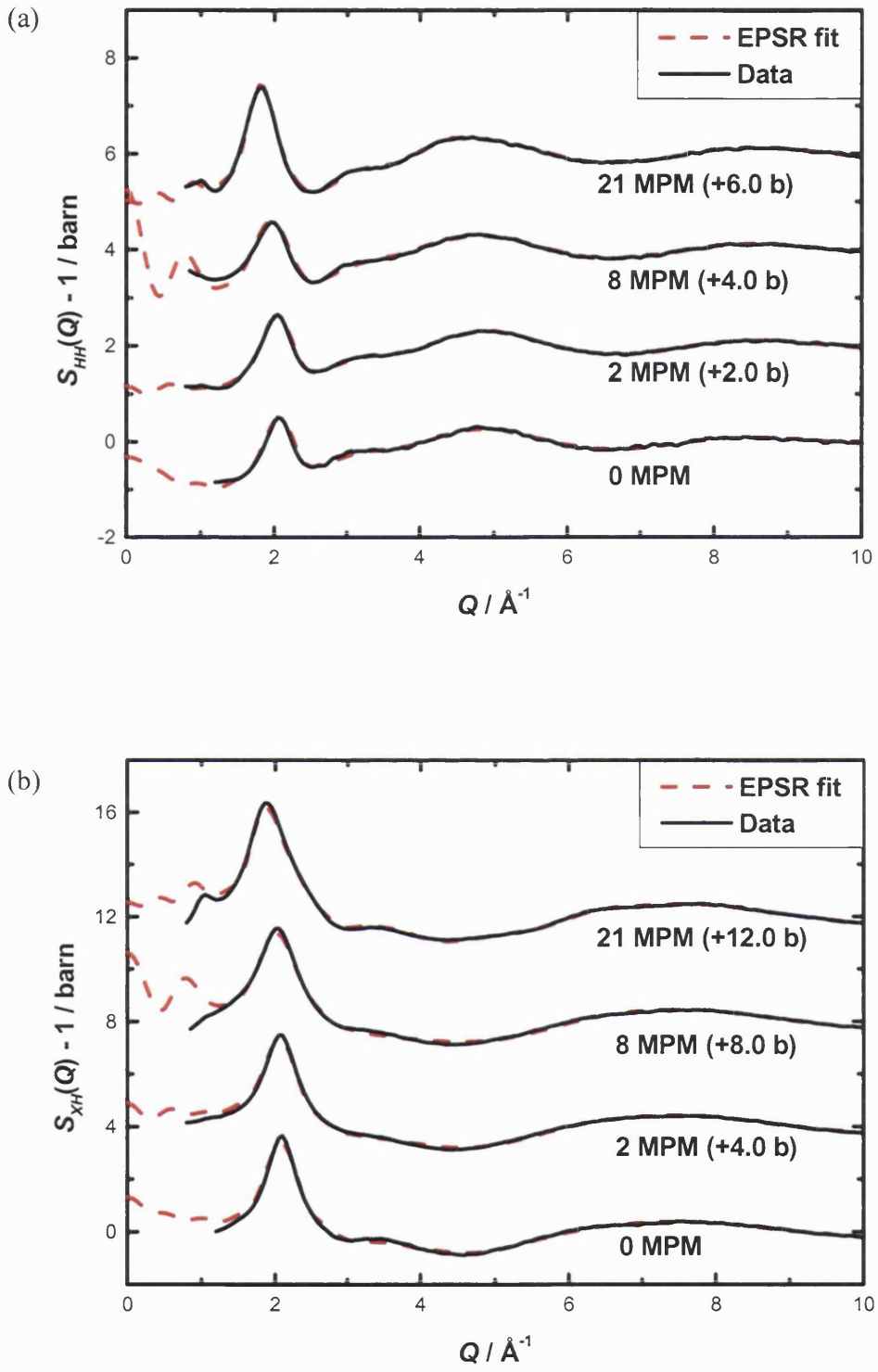

Figure 5.13 (a) and (b) Comparison of the EPSR fits to the measured H-H and X-H composite partial structure factors.

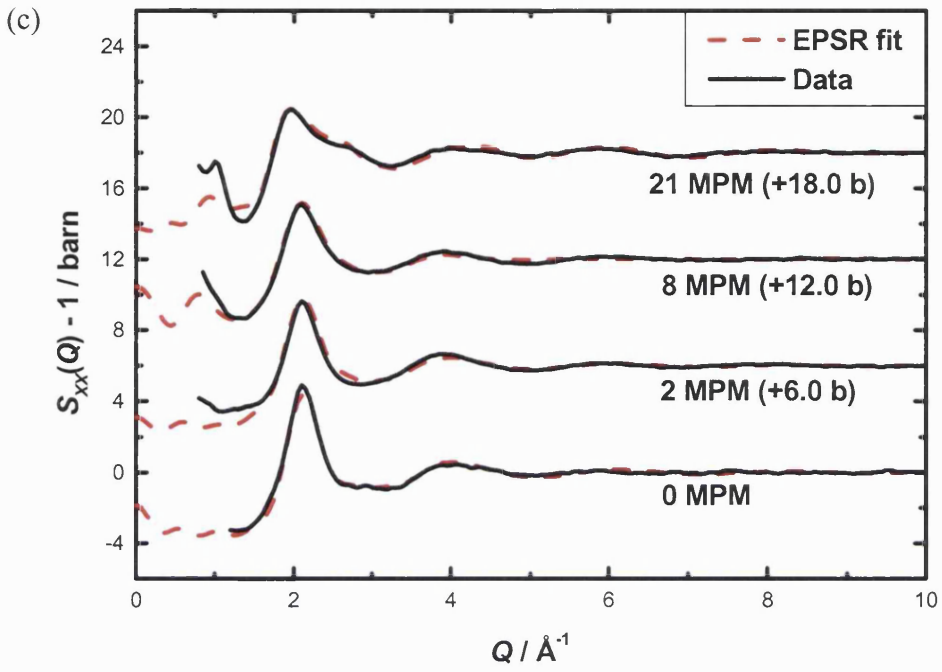

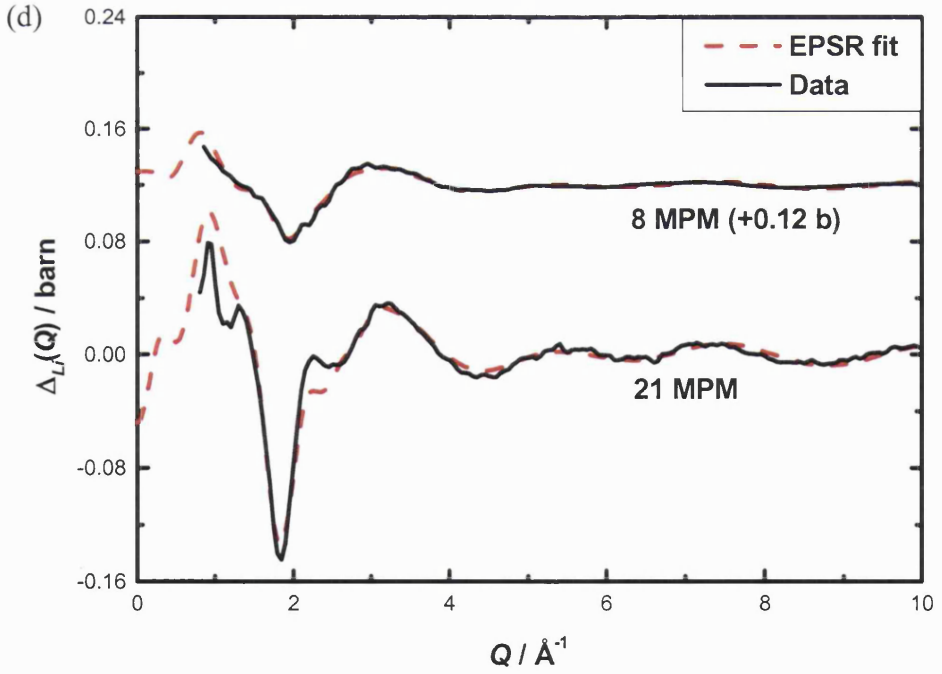

Figure 5.13 (c) and (d) Comparison of the EPSR fits to the measured X-X composite partial structure factor and the first order lithium difference function.

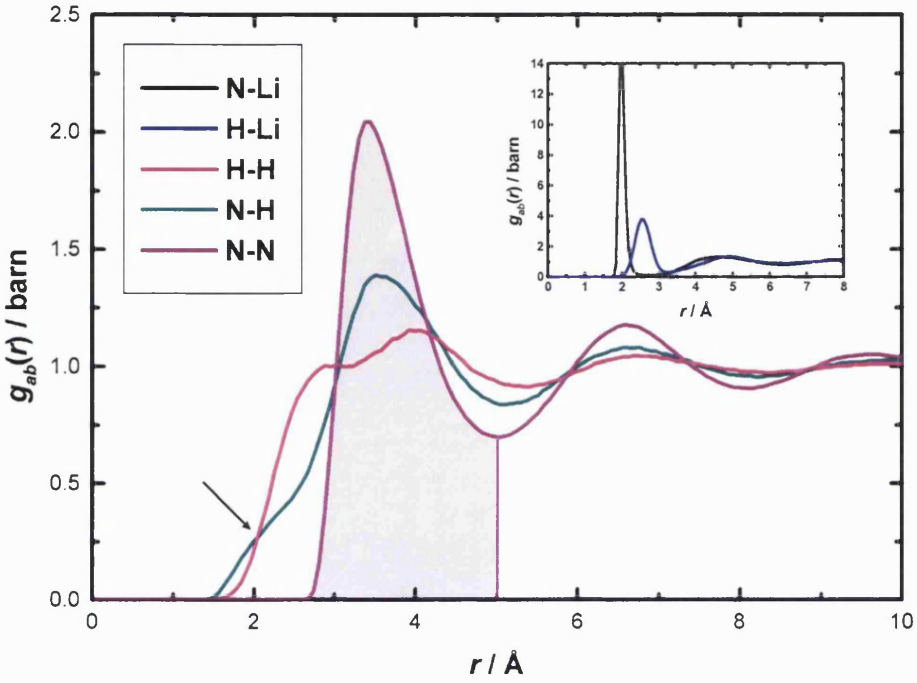

Figure 5.14 Example partial pair correlation functions for the 2 MPM lithium-ammonia solution, obtained via the EPSR simulation. Note that the first N-N shell extending to ~5 Å contains a significant contribution from hydrogen-bonded solvent molecules, illustrated by the hydrogen-bonded shoulder at ~2.4 and 2.7 Å respectively in the N-H and H-H pair correlation functions. Inset: Li-N and Li-H pair correlation functions showing the first ionic solvation shell of ~4.0 ammonia molecules.

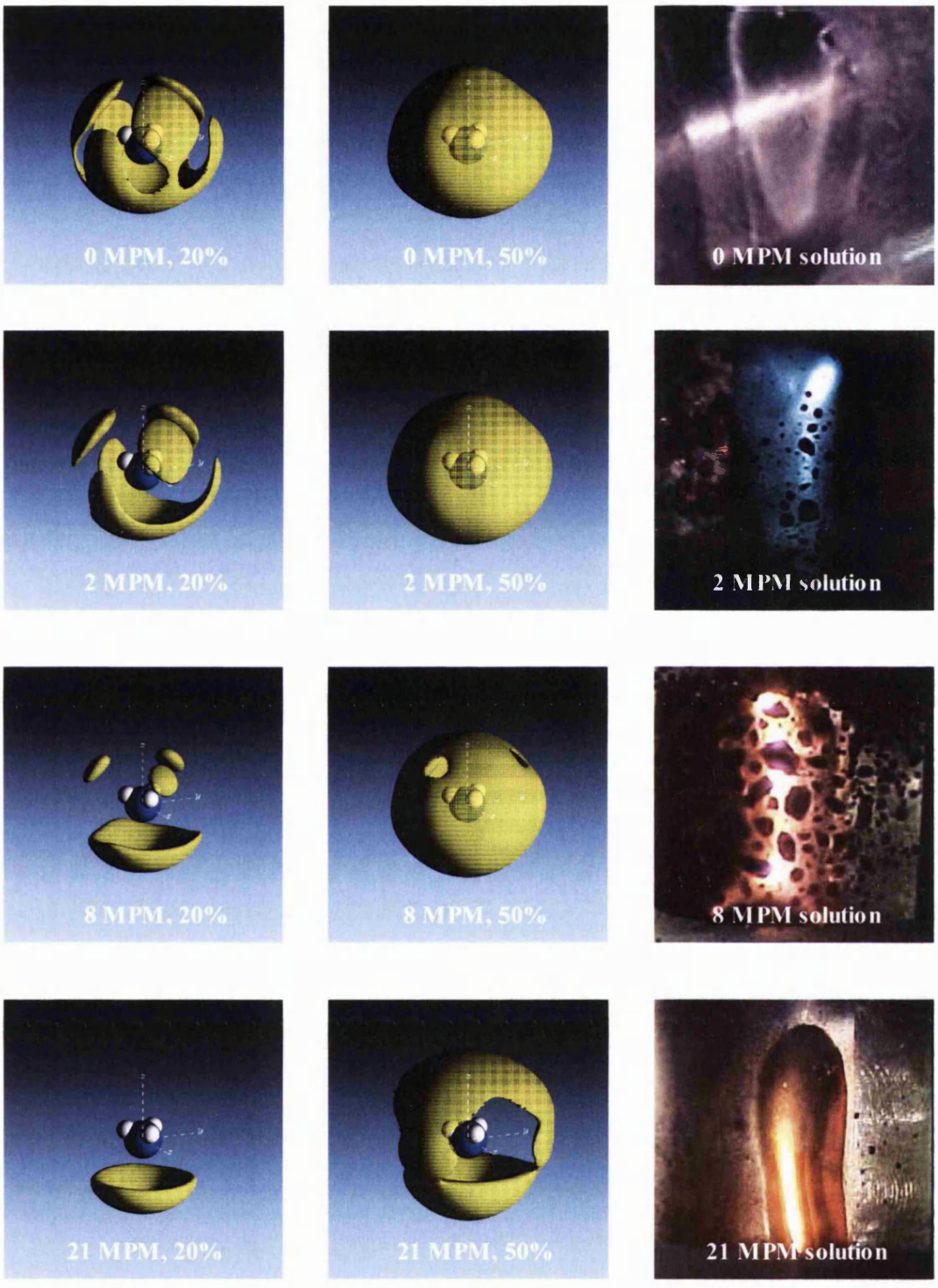

Figure 5.15 Spatial density plots of the first N-N shell for liquid ammonia and 2 MPM, 8 MPM and 21 MPM lithium-ammonia solutions. The yellow coloured regions show the most likely angular positions of nearest neighbour nitrogen atoms around a central ammonia molecule.

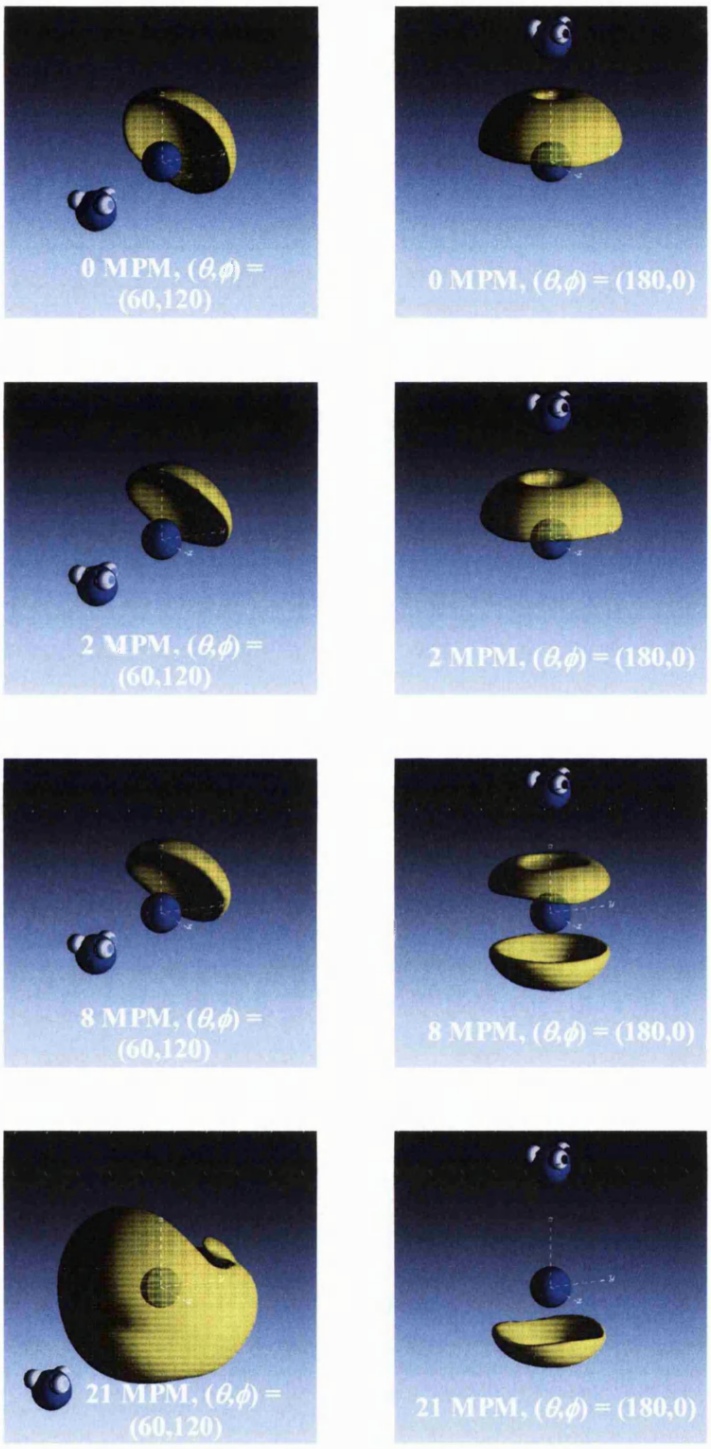

Figure 5.16 Dipole orientations of the ammonia molecules in the first N-N shell in liquid ammonia and 2 MPM, 8 MPM and 21 MPM lithium-ammonia solutions. The yellow regions represent the most likely directions in which the dipole moment of the ammonia molecule is directed, the fraction of ammonia molecules shown is 30%.

5.4.2 Polaronic cavity formation and electron solvation

With increasing metal concentration, the degree to which ionic solvation influences the structure increases relative to that of hydrogen bonding. However, it is apparent that an additional mechanism is responsible for the hydrogen-bonding disruption with metal concentration. The graph in figure 5.17 shows the calculated number of hydrogen bonds per nitrogen atom, assuming that the disruption to hydrogen bonding is solely due to tetrahedral solvation of the cations, together with the measured number of hydrogen bonds per nitrogen atom. The calculated number of hydrogen bonds per nitrogen atom was carried out as follows:

$$\overline{n}_{N-H} = \left(1 - \frac{n_{ion-bound}}{n_{total}}\right) \times 2.0 \qquad (5.1)$$

where $\overline{n}_{N-H}$ is the estimated number of hydrogen-bonds per nitrogen atom, $n_{ion-bound}$ is the number of ammonia molecules bound to a cation, n_{total} is the total number of ammonia molecules and the multiplicative factor of 2.0 is the average number of hydrogen-bonds per nitrogen atom in pure ammonia. It is clear from the graph that the disruption to the hydrogen-bonding is significantly greater than that expected if ionic solvation were the only factor responsible.

It is proposed that the additional decrease in hydrogen-bonding is caused by the accommodation of the dissociated electrons within the solution. In order to investigate the direct influence of the electrons on the solvent structure, the molecular configurations obtained via EPSR have been analyzed for voids of ~5 Å

diameter such that their distribution may be plotted relative to the ammonia molecules.

The angular distribution of electronic voids around a central ammonia molecule is shown in figure 5.18. Pair correlation functions (NH_3 – void) alone show only a one-dimensional average of the distribution of ammonia molecules around a void, and it is difficult to visualise the orientation of these ammonia molecules relative to the void. Spatial density functions provide fresh insight into the re-orientation of the ammonia molecules as the concentration of electrons and ions increases, and are able to shed more light on the mechanism of electron solvation. Note that even in the case of pure ammonia, a small number of voids are evident in between the hydrogen-bonded lobes shown in figure 5.15.

In the 2 MPM solution, the solvent structure around the electronic cavities is clearly very different: ammonia molecules in the first coordination shell direct one hydrogen atom per molecule towards the centre of the void, forming a Bjerrum-type defect.[33] At this metal concentration, the electrons are fully solvated, and the first solvation shell comprises ~ 9 ± 2 ammonia molecules, in agreement with the number predicted by path-integral Monte Carlo and molecular dynamics simulations and magnetic resonance studies.[32,34]

Upon increasing the metal concentration from 2 MPM to 8 MPM, it can be seen that the orientation of the ammonia molecules around the polaronic cavities changes dramatically, such that two hydrogen atoms per ammonia molecule are now directed towards the void. At 8 MPM, the number of 'free' ammonia molecules per electron is only ~7.5. It has been suggested that this number is too few to be able to

solvate the electron completely,[24] since at this concentration the lithium-ammonia solution is truly metallic with an electrical conductivity of ~1000 $\Omega^{-1}cm^{-1}$. Therefore, it is likely that the observed re-orientation of the ammonia molecules compensates for the lack of free ammonia molecules available for electron solvation.

Finally, at saturation, all the ammonia molecules have become incorporated into the first cation solvation shells. At this concentration, percolation channels form between the Li-$(NH_3)_4^+$ complexes, and the dipole moments of the ammonia molecules must be directed towards these electron channels, as is shown to be the case in figure 5.18.

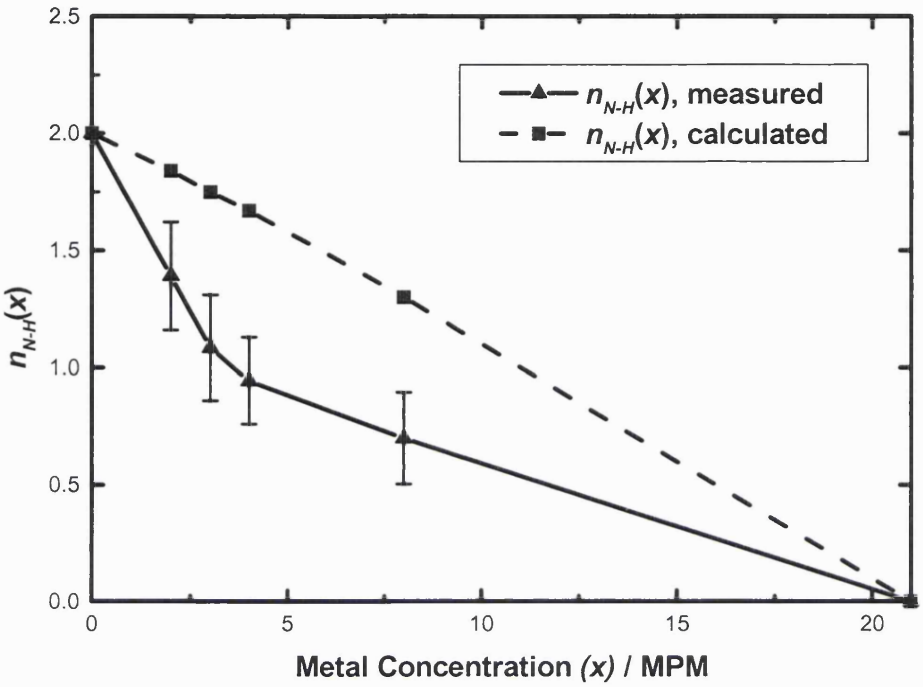

Figure 5.17 Graph showing the measured number of hydrogen bonds per nitrogen atom (triangles, solid line) and the calculated average number of hydrogen bonds per nitrogen atom if ionic solvation, i.e. the formation of Li-$(NH_3)_4^+$ complexes, were the sole mechanism responsible for hydrogen bonding disruption (squares, dashed line) versus metal concentration.

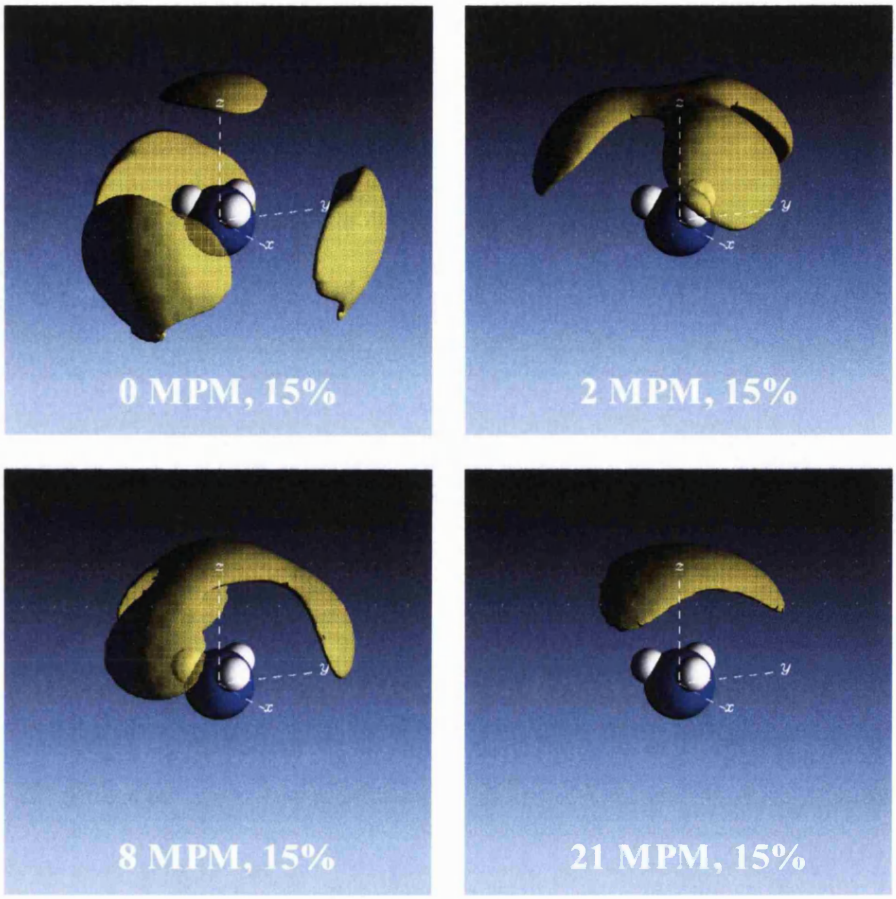

Figure 5.18 Angular distribution of voids (shaded regions), caused by accommodation of excess electrons, relative to the ammonia molecules. The fraction of voids plotted is 15%.

5.4.3 Conclusions via EPSR analysis

In summary, via a full interpretation of experimental data in terms of co-ordination numbers and 3-D modelling, it has been possible to observe the active role of the electron on the structure of lithium-ammonia solutions. The visualisation technique employed here has revealed that electron solvation is the additional factor in determining the decrease in hydrogen-bonding with metal concentration, further to that caused by ionic solvation. In addition, the EPSR model provides new insight which is crucial to our understanding of the interplay between hydrogen-bonding and electron localisation/delocalisation across the metal-nonmetal transition. Upon increasing the electron concentration from 2 MPM to 8 MPM, a striking change in the orientation of ammonia molecules in the first electronic solvation shell is observed. This re-orientation is likely to be caused by the fact that there are too few free ammonia molecules available at this concentration to solvate the excess electrons.[22] This leads to the delocalization of the electrons and the formation of channels between the Li-$(NH_3)_4^+$ complexes, which give rise to the highly conducting metallic state.

5.5 References

[1] R. W. Impey, M. Sprik and M. L. Klein, J. Am. Chem. Soc. **109**, 5900 (1987).

[2] Z. Deng, G. J. Martyna and M. L . Klein, Phys. Rev. Lett. **71**, 267 (1993).

[3] M. Diraison, G. J. Martyna and M. E. Tuckerman, J. Chem. Phys, **111**, 1096 (1999).

[4] D. T. Bowron, A. K. Soper and J. L. Finney, J. Chem. Phys. **114**, 6203 (2001).

[5] A. K. Soper, W. S. Howells and A. C. Hannon, *Atlas-Analysis of Time-of-flight Diffraction data from Liquid and Amorphous Samples* (Rutherford Appleton Laboratory Report RAL-89-046, 1989).

[6] A. K. Soper, in *Neutron Scattering Data Analysis 1990*, edited by M. W. Johnson (IOP Conference Series Number 107), IOP Publishing, Bristol, 1990, pp. 57-67.

[7] A. K. Soper, C. Andreani and M. Nardone, Phys. Rev. E. **47**, 2598 (1993).

[8] R. L. McGreevy and M. A. Howe, Ann. Rev. Mat. Sci. **22**, 217 (1992).

[9] J. C. Wasse, S. Hayama, N. T. Skipper and H. E. Fischer, Phys. Rev. B. **61**, 11993 (2000).

[10] J. C. Wasse, S. Hayama, N. T. Skipper, C. J. Benmore and A. K. Soper, J. Chem. Phys. **112**, 16 (2000).

[11] J. C. Wasse, S. Hayama, S. Masmanidis, S. L. Stebbings and N. T. Skipper, J. Chem. Phys. **118,** 7486 (2003).

[12] A. K. Soper, Chem. Phys. **202**, 295 (1996).

[13] D. T. Bowron, J. L. Finney and A. K. Soper, J. Phys. Chem. B. **102**, 3551 (1998).

[14] A. K. Soper, Mol. Phys. **99**, 1503 (2001)

[15] H. Thompson, J. C. Wasse, N. T. Skipper, S. Hayama, D. T. Bowron and A. K. Soper, J. Am. Chem. Soc. **125**, 2572 (2003).

[16] R. C. Rizzo and W. L. Jorgensen, J. Am. Chem. Soc. **121**, 4827 (1999).

[17] J. Chandrasekhar, D. Spellmeyer and W. L. Jorgensen, J.Am.Chem.Soc. **106**, 903 (1984).

[18] M. A. Ricci, M. Nardone, F. P. Ricci, C. Andreani and A. K. Soper, J. Chem. Phys. **102**, 7650 (1995).

[19] J. C. Wasse, S. Hayama, N. T. Skipper, C. J. Benmore and A. K. Soper, J. Chem. Phys. **112**, 7147 (2000).

[20] J. C. Thompson, *Electrons in Liquid Ammonia*, Oxford, Clarendon (1976).

[21] J. W. Reed and P. M. Harris, J. Chem. Phys. **35**, 1730 (1961).

[22] A. W. Hewat and C. Riekel, Acta Cryst. **A35**, 569 (1979).

[23] I. Olovsson and D. H. Templeton, Acta Cryst. **12**, 832 (1959).

[24] S. Hayama, J. C. Wasse, N. T. Skipper and H. Thompson, J. Chem. Phys. **116**, 2991 (2002).

[25] A. H. Narten, J. Chem. Phys, **66**, 3117 (1977).

[26] S. Hayama, J. C. Wasse, and N. T. Skipper and A. K. Soper, J. Phys. Chem. B. **106**, 11 (2001).

[27] S. Hayama, J. C. Wasse, N. T. Skipper and J. K. Walters, Mol. Phys. **99**, 779 (2001).

[28] R. W. Impey, M. Sprik and M. L. Klein, J. Am. Chem. Soc. **109**, 5900 (1987).

[29] D. Holton and P. P. Edwards, Chemistry in Britain, **1007** (1985).

[30] P. P. Edwards, Phys. Chem. Liq. **10**, 189 (1981).

[31] P. P. Edwards, Adv. Inorg. Chem. Radiochem. **25**, 135 (1982).

[32] P. P. Edwards, J. Phys. Chem **88**, 3772 (1984).

[33] R. Catterall and N. F. Mott, Adv. Phys. **18**, 665 (1969).

[34] M. Marchi, M. Sprik and M. L. Klein, Faraday Discuss. Chem. Soc. **85**, 373 (1988).

CHAPTER 6

RESULTS II:
DYNAMICS OF LITHIUM-AMMONIA SOLUTIONS

6.1 Introduction

Quasi-elastic neutron scattering has been used to study the dynamics of ammonia and lithium-ammonia solutions at concentrations of 4, 12 and 21 MPM over a range of temperatures from 40 K to 230 K. In the liquid states at 230 K, it is found that the proton diffusion coefficient increases with metal concentration, from 5.61×10^{-5} $cm^2 s^{-1}$ in ammonia, to 7.84×10^{-5} $cm^2 s^{-1}$ at 12 MPM, and decreases at higher metal concentrations - results which are in close agreement with NMR measurements.[1] The saturated solution remains a liquid down to 88 K,[2] and the proton diffusion coefficient shows a rapid decrease upon cooling. Below the liquid-solid phase transition temperature, slow diffusion at a rate of 1.79×10^{-5} $cm^2 s^{-1}$ is observed, suggesting that the sample under study was in fact a supercooled liquid. A further solid-solid phase transition occurs at 82.2 K,[3] and upon cooling below this temperature no diffusion is observed. However, the spectra for saturated lithium-

ammonia solutions at 75 K and 40 K show clear Q-independent broadening, indicating a localised rotation of the ammonia molecules. In the liquid ammonia samples, a diffusion rate which is in close agreement with previous NMR studies[1] is observed. In solid ammonia, no QENS broadening is observed at temperatures of 40 K and 80 K, but increasing the temperature to 150 K gives rise to a slow rotation of the ammonia molecule.

Molecular dynamics simulations have also been performed on liquid ammonia and lithium-ammonia solutions at concentrations of 4, 12 and 21 MPM, all at 230 K. The radial distribution functions extracted show good agreement with the measured structural data from Chapter 5, and the diffusion coefficients follow a similar trend to the diffusion rates obtained via QENS. However, for the 4 MPM lithium-ammonia solution, the diffusion rate obtained via molecular dynamics simulation is significantly greater than the experimental measurement. This is attributed to the fact that at lower metal and electron concentrations, the complete solvation of the electron will impede the motion of the surrounding ammonia molecules. In the MD simulation cell, however, the electrons were included only as a background charge, and so the possibility of the electrons being responsible for slowing down the motion of the ammonia molecules in their solvation shells is not fully taken into account.

6.2 Experimental details

Quasi-elastic neutron scattering experiments have been performed on ammonia at 40 K, 80 K, 150 K and 230 K, 4 MPM and 12 MPM lithium-ammonia solutions at 230 K and saturated (21 MPM) solutions at 40 K, 75 K, 85 K, 100 K and 230 K. The experiments were performed on the high-resolution inverted spectrometer IRIS at the pulsed neutron spallation source ISIS of the Rutherford Appleton Laboratory.[4] The samples were prepared *in-situ*: ammonia was condensed onto a piece of lithium metal held at 230 K. A specially designed stainless steel annular cell, with wall thicknesses of 0.2 mm and an annular sample thickness of 1 mm, was used to contain the sample. Each sample spectrum was measured using the graphite PG002, PG002_offset1 and PG004 analysers, in order to observe both the very narrow and very broad components present in the data. The energy windows were from -400 μeV to 400 μeV for the PG002 analyser, -200 μeV to 1200 μeV for the PG002_offset1 analyser and -3500 to 4000 for the PG004 analyser. The elastic energy resolution was 17.5 μeV for the PG002 analysers and 54.5 μeV for the PG004 analyser.[4] The 51 detectors were grouped into 17 groups of three detectors in each case, giving a momentum transfer range of 0.46 – 1.84 $Å^{-1}$ and 0.93 – 3.69 $Å^{-1}$ for the PG002 and PG004 analysers respectively.

The experiments give rise to scattering functions $S(Q,\omega)$ after corrections for absorption and background and empty can subtraction. These functions were analysed using the Bayesian fitting routine QUASILINES,[5] a method which determines the most likely number of Lorentzian components required to fit the data. The fitting routine is described in detail in section 3.5.3. This procedure allows the

dependence of the full width at half maximum of the Lorentzian components on Q to be determined. A linear dependence of the FWHM with Q^2 at small Q-values represents a diffusion process, its gradient being equal to $2D$, where D is the proton diffusion coefficient.[6] Independence of the FWHM with Q indicates a localized motion.

6.3 Molecular dynamics – simulation details

Molecular dynamics simulations were performed on liquid ammonia and lithium-ammonia solutions at concentrations of 4, 12 and 21 MPM at 230 K. The simulations used the code MOLDY,[7] and were run under an (N,V,E) ensemble (constant number of particles, volume and energy). The simulations comprised a minimum of 200 molecules, with the box sizes greater than 20 Å. The atomic number densities were set to the experimentally measured values in all cases.

The OPLS model of the ammonia molecule[8,9] was used, with the Lennard-Jones potentials and partial charges given in table 5.1. In all cases, the electrons were represented by a diffuse background charge to balance the positive charge of the lithium ions. The potentials for the lithium ions are taken from ref. 8, and are also given in table 5.1.

The initial configuration was equilibrated using the Monte Carlo algorithm MONTE[10] and scaling was performed at the start of the MD simulation for a further 50 ps. MOLDY uses an 'all-image' convention, which means that the list of neighbouring cells includes all periodic images of a particle which are within the

interaction cut-off. The Ewald sum method[11] was used to calculate the long-range Coulomb interactions beyond the cut-off distance. The parameters used in the Ewald sum were optimised by MOLDY, as were the values of the real-space cut-off. The exact values for each simulation are given in table 6.1, together with the simulation cell sizes and the number of lithium ions and ammonia molecules.

Each simulation was run for a total elapsed time of 550 ps, with 0.5 fs timesteps. The intermediate configurations were saved every 50 timesteps, in order to calculate the self-diffusion coefficients of the ammonia molecules and lithium ions. The diffusion rate of a particular species may then be extracted via the Einstein relation,[7] given by:

$$\langle | r(t) - r(0) |^2 \rangle = 6Dt \tag{6.1}$$

For a species of N particles, the mean square displacement is calculated via:

$$\langle | r(t) - r(0) |^2 \rangle = \frac{1}{N\, N_t} \sum_{n=1}^{N} \sum_{t_0}^{N_t} | r_n(t + t_0) - r_n(t_0) |^2 \tag{6.2}$$

where $r_n(t)$ is the position of particle n at time t.

Sample	Number of particles		cell size / Å	cut-off / Å	k cut-off / $Å^{-1}$	α / $Å^{-1}$
	Li	NH_3				
0 MPM	0	300	22.97	10.15	2.27	0.334
4 MPM	8	192	20.60	9.79	2.35	0.346
12 MPM	24	176	21.06	10.11	2.27	0.335
21 MPM	42	158	21.58	10.50	2.19	0.323

Table 6.1 The Ewald sum parameters: the reciprocal space cut-off and alpha parameter, together with the number of particles of each type, the cell size and the real-space cut-off for each simulation run.

6.4 Results and Discussion – QENS data

In all cases the scattering function was well-represented by a single Lorentzian component. A typical fit to the quasi-elastic neutron spectra is presented in figure 6.1, in which the data are shown together with the least squares curve fit of the elastic line and the Lorentzian component convoluted with the resolution function plus the sloping background. Figure 6.2 shows an example of the broadening of the measured spectra with Q for the saturated lithium-ammonia solution at 230 K.

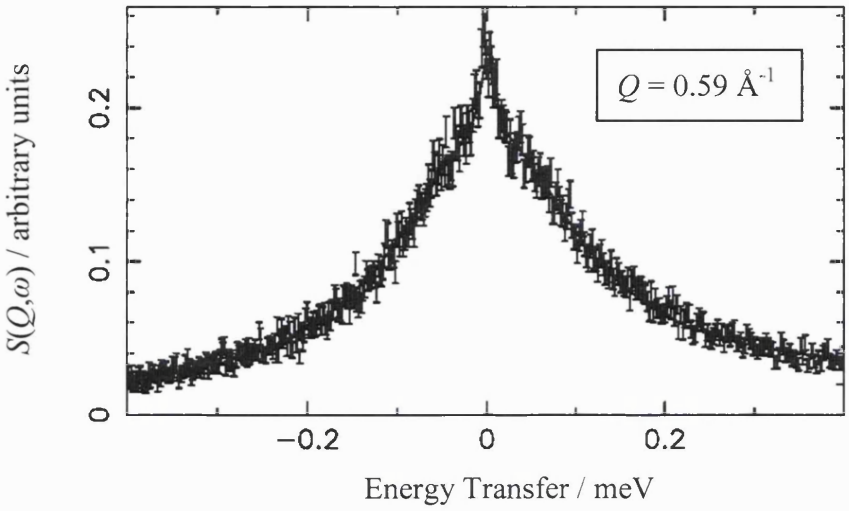

Figure 6.1 Example of the fit to the quasi-elastic neutron scattering spectrum at Q = 0.59 Å^{-1} using the PG002 graphite analyser: 4 MPM lithium-ammonia solution at 230 K, uncertainty limits: data, solid line: Bayesian fit.

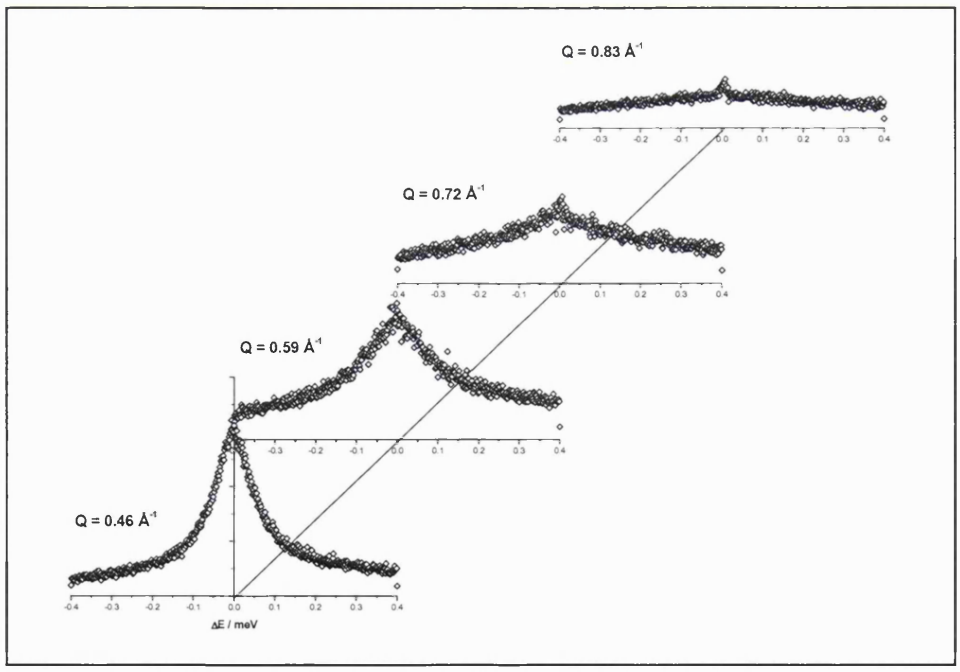

Figure 6.2 Example of the broadening of the quasi-elastic neutron scattering spectrum with Q obtained using the PG002 graphite analyser: 21 MPM lithium-ammonia solution at 230K.

The plots of the FWHM vs. Q^2 are shown in figures 6.3 to 6.4, together with the Chudley-Elliott model or Fick's Law fits. It can be seen that for the liquid samples at 230 K, a simple diffusion model (Fick's law) provides a satisfactory fit to the data. At higher Q-values, there is a slight discrepancy between the PG002 and PG002 offset datasets. This arises because at these Q-values, the FWHM is close to or beyond the limit of the PG002 energy window of 800 μeV: in these cases the PG002 offset data is likely to give more accurate measurements. The diffusion coefficients obtained from the Fick's Law fit to the PG002 offset data and the PG002 data are given in table 6.2.

The data taken from liquid samples at lower temperatures (figure 6.4) have FWHMs which are well within the energy window of the PG002 analyser. There is still a difference between the data taken using the PG002 and the PG002 offset analysers, which is due to the fact that the PG002 offset energy window is not symmetric. Therefore, the fitting procedure for the offset analyser would be less accurate as it is not able to see enough of the energy range on the 'short' side. For these samples, the data sets taken using the PG002 analyser have been fitted with the Chudley-Elliott model for jump diffusion processes;[12] the resulting parameters and diffusion coefficients are given in table 6.3.

The data obtained using the PG004 analyser were found to be inconsistent with the PG002 and PG002 offset data. This is perhaps due to inelastic scattering by phonons, which the QUASILINES routine will try to fit as a very broad Lorentzian component. Furthermore, the plots of the FWHMs vs. Q^2 measured using the PG004 analyser cannot be fitted with a straight line which passes through the origin (Fick's

law). The PG004 data were therefore deemed to be less reliable than the PG002 and PG002 offset data, and so are not presented here.

For the crystalline samples, the FWHMs again did not exceed the energy window for the PG002 analyser. The PG004 data taken for these samples was again less reliable than the PG002 data, due to the poorer energy resolution of the PG004 analyser crystal. The PG002 datasets have therefore been used to determine the energies of the rotational motion here, for the reasons given above. These are shown in figure 6.5.

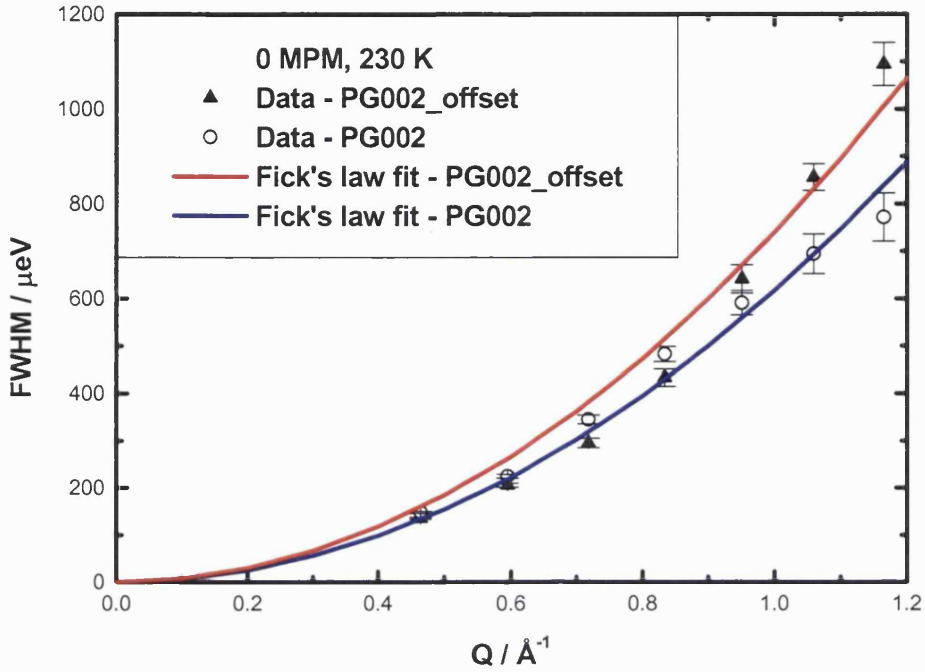
0 MPM, 230 K
Data - PG002_offset
Data - PG002
Fick's law fit - PG002_offset
Fick's law fit - PG002
FWHM / μeV
Q / Å-1
0
200
400
600
800
1000
1200
0.0
0.2
0.4
0.6
0.8
1.0
1.2

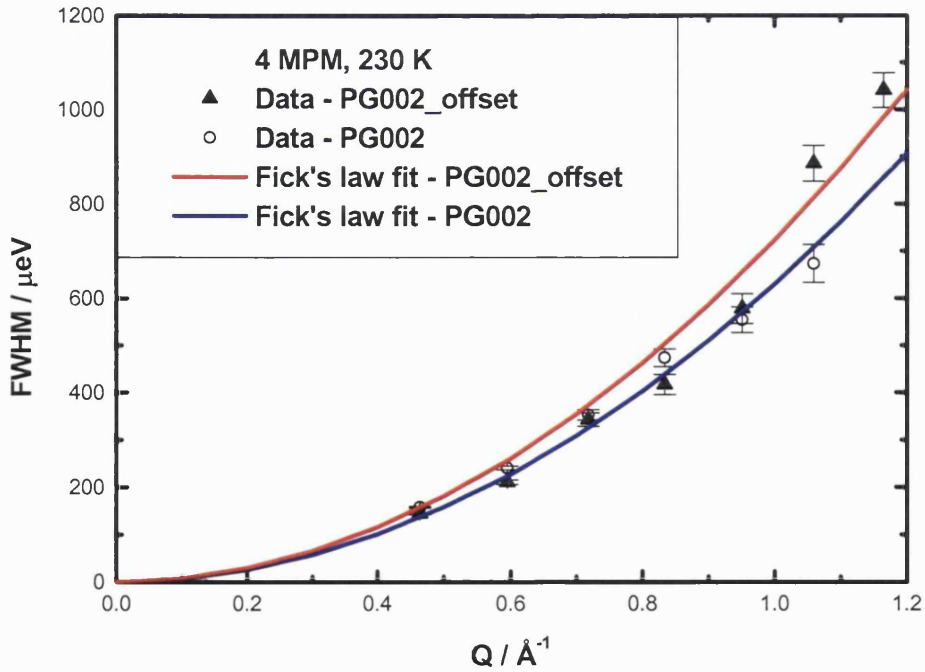
4 MPM, 230 K
Data - PG002_offset
Data - PG002
Fick's law fit - PG002_offset
Fick's law fit - PG002
FWHM / μeV
Q / Å-1
0
200
400
600
800
1000
1200
0.0
0.2
0.4
0.6
0.8
1.0
1.2

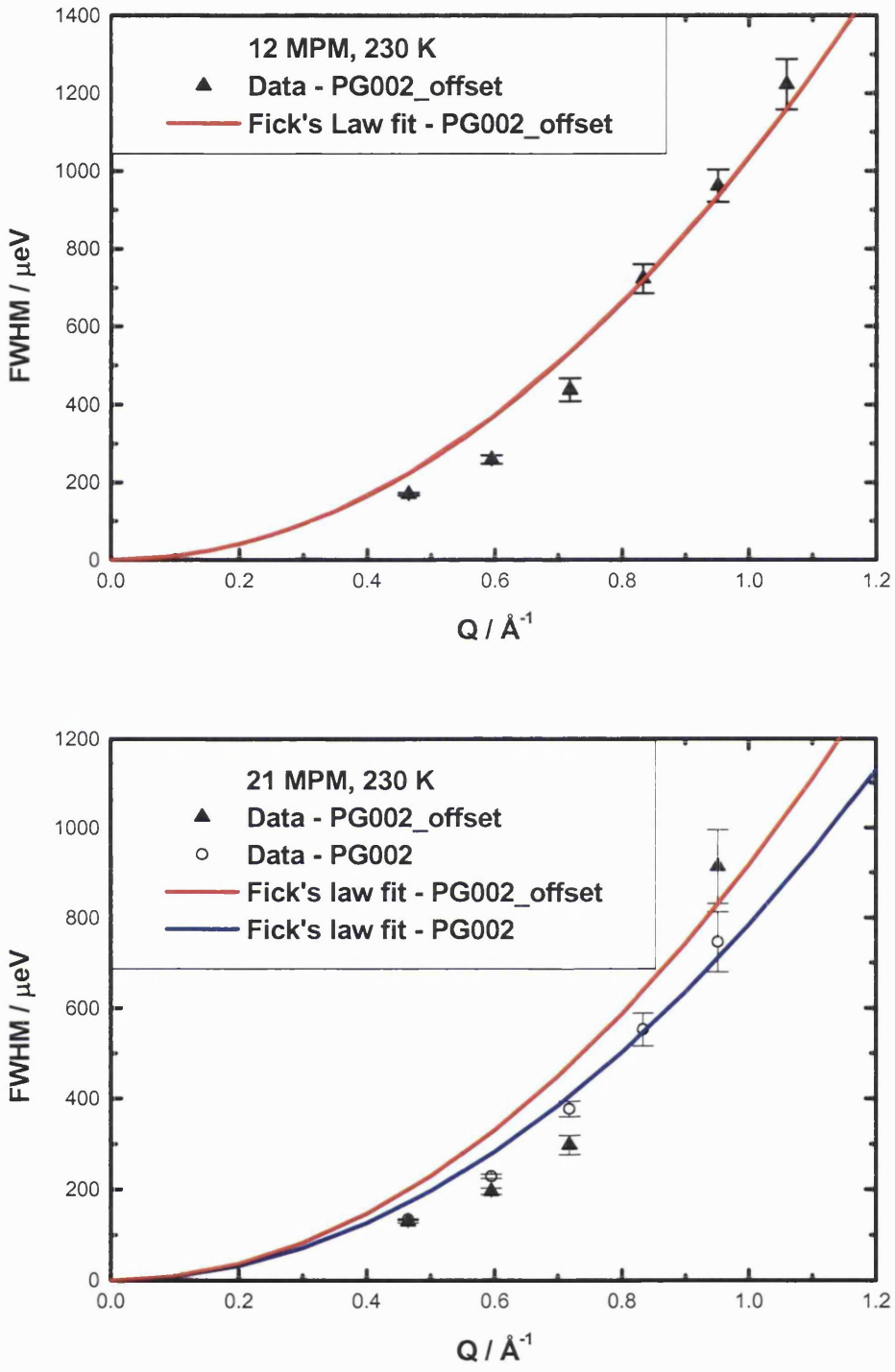

Figure 6.3 Graphs showing the FWHMs vs. Q together with the Fick's Law fit to the data, for the PG002 and PG002 offset datasets. The samples comprise liquid ammonia and lithium-ammonia solutions at 4 MPM, 12 MPM and 21 MPM at 230 K.

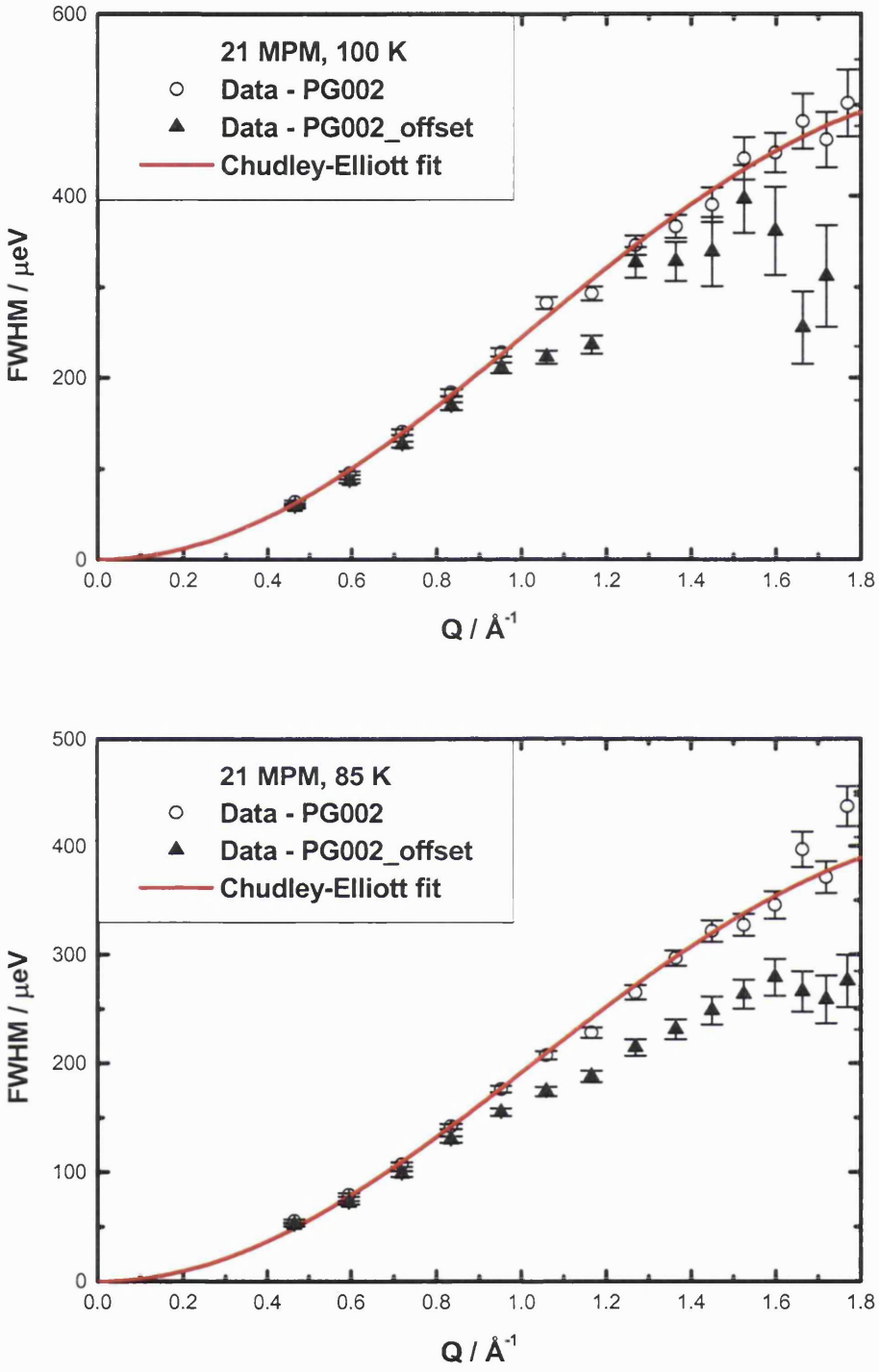

Figure 6.4 Graphs showing the FWHMs vs. Q for the PG002 and PG002 offset datasets, together with the Chudley-Elliott jump diffusion model fit to the PG002 data. The samples are saturated lithium-ammonia solutions at 100 K and 85 K.

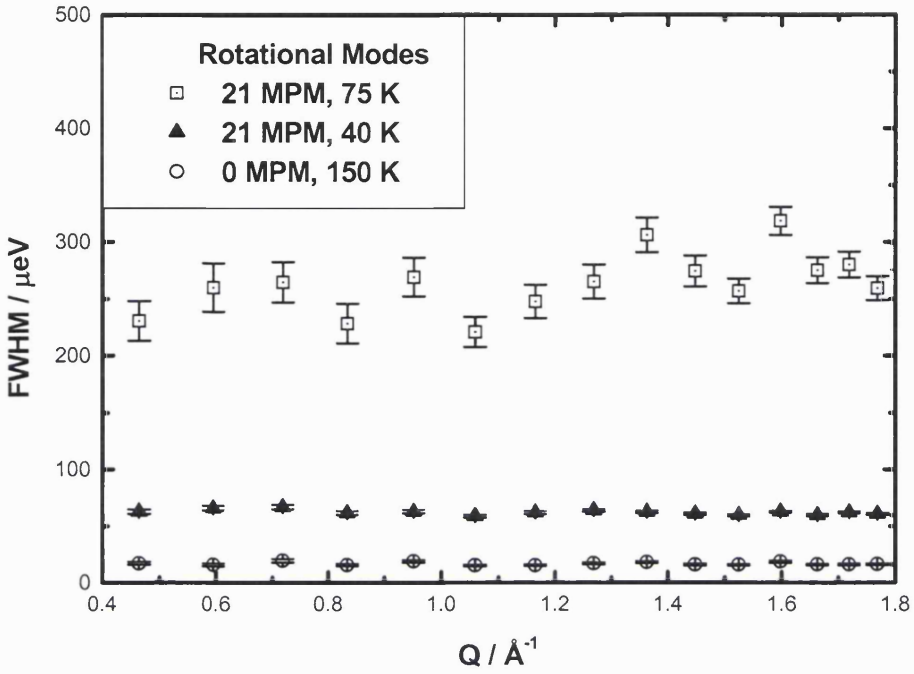

Figure 6.5 Graphs showing the *Q*-independent quasi-elastic broadening representing localised motion in crystalline samples of ammonia at 150 K and saturated lithium-ammonia at 75 K and 40 K.

Sample	Diffusion Coefficient / 10^{-5} cm^2 s^{-1}	
	PG002 offset	PG002
0 MPM	5.61 ± 0.50	4.68 ± 0.14
4 MPM	5.48 ± 0.71	4.77 ± 0.41
12 MPM	7.84 ± 0.79	-
21 MPM	6.96 ± 0.71	5.95 ± 0.67

Table 6.2 Diffusion coefficients for the ammonia and lithium-ammonia solutions at 230 K, measured using the PG002 and PG002 offset analyser.

Sample	L / Å	t / ps	D / 10^{-5} cm^2 s^{-1}
21 MPM, 100 K	2.05 ± 0.03	3.06 ± 0.06	2.29 ± 0.11
21 MPM, 85 K	2.03 ± 0.04	3.85 ± 0.12	1.79 ± 0.13

Table 6.3 Diffusion coefficients and Chudley-Elliott model parameters for the saturated lithium-ammonia solutions at 100 K and 85 K.

6.5 Results from molecular dynamics simulation

The radial distribution functions arising from the MD simulations (figure 6.6) show good agreement with the structural data from Chapter 5, and demonstrate the accuracy of the simulations. Unlike QENS experiments, MD simulations allow the diffusion rates of both the lithium ions and the ammonia molecules to be extracted. The mean square displacements of the molecules and ions vs. time are plotted in figure 6.7. The diffusion coefficient can be extracted via the Einstein relation, given by eq. 6.1. The gradient of a graph of $\langle | r(t) - r(0) |^2 \rangle$ vs. time is then equal to $6D$, where D is the diffusion coefficient of a particular species.[7] The values of the diffusion coefficients for the lithium ion and ammonia molecules calculated via this method are given in table 6.4. In the 21 MPM simulation, it can be seen that the mean square displacements vs. time for both the nitrogen atoms and lithium ions exhibit a slight non-linearity at long times. However, the total energy of the system was found to be constant to within 0.03 %, and there was no increase in temperature over the course of the simulation.

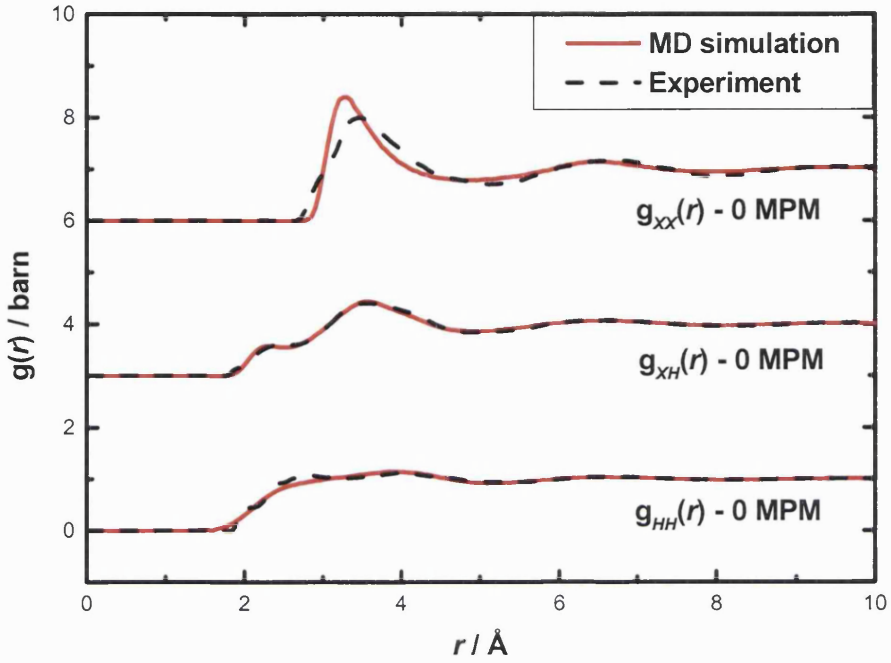
MD simulation
Experiment
$g_{XX}(r)$ - 0 MPM
$g_{XH}(r)$ - 0 MPM
$g_{HH}(r)$ - 0 MPM
g(r) / barn
r / Å
0
2
4
6
8
10

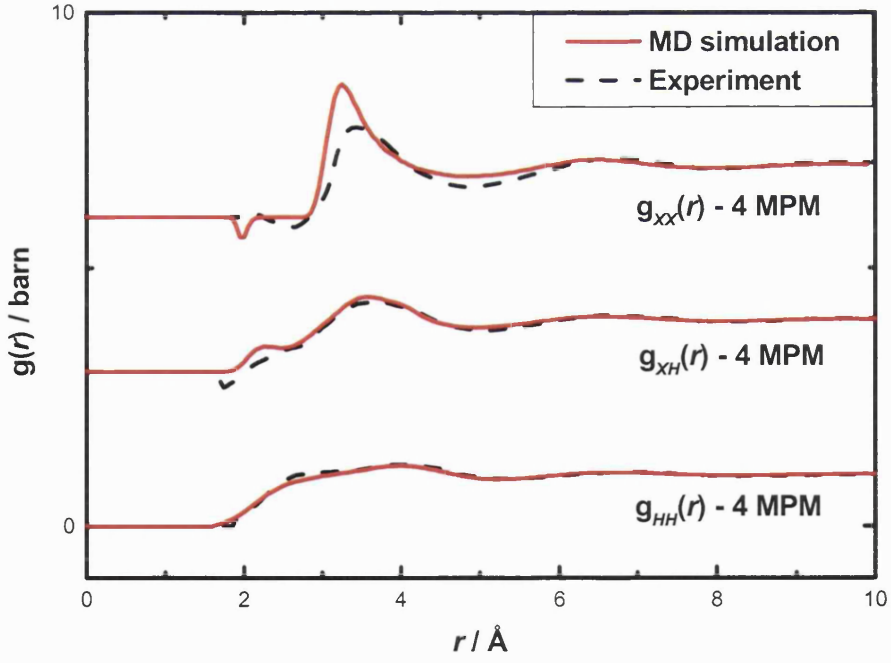
MD simulation
Experiment
$g_{XX}(r)$ - 4 MPM
$g_{XH}(r)$ - 4 MPM
$g_{HH}(r)$ - 4 MPM
g(r) / barn
r / Å
0
2
4
6
8
10

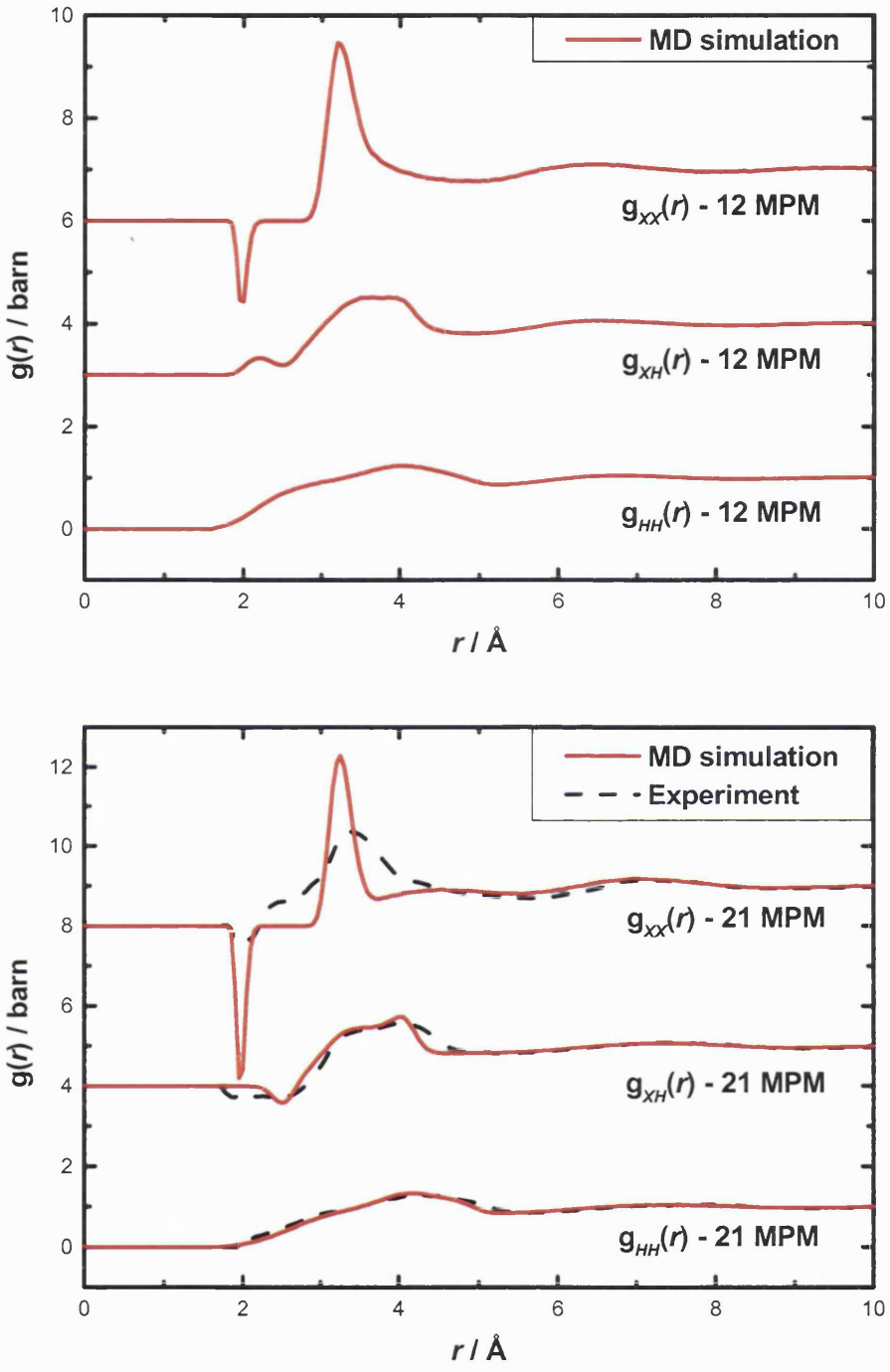

Figure 6.6 The simulated and measured intermolecular H-H, X-H and X-X partial pair correlation functions for ammonia and the 4 MPM, 12 MPM and 21 MPM lithium-ammonia solutions at 230 K. The simulated partial pair correlation functions for the 12 MPM solution have no experimentally measured counterpart.

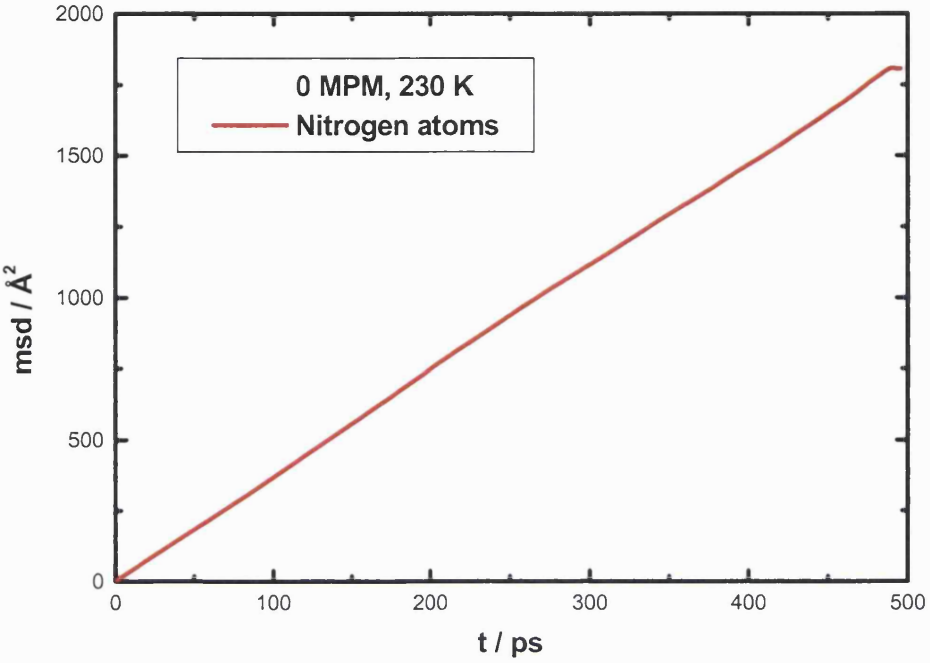
0 MPM, 230 K
Nitrogen atoms
msd / Å²
t / ps
0
500
1000
1500
2000
0
100
200
300
400
500

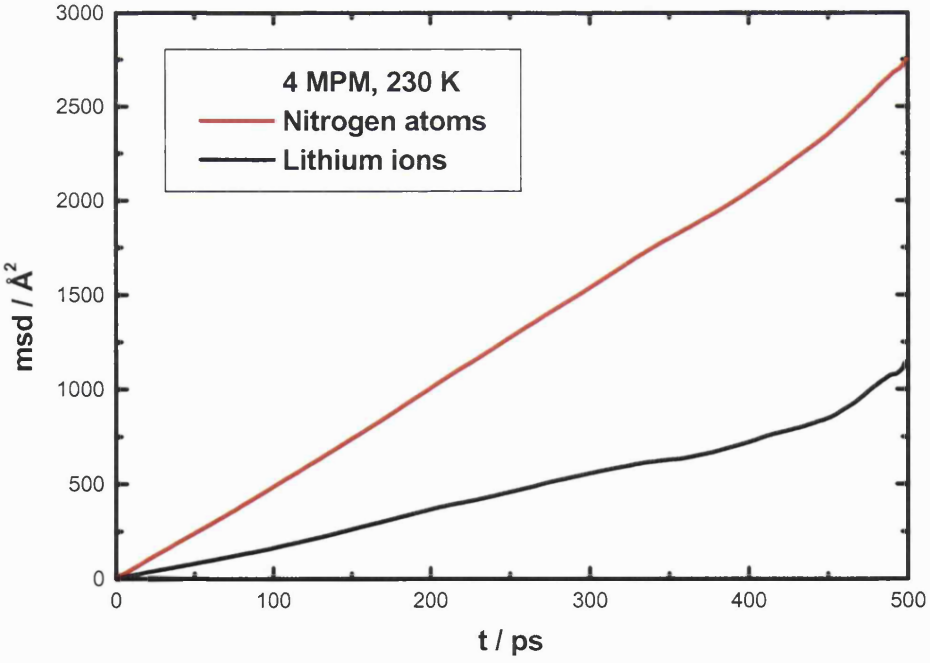
4 MPM, 230 K
Nitrogen atoms
Lithium ions
msd / Å²
t / ps
0
500
1000
1500
2000
2500
3000
0
100
200
300
400
500

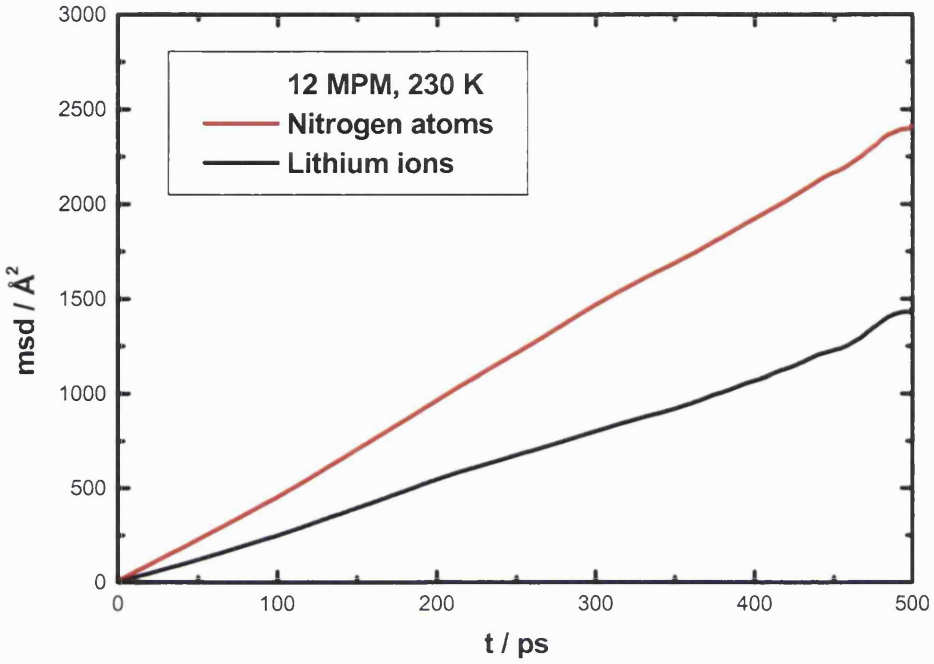

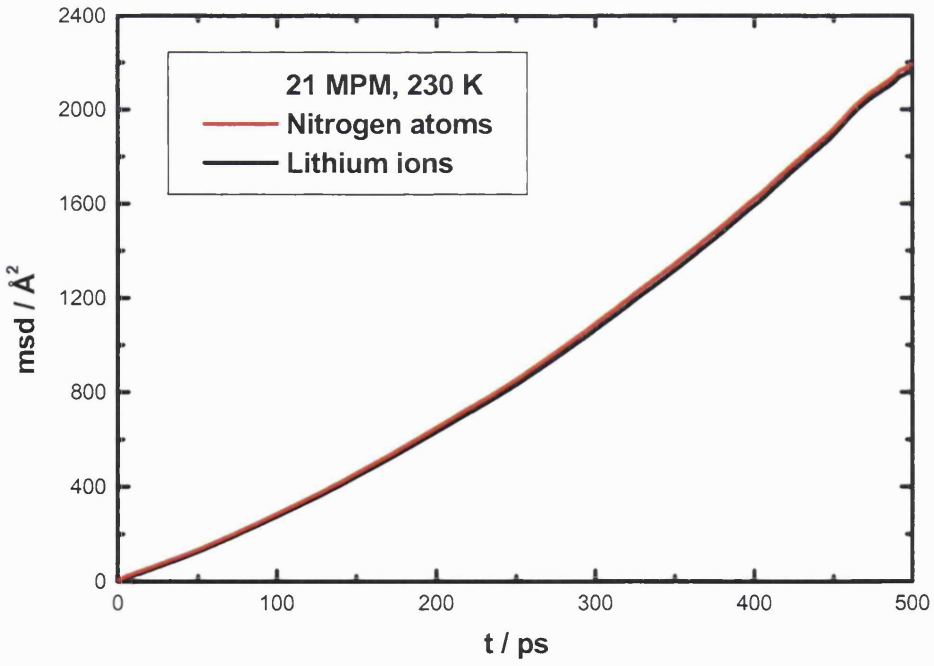

Figure 6.7 Graphs of the mean square displacement of the lithium ions and nitrogen atoms vs. time. The gradient is equal to $6D$, where D is the diffusion coefficient.

Sample	Diffusion coefficient / 10^{-5} cm^2 s^{-1}	
	Lithium ions	Nitrogen atoms
0 MPM	-	6.15 ± 0.05
4 MPM	3.02 ± 0.06	8.63 ± 0.32
12 MPM	4.53 ± 0.07	8.04 ± 0.12
21 MPM	5.3 ± 1.2	5.2 ± 1.4

Table 6.4 Diffusion coefficients obtained via the MD simulations of ammonia and lithium-ammonia solutions at 230 K.

6.6 Comparison of QENS and MD simulation results with NMR data: general conclusions

The graph in figure 6.8 shows the dependence of the proton diffusion coefficients (measured using QENS and MD simulation) on metal concentration for the lithium-ammonia solutions at 230 K as compared to previous NMR measurements.[1] Figure 6.9 shows the dependence of the proton diffusion coefficient extracted from the QENS data on temperature for the saturated lithium-ammonia solutions.

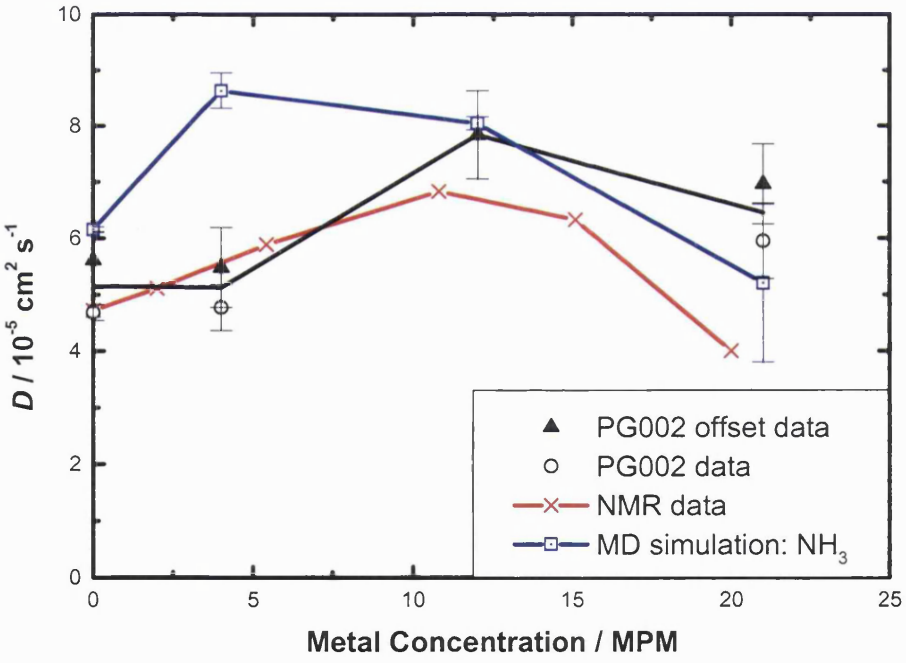

Figure 6.8 Graph of the proton diffusion coefficients for ammonia and lithium-ammonia solutions of varying concentrations at 230 K: comparison of QENS and MD simulation data with NMR measurements taken from Ref. [1].

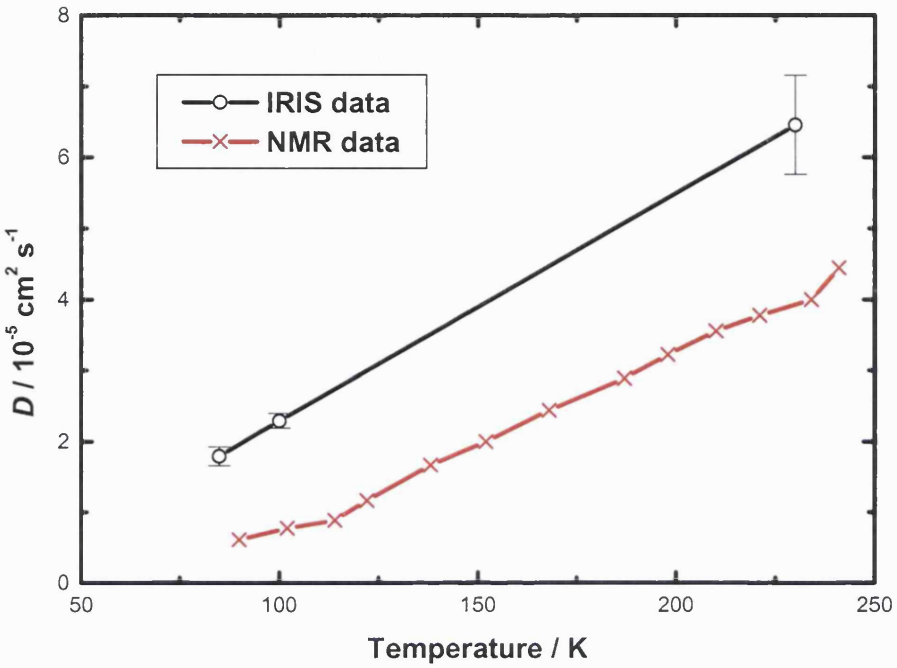

Figure 6.9 Graph of the diffusion coefficients for the saturated lithium-ammonia solutions at varying temperatures: comparison between QENS measurements and NMR data taken from Ref. [1].

6.6.1 Proton dynamics in ammonia

The solid phase of ammonia was measured primarily in order to provide a comparison with the solid 21 MPM compounds. No quasi-elastic broadening was observed in solid ammonia at temperatures of 40 K and 80 K, and a slow rotational mode was evident in solid ammonia at 150 K. The diffraction window for the PG004 datasets showed small Bragg peaks at all the solid temperatures measured, while the PG002 dataset showed Bragg peaks at 40 K, which became barely visible at 150 K. This was most likely to be due to the high atomic fraction of hydrogen present in the samples. The freezing of ammonia leads to an increase in the number of hydrogen bonds per ammonia molecule (6 rather than 4)[13-15] and so forms an extended hydrogen-bonded network which impedes the diffusion process and significantly slows down any molecular rotation.

In liquid ammonia at 230 K, a single Lorentzian convoluted with the resolution function fitted the data satisfactorily. The FWHM of the quasielastic component showed a clear Q^2 dependence, giving a diffusion coefficient of ~5.61 × 10^{-5} cm^2 s^{-1}, in agreement with the value obtained by NMR[1] of 4.7 × 10^{-5} cm^2 s^{-1}. The diffusion coefficient obtained via MD simulation is 6.15 × 10^{-5} cm^2 s^{-1} which is consistent with the experimentally determined values.

6.6.2 Diffusion processes in lithium-ammonia solutions.

Increasing the concentration of metal present in solution gives rise to a large increase in volume of 12%, 29% and 48% with respect to pure ammonia for solutions of 4, 12 and 21 MPM respectively, caused by the accommodation of excess electrons in the solution.[2,16,17] In addition, the hydrogen-bonding is progressively disrupted as the metal content is increased.[18] These are likely to be the dominant mechanisms which allow the observed concomitant increase in the rate of diffusion with concentration, from 5.48×10^{-5} cm^2 s^{-1} at 4 MPM, to 7.84×10^{-5} cm^2 s^{-1} at 12 MPM. Again these values are in close agreement with those obtained via NMR.[1]

The diffusion rates obtained from the MD simulations of the lithium-ammonia solutions show a similar trend: increasing to a maximum at ~12 MPM and slowing down thereafter. However, for the 4 MPM solution, the diffusion coefficient measured from the MD simulation is significantly greater than that obtained via experiment. In the simulations, the electrons were not explicitly included, and so the influence of the electrons on the motion of the solvent molecules in the electronic solvation shells would not be taken into account. Instead, the ammonia molecules would have more freedom than in the pure ammonia simulation, as the solution density is lower. The discrepancy in the diffusion rates is therefore likely to be caused by the localisation of the electrons and their influence on the solvation shells of solvent molecules. The data clearly show that the electrons play an important role in determining the dynamics of metal-amine solutions in addition to having a significant effect on the solution structure.

Upon increasing the metal concentration beyond 4 MPM, the diffusion rates measured via experimental methods and MD simulation are again consistent. This shows that when the electrons become delocalised, they have less influence on the solvent molecules dynamics, and the electrons can be modelled as a diffuse background charge.

Given the reduction in hydrogen bonding in addition to the decrease in viscosity as the concentration is increased from 0 MPM to 12 MPM, a large increase in the rate of proton diffusion is expected. The degree of hydrogen-bonding decreases further upon increasing the metal concentration, such that at 21 MPM, no trace of hydrogen-bonding remains. This leads one to expect a further increase in the rate of diffusion. In fact, the diffusion rate *decreases* to 6.96×10^{-5} cm^2 s^{-1} at saturation. At concentrations above 12 MPM, the majority of ammonia molecules are incorporated into the solvation shell of the lithium cation, and it has been suggested that the rate of diffusion of these four-fold ionic species is then restricted by their increased mass[1] and steric hindrance. This is also illustrated in the results of the MD simulations, where the diffusion rates of both the lithium ions and ammonia molecules may be measured. As the concentration is increased from 4 MPM to 21 MPM, the lithium ions become more mobile as the solution density decreases: the ion diffusion rates increase from 3.02×10^{-5} cm^2 s^{-1} at 4 MPM, to 4.53×10^{-5} cm^2 s^{-1} at 12 MPM. It is only at 21 MPM that the diffusion rate of the ammonia molecules (5.2×10^{-5} cm^2 s^{-1}) becomes comparable with the diffusion rate of 5.3×10^{-5} cm^2 s^{-1} of the lithium ions.

The diffusion processes in ammonia and lithium-ammonia solutions are therefore governed by a subtle balance between hydrogen-bonding within the solvent and ionic solvation. This also has interesting implications for the lithium-methylamine system, where the greater mass of the solvated ion species may further impede the diffusion of the solvent molecules. Furthermore, the solvation of the excess electrons, which occurs only at dilute metal concentrations in lithium-ammonia solutions, but is observable up to saturation in the lithium-methylamine system,[2] may indeed give rise to a further reduction in the proton diffusion rate.

6.6.3 Saturated lithium-ammonia solutions: rotational dynamics

The phase diagram of lithium-ammonia exhibits a deep pseudoeutectic at saturation: the 21 MPM solution remains a liquid down to 88.8 K, giving one of the lowest temperature liquid metals known.[2] Below this temperature, the solid undergoes several important crystal phase transitions. Between 88.8 K and 82.2 K (phase I), the solid compound exists in a cubic form with $a_0 = 9.55$ Å, and below 82.2 K (phase II) the crystal lattice is hexagonal, having $a = 7.0$ Å and $c = 11.1$ Å.[3] More recently, Stacy and Sienko found that the structure of both phase I and phase II are better indexed as a single bcc phase.[19] This has been confirmed via a neutron diffraction study of $Li(ND_3)_4$ above the antiferromagnetic transition temperature.[20] However, the low temperature magnetic susceptibility of $Li(NH_3)_4$ does indeed exhibit discontinuities at 89 and 82 K,[21-22] showing a solid-solid phase transition at 82 K which is suppressed by deuteration of the compound.[23]

There is also limited evidence for a further transition at ~69 K:[1] resistivity anomalies have been observed around this temperature,[24-25] although the precise heat capacity measurements show nothing unusual.[26] The temperatures at which QENS data was collected were therefore chosen to lie well within each reported solid phase.

It has been suggested that the anomalies observed in $Eu(NH_3)_6$ could be due to a cessation of the rotation of the ammonia molecules around the dipole axis,[27] and that a similar mechanism may be responsible for the effects observed in the solid lithium-ammonia compound at ~69 K.[1] The experimental data show that this is not in fact the case: at a temperature of 40 K, clear quasi-elastic broadening is observed. The QENS spectra may be fitted satisfactorily with a single Lorentzian convoluted with the resolution function. This component does not show any systematic Q^2 dependence and can be assigned to a rotation at ~60 μeV of the ammonia molecule around its axis of symmetry. For the saturated lithium-ammonia solution at 75 K, the rotation occurs at a higher energy of ~250 μeV.

This rotation can only occur when any second shell of ammonia molecules have relatively little interaction with those in the first shell, and any nearest-neighbour molecules are few in number. Such a rotation only becomes possible at saturation, due to the fact that the hydrogen bonding is disrupted completely at this metal concentration. Here, the hydrogen-bonding which is present in more dilute solutions gives way to the tetrahedral solvation of the lithium ions by the ammonia molecules. The second cationic solvation shell is therefore composed of solvent molecules involved in the primary solvation shell of the next nearest cation, and the nearest-neighbour N-N co-ordination number becomes as low as ~6.[18] The $Li(NH_3)_4$ species thus form an expanded metal compound which gives the ammonia molecules

the freedom to rotate around their axes while still being bound to the cations. As the metal concentration decreases, the second solvation shell becomes composed of 'free' ammonia molecules (i.e. those not bound to a cation). This second shell exhibits a degree of hydrogen-bonding, and is likely to hinder any rotation of ammonia molecules around their axes. Furthermore, the nearest N-N co-ordination number increases to ~8 and ~12 for 8 MPM and 0 MPM solutions respectively,[18] further inhibiting any possible rotational mode.

The diffraction window for these datasets collected using the PG002 analyser showed some Bragg peaks for the solution at 40 K, although at 75 K and 85 K any Bragg peaks were indistinguishable from the background. For the datasets collected using the PG004 analyser, only very minute differences were observed in the diffraction pattern upon freezing the solution.

6.6.4 Diffusion in saturated lithium-ammonia solutions

Increasing the temperature of the 21 MPM sample to 85 K takes the compound through its solid-solid phase transition, yielding a change in structure which in turn gives rise to vastly different molecular dynamics. Here, the Lorentzian component required to fit the data has a definite Q^2 dependence: the sample exhibits diffusion at a rate of 1.79×10^{-5} cm^2 s^{-1}, leading to the conclusion that the phase under study was in fact a supercooled liquid, rather than the predicted crystalline cubic compound.

Upon increasing the temperature beyond the pseudoeutectic temperature, the diffusion coefficient increases to 2.29×10^{-5} cm^2 s^{-1} and 6.96×10^{-5} cm^2 s^{-1} for

solutions at 100 K and 230 K respectively. As can be seen from the graph in figure 6.9, these values are greater than those measured via NMR techniques, but again are highly likely, given the extremely low viscosities and densities of saturated lithium-ammonia solutions.

6.7 References

[1] A. N. Garroway and R. M. Cotts, Phys. Rev. A. **7**, 635 (1973).

[2] J. C. Thompson, *Electrons in Liquid Ammonia*, Oxford, Clarendon (1976).

[3] N. Mammano and M. J. Sienko, J. Am. Chem. Soc. **90**, 6322

[4] M. A. Adams, W. S. Howells and M. T. F. Telling, The IRIS User Guide, 2nd edition, Rutherford Appleton Laboratory Technical Report (RAL-TR-2001-002, 2001)

[5] D. S. Sivia, C. J. Carlile, W. S. Howells and S. Konig, Physica B. **182**, 341 (1992).

[6] R. Hempelmann, *Quasielastic neutron scattering and solid state diffusion,* Oxford, Clarendon (2000).

[7] K. Refson, *Moldy User's Manual* (*Revision 2.25.2.6*) (1988).

[8] R. C. Rizzo and W. L. Jorgensen, J. Am. Chem. Soc. **121**, 4827 (1999).

[9] J. Chandrasekhar, D. Spellmeyer and W. L. Jorgensen, J.Am.Chem.Soc. **106**, 903 (1984).

[10] N. Skipper, *Monte version 4.3 User's Manual* (2001).

[11] M. P. Allen and D. J. Tildesley, *Computer Simulations of Liquids*, Oxford, Clarendon (1987).

[12] C. T. Chudley and R. J. Elliott, Proceedings of the Physical Society (London), **77**, 353 (1961)

[13] J. W. Reed and P. M. Harris, J. Chem. Phys. **35**, 1730 (1961).

[14] A. W. Hewat and C. Riekel, Acta Cryst. **A35**, 569 (1979).

[15] I. Olovsson and D. H. Templeton, Acta Cryst. **12**, 832 (1959).

[16] Z. Deng, G. J. Martyna and M. L . Klein, Phys. Rev. Lett. **71**, 267 (1993).

[17] M. Diraison, G. J. Martyna and M. E. Tuckerman, J. Chem. Phys, **111**, 1096 (1999).

[18] H. Thompson, J. C. Wasse, N. T. Skipper, S. Hayama, D. T. Bowron and A. K. Soper, J. Am. Chem. Soc. **125**, 2572 (2003).

[19] A. M. Stacy and M. J. Sienko, Inorg. Chem. **21**, 2294 (1982).

[20] V. G. Young, Jr., W. S. Glausinger and R. B. Von Dreele, J. Am. Chem. Soc. **111**, 9260 (1989).

[21] A. M. Stacy, D. C. Johnson and M. J. Sienko, J. Chem. Phys. **76**, 4248 (1982).

[22] W. S. Glausinger, S. Zolotov and M. J. Sienko, J. Chem. Phys. **56**, 4756 (1972).

[23] P. Chieux, M. J. Sienko and F. DeBaecker, J. Phys. Chem. **79**, 2996 (1975).

[24] M. D. Rosenthal and B. W. Maxfield, J. Solid State Chem. **7**, 109 (1973)

[25] J. A. Morgan, R. L. Schroeder and J. C. Thompson, J. Chem. Phys. **43**, 4494 (1965).

[26] N. Mammano and L. V. Coulter, J. Chem. Phys. **47**, 1564 (1967).

[27] J. T. Parker and M. Kaplan, Phys. Rev. B. **8**, 4318 (1973).

CHAPTER 7

RESULTS III:
STRUCTURE OF MIXED SOLVENTS AND LITHIUM-MIXED SOLVENT SOLUTIONS

7.1 Introduction

Alkali-metals dissolve readily in both ammonia and methylamine, forming metastable solutions in which the valence electron is released into solution via solvation of the metal cation. However, lithium-ammonia solutions and lithium-methylamine solutions exhibit several differences,[1] which are detailed in Chapter 1. Lithium-ammonia solutions are brilliant gold in colour in the metallic phase: here the electrons are genuinely delocalised, and the conductivity reaches 15000 $\Omega^{-1}cm^{-1}$ at saturation.[1] The electrons only become localised at ~4 MPM, when enough 'unbound' molecules remain to be able to solvate the electrons. In contrast to lithium-ammonia solutions, saturated solutions of lithium in methylamine are deep-blue in colour throughout the entire concentration range. The larger methylamine molecules are therefore able to localise the electron even at high metal

concentrations, when the majority of solvent molecules are involved in ionic solvation. The way in which the excess electrons are accommodated therefore plays an important role in the differing properties of lithium-ammonia and lithium-methylamine solutions. Via a detailed investigation into the solvent structure of a lithium-mixed solvent solution, it is possible to focus upon the mechanism behind electronic solvation by both ammonia and methylamine molecules, and determine which of the ammonia ($-NH_3$), amine ($-NH_2$) and methyl ($-CH_3$) groups play the key role in hydrogen-bonding and both electron and ion solvation.

The phase diagram of the lithium-mixed solvent solution exhibits a large region of liquid-liquid phase separation below ~19 MPM. In order to understand the origin of this immiscibility gap, and whether it is driven by solvent molecule segregation[2] or the accommodation of ionic and electronic species, it is first necessary to study the mixed solvent system in the absence of any solute. The two extremes of the mixed solvent system have been chosen for investigation here: the pure mixed solvent system at three different methylamine:ammonia molar ratios, and a saturated solution of lithium in a 50:50 molar ratio of ammonia and methylamine. At saturation, it should be noted that the solution comprises four solvent molecules per metal atom, hence all the solvent molecules are involved in the primary cation solvation shells. Experimental data alone show only the average distribution of solvent molecules around the cations: three-dimensional simulation studies are therefore necessary to determine whether any preferential solvation of the ionic species occurs.

Jortner provided the first detailed model of the solvated electron, in which the potential experienced by the electron depends on the dielectric constant of the

surrounding solvent.[3-6] Methylamine has a lower dielectric constant than ammonia, and is less polarisable[7] (see table 1.1). Therefore, via a systematic change in dielectric constant, from ammonia to methylamine, it will be possible to observe the effect of a change in the potential $V(r)$ on electron localisation in the solutions.

7.2 Mixed solvent liquids - introduction

Hydrogen/deuterium isotopic substitution neutron diffraction experiments were performed on mixed solvent solutions of molar ratios 80:20, 50:50 and 20:80 methylamine:ammonia. The data have been analysed in conjunction with Empirical Potential Structure Refinement (EPSR),[8-11] a three-dimensional simulation technique, in order to generate all atom-atom correlations and molecular orientations. We find that the amine groups play the key role in hydrogen-bonding in this system: hydrogen-bond acceptor lobes are observed above the hydrogen atoms on the ammonia molecules and the amine group of the methylamine molecules, and donor lobes are located opposite the lone electron pairs. Analysis of the ammonia-methylamine orientational correlations reveals that methylamine-nitrogen to ammonia-hydrogen correlations have a greater contribution to the hydrogen-bonding than the ammonia-nitrogen to methylamine-hydrogen correlations. In general, however, the degree of hydrogen bonding arising from particular molecule-molecule interactions is governed by the relative mole fraction of each solvent in the mixture. No clustering of molecules of the same type (or preferential solvation) is observed in the 3-D configuration, therefore the mixed solvent system is fully homogeneous even on a microscopic scale.

7.2.1 Experimental details

For the pure mixed solvent systems, H/D substitution was carried out on the ammonia molecules alone. The samples here comprised: (a) [ND_3:CD_3ND_2], (b) [NH_3:CD_3ND_2] and (c) a 50:50 mixture of samples (a) and (b), at the three methylamine:ammonia molar ratios of 80:20, 50:50 and 20:80. However, the co-ordination numbers calculated from the resulting partial pair correlation functions showed that in-solution isotopic exchange occurs between the hydrogen atoms on the ammonia molecules and the hydrogen atoms of the amine groups on the methylamine molecules. In effect, the substituted atoms comprised the hydrogen atoms on the ammonia molecules and the amine groups of the methylamine molecules, but with a smaller contrast between the light and heavy samples. In calculating the weightings of the individual atom-atom correlations contained within the partial structure factors, this was taken into account. The average scattering length of hydrogen in the heavy sample was therefore that of deuterium, and the average scattering length of hydrogen in the light sample was taken to be:

$$\bar{b} = (c_{DA} b_H + c_{DN} b_D)/(c_{DA} + c_{DN}) \tag{7.1}$$

where $\bar{b}$ is the average hydrogen scattering length of the light sample, and c and b are the atomic fractions and scattering lengths of the atomic species. Subscripts *DA* and *DN* represent hydrogen atoms on the ammonia molecule and the amine group of the methylamine molecule respectively. The scattering length of light hydrogen was then replaced with the average scattering length of hydrogen $\bar{b}$ within the

simultaneous equations used to calculate the partial structure factors (eqs. 3.34 – 3.37), and the fraction of the light sample in the mixture was 0.5.

7.2.2 Results and discussion - mixed solvent system

The measured total structure factors arising from the deuterated mixed solvent liquids after empty cell subtraction and corrections for absorption, multiple scattering and self-scattering, are presented in figure 7.1 together with the total pair correlation functions and minimum noise fits. As the ratio of methylamine to ammonia increases, the principal peak shifts inwards, from 2.02 $Å^{-1}$ in the liquid with a methylamine:ammonia ratio of 20:80, to 1.92 $Å^{-1}$ and 1.81 $Å^{-1}$ in the liquids of methylamine:ammonia ratios of 50:50 and 80:20 respectively. This can be compared with data for the two neat solvents: in liquid ammonia[12,13] the principal peak is at 2.07 $Å^{-1}$, and in liquid methylamine,[14] at 1.75 $Å^{-1}$. The shift in peak position has a linear dependence on the change in relative solvent concentration, and is consistent with the decrease in molecular number density as the mole fraction of methylamine increases, and shows that the two solvents are fully mixed.

The composite partial structure factors, H-H, X-H and X-X, are shown in figures 7.2 – 7.4. Here, H represents the hydrogen atoms on the ammonia molecules and the amine group of the methylamine molecules (labelled DA and DN respectively), and X represents the remaining atomic species: carbon, deuterium and nitrogen on the methylamine molecule, and nitrogen on the ammonia molecule (labelled CM, DC, NM and NA respectively). All the composite partial structure

factors show a similar decrease in principal peak position as the mole fraction of methylamine is increased.

The X-H pair correlation function has a broad intermolecular peak, which extends to as low as ~1.8 Å. The low-*r* region of this feature can be assigned to hydrogen-bonding between the ammonia molecules and the amine groups of the methylamine molecules. The size of this shoulder appears to decrease and move to higher *r* as the mole fraction of methylamine increases. This is to be expected, given that liquid ammonia has a greater degree of hydrogen-bonding (~2.0 hydrogen bonds per nitrogen atom[12]) than methylamine (~1.0 hydrogen bond per nitrogen atom[14]).

The shoulder at ~2.7 $Å^{-1}$ in the H-H pair correlation function is the counterpart to the hydrogen-bonded feature in the X-H function. The trend in the size and position of this feature with increasing methylamine:ammonia ratio is similar to that in the X-H function. It is not possible to determine experimentally the individual contributions to the hydrogen bonded structure by ammonia or methylamine molecules, or whether any preferential solvation occurs within the mixture, since in-solution hydrogen exchange leads to the labelling of both the ammonia molecules and the amine group of the methylamine molecules. For this reason, the technique of Empirical Potential Structure Refinement (EPSR) has been used to produce a 3-D molecular configuration which is consistent with the experimental data, from which all atom-atom pair correlation functions may be extracted.

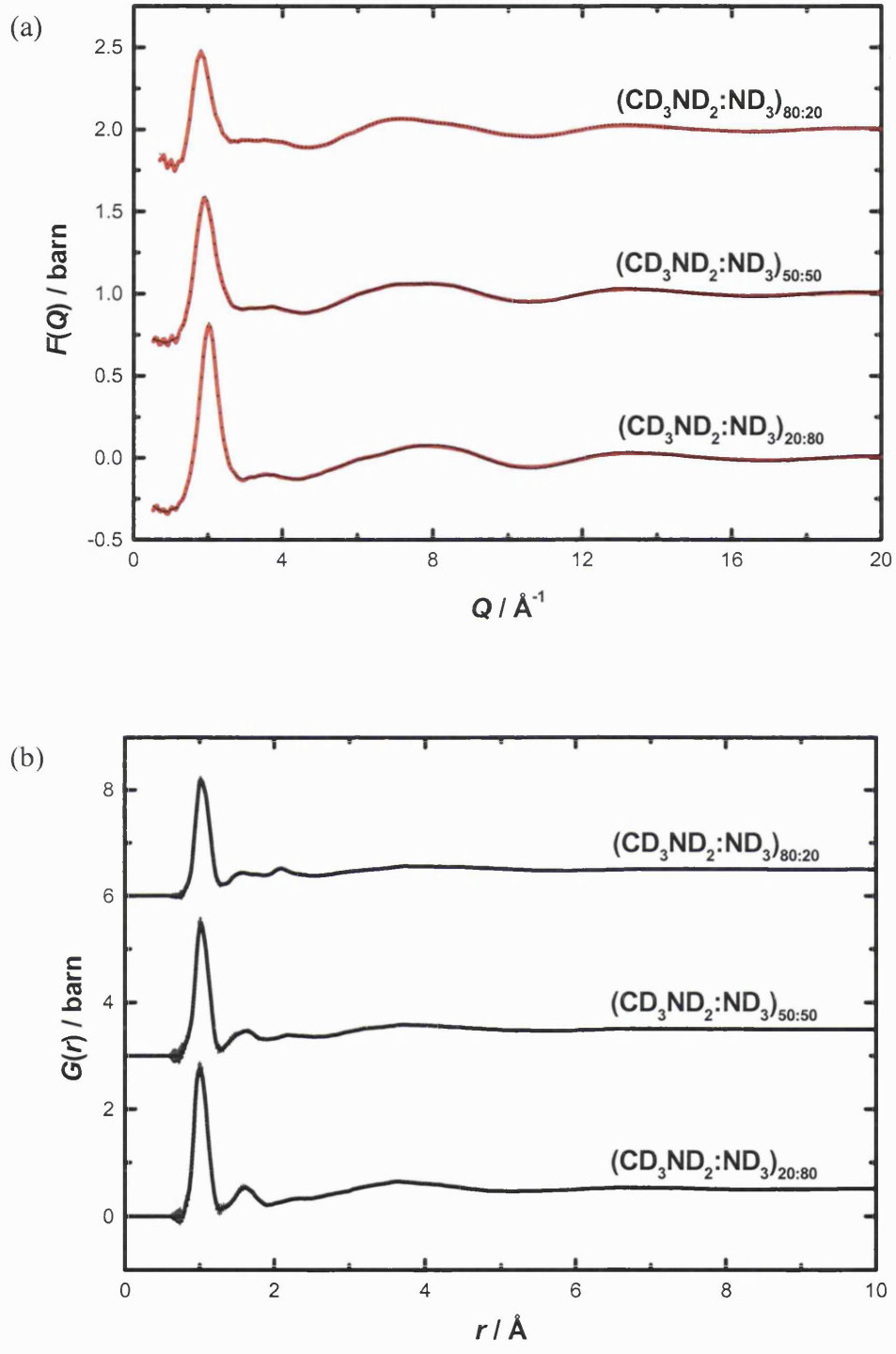

Figure 7.1 (a) Total structure factors (error bars) and minimum noise fit (solid line) and (b) total pair correlation functions for the deuterated methylamine-ammonia samples. Note the shift inwards of the principal peak in $F(Q)$ as the relative mole fraction of methylamine is increased.

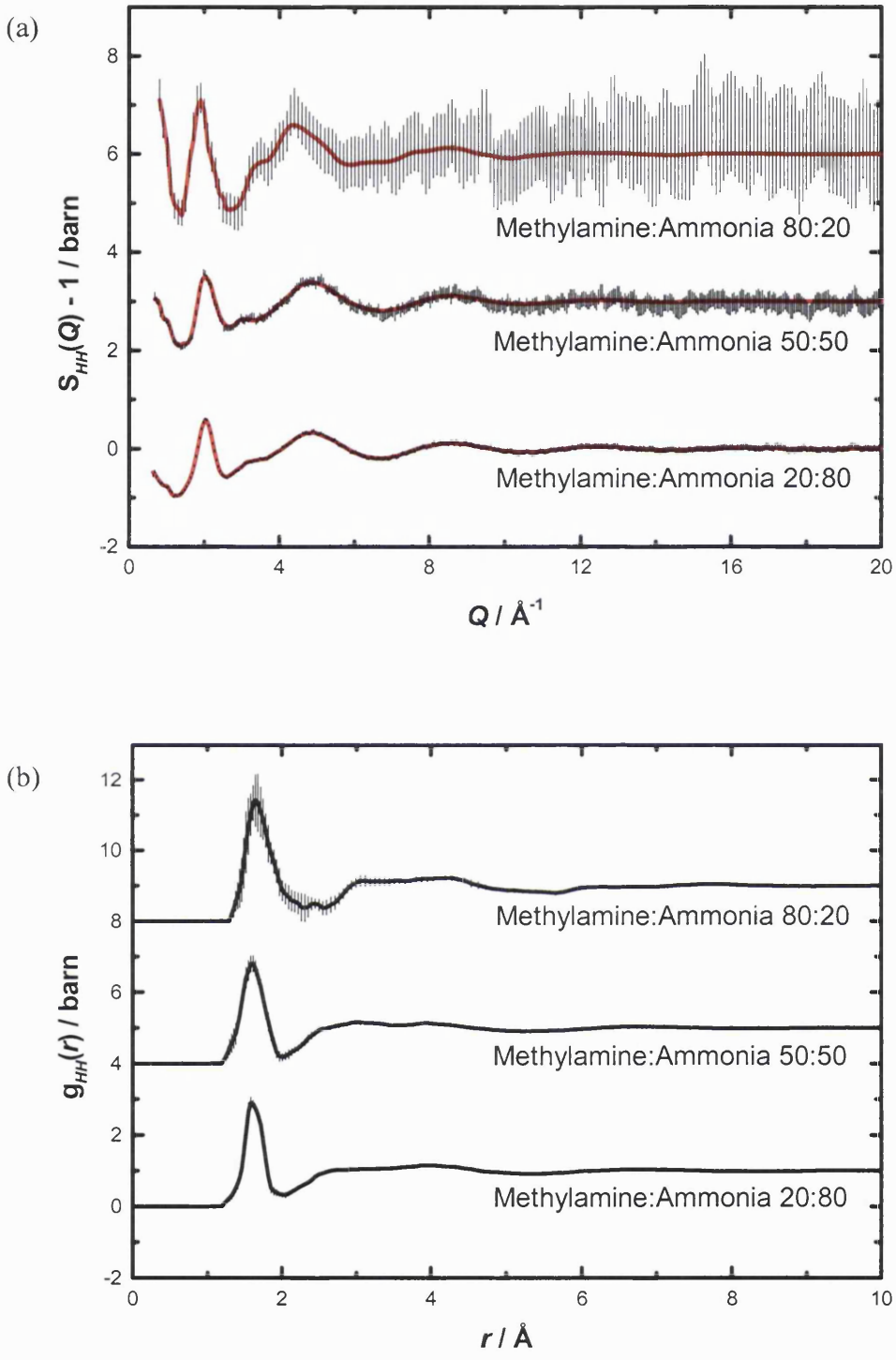

Figure 7.2 (a) H-H partial structure factors (error bars) and minimum noise fit (solid line) and (b) H-H partial pair correlation functions for the methylamine-ammonia liquids.

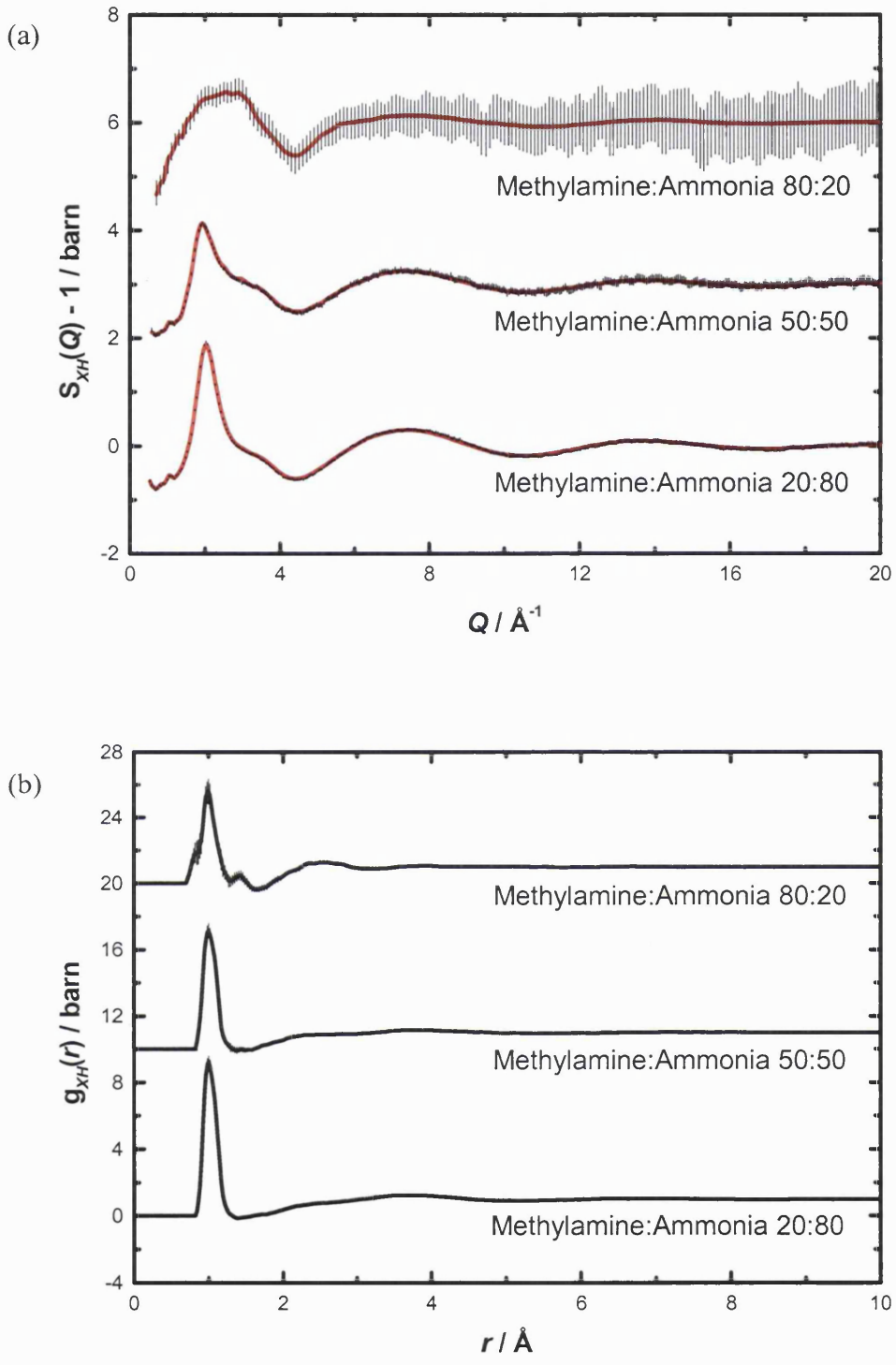

Figure 7.3 (a) X-H partial structure factors (error bars) and minimum noise fit (solid line) and (b) X-H partial pair correlation functions for the methylamine-ammonia liquids.

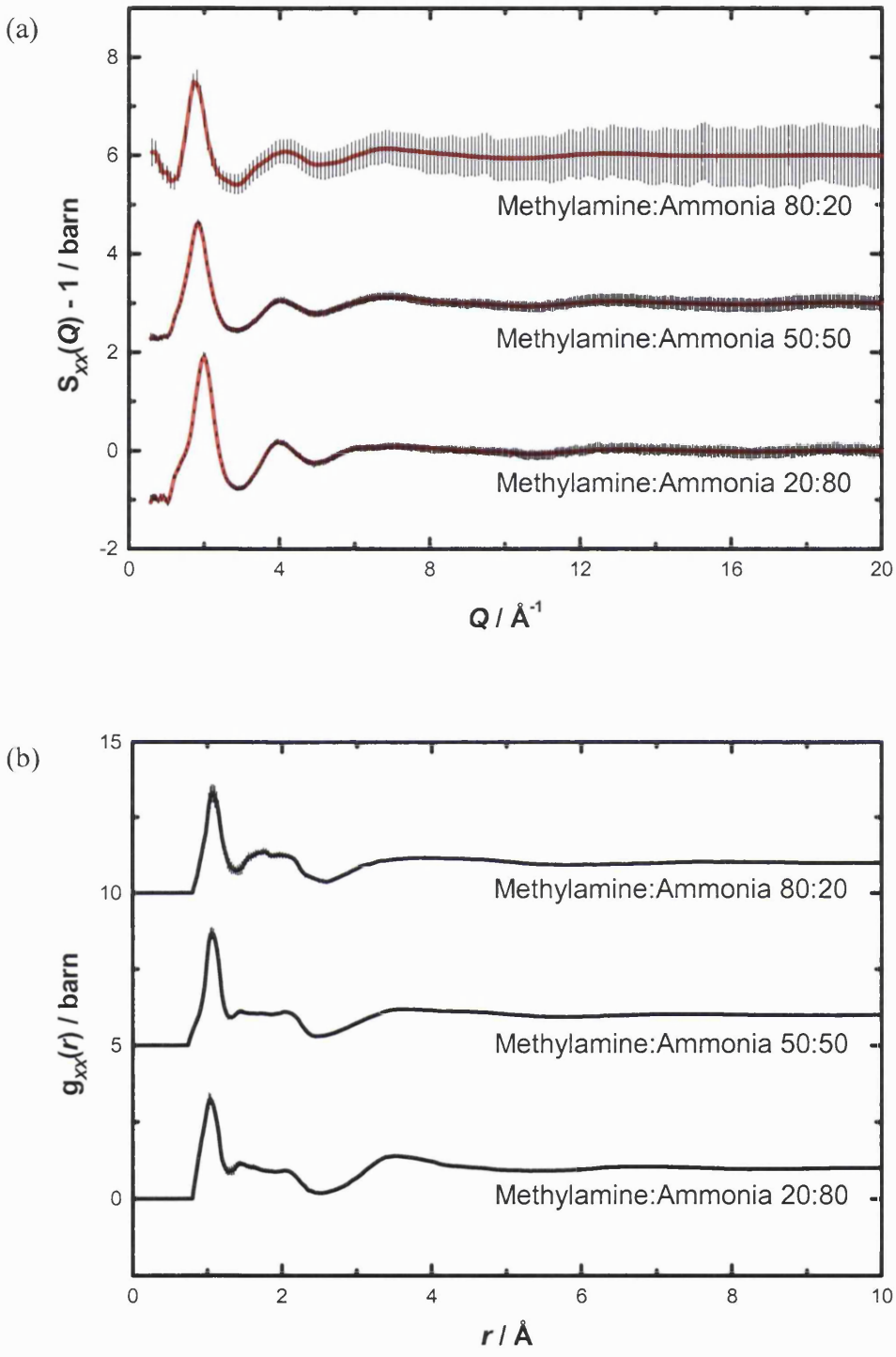

Figure 7.4 (a) X-X partial structure factors (error bars) and minimum noise fit (solid line) and (b) X-X partial pair correlation functions for the methylamine-ammonia liquids.

Figure 7.5 shows the EPSR fit to the experimentally determined partial structure factors. The individual partial pair correlation functions for NA-DA, NM-DN, NA-DN and NM-DA correlations are shown in figure 7.6, and show that both ammonia and the amine group of the methylamine molecules contribute significantly to the hydrogen-bonding present, in liquids of all three methylamine:ammonia ratios. During the EPSR procedure, the coordination numbers for these four correlations were evaluated over the range $r = 1.8 - 2.7$ Å. These are shown in table 7.1.

In addition to the individual partial pair correlation functions, it is also possible to extract the orientational inter-molecular correlations. Figure 7.7 shows the most likely positions of ammonia and methylamine nitrogen atoms around a central solvent molecule of ammonia or methylamine. The hydrogen-bonded lobes of ammonia and methylamine nitrogen atoms around a central ammonia molecule are similar to that observed in pure liquid ammonia, with three hydrogen-bond accepting lobes above the hydrogen atoms, and a trefoil-shaped donor lobe located below. Around a central methylamine molecule, two hydrogen-bond accepting lobes are observed above the hydrogen atoms on the amine group, with an elongated donor lobe opposite the lone pair of electrons on the nitrogen atom.

However, the NA-NM orientational distribution in the 50:50 mixture shows the donor lobe (due to hydrogen bonds between NA and DN) to be relatively smaller than the hydrogen-bond accepting lobes (representing hydrogen bonds between NM and DA). As is to be expected, the reverse picture which shows the NM-NA orientational distribution reveals a relatively larger donor lobe (representing NM-DA hydrogen-bonds) and smaller acceptor lobes (NA-DN hydrogen-bonds). This suggests that methylamine-nitrogen to ammonia-hydrogen atoms (NM-DA

correlations) have a greater contribution to the hydrogen-bonding between the two solvent species than the ammonia-nitrogen to methylamine-hydrogen (NA-DN) correlations. At methylamine:ammonia ratios of 20:80 and 80:20, the number of hydrogen-bonds is determined primarily by the relative concentration of each solvent. This is apparent in table 7.1 which shows the estimated number of hydrogen bonds per nitrogen atom arising from each hydrogen-bonding atom pair.

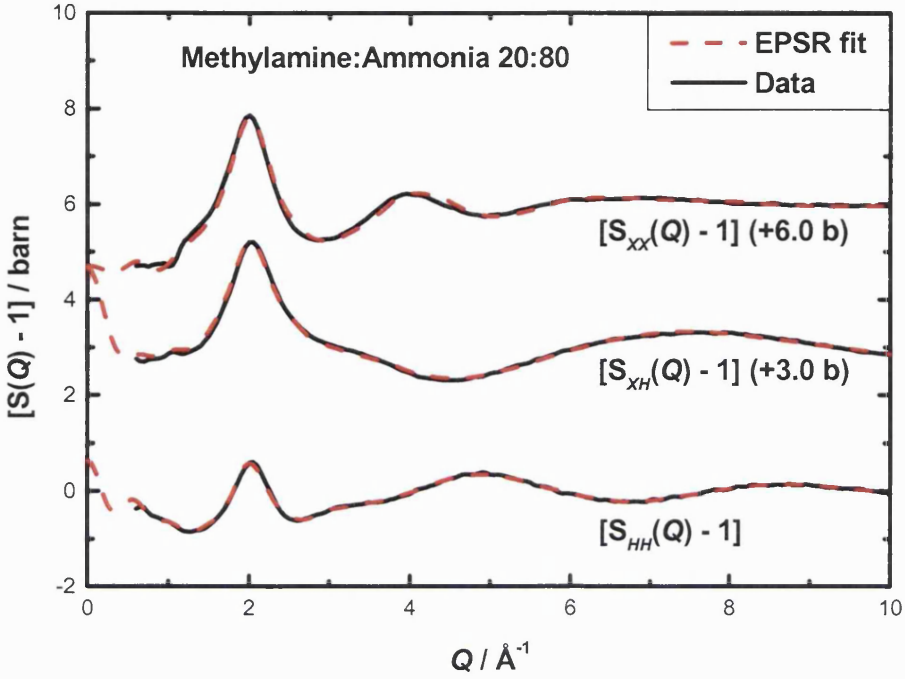
Methylamine:Ammonia 20:80
EPSR fit
Data
[S_XX(Q) - 1] (+6.0 b)
[S_XH(Q) - 1] (+3.0 b)
[S_HH(Q) - 1]
[S(Q) - 1] / barn
Q / Å^-1

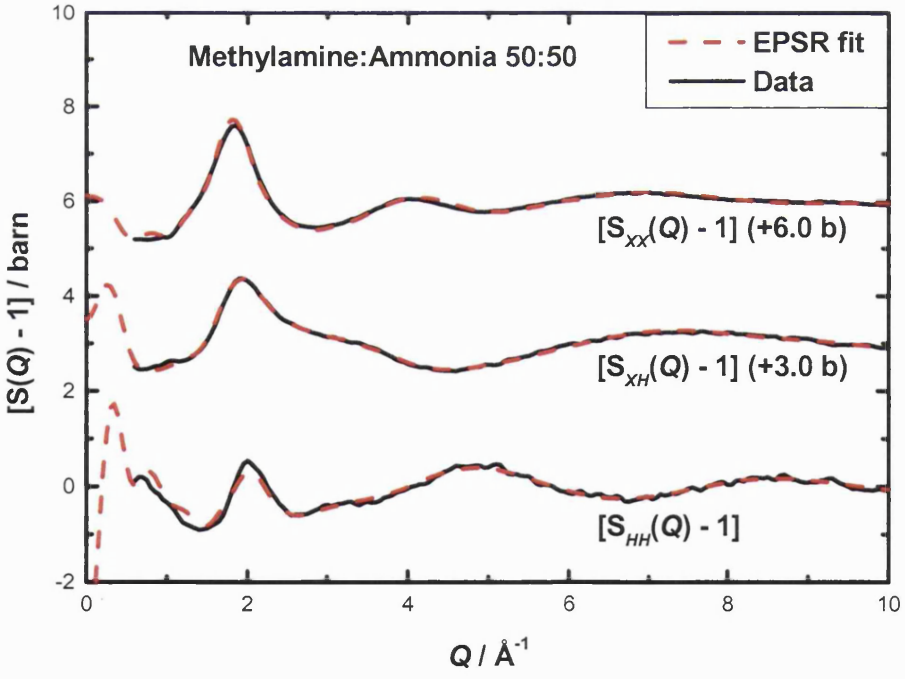
Methylamine:Ammonia 50:50
EPSR fit
Data
[S_XX(Q) - 1] (+6.0 b)
[S_XH(Q) - 1] (+3.0 b)
[S_HH(Q) - 1]
[S(Q) - 1] / barn
Q / Å^-1

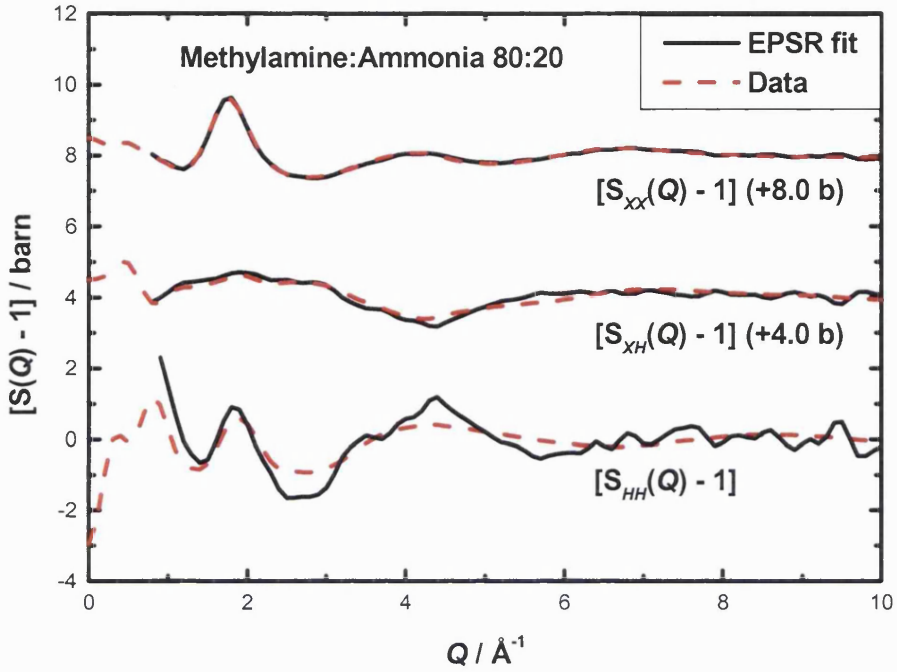

Figure 7.5 EPSR fit to the measured data for the 20:80, 50:50 and 80:20 methylamine:ammonia mixed solvent system. The substituted hydrogen atoms comprised solely those on the ammonia molecules, although in-solution isotopic exchange occurs between the hydrogen atoms on the ammonia molecules and the hydrogen atoms on the amine groups of the methylamine molecules.

N-H correlation	Methylamine:Ammonia ratio		
	20:80	50:50	80:20
NA-DA	1.43 ± 0.05	0.80 ± 0.04	0.58 ± 0.03
NA-DN	0.32 ± 0.02	0.64 ± 0.03	1.19 ± 0.05
NM-DA	0.80 ± 0.03	0.79 ± 0.03	0.25 ± 0.02
NM-DN	0.16 ± 0.01	0.51 ± 0.03	0.63 ± 0.03

Table 7.1 Number of hydrogen bonds per nitrogen atom arising from each hydrogen-bonding atom-pair, evaluated over the range r = 1.8 – 2.7 Å.

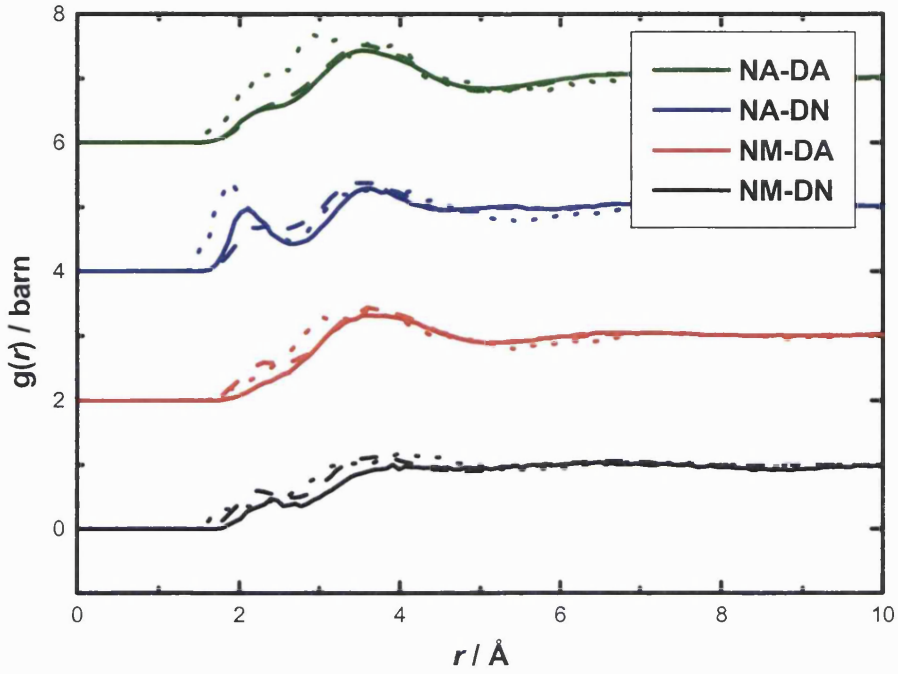

Figure 7.6 Partial pair correlation functions showing the hydrogen-bonding at $r \sim$ 1.8 – 2.7 Å arising from NA-DA, NA-DN, NM-DA and NM-DN correlations. Dotted line: 80:20, dashed line: 50:50 and solid line: 20:80 methylamine:ammonia ratios respectively.

NA-NA, r = 2.2 – 5.0 Å, 20%
Methylamine:Ammonia 20:80

NA-NA, r = 2.2 – 5.0 Å, 20%
Methylamine:Ammonia 50:50

NA-NA, r = 2.2 – 5.0 Å, 20%
Methylamine:Ammonia 80:20

NA-NM, r = 2.2 – 5.0 Å, 20%
Methylamine:Ammonia 20:80

NA-NM, r = 2.2 – 5.0 Å, 20%
Methylamine:Ammonia 50:50

NA-NM, r = 2.2 – 5.0 Å, 20%
Methylamine:Ammonia 80:20

NM-NA, r = 2.2 – 5.0 Å, 15%
Methylamine:Ammonia 20:80

NM-NA, r = 2.2 – 5.0 Å, 15%
Methylamine:Ammonia 50:50

NM-NA, r = 2.2 – 5.0 Å, 15%
Methylamine:Ammonia 80:20

NM-NM, r = 2.2 – 4.0 Å, 20%
Methylamine:Ammonia 20:80

NM-NM, r = 2.2 – 4.0 Å, 20%
Methylamine:Ammonia 50:50

NM-NM, r = 2.2 – 4.0 Å, 20%
Methylamine:Ammonia 80:20

Figure 7.7 Most likely orientational distribution of ammonia or methylamine nitrogen atoms around a central ammonia or methylamine molecule, shown by the yellow-shaded areas.

7.3 Lithium-mixed solvent solutions - introduction

Neutron diffraction experiments have been performed on a saturated solution of lithium-ammonia-methylamine (20 Li - 40 NH_3 - 40 CH_3NH_2). The data have been analysed in conjunction with a three-dimensional simulation technique, in order to probe all atom-atom correlations and molecular orientations. In the saturated solution of lithium-ammonia-methylamine the hydrogen-bonding is completely disrupted as all the solvent molecules are involved in the solvation shells of the lithium cations. The first ionic solvation shell comprises ~2 ammonia and ~2 methylamine molecules; the presence of the methylamine molecules serves to distort the tetrahedral shape of the solvation shell found in lithium-ammonia solutions.

The arrangement of the solvent molecules around the cations has a significant effect on the way the electrons are accommodated in the solution: they have a tendency to reside around the circumference of the ammonia molecules, and opposite the hydrogen atoms on the amine group of the methylamine molecules. Upon decreasing the metal concentration, a large region of liquid-liquid phase separation between metal concentrations of ~2.5 MPM and ~19 MPM was observed for the first time. Given that there is no evidence of molecular segregation within the pure solvent system, it is likely that the observed separation into predominantly lithium-ammonia and lithium-methylamine phases is driven by the electronic species present in solution.

7.3.1 Experimental details

Hydrogen/deuterium isotopic substitution neutron diffraction experiments were performed on a saturated solution of lithium-ammonia-methylamine with a molar ratio of 20:40:40, using the SANDALS beamline[15] at the ISIS Facility, Rutherford Appleton Laboratory. H/D isotopic substitution was performed on (i) the hydrogen atoms on both the ammonia molecules and the amine group of the methylamine molecules, (ii) the hydrogen atoms on the methyl groups of the methylamine molecules, and (iii) the hydrogen atoms on the ammonia molecules and on the amine and methyl groups of the methylamine molecules. These substitutions were chosen in order to maximise the scattering length contrast between each of the samples, since in-solution isotopic exchange had been found to occur between the hydrogen atoms on the amine groups of the methylamine molecules and those on the ammonia molecules. In addition, a first order $^{6}Li/^{nat}Li$ lithium difference was performed. The samples comprised:

(a) $Li\text{-}ND_3/CD_3ND_2$,

(b) $Li\text{-}NH_3/CD_3NH_2$,

(c) $Li\text{-}(NH_3{:}ND_3)_{50:50}/CD_3(NH_2{:}ND_2)_{50:50}$,

(d) $Li\text{-}ND_3/CH_3ND_2$,

(e) $Li\text{-}ND_3/(CD_3{:}CH_3)_{50:50}ND_2$,

(f) $Li\text{-}NH_3/CH_3NH_2$,

(g) $Li\text{-}(NH_3{:}ND_3)_{50:50}/(CD_3{:}CH_3)_{50:50}(ND_2{:}NH_2)_{50:50}$ and

(h) $^{6}Li\text{-}\ ND_3/CD_3ND_2$.

the ammonia:methylamine ratio being 50:50 for each sample studied. Samples (a), (b) and (c) were used to extract the partial structure factors H-H, X-H and X-X, where H represents the substituted hydrogen atoms (i.e: those on the ammonia molecules and the amine groups of the methylamine molecules), and X represents any non-substituted atomic species (including the hydrogen atoms on the methyl groups of the methylamine molecules). Similarly, samples (a), (d) and (e) were used to produce the three partial structure factors where H represents the hydrogen atoms on the methyl groups of the methylamine molecules, and samples (a), (f) and (g) give rise to partial structure factors where H represents the hydrogen atoms on the ammonia molecules and on both the amine group and methyl group of the methylamine molecules. Samples (a) and (h) provide the first-order lithium difference partial structure factor, which yields information concerning the solvation shells of the lithium cation. The three sets of H/D substitution and the lithium difference therefore provide a total of 10 partial structure factors, which act as rigorous constraints for the EPSR simulation.

(a) (b)

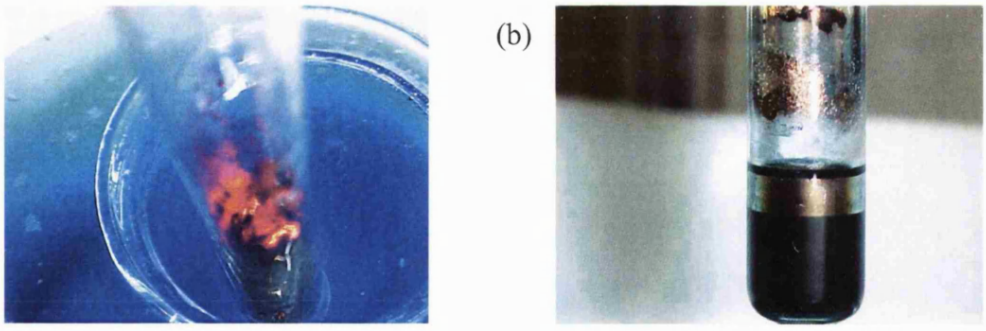

Figure 7.8 (a) The red-gold colour of a saturated lithium-ammonia-methylamine solution (20:40:40 molar ratio), and (b) phase separation occurring as the solution is diluted with methylamine. The lithium-ammonia-methylamine solution is found to be homogeneous at concentrations above ~19 MPM. Phase separation is observed at lower concentrations down to ~2.5 MPM.

The technique normally used to make alkali metal-amine solutions involves condensing a known volume of solvent gas onto lithium metal held at 230 K. In this case, however, the difference in the boiling points of ammonia and methylamine meant that the solvent gases could not be pre-mixed in excess and then condensed, as preferential condensation of methylamine would occur, and the exact composition of the sample under study would be unknown. Instead, the exact volume of solvent gas, in the required proportions, was mixed in a single stainless steel buffer on the gas panel. All of the solvent mixture was then cryopumped onto the sample, held at ~60 K. The valve to the buffer was then closed before the sample was warmed to 240 K (chosen to ensure that the large immiscibility gap, observed upon diluting or cooling the saturated solution, is avoided). During the experiments, the accuracy of the final composition of the sample was checked by comparing the measured scattering level at high-Q with the calculated level.[16] Diffraction patterns were recorded as the sample was warmed to the required temperature, to ensure that the solutions were fully mixed.

7.3.2 Results and discussion - lithium-mixed solvent solutions

The total and partial structure factors, together with the minimum noise fit and corresponding pair correlation functions for the saturated lithium-ammonia-methylamine solution are shown in figures 7.9 – 7.13. The minimum noise fit to both the total and partial structure factors is good, and integration of the intra-molecular peaks gives the expected co-ordination numbers.

The principal peak position shifts to a lower Q-value of 1.75 $Å^{-1}$, as compared to 1.92 $Å^{-1}$ in the pure mixed solvent liquid with a methylamine:ammonia ratio of 50:50, as the solvent expands to accommodate the excess electrons. This value is between that of saturated lithium-ammonia and saturated lithium-methylamine (1.85 $Å^{-1}$ and 1.60 $Å^{-1}$ respectively[12,14]), indicating that the solution is a homogeneous mixture of the two types of solvent molecule. Furthermore, the pre-peak at 0.97 $Å^{-1}$ (which survives in almost all the partial structure factors) indicates that the intermediate range ordering in the saturated solution is caused by correlations between the host solvent molecules at a distance of $2\pi / k \approx 6.5$ Å with a coherence length of $2\pi / \Delta k \approx 26$ Å. This feature has also been observed in saturated lithium-ammonia and saturated lithium-methylamine solutions, at 1.01 $Å^{-1}$ and 0.88 $Å^{-1}$ respectively.[12,14]

These pre-peaks have been attributed to correlations between solvated cations, which have a smaller radius in ammonia solutions than in methylamine.[14] The position of the first sharp diffraction peak for the lithium-mixed solvent solution lies between the values for lithium-ammonia and lithium-methylamine solutions, indicating that the average solvated cation size is in-between that for lithium-ammonia and lithium-methylamine. The Fourier transform of the first order lithium difference partial structure factor is consistent with an ion solvation shell of four solvent molecules, comprising on average, two methylamine and two ammonia molecules.

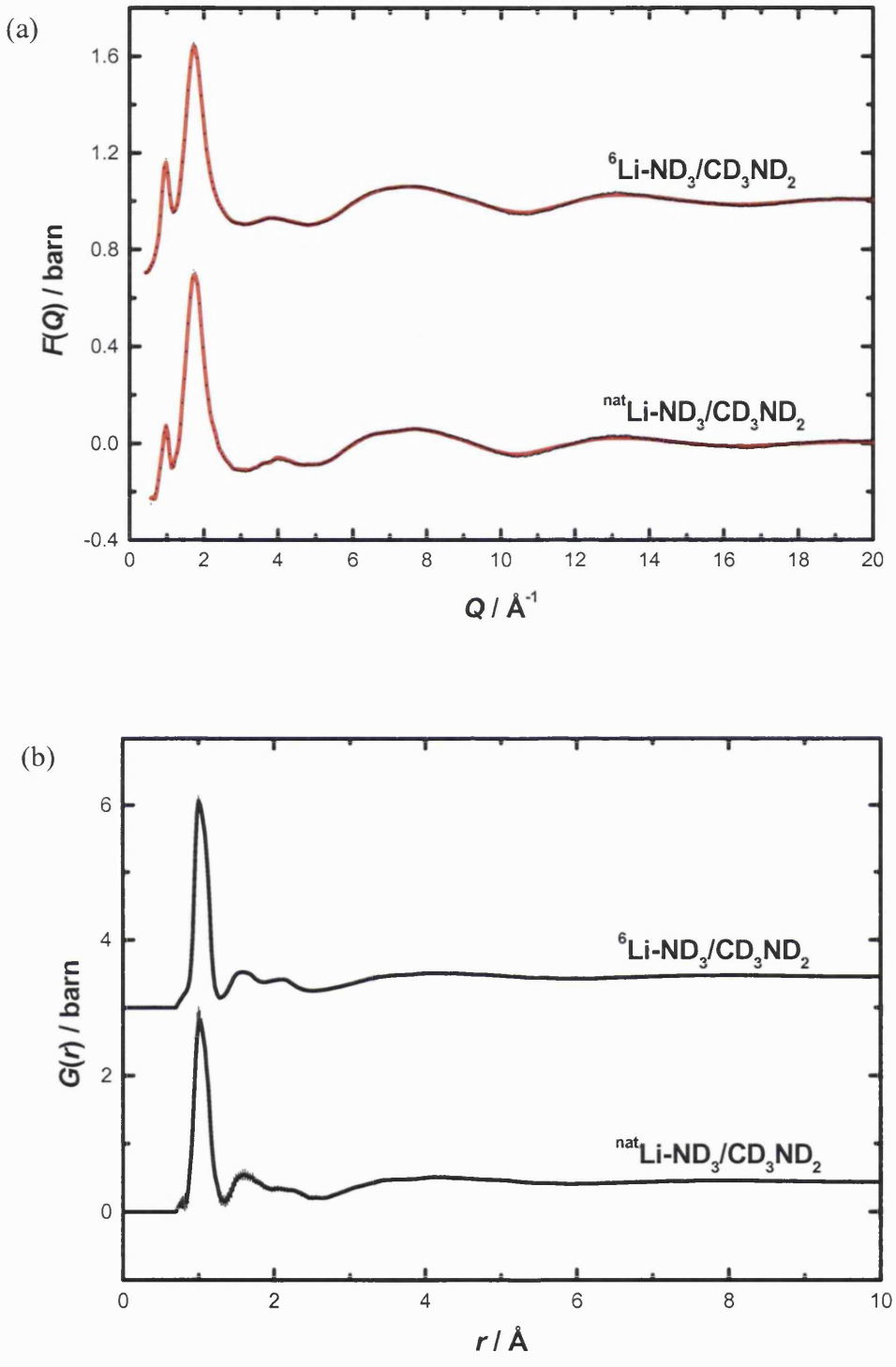

Figure 7.9 (a) Total structure factors (error bars) and minimum noise fit (solid line) and (b) total pair correlation functions for the deuterated lithium-ammonia-methylamine samples at 20 MPM.

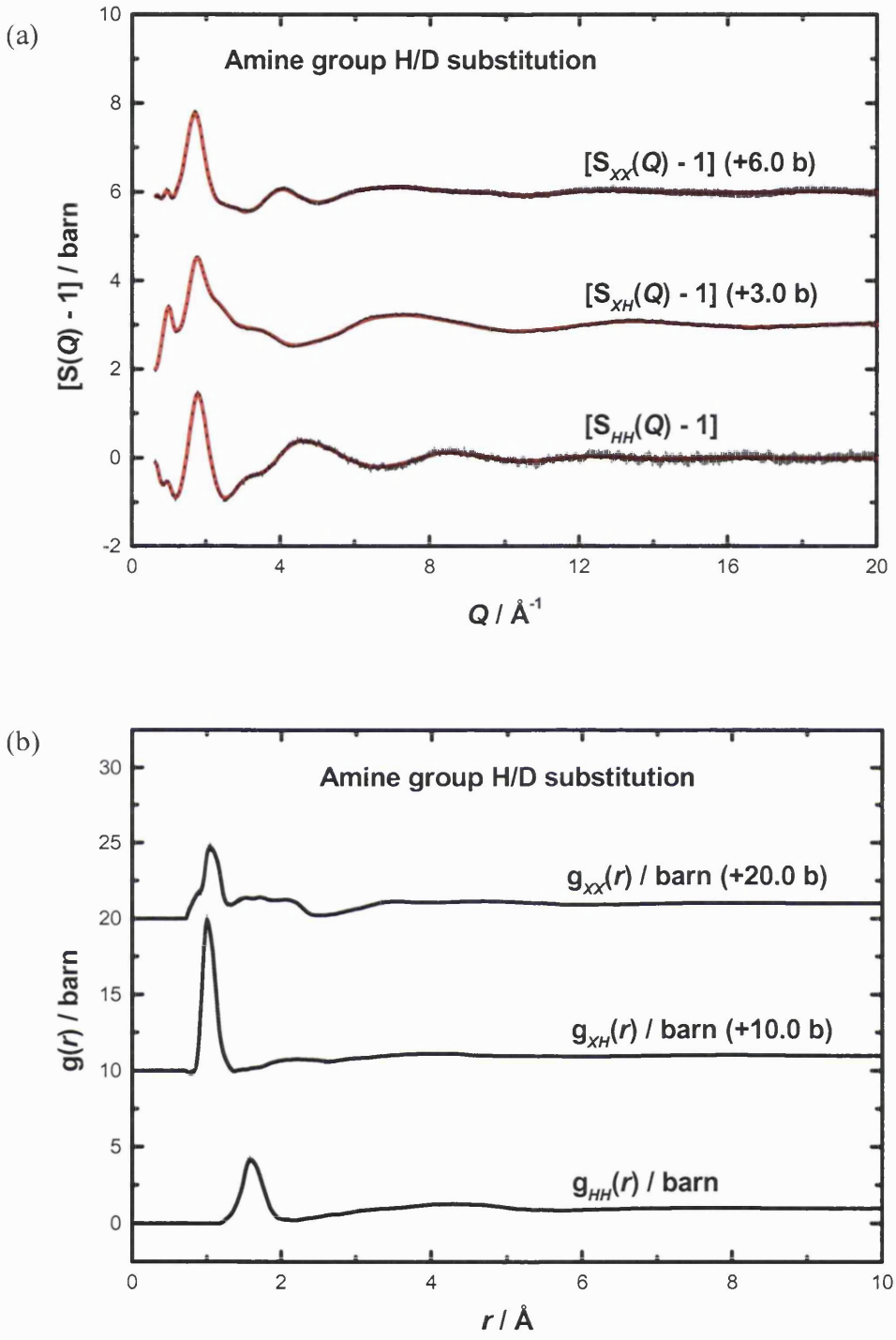

Figure 7.10 (a) Partial structure factors (error bars) and minimum noise fit (solid line) and (b) partial pair correlation functions for the 20 MPM lithium-ammonia-methylamine solution. The substituted hydrogen atoms comprise those on the ammonia molecules and those on the amine group of the methylamine molecules.

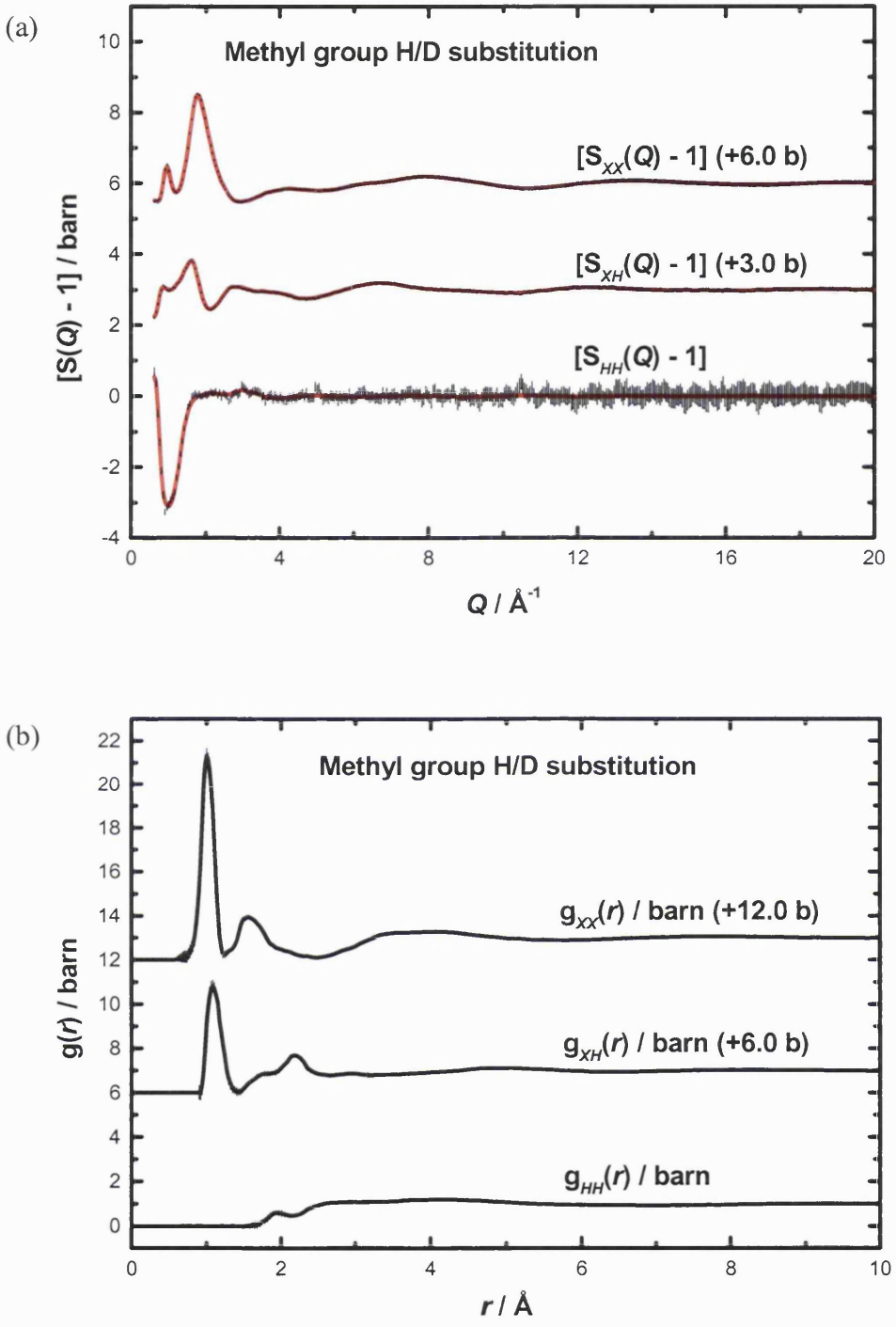

Figure 7.11 (a) Partial structure factors (error bars) and minimum noise fit (solid line) and (b) partial pair correlation functions for the 20 MPM lithium-ammonia-methylamine solution. The substituted hydrogen atoms comprise those on the methyl group of the methylamine molecules.

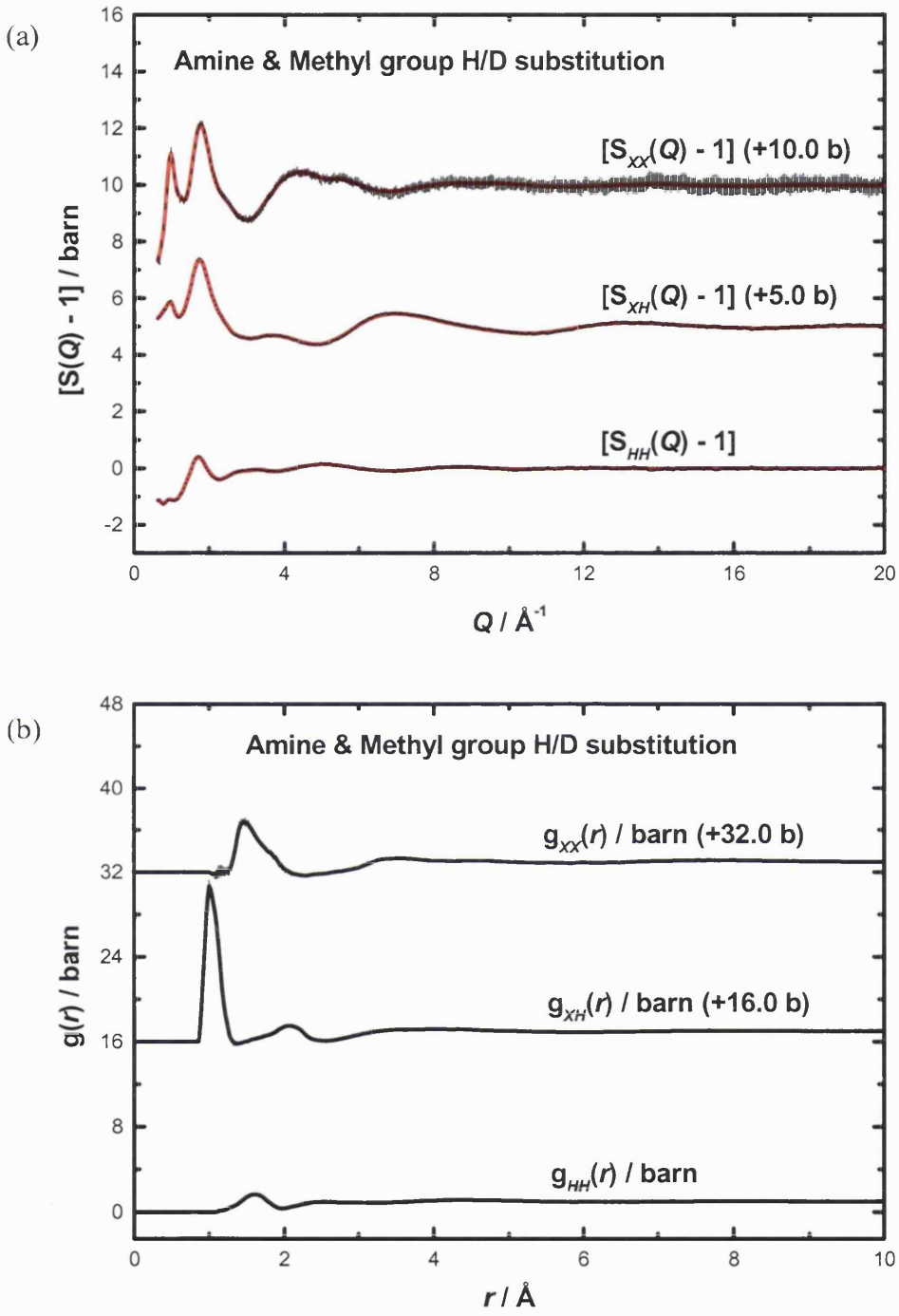

Figure 7.12 (a) Partial structure factors (error bars) and minimum noise fit (solid line) and (b) partial pair correlation functions for the 20 MPM lithium-ammonia-methylamine solution. The substituted hydrogen atoms comprise those on the ammonia molecules and those on the amine and methyl groups of the methylamine molecules.

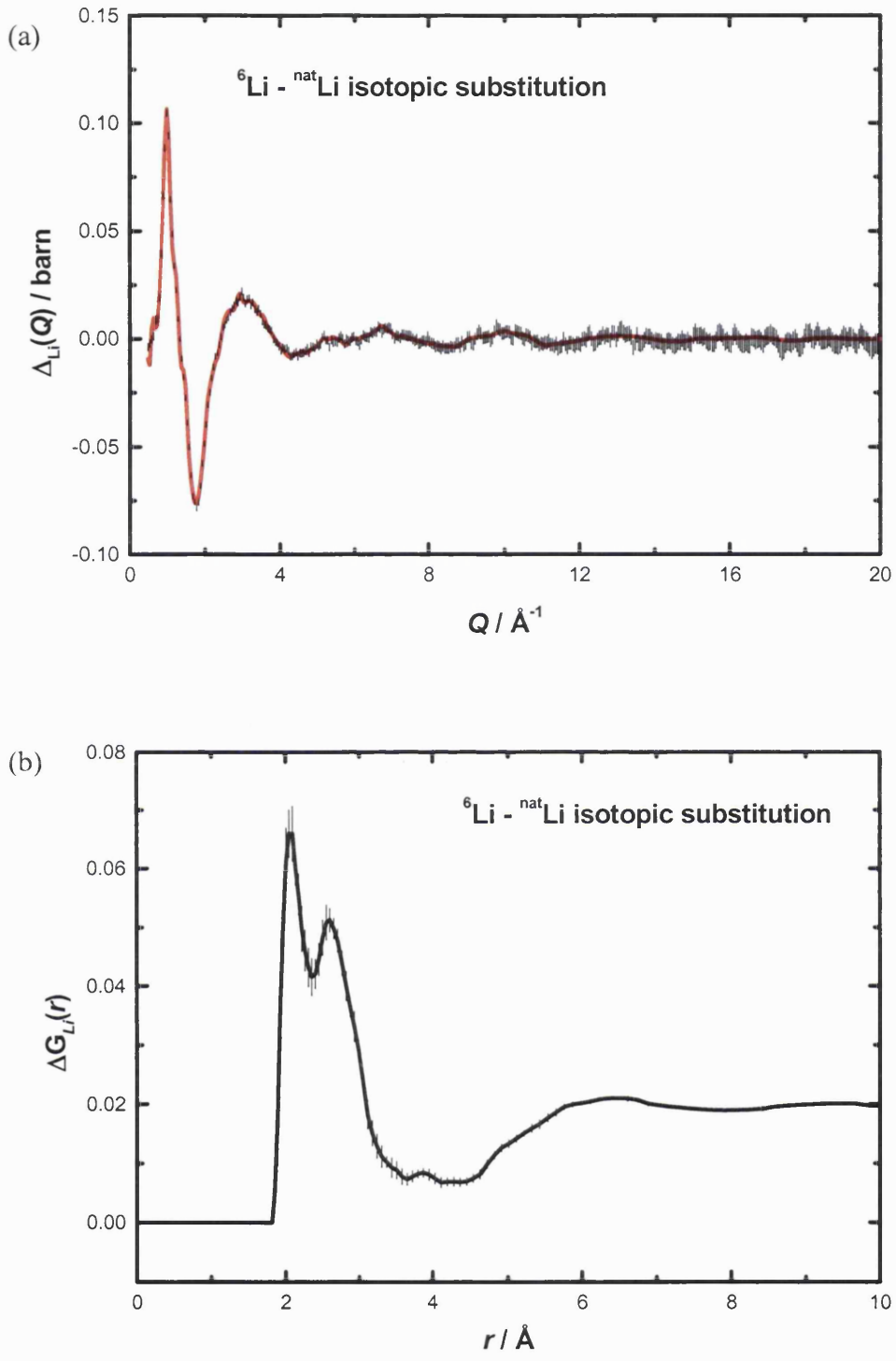

Figure 7.13 First order lithium difference data: (a) Partial structure factor (error bars) and minimum noise fit (solid line) and (b) partial pair correlation function for the 20 MPM lithium-ammonia-methylamine solution.

Figure 7.14 shows the EPSR fits to the experimentally determined partial structure factors. The partial pair correlation functions for NA-DA, NA-DN, NM-DA and NM-DN in the saturated lithium-ammonia-methylamine solution are shown in figure 7.15, together with the equivalent pair correlation functions in the mixed solvent liquid with a methylamine:ammonia ratio of 50:50. It is immediately apparent that the hydrogen-bonding present in the mixed solvent liquids is completely disrupted at saturation, as all the ammonia molecules and amine groups of the methylamine molecules are involved in solvating the cations.

In figure 7.16, the individual solvent-solvent pair correlation functions are presented, and are again compared with the equivalent pair correlation functions in the mixed solvent liquid of 50:50 methylamine:ammonia ratio. The correlations involving only atom species on the methylamine molecules show an increase in the peak position for the first shell, which is associated with the reduction in solvent density as the excess electrons are accommodated. However, the NA-NA partial pair correlation function shows a shift *inwards* of the nearest neighbour peak position to 3.2 Å, suggesting a 'tighter binding' between the ammonia molecules involved in the cation solvation shells than that existing between the ammonia molecules in the mixed solvent liquid. This is similar to the trend found in lithium-ammonia solutions as the concentration of metal is increased.[12,16] In the lithium-mixed solvent solution, however, the NA-NA distance of ~3.2 Å is smaller than the NA-NA distance of 3.42 Å[12,16] in the saturated lithium-ammonia solution. The presence of the methylamine molecules therefore serves to distort the tetrahedral shape of the primary ionic solvation shell observed in lithium-ammonia solutions.

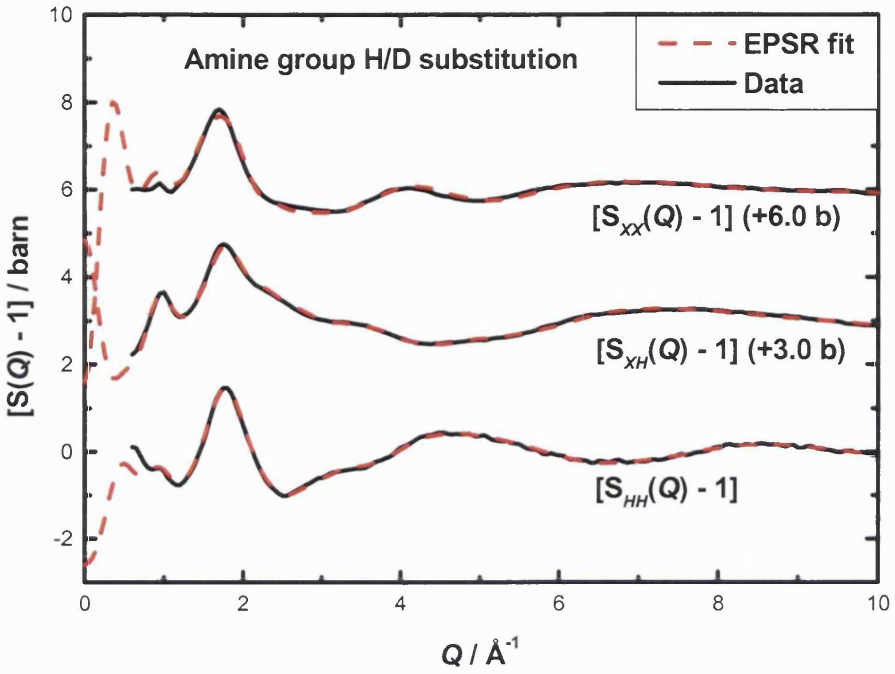
Amine group H/D substitution
EPSR fit
Data
[S_XX(Q) - 1] (+6.0 b)
[S_XH(Q) - 1] (+3.0 b)
[S_HH(Q) - 1]
[S(Q) - 1] / barn
Q / Å^-1

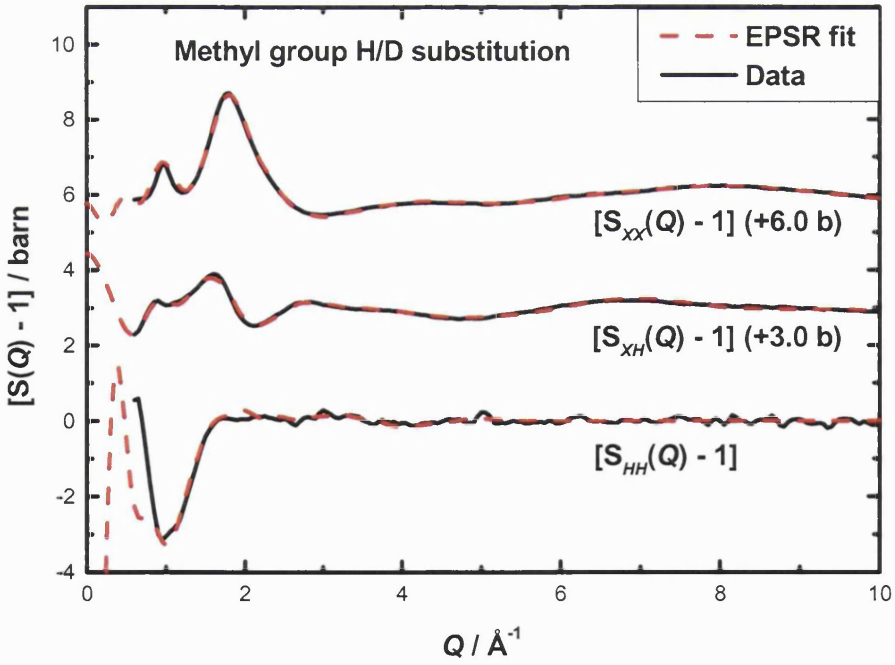
Methyl group H/D substitution
EPSR fit
Data
[S_XX(Q) - 1] (+6.0 b)
[S_XH(Q) - 1] (+3.0 b)
[S_HH(Q) - 1]
[S(Q) - 1] / barn
Q / Å^-1

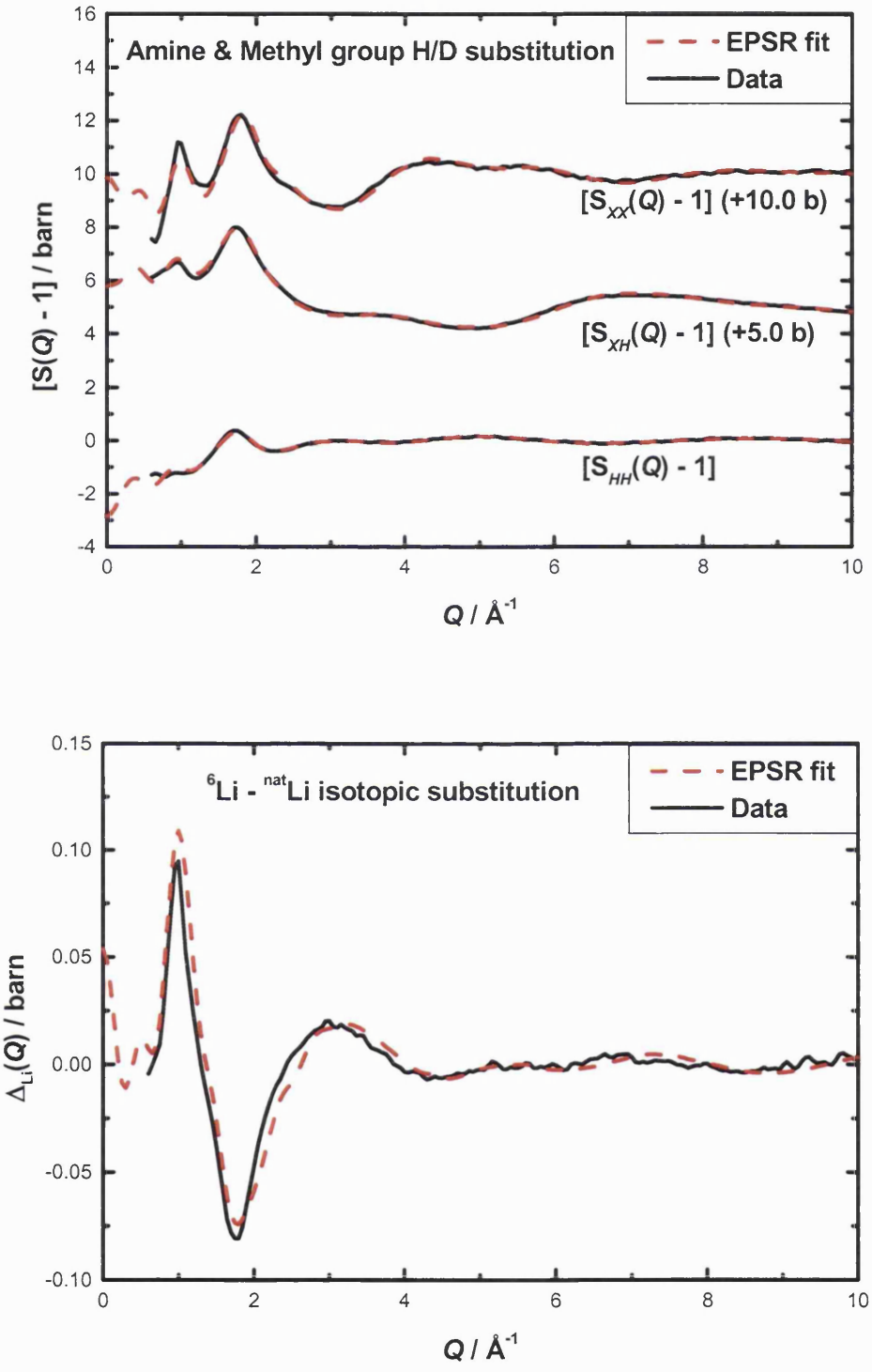

Figure 7.14 EPSR fits to the measured data for the saturated lithium-ammonia-methylamine solution.

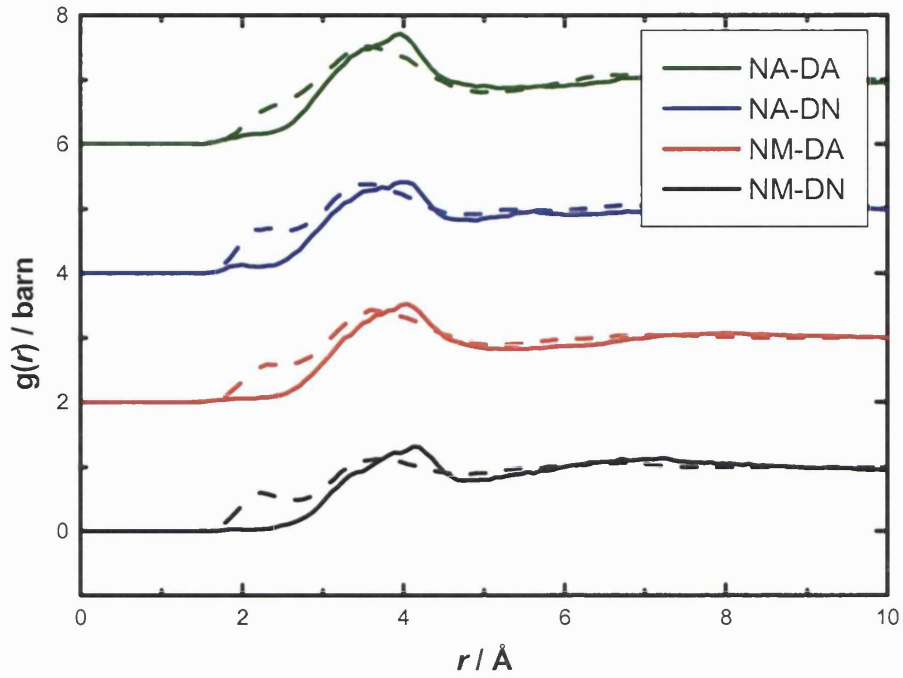

Figure 7.15 Amine group correlations: solid line: 20 MPM lithium-ammonia-methylamine, dashed line: 0 MPM ammonia-methylamine with molar ratio 50:50.

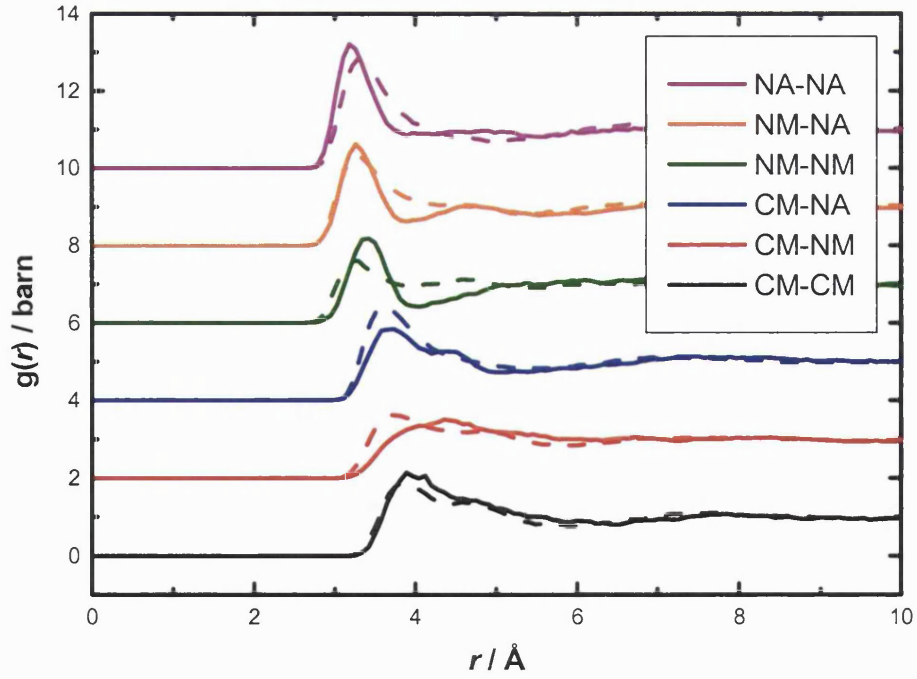

Figure 7.16 Solvent-solvent correlations: solid line: 20 MPM lithium-ammonia-methylamine, dashed line: 0 MPM ammonia-methylamine with molar ratio 50:50.

7.3.2.1 Cation solvation in mixed solvent solutions

Figure 7.17 shows the real-space distribution of solvent molecules around the lithium ions. The Li-NM and Li-NA distance is ~2.0 Å, in agreement with that observed in saturated lithium-ammonia and lithium-methylamine solutions.[12,17-20] Integration of the first ionic solvation shell gives co-ordination numbers of 1.78 and 1.63 for Li-NM and Li-NA respectively. The resulting 3-D configuration obtained via EPSR (figure 7.18) shows that in general, there are two ammonia molecules and two methylamine molecules in each ion's primary solvation shell.

In order to investigate the orientational distribution of solvent molecules around the ion, axes have been assigned to the lithium cation such that the first Li-N bond defines the *z*-axis, and the next Li-N bond lies in the *x*-*z* plane. Figures 7.19 and 7.20 show the distorted tetrahedral first ionic solvation shell, and the tendency of the solvent molecules in the second solvation shell to reside above the faces and edges of the primary shell tetrahedron. Again, this is similar to the arrangement of solvent molecules relative to the ion in lithium-ammonia solutions throughout the concentration range.

It is also possible to plot the orientation of solvent molecules in the first ionic solvation shell: figure 7.21(a) shows that the dipole moment of a nearest neighbour ammonia molecule is directed away from the cation. The methylamine molecules, however, are oriented at an angle of Li-NM-CM ~ 109°, (figure 7.21(b)) such that the dipole moment of the amine group is not pointing directly away from the cation.

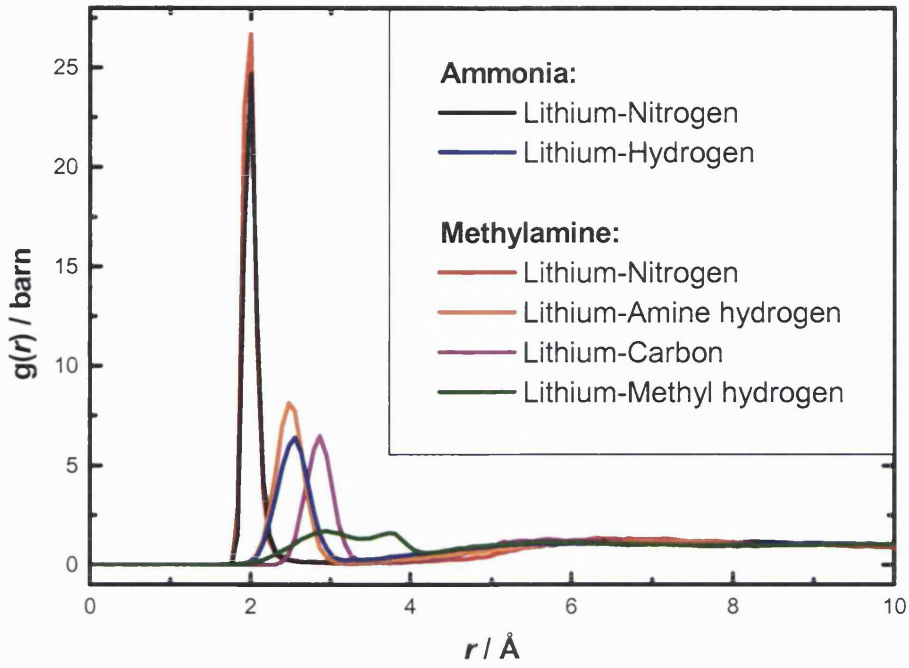

Figure 7.17 Lithium-centred partial pair correlation functions, obtained from the EPSR configuration.

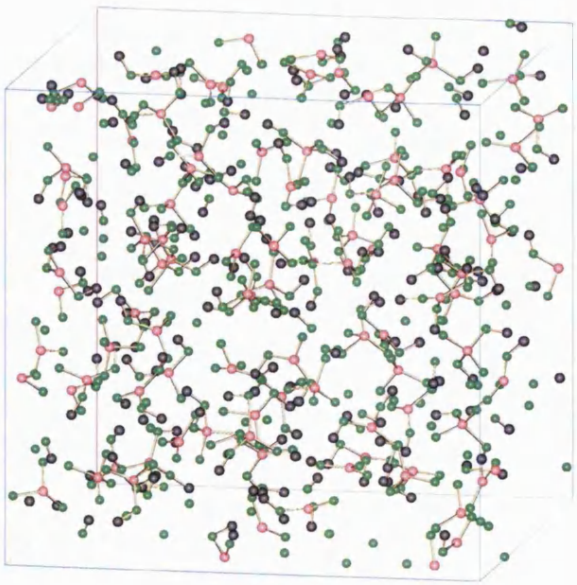

Figure 7.18 The EPSR three-dimensional configuration of the saturated lithium-ammonia-methylamine solution (molar ratio 20:40:40). Carbon atoms: grey, nitrogen atoms: green, lithium ions: red.

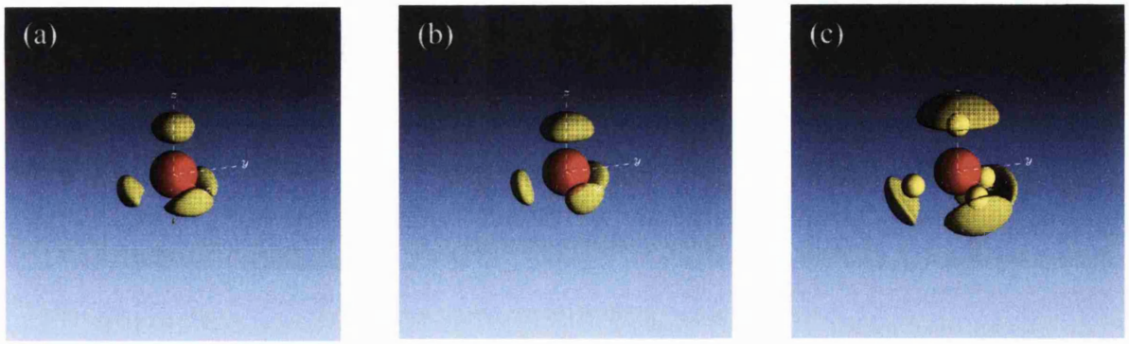

Li-NA, r = 1.5-2.5 Å, 80% Li-NM, r = 1.5-2.5 Å, 80% Li-CM, r = 2.0-3.5 Å, 50%

Figure 7.19 The tetrahedral first ionic solvation shell: (a) Li-NA, (b) Li-NM and (c) Li-NM+CM correlations.

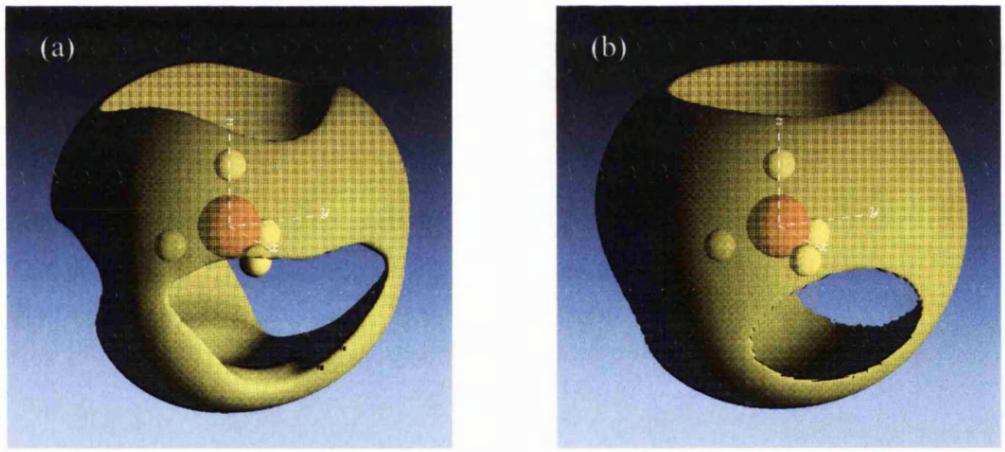

Li-NA, r = 2.5-6.0 Å, 50% Li-NM, r = 2.5-6.0 Å, 50%

Figure 7.20 The distribution of solvent molecules in the second ion solvation shell relative to the first shell: (a) lithium-ammonia nitrogen correlations and (b) lithium-methylamine nitrogen correlations.

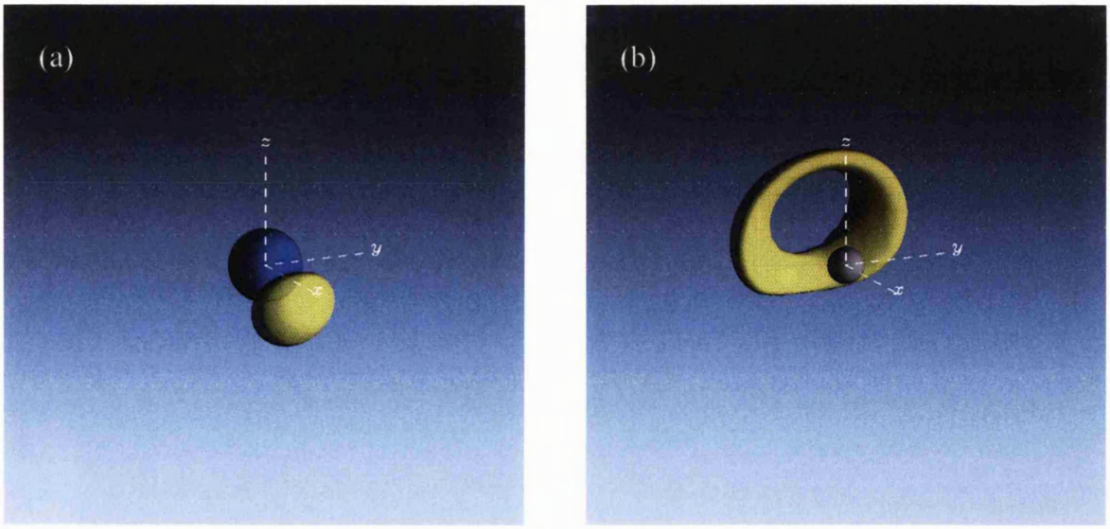

Li-ammonia dipole orientation,
r = 1.5-2.5 Å, 60%

Li-methylamine (CM-NM axis) orientation,
r = 2.0-3.5 Å, 50%

Figure 7.21 (a) the dipole orientation of ammonia molecules, and (b) the orientation of the CM-NM axis of the methylamine molecules in the first ionic solvation shell, relative to the lithium ion. The dipoles of the ammonia molecules are pointing directly away from the cation, while the CM-NM axis of the methylamine molecule is not parallel to the Li-CM direction.

7.3.2.2 Electron accommodation in lithium-mixed solvent solutions

Such an arrangement of solvent molecules relative to the ion will have a significant effect on the way in which the excess electrons are accommodated in the solution. In saturated lithium-ammonia solutions, continuous electron channels are formed between the solvated cation species, giving rise to the highly conducting metallic state.[12] Saturated lithium-methylamine solutions, on the other hand, have a conductivity which is just above the minimum for metallic behaviour. They are blue

in colour, the signature of solvated electrons, and conduction arises by hopping of electrons between neighbouring cavities, which have a mean separation of ~7Å.[17] Here, since the amine groups on the methylamine molecules are involved in ion solvation, it has been suggested that the methyl groups play an essential role in electron solvation.[17]

The saturated mixed-solvent solution is red-gold in colour and metallic, and lies on the threshold of homogeneity. A small decrease in metal concentration leads to a phase separated solution: in the more dense phase, the electrons are fully solvated, giving rise to the dark-blue colouration, and in the less dense phase, the electrons are delocalised, giving a gold-coloured metallic liquid.

In order to envisage the distribution of polaronic electron cavities relative to the solvent molecules, the resulting EPSR configuration has been analysed for spherical voids of ~5Å diameter. The most likely orientational distribution of the voids has been plotted relative to an ammonia molecule and a methylamine molecule in figure 7.22. The electron cavity distribution around an ammonia molecule is vastly different from that in saturated lithium-ammonia solutions: here the electrons tend to reside closer to the lithium ion, around the circumference of the ammonia molecule, rather than above the hydrogen atoms as in the saturated lithium-ammonia solution. The electron distribution relative to the methylamine molecules is opposite the hydrogen atoms on the amine group, approximately 5Å from the lithium ion.

7.3.2.3 Phase separation in lithium-mixed solvent solutions

Stupak, Golden and Tuttle have suggested a 'two-absorber model' to account for the observed absorption spectrum in dilute lithium-ammonia-methylamine solutions, which states that the electrons can be solvated by either ammonia or methylamine molecules, but not a mixture of the two.[21] Given such a model, and the fact that the phase separation region is much larger than that for the lithium-ammonia solution, it is possible that the initially homogeneous solution will tend towards two phases: one predominantly lithium-ammonia, containing delocalised electron channels which are shielded from the lithium ions by hydrogen atoms on ammonia molecules, and the other predominantly lithium-methylamine, where the electrons are fully solvated by the larger methylamine molecules. The phase-separation is therefore likely to be electron-driven: no evidence of microsegregation of ammonia and methylamine is observed in the pure mixed solvent liquids.

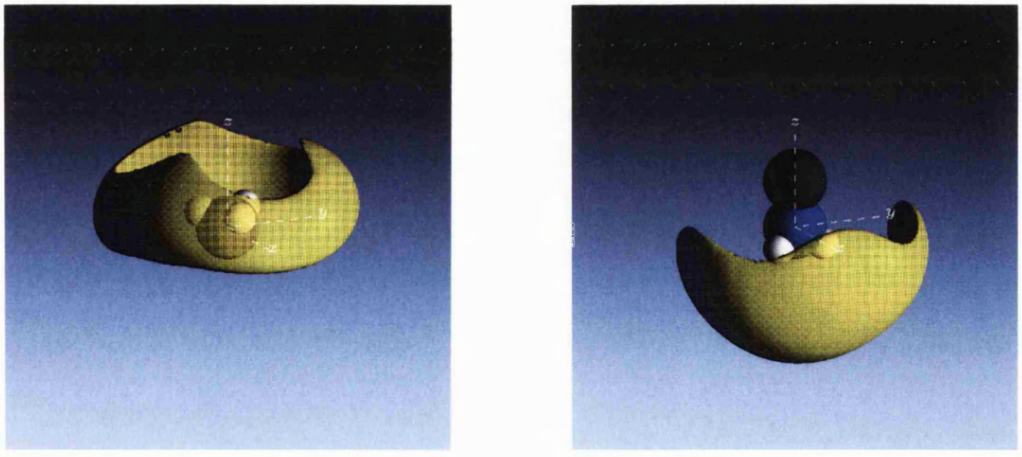

NA-void, r = 2.4-5.4 Å, 10% NM-void, r = 2.4-5.4 Å, 20%

Figure 7.22 The most likely orientational distribution of polaronic electron cavities relative to (a) an ammonia molecule and (b) a methylamine molecule.

7.4 References

[1] J. C. Thompson, *Electrons in Liquid Ammonia* (Clarendon, Oxford 1976).

[2] S. Dixit, J. Crain, W. C. K. Poon, J. L. Finney and A. K. Soper, Nature, **416,** 829 (2002).

[3] J. Jortner, J. Chem. Phys. **30**, 839 (1959).

[4] N. F. Mott, Adv. Phys. **16**, 49, (1967).

[5] M. H. Cohen, J. C. Thompson, Adv. Phys. **17**, 857 (1968).

[6] R. Catterall, N. F. Mott, Adv. Phys. **18**, 605 (1969).

[7] *CRC Handbook of Chemistry and Physics*, ed. D. R. Lide (CRC Press, Inc. 1994).

[8] A. K. Soper, Chem. Phys. **202**, 295 (1996).

[9] A. K. Soper, Chem. Phys. **258**, 121 (2000).

[10] A. K. Soper, Mol. Phys. **99**, 1503 (2001).

[11] A. K. Soper and D. T. Bowron, *EPSR – A User's Guide* (2000).

[12] H. Thompson, J. C. Wasse, N. T. Skipper, S. Hayama, D. T. Bowron and A. K. Soper, J. Am. Chem. Soc. **125**, 2572 (2003).

[13] M. A. Ricci, M. Nardone, F. P. Ricci, C. Andreani, A. K. Soper, J. Chem. Phys. **102**, 7650 (1995).

[14] S. Hayama, J. C. Wasse, N. T. Skipper, J. K. Walters, Mol. Phys. **99**, 779 (2001).

[15] C. Benmore and A. K. Soper, The SANDALS Manual, Rutherford Appleton Laboratory Technical Report (RAL-TR-98-006, 1998).

[16] S. Hayama, J. C. Wasse, N. T. Skipper and H. Thompson, J. Chem. Phys. **116**, 2991 (2002).

[17] S. Hayama, J. C. Wasse, N. T. Skipper, J. Phys. Chem. B. **106**, 11 (2002).

[18] J. C. Wasse, S. Hayama, S. Masmanidis, S. L. Stebbings and N. T. Skipper, J. Chem. Phys. **118,** 7486 (2003).

[19] J. C. Wasse, S. Hayama, N. T. Skipper and H. E. Fischer, Phys. Rev. B. **61**, 11993 (2000).

[20] J. C. Wasse, S. Hayama, N. T. Skipper, C. J. Benmore and A. K. Soper, J. Chem. Phys. **112**, 7147 (2000).

[21] C. M. Stupak, T. R. Tuttle, Jr. and S. Golden, J. Phys. Chem. **88**, 3804 (1984).

CHAPTER 8

SUMMARY OF CONCLUSIONS AND FUTURE WORK

8.1 Structure of alkali metal-amine solutions

The structure of lithium-ammonia solutions and lithium-ammonia-methylamine solutions has been investigated via the method of isotopic substitution in neutron diffraction. The data have been analysed in conjunction with two classical simulation techniques: reverse Monte Carlo and Empirical Potential Structure Refinement. These techniques have enabled me to construct three-dimensional models which are consistent with the experimental data, such that orientational correlations between molecules and the way in which excess electrons are accommodated in the solution can be investigated. This method has provided further insight into the role of the electron in the structure of the solutions, in addition to an understanding of how the macroscopic properties relate to the microscopic structure. The main conclusions are outlined below.

8.1.1 Hydrogen-bonding and its disruption

The degree of hydrogen-bonding in ammonia and lithium-ammonia solutions has been found to decrease rapidly with increasing metal concentration, such that no trace of hydrogen-bonding remains at saturation.[1] This disruption to the hydrogen-bonding is caused by both ion *and* electron solvation, and it is the subtle balance between hydrogen-bonding within the solvent and the solvation of ionic and electronic species which determines the structure of the lithium-ammonia solutions across the metal-nonmetal transition.

Via EPSR modelling, it has been shown that the directionality of the hydrogen bonds is reminiscent of that in solid ammonia,[2] with three hydrogen-bond accepting lobes above each of the hydrogen atoms on the reference molecule, and a trefoil-shaped donor lobe located below.

In the mixed solvent liquids, experimental data alone is unable to resolve which head groups are mainly responsible for the hydrogen-bonding. However, EPSR simulations of the systems show a clear tendency for the hydrogen-bonding to take place between the ammonia molecules and the amine groups of the methylamine molecules.

8.1.2 Cation solvation and cation-cation structure

For both the lithium-ammonia solutions[3] and lithium-ammonia-methylamine solutions, a second ionic solvation shell has been observed. Via RMC and EPSR modelling, we see a preference for the second shell solvent molecules to reside above the faces and edges of the primary shell tetrahedron.[1] In the saturated solutions, as all the solvent molecules are involved in the primary ionic solvation shell, any second shell must be formed by ammonia molecules in the primary solvation shell of neighbouring ions. This then gives rise to the intermediate range ordering observed in the solutions.

8.1.3 Percolation channels in lithium-ammonia solutions

The H/D isotopic substitution experiments on ammonia and lithium-ammonia solutions showed a slight decrease in the nearest-neighbour N-N distance with increasing metal concentration which is contrary to the density decrease as excess electrons are accommodated in the solution. This suggests that electronic cavities are formed *between* the solvated cation species. Although the electrons themselves are not visible directly via neutron diffraction, the models resulting from the RMC and EPSR simulations of the data can be used to map out the distribution of polaronic voids in lithium-ammonia solutions. In these three-dimensional configurations, regions of lower and higher atomic density are clearly observed, to allow percolation of the dissociated electrons, leading to the formation of the highly conducting metallic state.[1]

8.1.4 Electron solvation/delocalization

The mechanism of electron solvation/delocalization in lithium-ammonia solutions has also been investigated using the spherical harmonic expansion of the partial pair correlation functions. The EPSR simulations reveal a significant change in the orientation of the ammonia molecules relative to the void across the metal-nonmetal transition. This is associated with the reduction in the number of solvent molecules available for electron solvation,[4] which in turn leads to the delocalization of the electron at concentrations above 4 MPM.

8.1.5 Electron accommodation in lithium-methylamine-ammonia solutions

Diffraction measurements and EPSR simulations were performed on a saturated solution of lithium in a 50:50 mixture of ammonia and methylamine, showing the concentrated solution to be fully homogeneous. The ions were found to be solvated by two ammonia molecules and two methylamine molecules on average, and the orientation of the ammonia molecules relative to the ion was found to be similar to the saturated lithium-ammonia solutions.

However, there is a significant change in the way in which the excess electrons are accommodated in the mixed solvent solution. The polaronic voids have a tendency to reside around the circumference of the ammonia molecules and above the amine group of the methylamine molecules. The voids are therefore not outside the ion's solvation shell: this perhaps signals a change in the conduction mechanism,

from itinerant electron percolation in lithium-ammonia solutions to the hopping mechanism in lithium-methylamine solutions.

8.1.6 Phase separation in lithium-mixed solvent solutions

In preliminary experiments on lithium-mixed solvent solutions, a large region of liquid-liquid phase separation was observed between metal concentrations of ~2.5 MPM and ~19 MPM at 240 K. There is no evidence for preferential solvation of the lithium ions by either ammonia or methylamine molecules. However, Stupak, Tuttle and Golden have suggested a 'two-absorber model' to account for the absorption spectrum of solvated electrons in dilute lithium-ammonia-methylamine solutions.[5] This model states that the electrons can be solvated by either ammonia or methylamine molecules, but not a mixture. This is a possible explanation for the new observation of metal-insulator phase separation at higher metal concentrations, in which the blue phase is predominantly methylamine molecules which solvate the excess electrons, and the metallic phase comprises mainly ammonia molecules and delocalized electrons.

8.2 Dynamics of lithium-ammonia solutions

The dynamics of lithium-ammonia solutions have been investigated over a range of metal concentrations and temperatures, via quasi-elastic neutron scattering and molecular dynamics simulation. The conclusions are summarized as follows:

8.2.1 Solid lithium-ammonia compounds

In the 20 MPM lithium-ammonia compounds at 40 K and 75 K, QENS experiments revealed a rotation of the ammonia molecules. This rotation is faster than that observed in solid ammonia, due to the lower density and the fact that the hydrogen-bonding is completely disrupted in the saturated compound. The lithium-ammonia compound at 85 K, which was predicted to be a cubic crystalline phase, was found to be a supercooled liquid, exhibiting a slow diffusion of the ammonia molecules.

8.2.2 Diffusion in lithium-ammonia solutions

For the lithium-ammonia liquids at 230 K, the QENS experiments showed an increase in the proton diffusion rate with increasing metal concentration up to 12 MPM, which is due to the density decrease and reduction in the degree of hydrogen-bonding between the solvent molecules. Beyond this concentration, the majority of ammonia molecules are involved in ion solvation, and so the diffusion process is impeded by the increased mass of the Li-$(NH_3)_4$ species.[6]

8.2.3 Influence of the electrons on the dynamics

The diffusion coefficients obtained from the MD simulations show a similar trend to those measured via QENS. However, for the 4 MPM lithium-ammonia solution which marks the metal-nonmetal transition region, there is a discrepancy between

the simulated and measured diffusion rates. In the MD simulation, the electrons are not explicitly included, and the diffusion rate is high due to the decreased solution density. This immediately suggests that the solvation of electrons is the cause of the lower measured diffusion rate in the region of the metal-nonmetal transition.

8.3 Future Work

8.3.1 Lithium-mixed solvent solutions

There are several metal-amine systems which would benefit from further study using neutron scattering, X-ray diffraction and various complementary techniques. The first of these is the lithium-mixed solvent system. Unlike lithium-ammonia solutions, there is a shortage of information regarding the macroscopic properties of mixed solvent solutions, despite their importance in determining the role of the solvent polarisability in metal-amine solutions. Particular areas which are not yet fully understood include the phenomenon of liquid-liquid phase separation and the molecular dynamics of lithium-ammonia-methylamine solutions.

- Neutron or X-ray diffraction should be used to determine the microscopic structure of each of the phases of the lithium-ammonia-methylamine solutions in the intermediate concentration range (2 – 18 MPM). This could be compared with data on both lithium-ammonia and lithium-methylamine solutions, and indicate whether each phase could indeed be composed of predominantly one type of solvent molecule.

- Chemical shifts, as investigated via nuclear magnetic resonance (NMR), could be used to determine the onset of phase separation. Additionally, both NMR and electron spin resonance (ESR) techniques could be used to investigate the electronic state of each phase.

- Conductivity measurements should be used to map out the phase diagram of the mixed solvent system. The conductivity of each of the phases could be compared with those of lithium-ammonia and lithium-methylamine solutions, in order to test the hypothesis regarding the cause of the observed phase separation. Similar measurements on the 20 MPM homogeneous lithium-mixed solvent solution may also provide further insight into the conduction mechanism.

- The method of isotopic substitution could be used in QENS to label the methyl groups of the methylamine molecules in a mixed solvent system, to observe directly the effect of electron solvation on the molecules' dynamics. QENS experiments should also be performed on the pure methylamine solvent and lithium-methylamine solutions, to observe the influence of electron localization and ion solvation on the dynamics of a solvent with a lower dielectric constant.

- The application of pressure to alkali metal-mixed solvent solutions may induce a metal-nonmetal transition and change the concentration at which the solution phase separates. The effect of pressure will be crucial to our future understanding of the mechanisms behind the metal-nonmetal transition.

8.3.2 Quenched metal-amine solutions

The glasses formed by quenching metal-amine solutions have also generated a great deal of interest. The structure of a glass is disordered, much like that of a liquid: the essential difference is in the rapid slowing down of molecular motion that accompanies the liquid-glass transition. The work performed on the structure of the metal-amine solutions and the dynamics of metal-amine systems in both liquid and crystalline forms should therefore be extended to the glass states. The structural and dynamical models presented in this work will provide a sound basis for comparison with models of the glasses.

8.3.3 Confinement of amines and metal-amine solutions

One-dimensional confinement of both ammonia and lithium-ammonia solutions will yield a change in the hydrogen-bonded structure and the nature of electronic solvation and percolation. It has been shown that hydrogen-bonding plays a significant role in the structure of bulk metal-amine solutions. In 1-D confined solutions contained in MCM porous glasses of controllable pore sizes, it is anticipated that bonding to the MCM surface will dominate at the expense of hydrogen-bonding in the liquid, giving rise to changes in the solvent structure and the macroscopic properties of the solution. The results from experiments to probe both the structure and dynamics of these quasi 1-D confined solutions should be compared with existing measurements on the bulk liquid and 2-D confined solutions (graphite intercalates). Complementary techniques such as conductivity and

magnetic resonance should also be used to investigate the fundamental issue of whether the quasi one-dimensional solutions are metallic or insulating.

8.3.4 3-D modelling and data interpretation

There is scope for further work to be carried out in the field of 3-D modelling of structural and dynamical data. The empirical potentials obtained via EPSR simulations should be tested in a molecular dynamics simulation to determine whether the resulting dynamics would resemble those obtained experimentally, and therefore whether the empirical potential provides a full physical representation of the system rather than one which is consistent with the structural data alone.

Iterative refinement of a dynamical model would be an alternative method by which dynamical information which is fully consistent with the structural data could be obtained. Given a well-sampled MD simulation which is run for a long enough time, a direct comparison could be made between the simulation and the scattering function $S(Q,\omega)$ obtained via QENS.

8.4 Concluding remarks

Metal-amine solutions are remarkable in that they exhibit a vast range of fascinating phenomena which are largely driven by the behaviour of the electron in solution. These have been summarized in Chapter 1. To date, many theoretical models of the

structure have been proposed to account for these macroscopic properties, but until recently, many of these could not be confirmed experimentally. This thesis has demonstrated the importance of 3-D modelling of structural data to reveal the crucial role of hydrogen-bonding, ionic solvation and electron solvation/delocalisation in both the structure and dynamics of alkali metal-amine solutions. In particular, this work has provided new insight into the mechanisms which govern the bulk properties such as conductivity, liquid-liquid phase separation and the metal-nonmetal transition.

8.5 References

[1] H. Thompson, J. C. Wasse, N. T. Skipper, S. Hayama, D. T. Bowron and A. K. Soper, J. Am. Chem. Soc. **125**, 2572 (2003).

[2] I. Olovsson and D. H. Templeton, Acta Cryst. **12**, 832 (1959).

[3] J. C. Wasse, S. Hayama, N. T. Skipper and H. E. Fischer, Phys. Rev. B. **61**, 11993 (2000).

[4] S. Hayama, J. C. Wasse, N. T. Skipper and H. Thompson, J. Chem. Phys. **116**, 2991 (2002).

[5] C. M. Stupak, T. R. Tuttle, Jr. and S. Golden, J. Phys. Chem. **88**, 3804 (1984).

[6] A. N. Garroway and R. M. Cotts, Phys. Rev. A. **7**, 635 (1973).